# JOURNAL OF CONDENSED MATTER NUCLEAR SCIENCE

## Experiments and Methods in Cold Fusion

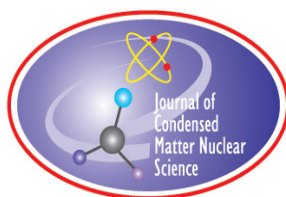# JOURNAL OF CONDENSED MATTER NUCLEAR SCIENCE

Experiments and Methods in Cold Fusion

# JOURNAL OF CONDENSED MATTER NUCLEAR SCIENCE

## Volume 8,   May 2012

# JOURNAL OF CONDENSED MATTER NUCLEAR SCIENCE

Volume 8                                                                                           2012

## CONTENTS

PREFACE

### RESEARCH ARTICLES

# PREFACE

It is a little over a year since the 16th International Conference on Condensed Matter Nuclear Science (ICCF 16) was held in Chennai, India, during February 2011. In all 85 registered participants attended the meeting of whom 55 were from overseas. Altogether 52 papers were presented inclusive of both oral and poster presentations. Of these, this first volume of the special issue of EJCMNS on ICCF 16 papers includes 20 reviewed and accepted papers.

The year gone by has indeed been a tumultuous one for the field of Condensed Matter Nuclear Science with a major breakthrough in nickel-hydrogen systems "seeming to have taken place". I say seeming because there are no peer reviewed papers on the new claims although many observers are inclined to believe, based on the reported third party witnessed semi-public demonstrations, that a breakthrough in releasing industrial level nuclear heat has indeed taken place for the first time in CMNS history since the inception of the field. These events have brought to the forefront the clash of interests between the traditional scientific procedure of reporting new findings in peer reviewed publications on the one hand and the reluctance of inventors to give out details of their discovery/invention with a view to protect the commercial and market interests of their research on the other hand. The inventors of the new Ni-H reactor technology have obviously preferred to follow the second path. However, we are confident that the science underlying these inventions will eventually get published and integrated into the body of knowledge regarded as Science, following established scientific traditions. Thus at this point in time it does appear that the field of CMNS is witnessing a major turning point of sorts.

The papers included in this issue will hopefully serve to provide a more complete picture of the Science behind these novel Low-energy Nuclear Reactions which are destined to play a crucial role in moving Nuclear Science forward into uncharted and exciting realms in service of humanity!

*Mahadeva Srinivasan*
*Chairman, Organizing Committee for ICCF 16*
*May 2012*

Research Article

# Nuclear Exothermic Reactions in Lattices Pd: A Theoretical Study of d–d Reaction

## Fulvio Frisone*

*Department of Physics, University of Catania, Via Santa Sofia 64, I- 95123 Catania*

## Abstract

The aim of this paper is to demonstrate that the Coulomb barrier has variations in both time and space. Further, in this paper, we have taken the interaction between deuteron-optical photons, we want to clarify this point, of course, these photons have a vibrational frequency of interest because it was discovered that the interaction between photons and deuterons causes the Coulomb barrier is not static, that has of oscillations in different directions within the lattice. So we can conclude that this phenomenon of cold fusion that breaks new ground in modern nuclear physics. In recent years, over 20 years, have seen thousands of experiments and theoretical models to explain the phenomenon of fusion at low energy (LENR) in specialized heavy hydrogen systems. We can say that a new possible way to obtain nuclear energy without waste is emerging. Nevertheless in spite of experimental contributions, the theoretical framework is not known. In this work, we try to explain the deuteron–deuteron reactions within palladium lattice by means of the coherence theory of nuclear and condensed matter. The coherence model of condensed matter affirms that within a deuteron-loaded palladium lattice there are three different plasmas: electrons, ions and deuterons plasma. Then, according to the loading percentage $x = D/Pd$, the ions deuterium can take place on the octahedrical sites or in the tetrahedral in the (1,0,0)-plane. In the coherence theory it is called $\beta$-plasma the deuterons plasma in the octahedral site and $\gamma$-plasma which in tetrahedral. We propose a general model of effective local time-dependent deuteron–deuteron potential, that takes into account the electrons and ions plasma oscillations. The main features of this potential are extracted by means of many-body theory considering the interaction deuteron–phonon–deuteron. In fact the phonon exchange produces a attractive component between two deuteron within the $D_2$ molecular. This attractive force is able to reduce the inter-nuclear distance from about 0.7 to 0.16 Å. It means that the lattice strongly modifies the nuclear environment with respect to free space. In this way according to deuterons energy, loading percentage and plasma frequency we are able to predict high o low tunneling probability. The fusion rates (s$^{-1}$) computed vary from $10^{-70}$ to $10^{-17}$ and also a set of other mechanism, which could be enhanced these values, are proposed. In this way we hope that by means of this approach in the future will be possible to realize and control the nuclear exothermic reactions that take place in the condensed matter in order to obtain clean energy.
© 2012 ISCMNS. All rights reserved. ISSN 2227-3123

*Keywords:* Cold fusion, Coulomb barrier, d–d Reactions, Many body

*E-mail: fulvio.frisone@ct.infn.it; Tel.: +390953785227; Fax: +390953785227

## 1. Introduction

In this model of lattice takes place within the Coherence Theory of Condensed Matter and represents a general theoretical framework accepted from most of scientists that work on cold fusion phenomena. In the coherence theory of condensed matter [5], it is assumed that the electromagnetic (e.m.) field due to elementary constituents of matter (i.e. ions and electrons) plays a very important role on system dynamics. In fact considering the coupling between (e.m.) equations, due to charged matter, and the Srödinger equation of field matter operator, it is possible demonstrate that in proximity of e.m. frequency, $\omega_0$, the matter system shows a coherence dynamics. For this reason, it is possible to speak about coherence domains whose length is about $\lambda_{CD} = 2\pi/\omega_0$. Of course, the simplest model of matter with coherence domain is the plasma system. In the usual plasma theory, we must consider the plasma frequency $\omega_p$ and the Debey length that measures the Coulomb force extension, i.e. the coherence domain length. For a system with $N$ charge $Q$ of $m$ mass within a volume, $V$, the plasma frequency can be written as

$$\omega_p = \frac{Q}{\sqrt{m}}\sqrt{\frac{N}{V}}, \tag{1}$$

$$\omega_p \approx 10 \text{ eV}/\hbar.$$

In this work, we study the "nuclear environment" that it is supposed existent within the palladium lattice $D_2$-loaded and at room temperature as predicted by Coherence Theory. In fact when the palladium lattice is loaded with deuterium gas, some peoples declared that it is possible observe traces of nuclear reactions [1–3]. For this reason, many physicist speak about Low-energy Nuclear Reaction (LENR). The more robust experiments tell us that in the $D_2$-loaded palladium case the nuclear reactions more frequent are [3,4]:

$$D + D \rightarrow {}^3H + p + 4.03 \text{ MeV}, \quad D + D \rightarrow {}^4He + 23.85 \text{ MeV}. \tag{2}$$
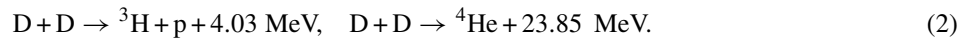
Thus, an experimental analysis of this phenomenon requires neutron, proton and gamma rays detectors. A brief list follows of detectors that are most frequently quoted in the literature. Further (n = neutron, p = proton, in parenthesis the probabilities of the three final branches). The first step in the reaction is the creation of a ${}^4He$ nucleus with an excess energy of 24 MeV.

This reaction has been extensively studied, mostly, through experiments performed with the help of particle accelerators, which means in quasi-vacuum and with energetic particles (>105 eV). This is quite different from the CF experiments, which take place in condensed matter at room temperature (energies of the order of a small fraction of an eV).

In this work, we also propose a 'coherence' model by means of which we can explain the occurrence of nuclear reactions and their probability according to the more reliable experiments. First, we will start from the analyze of environment, i.e., of plasmas present within palladium (d-electron, s-electron, Pd-ions and D-ions) using the coherence theory of matter; finally, we will use the effective potential reported in [7,8] adding the role of lattice perturbations by means of which we compute the d–d tunneling probability.

## 2. The Plasmas Present within No Loaded Palladium

According to Coherence Theory of Condensed Matter, in a Pd crystal at room temperature the electron shells are in a coherent regime within coherent domain. In fact, they oscillate in tune with a coherent e.m. field trapped in the coherent domains. For this reason, in order to describe the lattice environment, we must take into account the plasma of s-electron and d-electron.

2.1. The plasma of the d-electrons

They are formed by electrons of palladium d-shell. We can start computing:

$$\omega_{\mathrm{d}} = \frac{e}{\sqrt{m}} \sqrt{\frac{n_{\mathrm{d}} N}{V}} \tag{3}$$

as d-electrons plasma frequency. As already seen in the chapter about plasmas, this value must be increased by a 1.38 factor in the case of a real plasma, due to distribution of neutralizing charges (Pd ions, in this case).

We can understand this correction observing that formula (**??**) is obtained assuming a uniform d-electron charge distribution. But of course the d-electron plasma is localized in a shell of radius $R$ (that is about 1 Å), so the geometrical contribution is

$$\sqrt{\frac{6}{\pi R}} = 1.38. \tag{4}$$

Labeled with $\omega_{\mathrm{de}}$ the *renormalized* d-electron plasma frequency, we have [5]:

$$\omega_{\mathrm{de}} = 41.5 \ \mathrm{eV}/\hbar \tag{5}$$

and the maximum oscillation amplitude $\xi_{\mathrm{d}}$ is about 0.5 Å.

2.2. The plasma of delocalized s-electrons

The s-electrons are those which in the lattice neutralize the adsorbed deuterons ions. They are delocalized and their plasma frequency depends on loading ratio (D/Pd percentage) by means of the following formula [5]:

$$\omega_{\mathrm{se}} = \frac{e}{\sqrt{m}} \sqrt{\frac{N}{V}} \sqrt{\frac{x}{\lambda_{\mathrm{a}}}}, \tag{6}$$

where

$$\lambda_{\mathrm{a}} = \left[ 1 - \frac{N}{V} V_{\mathrm{pd}} \right] \tag{7}$$

and $V_{\mathrm{pd}}$ is the volume effectively occupied by the Pd-atom. As reported in [5], we have

$$\omega_{\mathrm{se}} \approx x^{1/2} 15.2 \ \mathrm{eV}/\hbar. \tag{8}$$

For example for $x = 0.5$, we have $\omega_{\mathrm{se}} \sim 10.7 \ \mathrm{eV}/\hbar$.

2.3. The plasma of Pd-ions

Finally, we must consider the plasma due to palladium ions that form the lattice structure. In this case, it is possible to demonstrate that the frequency is [5]

$$\omega_{\mathrm{pd}} = 0.1 \ \mathrm{eV}/\hbar. \tag{9}$$

## 3.  The Plasmas Present within D$_2$-loaded Palladium

We know that the deuterium is adsorbed when is placed near to palladium surface. This loading can be enhanced using electrolytic cells or vacuum chambers working at opportune pressure [9,10]. By means theory of Condensed Matter, we are assumed that according to the ratio $x =$ D/Pd, three phases concerning the D$_2$–Pd system exist:

  (1)  phase $\alpha$    for $x < 0.1$,
  (2)  phase $\beta$     for $0.1 < x < 0.7$,
  (3)  phase $\gamma$    for $x > 0.7$.

In the $\alpha$tphase, the D$_2$ is in a disordered and not coherent state (D$_2$ is not charged!). Regarding the other phases, we start remembering that on surface, due to lattice e.m., takes place the following ionization reaction:

$$D_{lattice} \rightarrow D^+ + e^-. \tag{10}$$

Then, according to the loading percentage $x =$ D/Pd, the ions deuterium can take place on the octahedrical sites or in the tetrahedral in the (1,0,0)-plane. In the coherence theory it is called $\beta$-plasma the deuterons plasma in the octahedral site and $\gamma$-plasma which in tetrahedral. Regarding to $\beta$-plasma it is possible affirms that the plasma frequency is given by [5]:

$$\omega_\beta = \omega_{\beta 0}(x + 0.05)^{1/2}, \tag{11}$$

where

$$\omega_{\beta 0} = \frac{e}{\sqrt{m_D}} \left( \frac{N}{V} \right)^{1/2} \frac{1}{\lambda_a^{1/2}} = \frac{0.15}{\lambda_a^{1/2}} \ eV/\hbar. \tag{12}$$

For example, if we use $\lambda_a = 0.4$ and $x = 0.5$ it is obtained $\omega_{\beta g}$ 0.168 eV/$\hbar$.

In the tetrahedral sites, the D$^+$ can occupy the thin disk which encompass two sites.

They present to the D$^+$ ions a barrier. Note that the electrons of the d-shell oscillate past the equilibrium distance $y_0$ (about 1.4 Å ) thus embedding the ions in a static cloud of negative charge (whose can screen the Coulomb barrier). So, as reported in [5], we have

$$\omega_\gamma = \sqrt{\frac{4Z_{eff}\alpha}{m_D y_0^2}} \approx 0.65 \ eV/\hbar. \tag{13}$$

Of course, this frequency depends also on chemical condition of palladium (impurities, temperature, etc.). Due to a large plasma oscillation of d-electrons, in the disk-like tetrahedral region (where the $\gamma$-phase D$^+$'s are located) a high-density negative charge condenses giving rise to a screening potential $W(t)$.

We emphasize that the $\gamma$-phase depends on $x$ value and that this new phase has been experimentally observed [11].

## 4.  The d–d Potential

In [7], it was shown that the phenomenon of fusion between many body, i.e. nuclei of deuterium in the lattice of a metal is conditioned by the structural characteristics, by the dynamic conditions of the system, and also by the concentration of impurities present in the metal under examination. In fact, studying the curves of the potential of interaction between deuterons (including the deuteron–plasmon contribution) in this case typical metals Pd, a three-dimensional model showed that the height of the Coulomb barrier decreases on varying the total energy and the concentration of impurities

present in the metal itself. The starting potential that links like-Morse attraction and like-Coulomb repulsion can be written in this way [7,8]:

$$V(r) = k_0 \frac{q^2}{r} \left( V(r)_{\mathrm{M}} - \frac{A}{r} \right). \tag{14}$$

In (**??**), $V(r)_{\mathrm{M}}$ is a like-Morse potential and is given by:

$$V(r)_{\mathrm{M}} = D \left\{ \exp\left( -2\varphi\ (r - r_0)\right) 2 \exp\left( -\varphi\ (r - r_0)\right) \right\}, \tag{15}$$

Here, the parameters $A$, $\varphi$ and $r_0$ depend on model. In fact the potential (**??**) is an effective potential whose reliability is demonstrated from its ability to fit the Coulomb potential for $r \to 0$ and the Morse potential in the attractive zone. In this way, following Siclen and Jones [12] define $\rho$ the point where the Coulomb potential is linked by Morse trend, $r_0'$ the equilibrium distance and $D'$ the well. Of course, in the free space for a $D_2$ molecular $\rho$ is about 0.3 Å , $r_0'$ is about 0.7 Å and $D'$ is – 4.6 eV. But within the lattice the screening effect and the deuteron–deuteron interaction by means of phonon exchange modify very much these parameter values.

Taking into account, the role of coupling between deuteron and plasmons, in [13] the authors have numerically evaluated a d–d potential having the features of potential (**??**) with $D' = -50$ eV and $r_0' = 0.5$ Å and $\rho = 0.2$ Å (in [13] the authors consider only two plasmon excitations at 7.5 and 26.5 eV).

Since the screening effect can be modulated by donor atoms, we have considered in [7,8] the role on impurities and has been demonstrated that we can put:

$$A = JKTR \tag{16}$$

and

$$B = J/\varsigma. \tag{17}$$

Here, $J$ is the impurities concentration, $KT$ the lattice temperature, $R$ the nuclear radius and $\zeta$ a parameter to evaluate by fitting.

Finally, we can write the effective d–d potential in this way:

$$V(r) = k_0 \frac{q^2}{r} \left( V(r)_{\mathrm{M}} - \frac{JKTR}{r} \right). \tag{18}$$

In this work, according to coherence theory of condensed matter, we study the role of potential (**??**) in the three different phases: $\alpha$, $\beta$ and $\gamma$. Whereas regarding the second point, the question is more complicate. In fact, the lattice environment is a mixing of coherent plasmas (ion Pd, electron and deuterons plasma) at different temperature, due to different masses, thus describing a emerging potential is very hard office. The method that in this work we propose is the following: considering the total screening contribution of lattice environment at d–d interaction (i.e. $V_{\mathrm{tot}}$) as random potential $Q(t)$. So in this model we can write

$$V_{\mathrm{tot}}(t) = V(r) + Q(t). \tag{19}$$

Of course, we assume that:

$$\langle Q(t) \rangle_t \neq 0 \tag{20}$$

that is, we suppose that $Q(t)$ (a second-order potential contribution) is a periodic potential (the frequency will be labeled by $\omega_Q$) that oscillates between the maximum value $Q_{\mathrm{max}}$ and 0. More exactly, the charge oscillations of d-shell produce

a screening potential having an harmonic features:

$$eV(r) = -Z_d \frac{ke^2}{2a_0} r^2. \tag{21}$$

In [5], putting $Z_d = 10/3$ and $a_0 = 0.7$ Å, it is evaluated a screening potential $V_0$ of about 85 eV. In this way, we can compute $\rho g V_0/26.9$ and at last $\rho = 0.165$ Å.

To summarize, we can have the following cases in a palladium lattice according to loading ratio.

### 4.1. $\alpha$-Phase

In phase $\alpha$sghe deuterons are in a molecular state and the thermal motion is about:

$$0.02 \text{ eV} < \hbar\omega_\alpha < 0.1 \text{ eV}.$$

This phase takes places when $x$ is less than 0.1, and since $W(t)$ is zero, the d–d potential is

$$V(r) = k \frac{q^2}{r} \left( V_M(r) - \frac{J \hbar\omega_\alpha R}{r} \right). \tag{22}$$

Expression (**??**) has been partially evaluated in a previous paper [7] but in that case we was interesting only to the dependence of tunneling probability on impurities present within lattice. In this work, we examine the correlation between potential features and loading ratio. In the paragraph 5 we will show some numerical results.

### 4.2. $\beta$-Phase

When $x$ is bigger than 0.1 but less than 0.7, the phase $\beta$ happens. The interaction takes place between deuteron ions that oscillate by following energy values:

$$0.1 \text{ eV} < \hbar\omega_\beta < 0.2 \text{ eV}.$$

In this case, $W(t)$ is zero, so the potential is given expression (**??**):

$$V(r) = k \frac{q^2}{r} \left( V_M(r) \frac{J \hbar\omega_\beta R}{r} \right). \tag{23}$$

Comparing expressions (**??**) and (**??**) seems very clear that the weight of impurities is more important in the $\beta$-phase. Of course, this conclusion is in according to the previous papers [7,8], where we studied the role of temperature on tunneling effect.

### 4.3. $\gamma$-Phase

Finally, when the loading ratio is higher than 0.7, the deuteron–palladium system is in the phase $\gamma$.

This is the more interesting case. The deuterons undergo the screening due to d-electrons shell, so we suppose that the d–d potential must be computed assuming that the well present in potential 14, due to Morse contribution, disappears. In fact if we use a classical plasma model where are the D$^+$ ions the positive charge and the d-electrons the negative, it is very reasonable suppose that we must use the following potential:

$$V(r, t) = k \frac{q^2}{r} \left( V_M(r) \frac{J \hbar\omega_\gamma R}{r} \right) + Q(t). \tag{24}$$

We emphasize that $Q(t)$ is a not known perturbative potential. About it we can only say that:

$$\langle Q(t) \rangle_t \approx \frac{W_{\max}}{\sqrt{2}}. \tag{25}$$

As said previously, we suppose that it is the screening potential due to d-electrons and its role is that to reduce the repulsive barrier, i.e. $\rho$ and $r'0$.

In next evaluation, we put

$$\langle Q(t) \rangle_t \approx 85 \text{ eV}. \tag{26}$$

## 5. Results and Discussions

Now we present the d–d fusion probability normalized to number of events per second regarding the d–d interaction in all different phase. More exactly we compare the fusion probability in the phases $\alpha$, $\beta$ and $\gamma$ at varying of energy between −50 and 50 eV. We also consider the role of d-electrons screening as perturbative lattice potential. This treatment, which interests only the case where $Q(t)$ is different from zero, involves that we change the value of point on the $x$-axes where the Coulomb barrier takes place and, in this case, the final result is that the screening enhances the fusion probability. In order to evaluate the fusion rate ($\Lambda$), we applied this formula:

$$\Lambda = A\Gamma. \tag{27}$$

In this case, the Morse potential will be

$$V(r)_M = D \exp\left(-2\,\varphi\,(r-r_0)\right) 2 \exp\left(\varphi\,(r-r_0)\right),$$

$$E_1 = \text{a few eV},$$

$$E_2 = -D\left(1 - \frac{\gamma\,\hbar}{\sqrt{2\mu\,D}}\left(\nu + \frac{1}{2}\right)\right)^2,$$

$$E_3 \sim \left(\frac{m_e}{M_N}\right) E_1 \sim \frac{1}{1000} \text{ eV},$$

$$E_4 = D',$$

where $\gamma$ is the constant of anharmonicity of the metal and $\nu$ is the vibrational constant. Another important quantity is D′, which is the depth of the potential well: $D$ this is Morse potential

Now an energy tensor $E_{ij}$ can be built:

$$E_{11} = E_1, \quad E_{22} = E_2, \quad E_{33} = E_3, \quad E_{44} = E_4, \quad E_{ij} = E_i - E_j, \quad E_{ij} = -E_{ji}.$$

Thus, a square quadratic energy value can be determined.

For this case, we assumed a Morse potential as the most realistic.

$$I \approx \frac{e^2\pi Z_a Z_X}{4\pi\varepsilon_0\,\hbar\,\nu}$$

is the Gamow factor and $A$ is the nuclear reaction constant obtained from measured cross sections (value used was $10^{22}$ s$^{-1}$).
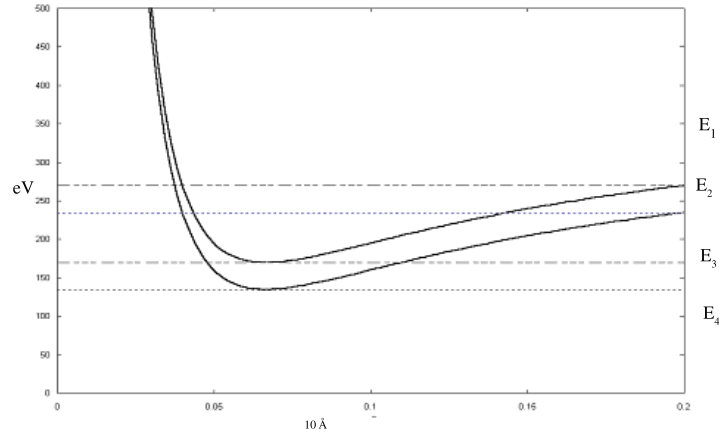
**Figure 1.** Features of $V(r)$ and $V(r) + W_{\max}/\sqrt{2}$.

The probability partial reaction that takes into account the factor penetration of the barrier, with $\Gamma$ Gamow factor. Furthermore, the potential can be considered adiabatic to a very good approximation. In fact, the adiabatic parameter $\hbar(I/V(R))(dV(R)/dt) < 0.1$ eV, which is much smaller than the plasmon energies (or other typical electron excitation energy).

To have an estimate of the consequence of this result on the d–d fusion rate, let us model the deuterons inside palladium as a classical gas interacting through the total conservative potential depicted in Fig. 1 (full line), at a temperature $T'$.

From the point of experimental view, in the cold fusion phenomenology, it is possible to affirm that there are three typology of experiments [14]:

(1) those that have given negative results,
(2) those that have given some results (little detection signs with respect to background, fusion probability about $10^{-23}$ using a very high loading ratio
(3) those that have given clear positive results as Fleischmann and Pons experiments.

Nevertheless, we think that the experiment like 3-point are few accurate from a point of experimental view. For this reason, we believe that a theoretical model of controversial phenomenon of cold fusion, must explain only the experiments like points 1 and 2. In this case need consider the role of loading ratio on the experimental results. Now, let us begin from $\alpha$-phase. It is possible affirms that if we load the deuterium with a percentage $x < 0.2$ we do not observe any fusion event! The same absence of nuclear phenomenon is compatible for a loading ratio of about 0.7. Since in this case the predicted fusion probability is less than $10^{-42}$. These predictions, of course, are in agreement to the experimental results. But for $x > 0.7$ a set of valid experiments on cold fusion report some background spikes (e.g. see [6]). The remarkable result of our model is that in the $\gamma$-phase, as shown in Table 3, we can really observe some background fluctuations, since we predict a fusion probability about $10^{-22}$ due to a very high loading ratio. This represents a new result with respect to [7,8] since, in those cases, the fusion probability was independent on loading ratio. To conclude we shown that the model proposed in this paper (which unify nuclear physics with condensed matter) can explain some anomaly nuclear traces in the solids. Regarding the experiments at point 3 supposing that they could
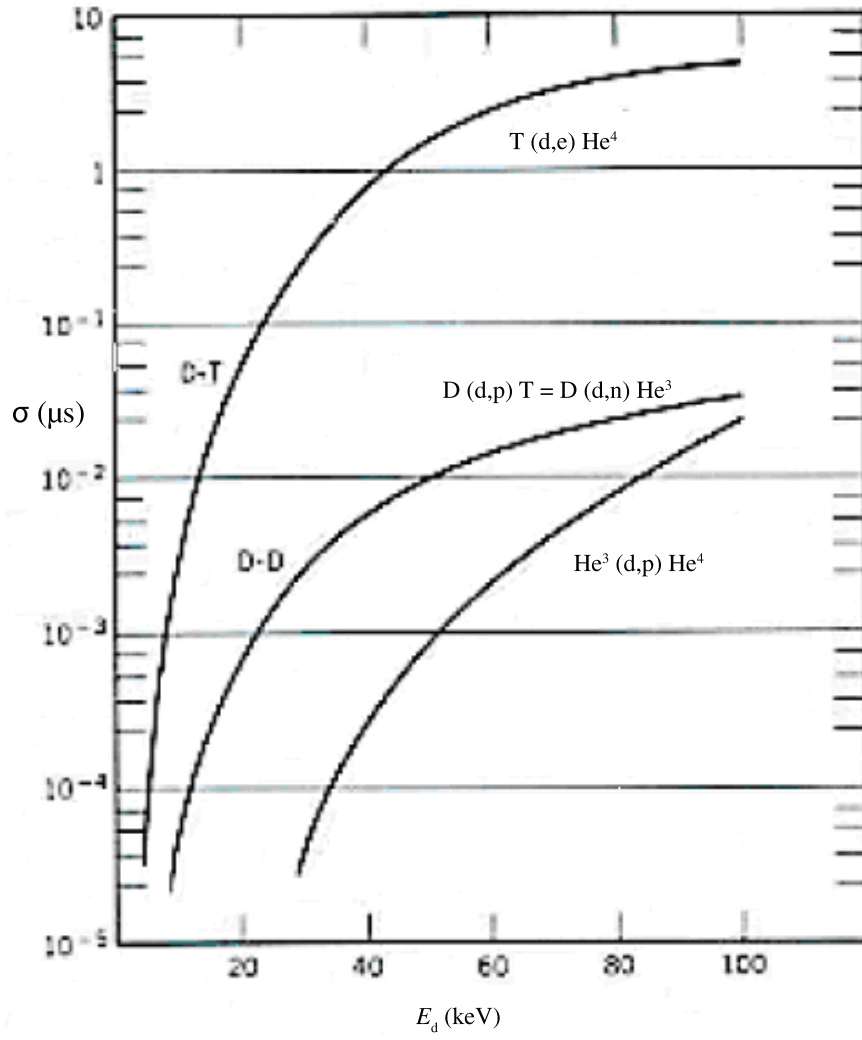
**Figure 2.**   xxx.
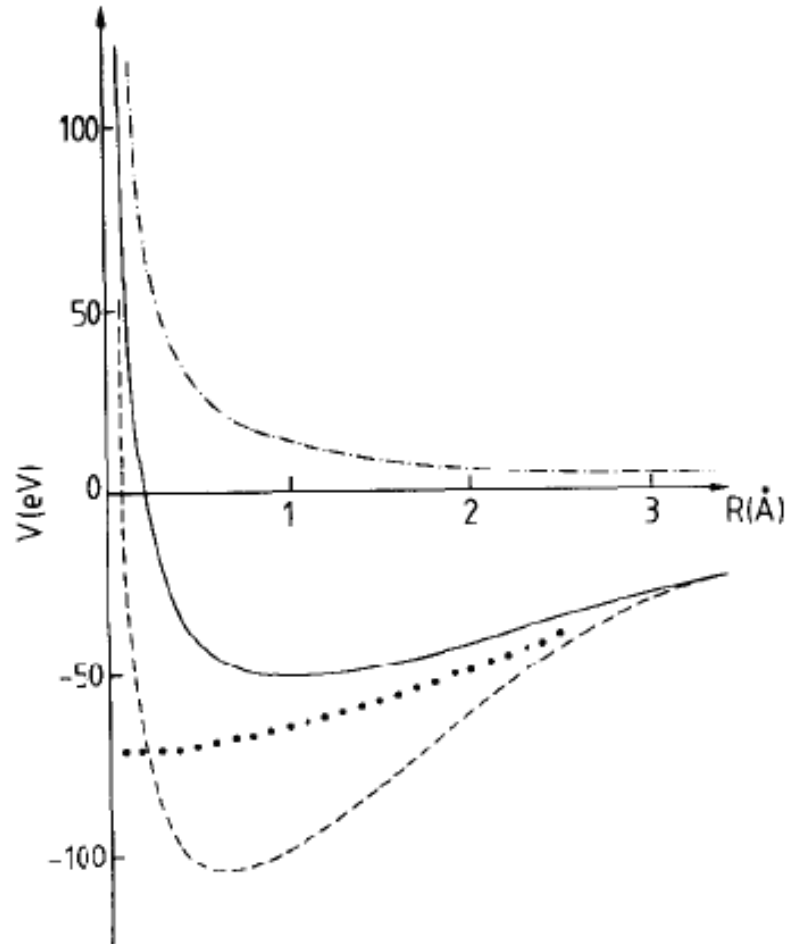
**Figure 3.**   Interaction potentials in eV as a function of d–d distance $R$ in Å.

be real, we would invoke other contribution as micro-deformation occurrence in order to explain the very high fusion rate. The role of micro-crack and of impurities linked by loading ratio will be explored in other speculative works. May be the nuclear physics within condensed matter will be a new very productive scientific topic.

**References**

[1]   G. Preparata et al., *Glasses: A New View from QED Coherence*, MITH-98/9,
           http://arxiv.org/abs/cond-mat/9906395v1
[2]   G. Preparata, *Bose–Einstein vs. Electrodynamic Condensates: The Question of Order and Coherence*, MITH-98/8,
         http://arxiv.org/abs/cond-mat/9812018v1
[3]   G. Preparata, A *Tale of Two Condensates: the Odd Bose–Einstein Condensation of
           atomic Hydrogen,* MITH-98/10, http://arxiv.org/abs/cond-mat/9812011v1

[4]   Melvin H. Miles et al., *Fusion Technol.* **25** (1994) 478.
[5]   G. Preparata, *QED Coherence in Matter*, World Scientific, Singapore, 1995.
[6]   S. Aiello et al., *Fusion Techno.* **18** (1990).
[7]   F. Frisone, *Fusion Technol.* **39** (2001) 260.
[8]   F. Frisone, *Fusion Technol.* **40** (2001) 139.
[9]   M. Fleishmann and S. Pons, *J. Electroanal. Chem.* **261** (1989) 301–308.
[10]  A. De Ninno et al., *Europhys. Lett.* **9** (**??**) (1989) 221–224.
[11]  G. Mengoli et al., *J. Electroanal. Chem*. **350** (1989) 57.
[12]  C. DeW Van Siclen and S. E. Jones, *J. Phys. G. Nucl. Phys*. **12** (1986).
[13]  M. Baldo and R. Pucci, *Fusion Technol.* **18** (1990) 47.
[14]  D. Morrison, *Physics World*, 1990.

Research Article

# Investigations of Possible Shuttle Reactions in Co-deposition Systems

Melvin H. Miles*

*Dixie State College, St. George, UT 84770, USA*

## Abstract

Experiments in the 0.025 M $PdCl_2$ + 0.15 M $ND_4Cl$ + 0.15 M $ND_4OD/D_2O$ co-deposition system produced anomalous excess power in three out of three prior experiments in Japan. Completely new experiments have produced even larger excess power effects for this deuterated co-deposition system. The largest excess power effect in $D_2O$ produced 1.7 W or about 13 W/g of palladium (160 W/cm$^3$). These large excess power effects were absent in extensive studies of $H_2O$ controls. Excess power was also absent in various experiments involving the co-deposition of ruthenium (Ru), rhenium (Re), and nickel (Ni) in both $H_2O$ and $D_2O$ ammonia solutions. The statistical analysis of all 18 co-deposition experiments yields a probability of greater than 99.9989 % that the co-deposition excess power effect requires both palladium metal and $D_2O$. Shuttle reactions have been proposed to explain the reproducible excess power effect in this ammonia co-deposition system. However, various electrochemical studies show no evidence for any shuttle reactions in this ammonia system. Nevertheless, the initial chemistry for the Pd system is complex leading to large pH changes, chlorine ($Cl_2$) evolution, and the formation of nitrogen trichloride ($NCl_3$) during the first few days. However, the large excess power effects are observed later in the experiments after this chemistry is completed. A better understanding of the chemistry should be helpful in the reproduction of anomalous excess power in co-deposition systems.
© 2012 ISCMNS. All rights reserved. ISSN 2227-3123

*Keywords:* Ammonia, Calorimetry, Electrochemistry, Excess Power, Palladium

## 1. Introduction

Anomalous energy or power observed in the Pd/D system is often called the Fleischmann–Pons Effect (FPE) to avoid the controversy of labeling this as a nuclear process. However, the term Chemically Assisted Nuclear Reactions (CANR) is also used to stress the important role of chemistry. The understanding of the chemistry involved is especially important for this study of the FPE in Pd/D co-deposition systems.

Anomalous effects for Pd/D co-deposition were first reported by Szpak and Mosier-Boss using the $PdCl_2$ + $LiCl/D_2O$ system [1,2]. However, commercial electroplating baths for palladium are often based on $Pd(NH_3)_2Cl_2$ in aqueous $NH_4Cl/NH_3$ at pH 7–10 [3]. This related $PdCl_2$ + $ND_4Cl$ + $ND_4OD/D_2O$ ammonia system previously produced large

---

*E-mail: melmiles1@juno.com

excess power (FPE) in all three experiments conducted in 1998 at the New Hydrogen Energy (NHE) laboratory in Japan [4–6]. Features observed in this new co-deposition system such as the effect of thermal perturbations (positive feedback) and the effect of cell current perturbations (heat-after-death) were similar to anomalous effects observed in other Pd–D systems [6]. Nevertheless, the reproduction of co-deposition effects by other groups has proven to be illusive, hence a better understanding of the chemistry is needed. Recent studies [7] have shown that each $Pd^{++}$ ion deposited is replaced by two $H^+$ ($D^+$) ions to maintain electroneutrality, and the electrolysis gases gradually drive off the ammonia, thus large pH changes occur (pH = 8.87–1.25) during the first few days of electrolysis. Chlorine evolution and the formation of yellow nitrogen trichloride ($NCl_3$) are observed with Pd under acidic conditions, but these chemical effects dissipate within the first three days in an open system [7]. The large excess power effects measured in $D_2O$, but not in $H_2O$, occur after the yellow solution coloration due to the $NCl_3$ has cleared. Although the Naval Research Laboratory (NRL) reproduced an excess power effect for this $PdCl_2 + ND_4Cl + ND_4OD/D_2O$ system in 2009 using an open Seebeck calorimeter [8], they proposed that the effect may be due to chemical and electrochemical shuttle reactions (a form of recombination) involving nitrates or chlorates that may form in this system [9,10]. We report here various electrochemical studies designed to test for possible shuttle reactions involving nitrates, nitrites, and chlorates. Previous calorimetric experiments showed no excess power effects for either the potassium nitrate ($KNO_3$) electrolyte [11,12] or the sodium chlorate ($NaClO_3$) electrolyte [11].

## 2. Experimental

Electrochemical studies such as cyclic voltammetry (CVA) and electrochemical impedance spectroscopy (EIS) were performed using the Princeton Applied Research (PAR) PARSTAT 2273 with the appropriate software (PowerCV, PowerPULSE, PowerSINE). Calorimetric studies used a new isoperibolic design as previously reported [11,12]. Temperatures were measured to within $\pm 0.005$ K using a Cole Parmer Thermistor Thermometer unit consisting of five thermistor probes. The bath temperature was controlled to within $\pm 0.005$ K by use of a Techne TE-100 unit. The constant current used in calorimetric studies was provided by the PAR Model 363 Potentiostat/Galvanostat or by the PAR Model 362 Scanning Potentiostat. The solution pH was monitored using a Oakton pH 6 Acorn Series pH/mV/°C meter ($\pm 0.01$ pH units). Commercial chlorine detectors (Chromair System) were used to monitor the gases escaping from the cell. The deuterated chemicals used were ACROS $D_2O$ (99.8 atom% D), ACROS $ND_4Cl$ (98 atom% D), and ACROS $ND_4OD$ (99 atom% D) while Alfa-Aesar Premion $PdCl_2$ (99.999% metals basis) was the palladium source. A copper cathode ($0.318 \times 2$ cm, 99.999%) from Alfa-Aesar (Puratronic) served as the substrate ($A = 2.1$ cm$^2$).

## 3. Results

### 3.1. Reactivity of various metals with the solution

The 0.025 M $PdCl_2$ dissolves in the 0.15 M $ND_4Cl$ to give an orange solution. However, the addition of 0.15 M $ND_4OD$ produces an orange colored precipitate by the proposed reaction

$$PdCl_2 + 2\,ND_4OD \rightarrow Pd(OD)_2 + 2\,ND_4Cl, \qquad (1)$$

where $Pd^{++}$ ions removed by precipitation are replaced by additional $ND_4^+$ ions. The exact nature of this precipitate is unknown, but the addition of alkali to aqueous solutions of palladium ions ($Pd^{++}$) produces a precipitate of the hydrous oxide [13]. Nevertheless, the resulting low activity of palladium ions explains the stability of the copper cathode towards the displacement reaction, $Cu + Pd^{++} \rightarrow Cu^{++} + Pd$, in this initial solution. It was found experimentally that the metals Cu, Ag, Ni, Co, Fe and Al all showed displacement reactions with the $PdCl_2 + NH_4Cl$ solution prior to the addition of $NH_4OH$ or $ND_4OD$ that precipitates palladium ions (Eq. (1)). The displacement reaction involving the various metal wires could be visually observed by the darkening of the metal surface by the palladium deposit. These displacement

reactions can be a source for metal ion impurities in co-deposition systems that may affect the FPE reproducibility. No reactions were observed for these metals following the addition of the ammonia solution to give the precipitation reaction. However, placing the copper substrate directly into the orange colored precipitate where there was a higher palladium ion activity led to a gradual darkening of the copper. There were several metals (Pt, Mo, Ta and Hf) that gave no reactions before or after the palladium precipitation. Stable oxide films likely protect Mo, Ta, and Hf while Pt is an unreactive noble metal similar to Pd.

## 3.2. The palladium deposition step

A low current of 6.00 mA (2.86 mA/cm$^2$ based on the initial copper cathode area) was used for 24 h or more for the palladium deposition and gave a cell voltage of about 2 V. The net cell reaction for the palladium deposition step can be expressed as

$$Pd(OD)_2 \rightarrow Pd + {}^1/_2O_2 + D_2O. \tag{2}$$

Deuterium gas is also formed at the cathode and is co-deposited as $PdD_X$. Theoretically, the deposition of all of the palladium onto the copper cathode would require only 11.2 h at 6.00 mA if all of the cathodic current were used for the reduction of palladium ions. Thus, more than half of the cathodic current during the first 24 h is used for the reduction of $D_2O$ to form $D_2$ gas at the cathode, $2 D_2O + 2 e^- \rightarrow D_2 + 2 OD^-$, rather than palladium deposition, $Pd(OD)_2 + 2 e^- \rightarrow Pd + 2 OD^-$.

The deposition of palladium onto the copper substrate gradually produces a very large electrode capacitance ($C$). As reported previously [7], this increasing capacitance effect can be seen by the gradual tilting and collapsing of the cyclic voltammogram traces during the palladium deposition step. The black dendritic palladium deposit produces capacitance values equal to those of supercapacitor materials (370 F/g). The measured electrode capacitance indicates that the deposited palladium gives an effective surface area of $10^6$ cm$^2$ (Ref. [7]). The deposited dendritic black palladium is in the form of nanoparticles that have an unusually large capacitance [7]. The resulting large $RC$ time constant, where $R$ is the cell resistance, distorts the cyclic voltammograms into approximately Ohm's law behavior [7,14].

The $PdCl_2 + NH_4Cl + NH_4OH/H_2O$ system serves as a buffered solution, hence there are only slight pH changes during the palladium deposition step at 6.00 mA. In one $H_2O$ experiment, the initial pH was 8.87 while the pH was measured at 8.70 when the palladium deposition was complete. However, the application of higher currents drives off the ammonia, the buffering capacity is lost, and large pH changes are observed. The replacement of 0.025 M $Pd^{++}$ ions by 0.050 $H^+$ to maintain electroneutrality would give a measured pH of 1.30. This transition to an acidic solution at higher currents is always marked by a noticeable decrease in the magnitude of the cell voltage because $H^+$ ions are reduced more readily than $H_2O$ molecules. An example of this cell voltage change observed in a $H_2O$ control cell is shown in Fig. 1. The initial pH for the electrolysis at 20 mA (Fig. 1) was 8.70 and the final pH was 1.75. The sharp change in the cell voltage near 70,000 s mirrors the sharp transition to an acidic solution (pH = 8 to pH = 2).

There is a much higher overvoltage at the cathode for the reduction of $H_2O$ molecules, $2H_2O + 2e^- \rightarrow H_2 + 2 OH^-$, than there is for the direct reduction of hydrogen ions, $2 H^+ + 2e^- \rightarrow H_2$. Molecular bonds must be severed for $H_2O$ reduction but not for $H^+$ reduction. As soon as the reduction of $H^+$ can carry a significant fraction of the cathodic current, a net decrease in the magnitude of the cell voltage is observed. This effect has been seen in every experiment involving this system including the NRL experiments [8–10]. Previous studies have established that the reduction of hydrogen ions is the charge-transfer reaction in the acidic pH range, and the direct reduction of water is the predominant charge-transfer mechanism at higher pH values [15].

The observed change in pH can be simply explained by the equilibrium reaction

$$NH_3 + H^+ \leftrightarrow NH_4^+. \tag{3}$$

The presence of ammonia ($NH_3$) gas dissolved in water is often represented as $NH_4OH$, but this is not an actual compound. The dissolved ammonia acts as a buffer and converts the $H^+$ ions produced to $NH_4^+$ as shown in Eq. 3. However, when the dissolved $NH_3$ gas is driven off by the electrolysis gases, then this $NH_4^+$ reverts back to $H^+$. Thus, the simple chemistry of Eq. (3) readily explains the large pH change observed in this system at the higher currents. The measured pH of 1.25 following the palladium deposition and the loss of the ammonia is in close agreement with the net cell reaction

$$Pd^{++} + H_2O \rightarrow Pd + {}^1\!/_2 O_2 + 2H^+, \tag{4}$$

where Pd deposits at the cathode and oxygen forms at the anode and each deposited $Pd^{++}$ ion is replaced by two $H^+$ ions. Thus, the 0.0272 M $PdCl_2$ actually used in this experiment becomes 0.0544 M HCl (pH = 1.26) when the palladium deposition in the $H_2O$ experiment is completed and all the ammonia is driven off. This large pH change is the normal behavior expected for any palladium co-deposition system. Similar pH changes will occur for the deposition of other metals.

### 3.3. Production of chlorine and nitrogen trichloride

The transformation to acidic solution (HCl or DCl) shown in Fig. 1 makes chlorine evolution thermodynamically more competitive with the oxygen evolution at the anode, $2\,Cl^- \rightarrow Cl_2 + 2e^-$ versus $H_2O \rightarrow {}^1\!/_2\,O_2 + 2\,H^+ + 2e^-$ ($E_o$ = 1.3583 V for $Cl_2$ and 1.2288 V for $O_2$ in acid at standard conditions). Although oxygen evolution is still favored in acidic solutions by thermodynamics, the electrode kinetics are slow due to the breaking of bonds in the $H_2O$ molecule to form oxygen. Therefore, the formation of chlorine as well as oxygen occurs at the anode in acidic solutions. This was shown by the use of chlorine detectors [7]. The introduction of chlorine gas into an acidic $NH_4Cl$ solution is known to produce nitrogen trichloride

$$NH_4Cl + 3Cl_2 \rightarrow NCl_3 + 4HCl. \tag{5}$$

Nitrogen trichloride is a volatile, yellow oily liquid of high density (1.653 g/cm$^3$), only slightly soluble in water, and explosive in pure form. The formation of $NCl_3$ could be readily observed experimentally as a yellow solution
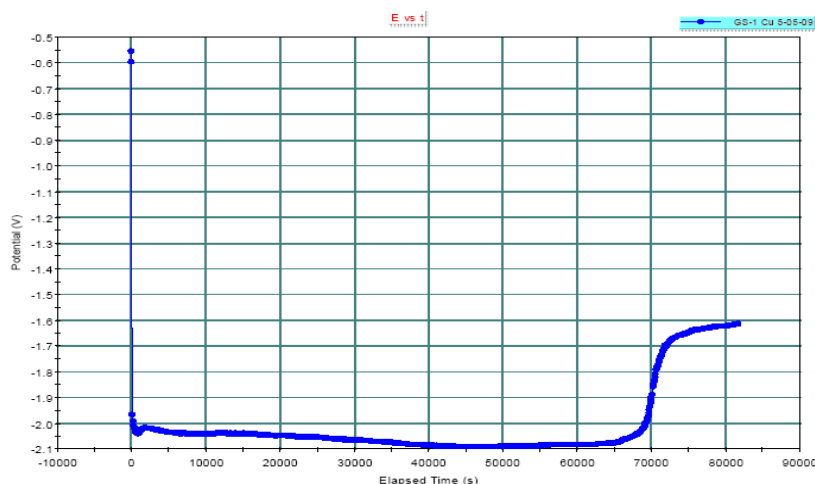


**Figure 1.** Change in cell voltage with time at a constant current of $I$ = 20 mA for the $PdCl_2 + NH_4Cl + NH_4OH\,/H_2O$ system.

coloration during the $Cl_2$ evolution period as well as by an unpleasant pungent odor. Sometimes the $NCl_3$ could be seen as a small yellow pool at the cell bottom. Although no incidents have been observed, the reported explosive nature of $NCl_3$ makes it mandatory to keep the cell behind a safety shield. A possible positive feature of $NCl_3$ formation is that this substance may react with and remove solution impurities and electrode poisons that block the FPE. This would explain the greater reproducibility in this ammonia co-deposition system.

## 3.4. Chemical excess power due to nitrogen trichloride

In every palladium co-deposition experiment in $H_2O$ or $D_2O$, a chemical excess power effect is observed for about one day when the yellow coloration due to $NCl_3$ is present. The dissolved $NCl_3$ that gives the yellow solution coloration likely reacts with the hydrogen generated at the cathode. This reaction

$$NCl_3 + 3H_2 \rightarrow NH_4Cl + 2HCl \tag{6}$$

is exothermic with an enthalpy change of $-864$ kJ/mol.

Figure 2 shows the calorimetric excess power effect measured in a $H_2O$ control for this chemical reaction of $NCl_3$ with $H_2$. The measured chemical power effect was near zero when the current was increased from 6 to 100 mA and then rose to a peak power of 112 mW. This chemical power effect was gone within 24 h. A similar chemical excess power effect was observed by NRL early in their experiment that used an open Seebeck calorimeter [8–10].

The total chemical enthalpy measured in Fig. 2 was $-5.40$ kJ that corresponds to the reaction of 0.00625 mol of $NCl_3$. Theoretically, the chemical excess power for Reaction 6 can be expressed as

$$P = (1 - \gamma)IE_H, \tag{7}$$

where $\gamma$ is the fraction of the electrogenerated hydrogen that does not react and escapes the cell, $I$ the current in Amperes, and $E_H$ is the thermoneutral potential for Reaction 6 (1.49 V at standard conditions). Initially, the dissolved $NCl_3$ may react with all of the electrogenerated hydrogen ($\gamma = 0$) to give a maximum theoretical peak power of 149 mW at $I = 0.100$ A, assuming $E_H = 1.49$ V. As more and more of the $NCl_3$ is consumed, $\gamma$ approaches unity and $P$ decreases as described by Eq. (7) and illustrated in Fig. 2. The chemical excess power due to $NCl_3$ is zero in less than 24 h. The yellow coloration due to $NCl_3$ is also gone at this point. In contrast to Pd, no chemical excess power or evidence for $NCl_3$ was found in the co-deposition of Ru, Re, and Ni in $H_2O$ or $D_2O$ solutions.

## 3.5. Anomalous excess power

Anomalous excess power (FPE) has been observed for the Pd/$D_2O$ co-deposition system but not for the Pd/$H_2O$ system. Including the NHE (Japan) studies, six out of six studies using the $PdCl_2 + ND_4Cl + ND_4OD/D_2O$ system have now given the FPE. The largest excess power effect in $D_2O$ produced 1.7 W or about 160 W per cubic centimeter of palladium (13 W/g). This recent experiment is shown in Fig. 3.

A small excess power effect was observed when the current was increased to $I = 100$ mA at 5.56 days. This FPE increased to more than 600 mW when the current was increased to $I = 200$ mA at 6.80 days. The largest FPE in this experiment was more than 1700 mW (1.7 W) after increasing the cell current to $I = 400$ mA at 8.80 days. This is the largest excess power observed in any of our Pd/D co-deposition experiments. Erroneous excess power due to shuttle reactions or recombination could not exceed the thermoneutral potential times the current (1.5267 $I$). This could only explain 305 mW at 200 mA and 610 mW at 400 mA, even if the shuttle reaction consumed 100% of the current.

Further measurements were not possible because of an overload problem for the PAR Model 363 instrument. Initially, a defective electrode contact was believed to be the problem, but this did not check out. Eventually, it was found that the electrolyte had become nearly depleted such that the cell could not sustain the 400 mA current. Follow up

Figure 2. Excess chemical power due to NCl$_3$ reacting with hydrogen.
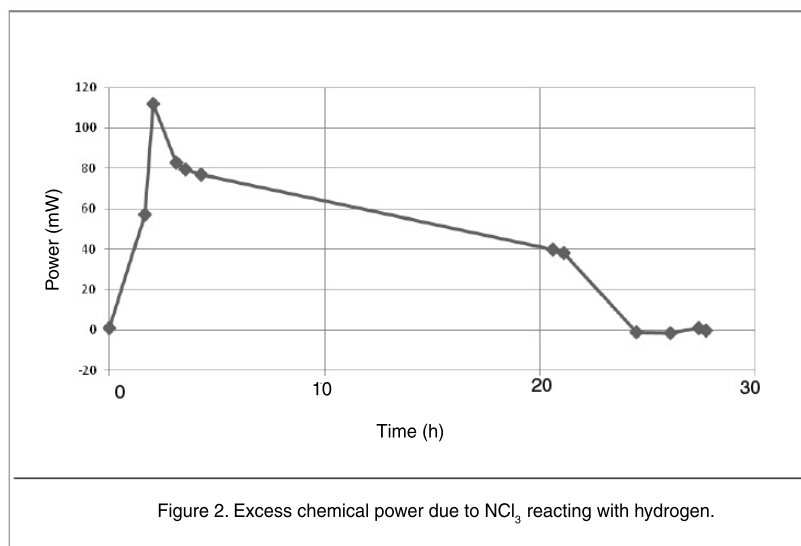
**Figure 2.**

experiments showed that a solution of 0.01 M NH$_4$Cl gave about the same cell voltage effect. This indicates a depletion of 95% of the 0.20 M NH$_4$Cl present following the precipitation reaction (Eq. (1)). A possible electrolyte depletion reaction is

$$2ND_4Cl \rightarrow 2ND_3 + D_2 + Cl_2, \tag{8}$$

where the ND$_4^+$ ions hydrolyze with water to form ND$_3$ that is driven off and D$_2$ and Cl$_2$ are formed at the cathode and anode, respectively. This reaction depleting the electrolyte is considerable more endothermic than D$_2$O electrolysis ($\Delta H° = 507.11$ kJ/mol, $E_H^o = -2.6279$ V for the NH$_4$Cl reaction at standard conditions) and could not contribute to any excess power effect. However, this electrolyte depletion effect for the D$_2$O experiment could not be reproduced in an exhaustive H$_2$O control study of PdCl$_2$ + NH$_4$Cl + NH$_4$OH. Perhaps the higher cell temperatures (over 70°C) for the D$_2$O study (Fig. 3) were needed to produce this electrolyte depletion effect. The cell temperature in the H$_2$O study, in contrast, never exceeded 43°C despite the use of currents up to 500 mA. There were two earlier China Lake experiments using D$_2$O that produced small excess power effects of 70 to 100 mW [7]. Both studies involved LiOD additions to avoid NCl$_3$ formation and had problems with the detachment of most of the palladium from the copper cathode early in the experiment [7].

Large increases in the cell voltages with time during electrolysis at constant current were observed in all three NHE D$_2$O studies that produced large excess power effects [4–6]. An even larger increase in the cell voltage with time was observed in the China Lake D$_2$O study (Fig. 3). These unusual increases in the magnitude of the cell voltage with time during electrolysis in the D$_2$O experiments that produced larger excess enthalpy effects suggest a gradual depletion of
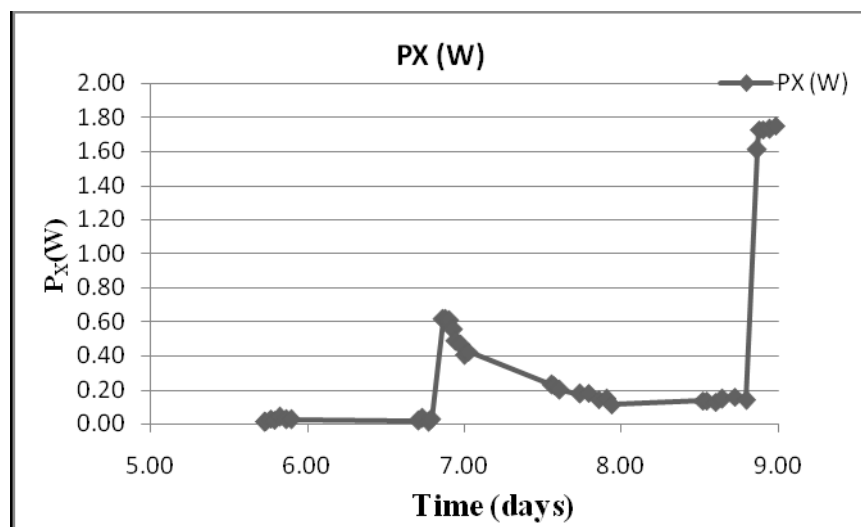
**Figure 3.** Large anomalous excess power effects for the $PdCl_2 + ND_4Cl + ND_4OD / D_2O$ system.

the electrolyte by some reaction such as Eq. (8). Normally, the cell voltage will decrease with time during electrolysis because the electrolyte becomes more concentrated due to the loss of $D_2O$ by the electrolysis. The normal decrease of the cell voltage with time was always observed for the exhaustive China Lake $H_2O$ control study. It is not known exactly why this electrolyte depletion occurs in the $D_2O$ cells but not in the $H_2O$ cells. The higher cell temperatures due to excess power in the $D_2O$ cells could be an important factor. Hot spots on the deposited palladium [16] or anomalous radiation [17] in the $D_2O$ systems could also be involved.

### 3.6. $H_2O$ and $D_2O$ consumption studies

It is always necessary to measure the amount of $H_2O$ or $D_2O$ consumed in every experiment to determine if the consumption is consistent with water electrolysis as the main electrochemical reaction. Any recombination or shuttle reactions would lower the measured consumption of $H_2O$ or $D_2O$. This measured consumption can always be compared to the theoretical consumption based on Faraday's law.

Table 1 presents measured and theoretical consumptions of $D_2O$ or $H_2O$ for various experiments using this ammonia co-deposition system. The three experiments producing large excess power effects at NHE in Japan are also included.

**Table 1.** Measured and theoretical consumptions of $D_2O$ or $H_2O$ in ammonia co-deposition experiments.

| Experiment | Measured (mL) | Theoretical (mL) | Ratio |
|---|---|---|---|
| NHE A-1 ($D_2O$) | 7.4 | 8.1 | 0.91 |
| NHE A-2 ($D_2O$) | 7.7 | 7.2 | 1.07 |
| NHE A-3 ($D_2O$) | 8.7 | 8.1 | 1.07 |
| China Lake ($H_2O$) | 6.0 | 5.0 | 1.20 |
| China Lake ($D_2O$) | 8.2 | 6.7 | 1.22 |
| China Lake ($H_2O$) | 42.5 | 40.8 | 1.04 |

The China Lake ($D_2O$) experiment produced the largest excess power effect as shown in Fig. 3. The first China Lake ($H_2O$) control experiment produced no anomalous excess power, yet it produced a similar measured/theoretical ratio. In most of these experiments, the experimental error in volume measurements was $\pm 1.0$ mL. For the NHE A-3 ($D_2O$) experiment, 82 kJ of excess enthalpy was produced. If this excess enthalpy were due to recombination, the measured volume of $D_2O$ consumed would be less by 5.0 mL and would be easily measurable. The NHE A-1 ($D_2O$) was the only experiment that did not consume more $D_2O$ than the theoretical, yet this NHE experiment had the smallest excess power effect [4–6]. The exhaustive, long-term China Lake ($H_2O$) study consumed 42.5 mL versus 40.8 mL theoretical. The measured/theoretical ratio of 1.04 is identical to that of a previous long-term experiments using a Pd-B cathode in $D_2O$ that produced significant excess power [18]. This China Lake $H_2O$ experiment was the failed attempt to reproduce the electrolyte depletion effect observed in the China Lake ($D_2O$) study (Fig. 3). No anomalous excess power was observed in this exhaustive $H_2O$ experiment. There are always about 4% extra amounts of $H_2O$ or $D_2O$ that are evaporated and carried out of the cell by the electrolysis gases. This can vary with the geometry and temperature of the gas outlet tube. The effect of evaporation is included in the calorimetric equations [18].

There is a small recombination effect due to the reaction of $NCl_3$ with $H_2$ as shown in Fig. 2. The measured chemical enthalpy (5.40 kJ) corresponds to the reaction of 0.00625 moles of $NCl_3$. This reaction (Eq. (6)) would reduce the $H_2O$ consumption by only 0.34 mL. The postulated endothermic electrolyte depletion reaction (Eq. (8)) would lower the $D_2O$ consumption by only 0.18 mL assuming the complete reaction of all of the $NH_4Cl$ (0.010 mol) present in the 50 mL of solution.

## 3.7. Electrochemical studies

Various electrochemical studies were conducted to determine if there were any shuttle reactions involving chlorates, nitrates, or nitrites. These studies included cyclic voltammetric (CVA) measurements, galvanostatic power pulse methods, and electrochemical impedance spectroscopy (EIS).

The CVA measurement at 50 mV/s using a platinum working electrode in the 0.156 M $NH_4Cl$ + 0.150 M $NaNO_3$ + 0.0311 M $NaClO_3/H_2O$ system is shown in Fig. 4. The reduction of $H_2O$ to form $H_2$ ($2H_2O + 2e^- \rightarrow H_2 + 2\,OH^-$) begins near $-0.7$ V vs. AgCl/Ag while the oxidation of $H_2O$ to form $O_2$ ($H_2O \rightarrow {}^1\!/_2\,O_2 + 2\,H^+ + 2\,e^-$) begins near 1.1 V. The small oxidation peak at $-0.75$ V is due to the oxidation of adsorbed hydrogen ($H_{ads} \rightarrow H^+ + e^-$) and the small reduction peak near 1.0 V is the reduction of PtO formed during the oxygen evolution. It is clearly obvious from Fig. 4 that the nitrates and chlorates present in this solution do not support any significant electrode reactions. The only significant electrode reactions even in the presence of chlorates and nitrates are the reduction of $H_2O$ to form hydrogen ($H_2$) and the oxidation of $H_2O$ to form oxygen ($O_2$).

A galvanostatic power pulse study of this same solution is shown in Fig. 5. A cathodic current pulse of $-0.45$ mA ($-1.0$ mA/cm$^2$) is applied for 100 s followed by an anodic current pulse of 0.45 mA for 100 s and then repeated a second time. There is nothing in the solution capable of sustaining any electrode reactions except the reduction of $H_2O$ near $-0.8$ V and the oxidation of $H_2O$ near 1.1 V. There are no measurable reactions of chlorates or nitrates that can sustain even these relatively small currents (0.45 mA) compared to the 100 mA or larger currents used in the co-deposition studies that produced excess power. The small peaks in Fig. 4 due to the oxidation of absorbed hydrogen or the reduction of PtO are seen as slight shoulders in Fig. 5 when the polarity of the current is changed.

As expected, the addition of 0.0330 M $NaNO_2$ (sodium nitrite) to this same solution produced an electrode oxidation reaction. It is well known to electrochemists that while chlorates, perchlorates, and nitrates are electrochemically stable under most conditions, nitrites, in contrast, are easily oxidized. The CVA study with the sodium nitrite present gave a small irreversible oxidation peak of 6.6 mA at 0.85 V. This nitrite oxidation can be represented by $NO_2^- \rightarrow NO + {}^1\!/_2$ $O_2 + e^-$. The NO and $O_2$ gases produced evolve from the solution, hence there is no corresponding reduction peak. Therefore, any nitrate/nitrite shuttle reaction would quickly terminate by the oxidation of nitrite at the anode.
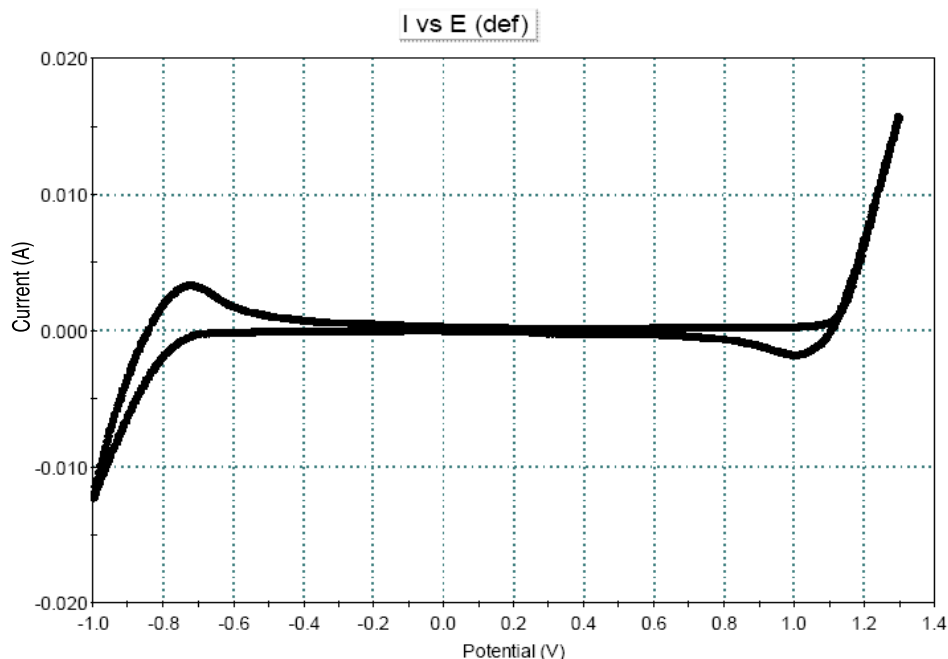
**Figure 4.**   Cyclic Voltammetry at 50 mV/s for the $NH_4Cl + NaNO_3 + NaClO_3/H_2O$ system.

Many other related solutions were studied by electrochemistry, but the results were always the same. There are no shuttle reactions involving chlorates, nitrates, or nitrites in these solutions. For example, various EIS studies show very slow kinetics for any electrochemical reactions involving chlorates or nitrates. The exchange current densities, $i_o$, measured by EIS are less than $10^{-6}$ A/cm$^2$ for any electrode reactions of chlorates or nitrates versus $10^{-3}$ A/cm$^2$ for the much faster hydrogen electrode reaction measured in the same solution.

## 4. Discussion

It is well known to electrochemists that electrode reactions cannot occur faster than solution mass transport or diffusion process that supplies the reactant to the electrode surface [19]. The mass transport process provides an equation for the limiting current, $i_L$ (A/cm$^2$)

$$i_L = DnFC°/\delta, \tag{9}$$

where $D$ is the diffusion coefficient (cm$^2$/s) of the reactant, $C°$ the bulk concentration of the reactant (mol/cm$^3$), $n$ the number of electrons transferred per reaction (eq/mol), $\delta$ the diffusion layer thickness (cm), and $F$ is Faraday's constant (96,485 A s/eq). Typically $D = 2 \times 10^{-5}$ cm$^2$/s and $\delta = 0.05$ cm (Ref. 19). According to the NRL group [8–10, 20], they detected a maximum of about 0.015 M ($0.15 \times 10^{-5}$ mol/cm$^3$) chlorate or nitrate ions in their co-deposition solution. Therefore, even if the chlorate or nitrate ions were extremely reactive electrochemically, the limiting current ($i_L$) would only be about 0.001 A/cm$^2$ for such shuttle reactions assuming a typical two-electron transfer step. The experimental results shown in Fig. 5 prove that even at higher concentrations, chlorates and nitrates cannot sustain a current density of 0.001 A/cm$^2$. In contrast, the calculated limiting current from Eq. (9) for water electrolysis is 4.3

A/cm$^2$ due to the high concentration of $H_2O$ ($55.5 \times 10^{-3}$ mol/cm$^3$). It could be debated that perhaps the diffusion layer thickness is 10 times smaller due to rapid stirring, but one cannot postulate simultaneously shuttle reactions occurring at the electrodes and rapid stirring by the electrogenerated hydrogen and oxygen gases due to $H_2O$ or $D_2O$ reactions.

For co–deposition experiments using $ND_4Cl+ND_4OD/D_2O$ solutions, anomalous excess power (FPE) was measured in 6/6 experiments for the Pd/D$_2$O systems. There was no anomalous excess power measured for 2/2 Pd/H$_2$O experiment, 4/4 Ru/H$_2$O or D$_2$O experiments, 2/2 Re/H$_2$O or D$_2$O experiments or 4/4 Ni/H$_2$O or D$_2$O experiments. The statistical analysis of all 18 experiments yields a probability greater than 99.9989 % that the anomalous excess power effect in these co-deposition studies requires the presence of both palladium metal and $D_2O$[21].

## 5. Summary

Studies of the $PdCl_2 + ND_4Cl + ND_4OD/D_2O$ co-deposition system have produced anomalous excess power effects in three out of three experiments at NHE in Japan and now in three out of three experiments at China Lake, California. A recent experiment produced the largest effect of 1.7 W. The large excess power effects are accompanied by an unusual increase in the cell voltage due to the gradual depletion of electrolyte ions. There was no evidence for any proposed shuttle or recombination reactions involving chlorates, nitrates, or nitrites. There was also no excess power for the co-deposition of Ru, Re, or Ni in H$_2$O or D$_2$O solutions. The anomalous excess power was observed only for the Pd/ D$_2$O co-deposition system. This was also the only deposited metal that showed significant outgassing after the cell current was turned off. This result suggests the necessity of absorbed deuterium within the bulk of the palladium for the production of anomalous excess power in these co-deposition experiments. The increased inorganic chemical knowledge gained by this co-deposition study gives a much better understanding of this Pd/D system and may lead to
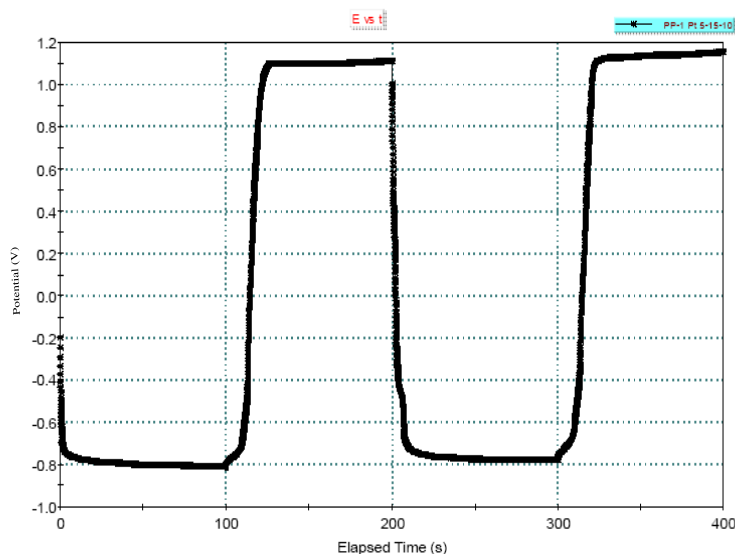


**Figure 5.** Galvanostatic power pulse study of the $NH_4Cl + NaNO_3 + NaClO_3/H_2O$ system using a platinum electrode ($A = 0.45$ cm$^2$).

reproducible excess power (FPE) experiments at other laboratories.

## References

[1] S. Szpak, P.A. Mosier-Boss, and J.J. Smith, On the behavior of Pd deposited in the presence of evolving deuterium , *J. Electroanal. Chem.* **302** (1991) 255.

[2] P.A. Mosier-Boss and S. Szpak, The Pd/(D) H systems; transport processes and development of thermal instabilities , *Nuovo Cimento Soc. Ital. Fis*. **A112** (1999) 577.

[3] R. Le Penven, W. Levason, and D. Pletcher, Studies of the electrodeposition of palladium from baths based on $[Pd(NH_3)_2X_2]$ salts] I. $[Pd(NH_3)_2Cl_2]$ baths , *J. Appl. Electrochem.* **20** (1990) 399.

[4] M.H. Miles, Electrochemical calorimetic studies of palladium and palladium alloys in heavy water , NEDO Final Report, Sapporo, Japan, March 31 (1998).

[5] S. Szpak, P.A. Mosier-Boss, and M.H. Miles, Calorimetry of the Pd + D co-deposition, *Fusion Technol*. **36** (1999) 234.

[6] S. Szpak, P.A. Mosier-Boss, M.H. Miles, and M. Fleischmann, Thermal behavior of polarized Pd/D electrodes prepared by co-deposition, *Thermochimica Acta* **410** (2004) 101.

[7] M.H. Miles, Investigations of co-deposition systems , *Proc. ICCF-15*, ENEA, Rome, Italy, 2009, pp. 33–37.

[8] D. Knies, Personal Communication (2009).

[9] K. Grabowski, E-mail Communications (2009).

[10] D. Kidwell, E-mail Communications (2009).

[11] M.H. Miles and M. Fleischmann, New Approaches to isoperibolic calorimetry , *Proc. ICCF-15*, ENEA Rome, Italy, 2009, pp. 22–26.

[12] M.H. Miles and M. Fleischmann, Measurements of excess power effects in $Pd/D_2O$ systems using a new isoperibolic calorimeter, in *Low Energy Nuclear Reactions*, J. Marwan, (Ed.), American Institute of Physics. Note: This LENR book publication was cancelled while in press by Fred Dylla of AIP.

[13] N.N. Greenwood and A. Earnshaw, *Chemistry of the Elements*, Pergamon Press, Oxford, UK, pp. 1335–1337 (1984).

[14] M.H. Miles, T.J. Groshens, and C.E. Johnson, Examination of linear potential sweep methods in determining the capacitance of hydrous ruthenium oxide materials in batteries and supercapacitors, G.A. Nazri, E. Tekeuchi, R. Koetz, ans B. Scrosati (Eds.), PV 2001; The Electrochemical Society Inc., Pennington, NJ, pp. 602–609 (2001).

[15] P. Delahay, *Double Layer and Electrode Kinetics*, Wiley, New York, NY, pp. 188–189 (1965).

[16] S. Szpak, P.A. Mosier-Boss, C. Young, and F.E. Gordon, Evidence of nuclear reactions in the Pd lattice ,*Naturwissenshaften* **92** (2005) 394.

[17] S. Szpak, P.A. Mosier-Boss, and F.E. Gordon, Further evidence of nuclear reactions in the Pd lattice: emission of charged particles, *Naturwissenschaften* **94** (2007) 511.

[18] M.H. Miles, M. Fleischmann, and M.A. Imam, Calorimetric analysis of a heavy water electrolysis experiment using a Pd–B alloy cathode; Report Number NRL/MR/6320-01-8526, p. 8, Naval Research Laboratory: Washington, DC, March 26, (2001).

[19] J.O'M. Bockris and A.K.N. Reddy, *Modern Electrochemistry*, Plenum Press, New York, NJ, Vol. 2, pp. 1059–1060 (1974).

[20] K.S. Grabowski, NRL Efforts Since 2002, LENR Workshop, Army Research Laboratories, Adelphi, MD, June 29 (2010).

[21] M.H. Miles, CMNS Discussion Group, June 17 (2011).

Research Article

# Initiation of the Cold Fusion Reactions by Air Components

## Sergey A. Tsvetkov *

*14-13 Kurchatov St., Zarechny, Sverdlovsk Region 624250, Russian Federation*

**Abstract**

The approach to cold fusion phenomenon based on interactions between deuterium and the components of air in titanium is considered. Experimental results which point at release of excess heat and neutrons are shown. On the basis of these results the nuclear fusion method and the device for its realization are patented. The application of this nuclear fusion method for nuclear waste transmutation, in particular caesium-137, is considered. On the basis of the calculations given conclusion about applicability of the method is made. According to the experimental data, saturation of titanium with deuterium–air mix results in temperature increase of the titanium deuteride sample by 45°C, in comparison with saturation of the same sample with pure deuterium. The calculation of excessive heat emission based on these results is given. The conditions necessary for the cold fusion reactions to occur are formulated.
© 2012 ISCMNS. All rights reserved. ISSN 2227-3123

*Keywords:* Deuterium, Nuclear reactions, Titanium

## 1. Introduction

Since 1989, we have been studying loading of titanium by gaseous deuterium [1]. Menlove et al. measured neutron emission from TiD in 1990 [2].

## 2. Experiments

Our loading sample parameters were as follows: the sample temperature was 550–580°C, deuterium pressure was 4, 32 and 50 atm. The cycling method consisted in loading and degassing of titanium sample was used. Degassing was implemented by vacuum pump and heating of the butt end of the sample by laser. The LTI-403 model of laser was used. This is a two-stage laser assembled in driving oscillator – amplifier pattern. Yttrium–Aluminum grenade crystals with Neodymium (Nd–YAG) were used as the active elements of the amplifier and driving oscillator. Optical pumping was used. The laser operated in free generation mode. In order to increase the laser radiation energy, power supply units were modernized. The experimental parameters of laser radiation were the following:

- Wavelength = $1.06\,\mu$m.

---

*E-mail: rossomahi@yandex.ru; Tel.:+7-9126037112

- Pulse energy = 1 J.
- Pulse duration = 1 $\mu$s.

- Pulse repetition rate = 33 Hz
- Average power = 33 W.

The block of neutron detectors and scintillation detector with NaI (Tl) single crystal were used to record neutron and gamma radiations. The block of neutron detectors consisted of 30 mm thick polyethylene neutron moderator and 15 SI-19N- type slow neutron counters filled with 97% $^3$He + 3% Ar gas mixture. Its rated parameters were the following:

- Efficiency of heat neutron registration: not less than 60%.
- Sensitivity to neutrons from plutonium–beryllium source: not less than 50 count/(neutron/sm$^2$).
- Intrinsic noise rate: not more than 0.1 count/s.
- Threshold of sensitivity to gamma radiation: not less than 200 $\mu$R/s.

Scintillation detector for registration of gamma radiation was of NaI (Tl) single crystal dimensions: 63 mm in diameter and 63 mm in height. The lateral surface of single crystal was shielded by 100 mm thick lead. Scintillation detector had the following technical parameters towards $^{137}$Cs source:

- Efficiency of the registration: not less than 57%.
- Sensitivity: not less than 21 count/(gamma/sm$^2$).
- Intrinsic noise rate: not more than 200 count/min.

In order to calibrate the neutron detectors block, sealed pin-type californium neutron source was used. The main technical parameters of this source were:

- Radioactive element: $^{252}$Cf.
- Neutron flow: $2.2 \times 10^6$ neutron/s.
- Measurement date: 06-28-1989.
- Efficient half-life: 2.638 years.
- Activity: not more than $2.4 \times 10^7$ Bq
- Average energy of neutrons under spontaneous fission: $E = 2.2 \pm 0.1$ MeV.

Scintillation detector was calibrated by the $^{60}$Co source with an activity of $3.7 \times 10^5$ Bq.

During the first experiments integral track neutron detectors from DKN set were used simultaneously with continuous registration of neutrons from the sample. Three experiments were carried out using the following system of detectors: four detectors based on $^{235}$U with muscovite recorder were placed behind a water moderator, 15 cm away from the sample, and three detectors based on $^{237}$Np with muscovite recorder were placed in front of the water moderator. One detector based on $^{235}$U was used for checking. On two detectors that were placed behind a water moderator we discovered three tracks, which are typical for fission fragments. The checking detector showed no tracks in the background. During following three experiments four track detectors based on $^{235}$U with muscovite recorder and four track detectors based on $^{235}$U with Lavsan recorder were used. Two of the latter were used for checking, while other detectors were placed behind the water moderator, 10 cm away from the sample. After these experiments we discovered on one of the detector, having with Lavsan recorder is discovered one track, typical for fission fragments. The checking detector showed no tracks in the background.

In the same experiments the second independent set of neutron detectors blocks with slow neutron counter, identical to the first set, was used. During degassing of the sample in one of the experiments synchronous neutron registration by both sets of neutron detectors blocks occurred.

"Flashes" of neutron and gamma radiation were observed during the experiment. Their duration was no more than 0.5 s, and their intensity was 500 neutrons/s in terms of neutron detectors block sensitivity to neutrons from $^{252}$Cf source and 5400 gamma/s in terms of scintillation detector sensitivity to $^{60}$Co source. Using the magnitude of deuterium pressure alterations at loading and velocities of the pump down at degassing the calculations were made. It showed that the moments of these radiation "flashes" correspond to phase transitions in titanium–deuterium system. The pulse type of radiation registered confirms the hypothesis about influence of phase transitions in titanium deuteride sample on the nuclear reactions taking place.

Thus, the mechanism of this effect becomes clear. During phase transitions the metal crystalline lattice undergoes rearrangement. For example, in pure titanium the atoms are arranged in structure of hexagonal close packing with the lattice period of 2.952 Å, but titanium deuteride with composition $TiD_{1.97}$ has face-centered cubic lattice of metal atoms with lattice period of 4.440 Å [4]. Therefore, while loading of titanium with deuterium and degassing, discontinuous changes in internal energy, electronic thermal capacity, magnetic receptivity and other parameters occur.

Simultaneously with the experiments, simulation of phase transitions in palladium–deuterium system was carried out using molecular dynamics methods. Deuterium behavior in this process was determined [5,6]. According to the calculation results, it was found that in the process of phase transition in a micro crystallite that consists of 500 Pd atoms and 250 D atoms, single deuterium atoms with energy more than 10 eV appear, as well as pairs of deuterium atoms that are drawn together within palladium micro-crystallite to the distances up to 0.70 Å. Normal distance between deuterium atoms in palladium deuteride is about 3 Å.

In the experiments, we used samples made by heat pressing method from titanium hydride powder with particles diameter 100 $\mu$m. This resulted in very large surface of the interaction between titanium and deuterium. Surfaces area of the sample was calculated to be more 80 cm$^2$/g.

It was observed that neutron "flashes" were registered only in cases when oxide film was found on the samples surface after the experiment. In cases of oxide film absence neutron ""flashes" were not registered. Therefore, we carried out experiments on the influence of air additives in gaseous deuterium on neutron and gamma-radiation intensity and frequency under phase transition [3]. The following results were received: when loading the sample with 1.5% air + deuterium mixture, separate gamma and neutron ""flashes" were registered. The nature of the radiation, intensity and frequency of "flashes" changed according to velocity of alteration of deuterium content in titanium, i.e. to absorption velocity of the gas mixture. At low absorption velocities gamma-radiation "flashes" were registered in amount of two "flashes" per absorption process. With increase of the absorption velocity the amount of neutron "flashes" increased up to 7 per absorption process. Neutron "flash" intensity was found to vary in direct proportion to the sample mass: since the sample masses in the experiments differed approximately in 2 times ($m_1 = 15.20$ g and $m_2 = 6.98$ g), neutron "flash" intensities differed approximately in 2 times as well ($m_1$ – in 60 and $m_2$ – in 32 times above background).

Results of these experiments were the basis for Russian patent "Method of the nuclear fusion and device for its realization" No. 2145123 [7].

Other experimental data reported [8] include neutron pulse registration with neutrons energy of 2.5; 4.5; 13 and 17 MeV with flow density $10^4$ neutrons/(cm$^2$·s) and gamma-radiation with energy up to 4.5 MeV. Considering this and the fact that we used neutron sensors with $^3$He for neutrons registration, we may suppose that as reactions described in patent [7] take place, interactions between deuterium and nitrogen and oxygen isotopes increased in air result in neutrons with higher energies [2].

Possible nuclear reactions between deuterium and nitrogen or oxygen isotopes are listed in Table 1 [9]. To judge from the products registered in the reaction of "cold fusion", the reaction $^{17}$O + D are more likely to occur. But this suggestion requires experimental proof.

Full cross-sections of $^3$He for neutrons with energy 2.4 and 14 MeV are known to differ nearly in three times [10], while cross-sections of (n,p)-reactions differ in 6 times. That is the neutron counter sensitivity to neutrons with energy more than 2.4 MeV is far less.

So it was considered necessary to recalibrate the neutron detectors block by neutron source with higher energy. For this purpose $^{239}$Pu-$\alpha$-Be source with external radiation in $2\pi$ angle 2.12 $\times10^5$ $\alpha$-particles/s and surfaces area $S_{\text{source}} = 160\,\text{cm}^2$ was chosen. In our earlier work [7], the magnitude of neutron flow was found to be about 500 neutrons/s in terms of sensitivity to neutrons from $^{252}$Cf source (the average energy of neutrons $E = 2.2$ MeV), while in case of $^{239}$Pu-$\alpha$-Be source, average energy of neutrons $E = 4$ MeV. So, experimental data allow us to define, which neutron flow was registered to this source.

As the result neutron detectors block sensitivity to neutron $^{239}$Pu-$\alpha$-Be source turned out to be $\chi = 5.974$ count·cm$^2$/s, which corresponds to the rated parameters of the neutron detectors block.

The magnitude of the neutron flow to $^{239}$Pu-$\alpha$-Be source was found to be $I = 1.68 \times 10^5$ neutron/s.

In the work [11] possible use of the cold nuclear fusion method for transmutation of nuclear wastes, in particular, for cesium-137 "destruction" was considered. The values of the neutron flow density obtained using oxygen and nitrogen isotopes are of the same order, but still 27 times less than the value of the neutron flow density for efficient cesium-137 "destruction" in fast neutrons reactor. It's possible to rise working mixture pressure up to 50 atm and working volume of the installation up to 10 m$^3$. This would enable to increase the weight of used hard body to 700 kg, which would lead to the neutron flow density increase by one more order of magnitude and reduce efficient half-life to $T_{1/2\text{c.f.}} = 0.338$ years.

It means that it would be necessary to irradiate the radioactive waste with $^{137}$Cs for 12.9 years in order to achieve the minimum significant specific $^{137}$Cs activity. Such timing and technical features of the process and installation are suitable for making the industrial installation.

In the experiments on loading the samples with deuterium + air mixture and degassing we observed a 45°C increase in temperature of the samples in comparison with the temperature at which absorption of pure deuterium by this sample takes place [3]. The calculated amount of excess heat in the process of loading of titanium sample with deuterium + 1.5% air mixture was found to be $Q = 85.002$cal $= 355.88$ J or about 50 kJ/kg sample.

Four nuclear reactions can occur between D and $^{17}$O (refer Table 1). But only in one of four cases neutrons may be observed. Relation between registered amount of neutrons and tritium amount in "cold fusion" reactions is experimentally defined and is T/n $= 10^9$ [12].

The value of energy released in one act of the supposed fusion reaction between deuterium and oxygen-17 isotope should be 13.22 MeV per fusion act which is commensurable with reference data. Thermonuclear fusion reactions D + T lead to release of 17.7 MeV per fusion act.

## 3. Conclusion

Thereby, we can say that addition of air in deuterium has initiating influence on reactions of cold fusion when loading titanium with gaseous deuterium.

The review of works in other branches of cold fusion shows that in all the system described, aside from deuterium and metal, oxygen is present, either in gaseous or in bounded form. Thus we can expect the cold fusion phenomenon to be connected with the fusion reactions between oxygen and deuterium nuclei within solid. Moreover, both the reaction products and their energy spectrum point at oxygen isotopes: $^{17}$O and $^{18}$O. Apparently, presence or absence of these isotopes in system subjected to deuterium loading defines reproducibility of experimental results and intensity of the cold fusion reactions.

We may describe the conditions necessary for the cold fusion reaction to occur:

(1) Presence of materials which are capable of absorbing deuterium in greater amount and undergoing phase transitions during this process, and also have large surface area.
(2) Presence of oxygen isotopes.
(3) Optimum phase transition rates should exist.

**Table 1.** Possible nuclear reactions of deuterium with nitrogen and oxygen isotopes, nitrogen and oxygen isotopes prevalence in nature.

| Nuclear reactions | Nitrogen and oxygen isotopes in nature (%) |
|---|---|
| $^{14}N + D \rightarrow 4\ ^4He + 6.3$ MeV | 99.63 |
| $\rightarrow\ ^{12}C + ^4He + 13.57$ MeV | |
| $\rightarrow\ ^{15}N + p + 8.61$ MeV | |
| $\rightarrow\ ^{15}O + n + 5.06$ MeV | |
| $\rightarrow\ ^{16}O + \gamma + 20.73$ MeV | |
| | |
| $^{15}N + D \rightarrow\ ^{13}C + ^4He + 7.68$ MeV | 0.37 |
| $\rightarrow\ ^{16}N + p + 0.262$ MeV | |
| $\rightarrow\ ^{16}O + n + 9.901$ MeV | |
| | |
| $^{16}O + D \rightarrow\ ^{14}N + ^4He + 3.11$ MeV | 99.76 |
| $\rightarrow\ ^{18}F + \gamma + 7.527$ MeV | |
| $\rightarrow\ ^{17}O + p + 1.918$ MeV | |
| | |
| $^{17}O + D \rightarrow\ ^{15}N + ^4He + 9.802$ MeV | 0.04 |
| $\rightarrow\ ^{16}O + ^3H + 2.115$ MeV | |
| $\rightarrow\ ^{18}O + p + 5.822$ MeV | |
| $\rightarrow\ ^{18}F + n + 3.384$ MeV | |
| | |
| $^{18}O + D \rightarrow\ ^{15}N + ^4He + n + 1.755$ MeV | 0.20 |
| $\rightarrow\ ^{16}N + ^4He + 4.245$ MeV | |
| $\rightarrow\ ^{19}O + p + 1.732$ MeV | |
| $\rightarrow\ ^{19}F + n + 5.768$ MeV | |

The equipment used for registration of the nuclear radiation must be capable to register pulse neutron and gamma-radiation. Otherwise in process of loading and degassing of the solid experimental conditions should be created in such a way that the largest possible volumes would undergo phase transition. Thereby, the cold fusion phenomenon does exist, but it is necessary to follow certain conditions for its observation.

We suppose that it is necessary to continue works on loading and degassing of titanium with mixture of deuterium with oxygen isotope in combination with spectrometry in order to increase the intensity and duration of the radiation, as well as check the nitrogen and carbon isotopes in mixture with deuterium at titanium loading for exact determination of the nuclear reaction channels.

## References

[1] I.L. Beltyukov, N.B. Bondarenko, A.A. Janelidze, M.Yu. Gapanov, K.G. Gribanov, S.V. Kondratov, A.G. Maltsev, P.I. Novikov, S.A. Tsvetkov and V.I. Zakharov, Laser-induced cold nuclear fusion in $T_i$–$H_2$–$D_2$–$T_2$ compositions, *Fusion Technol.* **20**(2) (1991) 234–238.

[2] H.O. Menlove, M.M. Fowler, E. Garcia, M.C. Miller, M.A. Paciotti, R.R. Ryan and S.E. Jones, Measurement of neutron emission from Ti and Pd in pressurized $D_2$ gas and $D_2O$ electrolysis cells, *J. Fusion Energy* **9** (1990) 495 and 215.

[3] S.A. Tsvetkov, Initiation of cold fusion by light admixture, *Cold Nuclear Fusion: Material 3rd Russian Conference on Cold Fusion and Transmutations Nuclear*, Dogomys, Russia, October 2–7, 1995, M.: SRC FTP Erzion, 1996, pp. 281–294.

[4] Metal Hydrides, V.M. Muller, D. Blekledzh and J. Libovic (Editors), M.: *Atomizdat*, 1973, 432 pp.

[5] A.N. Varaksin, A.A. Zhivoderov, N.B. Bondarenko and V.F. Shipitsin, Modeling on computer of phase transition in palladium deuteride (possible low temperature nuclear fusion mechanism), *Phys. Metal Metallovedenie* Issue 9 (1991) 30–34.

[6]   S.A. Tsvetkov, N.B. Bondarenko, I.L. Belityukov, A.N. Varaksin and A.A. Zhivoderov, Phase transition calculations by molecular dynamics method in system Pd–D and cold nuclear fusion, *Phys. Metal Metallovedenie* **76**(4) (1993) 94–97.
[7]   S.A. Tsvetkov, Patent RU No. 2145123, S1, 7 G 21 B 1/00, Method of the nuclear fusion and device for its realization, priority 12/10/1997, Inventions Bulletin No.25, 09/10/1999, pp. 135–136.
[8]   A.B. Karabut, Ya.R. Kucherov and I.B. Savvatimova, Investigation of deuterium nuclei fusion at glow discharge cathode, *Fusion Technol.* **20** (1991) 924–928.
[9]   *Physical Values Tables. The Reference Book*, I.K. Kikoin and M. (Editors): Atomizdat, 1976, pp. 945–946.
[10]  *Experimental Studies by Flap Gamma Radiations and Neutron,* Yu.A. Egorov (Editor), M.: Atomizdat, 1974, p.128.
[11]  S.A. Tsvetkov, Possibility of the use the cold nuclear fusion for transmutation nuclear departure, *Material 9th Russian Conference on Cold Transmutation Nuclear Chemical Element* (Dagomys-2001), M.: 2002, pp. 186–191.
[12]  V.A. Tsarev, Anomalous nuclear effects in solid (cold fusion): questions all else remain, *Successes Physical Sci. RAS* 162(10) (1992) 63–91.

Research Article

# Mechanisms for Heat Generation during Deuterium and Hydrogen Loading of Palladium Nanostructures

## O. Dmitriyeva [*], R. Cantwell and M. McConnell

*Coolescence, LLC, Boulder, CO, USA*

## G. Moddel

*University of Colorado at Boulder, CO, USA*

**Abstract**

Our group has confirmed excess heat production and isotope effects in alumina and zeolite powders containing highly dispersed Pd nanoparticles. Varying the pressures and loading rates produced correlations between the exothermic and endothermic aspects of the experiments. It was shown that the generated power is proportional to the pressurization rate times a quantity $\Phi$, which is the energy content of what we called "fuel". There are two types of fuels, both of which can trigger the reaction that can be either exothermic or endothermic depending on the gas used in the experiment (deuterium or hydrogen). Observed heat generation during the pressurization phase is most likely of a chemical nature.

*Keywords:* Excess heat, Gas-loading, Isotope effect, Nanoparticles, Palladium

## 1. Introduction

Recent studies of deuterium loading of palladium nanostructures demonstrated consistent and repeatable excess heat production [1–4]. Our group conducted a series of experiments on gas loading in Pd-enriched alumina and zeolite matrices to (1) confirm the excess heat production in the systems and (2) investigate heat generation mechanisms and their contribution to the overall excess heat production.

In previous work [5], we have successfully demonstrated (1) excess heat production in Pd-loaded alumina and zeolite matrices, (2) excess heat tapering off with repeated runs possibly due to Pd nanoparticle agglomeration, (3) excess heat generation at low Pd–D ratios, and (4) the amount of excess heat produced depending linearly on pressure (quantity of deuterium provided).

---

[*]E-mail: olga.dmitriyeva@colorado.edu; Also at University of Colorado at Boulder, CO, USA

In this paper, we report the results of our further investigation of the heat production during different stages of the gas loading process in nanoparticle systems. Detailed analysis is instructive when trying to answer questions about the state of the system and conditions required for excess heat generation.
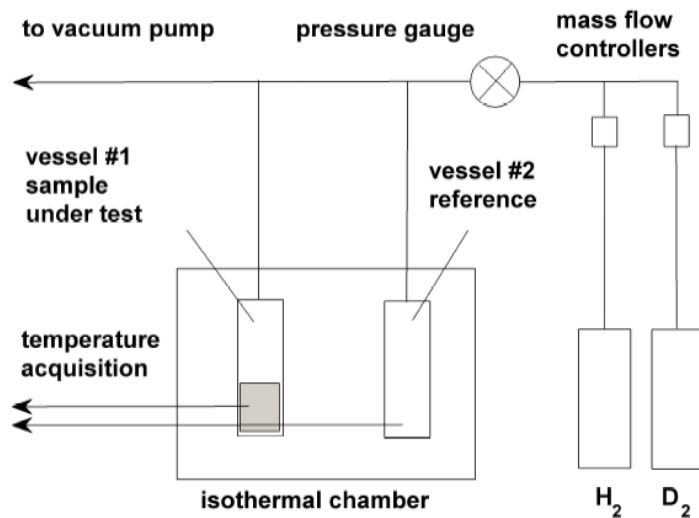


(a)
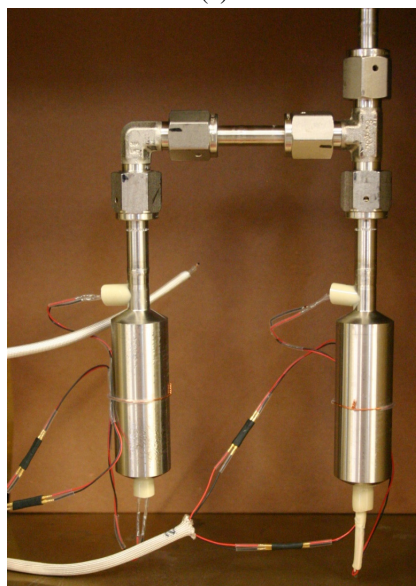


(b)

**Figure 1.** Experimental set-up for excess heat measurements. (a) Block diagram, and (b) stainless-steel vessels inside the isothermal chamber.
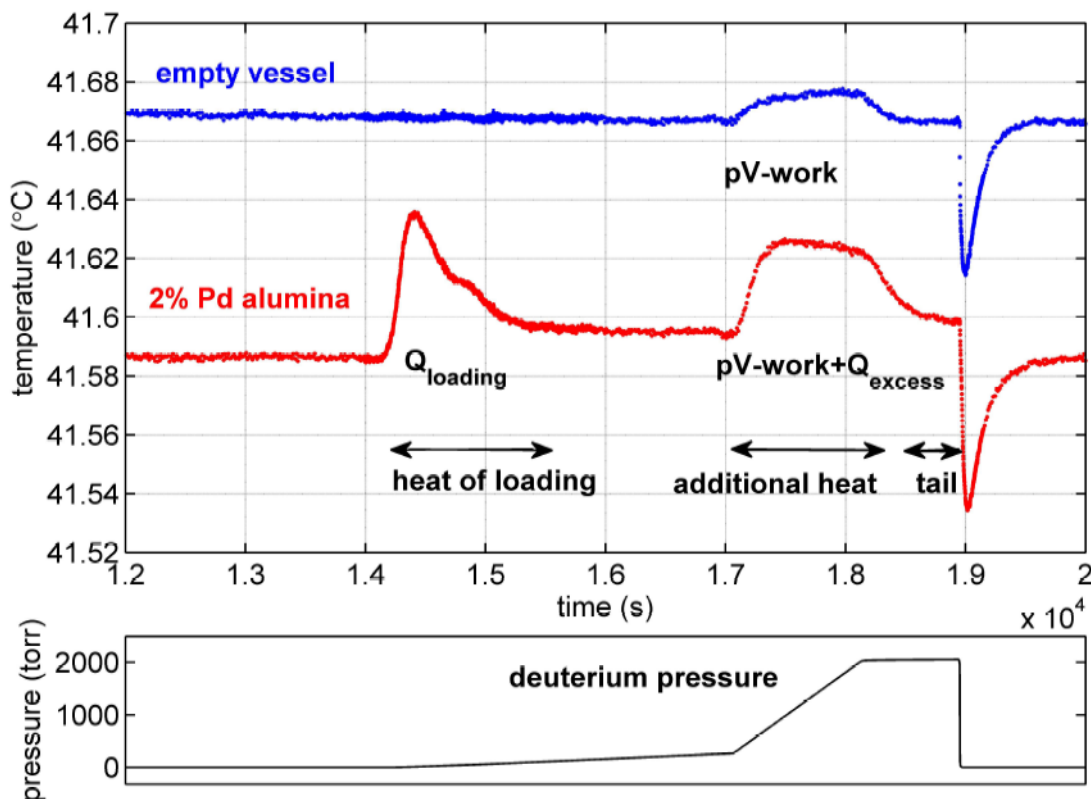
**Figure 2.**   Pressure and temperature change in the system.

## 2. Experimental Procedure

Powder zeolite samples containing 2.0% by weight of Pd were prepared from molecular sieves 13X (Sigma–Aldrich P/N:283592) by cationic exchange for $[Pd(NH_3)_4]^{2+}$ ions in a $[Pd(NH_3)_2Cl_2]$ solution [6,7]. The samples were then washed with de-ionized (DI) water and dried in air at room temperature. Alumina samples containing 2.0% of Pd by weight were fabricated by the incipient wetness method similar to Ref. [8] by impregnating hot $Pd(NH_3)_2Cl_2$ solution into 80–200 mesh $Al_2O_3$ (Fisher Scientific P/N: CAS 1344-28-1). Alumina slurry was then dried in air at room temperature without washing in DI. Neither zeolite nor alumina samples were calcined. Prior loading into an experimental apparatus, all the samples were baked in a vacuum oven at 120°C for 24 h.

Figure 1a shows the block diagram of the experimental set-up. It consists of an HP 5890A gas chromatograph (GC) oven that is capable of maintaining the temperature ±10 mK. The temperature of the oven is set to 313 K (40°C). Temperature changes that exceed background temperature fluctuations are associated with exothermic or endothermic heat generated in the system.

Two stainless steel vessels are placed inside the oven and connected to the gas line. One vessel contains 6 g of material. Another vessel remains empty and used as a reference.

Hydrogen, deuterium, and argon are supplied through the gas lines. $H_2$ and $D_2$ are introduced to the system through

an oxygen-removing hydrogen purifier. The $D_2$ gas is 99.8% pure and the $H_2$ gas is 99.99% pure. Argon is used to fill the system while the vessels are exchanged and new material is loaded.

Temperature is registered by thermistors, glued with epoxy to the bottom and the neck of the vessels (Fig. 1b).

The flow of gas into the system is regulated using a mass flow controller and can be set anywhere between 0.2 and 10 sccm. The system is pressurized up to 2000 torr. Evacuation of the gas lines is done manually by opening the vent valve towards the pump.
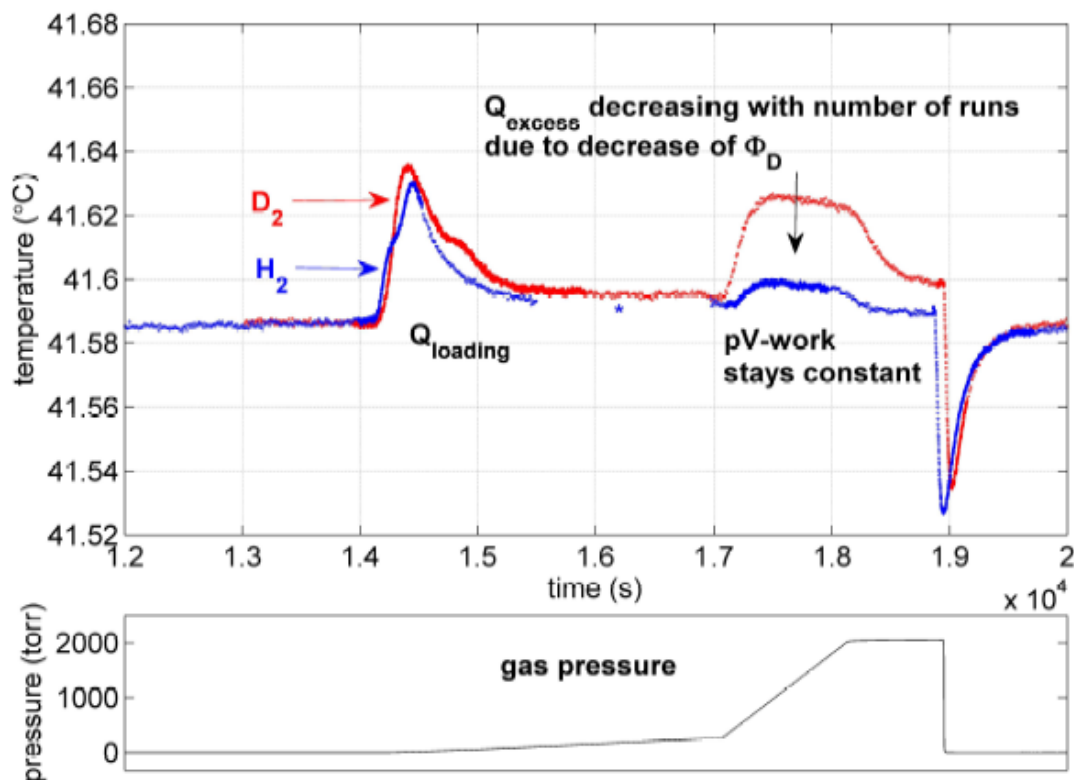


**Figure 3.**  Pressure and temperature change in the system for deuterium and hydrogen pressurization. * The time scale for the hydrogen run was split in order to align the slow and fast pressurization intervals with corresponding intervals from the deuterium run.

System control, temperature and pressure data acquisition was done using LabView software.

The calculations of the exothermic and endothermic heat are done by integrating the temperature data from the bottom thermistors over a period of time when the temperature of the system is changing with respect to the baseline. Heat is proportional to the temperature deviation times time, and is shown in units of °C sec.

Initially, the system was checked with alumina and zeolite powders without any Pd added. The heat produced by a process is proportional to the integration of temperature deviation over time. In the presence of hydrogen and deuterium we found that the exothermic heat due to the work of pressurization ($pV$-work) and endothermic heat (recovery of $pV$-work) during evacuation balanced each other and no excess heat was produced.
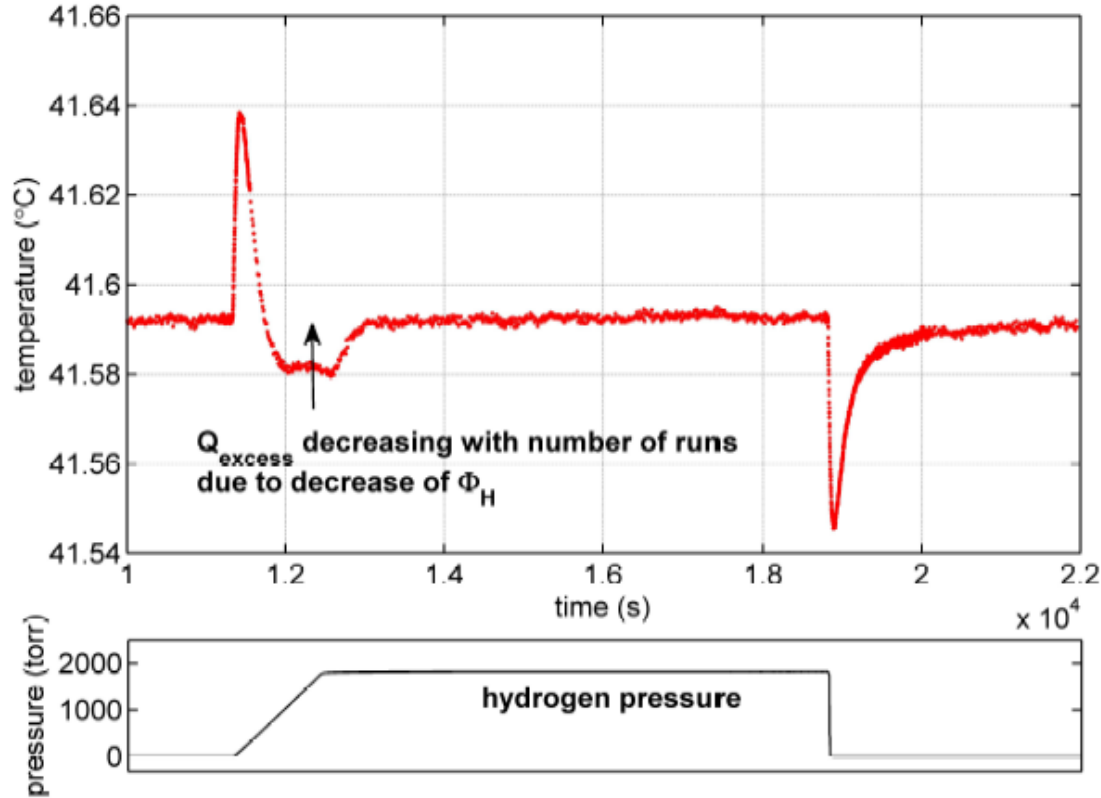
**Figure 4.**     Pressure and temperature change in the system during hydrogen pressurization following 14 deuterium runs.

## 3. Results and Discussion

### 3.1. Excess heat generation

Figure 2 shows the typical run done with a 2% Pd-loaded alumina matrix in the presence of deuterium gas.

A two-slope pressurization is needed to separate the processes of PdD formation (heat of loading-$Q_{\text{loading}}$) from the heat due to work of pressurization ($pV$-work). The first slope corresponds to a 0.5 sccm gas input flow and second slope to 10 sccm.

There are several differences in the temperature signal between the data from the reference (empty) vessel and the vessel loaded with material. These differences are summarized in Table 1.

Based on the data from the Table 1 we can write equation for the exothermic and endothermic portions of heat generated in the material:

$$\text{Exothermic Heat} = Q_{\text{loading}} + (pV \text{ work}) + Q_{\text{excess}}$$

$$\text{Endothermic Heat} = -Q_{\text{loading}} - (pV \text{ work})$$

As for excess heat produced during the fast pressurization step we can say that the power generated is proportional to the slope of pressurization times a quantity $\Phi$, which is the energy content of the "fuel":

$$Q_{\text{excess}}/\text{time} \propto \Phi \frac{\mathrm{d}p}{\mathrm{d}t}.$$

The fuel in the material can be exhausted or replenished (discussed further in Section 3.3). Along with nanoparticle agglomeration this leads to the decrease of excess heat production with an increasing number of runs.

### 3.2. Isotope effect

Anomalous heating, which is observed during deuterium loading of Pd nanostructures but not during hydrogen loading, is called an "isotope effect". The isotope effect has been attributed to the nuclear nature of the excess heat generation due to deuteron–deuteron fusion inside Pd lattice [9].

We have designed an experiment where one of two identical samples are subjected to hydrogen and the other to deuterium using the same two-step pressurization technique (Fig. 3).

Heats of PdD and PdH formation ($Q_{\text{loading}}$) are similar. Endothermic heat, which consists of $-Q_{\text{loading}} - (pV \text{ work})$, is the same for both materials. However, there is an isotope effect: extra heat is generated during the fast pressurization step with deuterium gas.

### 3.3. Fuel production within the system. Recharging

The results demonstrated in Section 3.1 suggest the existence of a fuel in our system that supports the reaction. Earlier experimental data have shown that repeated runs deplete this fuel [5]. However, the fuel can also be replenished in the system. To demonstrate this process we switched our system to hydrogen gas after multiple deuterium runs. Figure 4 shows the effect of hydrogen pressurization on 2% Pd-loaded zeolite powder that was subjected to 14 deuterium runs in which there was exothermic excess heat production.

During fast pressurization the process became endothermic. Fuel was generated during deuterium runs and supported the endothermic reaction in the presence of hydrogen.

Figure 5 shows the values of excess heat (exothermic and endothermic) due to switching of the gas from deuterium to hydrogen and back to deuterium. Exothermic excess heat was partially recovered after hydrogen pressurization. In

**Table 1.** Exothermic and endothermic heat generated during deuterium pressurization.

| Pressurization step | Reference (empty) vessel | Material loaded vessel |
| --- | --- | --- |
| Slow 0–66 min | The temperature of the empty vessel does not change because the heat of pressurization dissipates faster than it is generated. | Heat of loading we call $Q_{\text{loading}}$ |
| Fast 66–80 min | $pV$-work | $pV$-work and extra heat we call $Q_{\text{excess}}$ |
| Constant pressure 80–90 min | No temperature change | Excess heat, in the "tail". Excess heat associated with the tail typically disappears after 3–4 cycles. |
| Depressurization | Endothermic heat due to recovery of $pV$-work | Endothermic heat due to recovery of $pV$-work and $Q_{\text{loading}}$ |

other words, the system was recharged with more fuel during the hydrogen runs. Similar results were reported by the Naval Research Lab [2].

The fact that excess heat was recovered only partially may be explained by Pd-particle agglomeration. Smaller diameter particles produce more heat [2,10]. We suggest that repeated deuterium or hydrogen loadings of Pd material make the Pd nanoparticles cluster together [11] and reduce the active surface area of the Pd [12]. This process of agglomeration induces permanent damage to the system, and cannot be fixed by alternating the introduced deuterium and hydrogen gases.

To apply the formula for power production in the system to exothermic and endothermic processes we rewrite the heat production relation for deuterium runs:

$$Q_{\text{excess}}/\text{time} \propto \Phi_{\text{D}} \frac{\mathrm{d}p}{\mathrm{d}t}$$

and for hydrogen runs:

$$Q_{\text{excess}}/\text{time} \propto \Phi_{\text{H}} \frac{\mathrm{d}p}{\mathrm{d}t}.$$
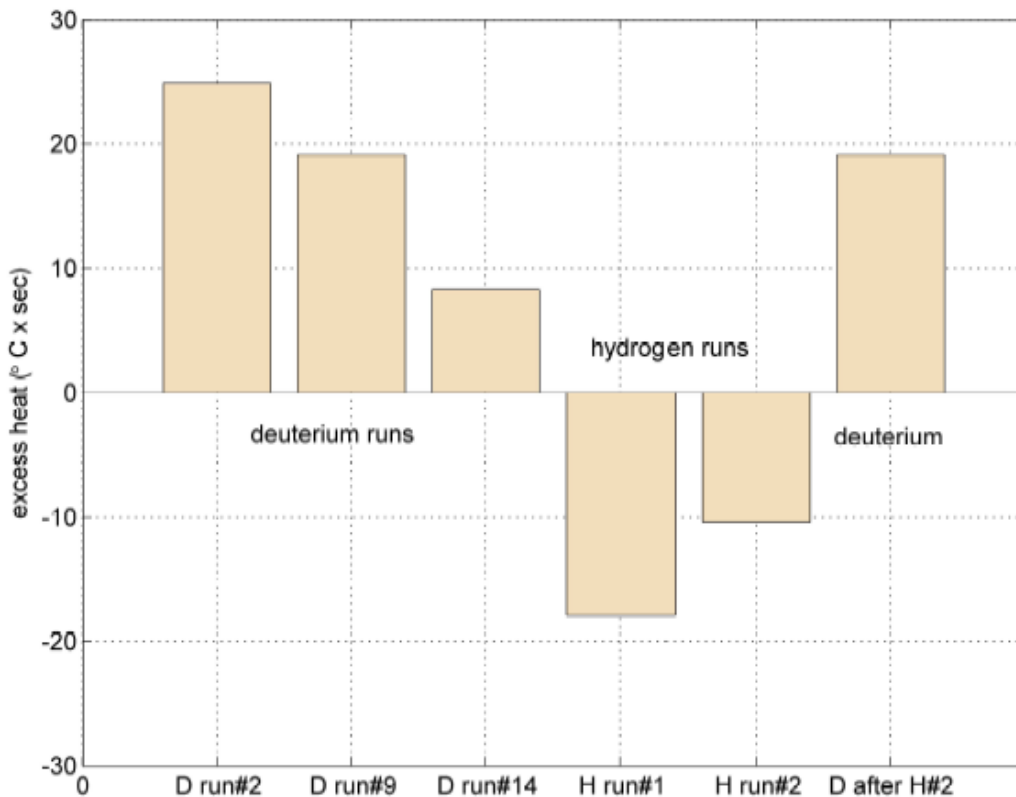


**Figure 5.** Effect of recharging the system by alternating deuterium and hydrogen pressurizations on 2% Pd-loaded zeolite.

Quantities $\Phi_D$ and $\Phi_H$ are not the same and we emphasize this fact by assigning different subscripts to them. $\Phi_D$ is positive and supports the exothermic reaction in the presence of deuterium while $\Phi_H$ is negative and supports the endothermic reaction in the presence of hydrogen.

## 4. Conclusions

By varying the pressurization rate in our experiments we were able to associate the exothermic and endothermic heat produced by the system with different mechanisms of heat production. We have looked at the heat of palladium loading, the heat of pressurization ($pV$-work) and the heat induced by a high rate of pressurization of the system.

We have found that heats of PdD and PdH formation are roughly the same and do not contribute to excess heat generation. Some excess heat is produced in the fast pressurization mode. The power of the heat generated during this mode is proportional to the slope of the pressure rise and the energy content of what we have termed fuel.

Fuel can be produced, exhausted or replenished within the system. The concept of fuel can explain the recharging effect, when excess heat is partially recovered by alternating deuterium and hydrogen pressurizations. Depending on the type of the fuel and reacting gas the system can produce either exothermic or endothermic excess heat. Because the system can be recharged with fuel and the sign of heat produced by the system can be reversed, it appears that the heat generated during the pressurization phase is the result of a chemical reaction.

## References

[1]  Y. Arata, Y. Zhang , and X. Wang, Production of He and energy in the "Solid Fusion", *ICCF-15*, Rome, Italy (2009).
[2]  D. Kidwell, A. Rogers, K. Grabowski, and D. Knies, Does gas loading produce anomalous heat?, *ICCF-15*, Rome, Italy (2009).
[3]  Y. Sasaki, A. Kitamura, Y. Miyoshi, T. Nohmi, A. Taniike, A.Takahashi, R. Seto, and Y. Fujita, Anomalous heat generation in charging of Pd powders with high density hydrogen isotopes. Results of absorption experiments using Pd powders, *ICCF-15*, Rome, Italy (2009).
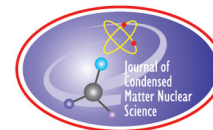[4]  T. Hioki, H. Azuma1, T. Nishi, A. Itoh, J. Gao, S. Hibi, T. Motohiro, and J. Kasagi, Hydrogen/deuterium absorption property of Pd fine particle systems and heat evolution associated with hydrogen/deuterium loading, *ICCF-15*, Rome, Italy (2009).
[5]  O. Dmitriyeva, R. Cantwell, M. McConnell, and G. Moddel, Deuterium & hydrogen loading into nano-Pd on zeolite and alumina matrices at low pressures, *9th International Workshop on Anomalies in Hydrogen/Deuterium Loaded Metals*, Sienna, Italy (2010).
[6]  K.M. Minachev, A.A. Detyuk, R.V. Dmitriyev, and P.I. Slyunyaev, Deuterium exchange with the surface hydrogen of zeolite catalysts 5. Palladium-containing zeolites, *Russian Chemical Bulletin* **27**(12) (1978) 2391–2394.
[7]  K.P. Prasanth, Renjith S. Pillai, Sunil A. Peter, H.C. Bajaj, R.V. Jasra, H.D. Chung, T.H. Kim, and S.D. Song, Hydrogen uptake in palladium and ruthenium exchanged zeolite X, *J. Alloys Compounds* **466** (2008) 439–446.
[8]  Sheng-Yang Huang, Chin-Da Huang, Both-Tze Chang, and Chuin-Tih Yeh, Chemical activity of palladium clusters: sorption of hydrogen, *J. Phys. Chem. B* **110** (2006) 21783–21787.
[9]  Y. Arata and Y. Zhang, Development of compact nuclear fusion reactor using solid pychnodeuterium as nuclear fusion, *ICCF-10*, Cambridge, USA (2003).
[10] A. Kitamura, T. Nohmi, Y. Sasaki, A. Takahashi, R. Seto, and Y. Fujita, Anomalous effects in charging of Pd powders with high density hydrogen isotopes, *Phys. Lett. A* **373** (2009) 3109–3112.
[11] D. Scarano, S. Bordiga, C. Lamberti, G. Ricchiardi, S. Bertarione, and G. Spoto, Hydrogen adsorption and spill-over effects on H-Y and Pd-containing Y zeolites. An experimental and theoretical investigation, *Appl. Catal. A* **307** (2006) 3–12.
[12] F. Guazzone. E. Engwall, and Y. Ma, Effects of surface activity, defects and mass transfer on hydrogen permeance and n-value in composite palladium-porous stainless steel membranes, *Catalyst Today* **118** (2006) 24–31.

Research Article

# Statistical Analysis of Unexpected Daily Variations in an Electrochemical Transmutation Experiment

Felix Scholkmann*

*Biomedical Optics Research Laboratory, Division of Neonatology, University Hospital Zurich, 8091 Zurich, Switzerland*

Tadahiko Mizuno

*Hokkaido University, Center for Advanced of Energy Conversion Materials, Sapporo 060-0813, Japan*

David J. Nagel

*The George Washington University, Washington, DC 20052, USA*

## Abstract

In two electrochemical transmutation experiments, unexpected oscillations in the recorded signals with a daily period were observed for deuterium/palladium loading ratio (D/Pd), temperature ($T$) and pressure ($P$). The aim of the present study was to analyze the time courses of the signals of one of the experiments using an advanced signal-processing framework. The experiment was a high temperature (375 K), high pressure (750 kPa) and long-term (866 h $\approx$ 35 days) electrochemical transmutation exploration done in 2008. The analysis was performed by (i) selecting the intervals of the D/Pd, $T$ and $P$ signals where the daily oscillations occurred, (ii) filtering the signals to remove low-frequency noise, (iii) analyzing the waveforms of the daily oscillations, (iv) applying Ensemble Empirical Mode Decomposition (EEMD) to decompose the signals into Intrinsic Mode Functions (IMFs), (v) performing a statistical test on the obtained IMFs in order to identify the physically most meaningful oscillation mode, (vi) performing an power spectral analysis, (vii) calculating the correlations between the signals, and (viii) determining the time-dependent phase synchronization between the signals. We found that (i) in all three signals (D/Pd, $T$ and $P$) a clear daily oscillation was present while the current density $J$ did not show such an oscillation, (ii) the daily oscillation in $T$ and $P$ had similar waveforms and where anti-correlated to the oscillation in D/Pd, (iii) D/Pd and $T$ had the highest correlation ($r = 0.7693$), (iv) all three signals exhibited phase synchronization over the whole signal length while the strongest phase synchronization took place between D/Pd and $T$. Possible origins of the daily oscillation were discussed and implications for further investigations and experiments were outlined.

*E-mail: Felix.Scholkmann@usz.ch; Tel.: +41-44-2559792; Fax.: +41-44-2554442

## 1. Introduction

Changes in the distribution of chemical elements and in their isotopic abundances where surprisingly reported to happen during electrolysis experiment using both heavy and light water [1–26]. The physical mechanisms of these low-energy transmutations processes are not yet understood. There are many indications that they are not based on conventional nuclear reaction mechanisms, especially since they took place at low energies. Therefore, the term "low-energy nuclear reactions" (LENR) was defined to refer to such kinds of nuclear reactions.

In two electrolysis experiments, besides the transmutations observed, an unexplained oscillation in the recorded signals (loading of deuterium (D) in a Pd lattice expressed as the D/Pd loading ratio, temperature and pressure) with a daily period (i.e. with a period of approx. 24 h) was observed [27]. This is surprising since it has been assumed that LENR were independent of the time of day.

To gain further insight into the daily oscillation, the aim of the present study was (i) to extend and refine the data analysis using the dataset with the best record of daily oscillations (the data set from the experiment conducted by Mizuno et al. [15] available, (ii) to discuss possible causes for the daily oscillations, and (iii) to outline the implications for further investigations and experiments.

## 2. Materials and Methods

### 2.1. Data

For the current analysis, we used the recorded data obtained by a high temperature (375 K), high pressure (750 kPa $\approx$ 7.4 times of the mean atmospheric pressure at mean sea level) and long-term (866 h $\approx$ 35 days) electrochemical transmutation experiment done in 2008 [5]. During the D/Pd loading, the following signals where recorded simultaneously: D/Pd loading ratio (D/Pd [%]), temperature ($T$ [K]), pressure ($P$ [atm]) and current density ($J$ [A/cm$^2$]). All of these four signals where recorded inside the experimental flask. The sampling frequency of the signals was 0.25/h, i.e., every 4 h a measurement was done. The D/Pd loading ratio was determined by continuously measuring the pressure of the oxygen gas inside the electrolysis cell and relating this to the amount of deuterium incorporated into the Pd sample.

### 2.2. Data pre-processing

Visual inspection of the four signals revealed a daily oscillation in the D/Pd, $T$ and $P$ signals when the D/Pd loading was above approximately 90%. This period started after approximately 320 h and ended after approximately 760 h, spanning a time of 440 h. According to this observation, for the next steps of the analysis only the data in this interval where used. The current density $J$ showed no oscillations; it had a constant value ($J = 0.2$ A/cm$^2$) over the whole time span.

In order to get rid of the low-frequency noise in the recorded signals, a finite impulse response (FIR) high-pass filer of order 20 and with a cut-off period of 57 h was applied to the signals. To avoid distortion of the phase of the signals due to the filtering, a zero-phase FIR filtering was realized by processing the input data in both the forward and reverse direction.

### 2.3. Waveform analysis

To analyze the waveforms of the daily oscillation, a block average was computed for all three signals by using the FIR-filtered version of the signals. The block average was calculated by segmenting the signals to intervals with duration of 24 h each, and calculating the mean and standard deviation of the block averaged signals for these intervals.

2.4. Ensemble Empirical Mode Decomposition and selection of intrinsic mode functions

In order to extract the daily oscillation from the signals optimally, an advance signal processing technique (Ensemble Empirical Mode Decomposition, EEMD) was used. It allows decomposing of the signals into characteristic oscillations modes (called Intrinsic Mode Functions, IMFs). EEMD is a further development of Empirical Mode Decomposition (EMD), first introduced 1998 by Huang et al. [28]. EMD can be regarded as a type of adaptive wavelet decomposition [29] or a time-varying filter bank consisting of band limited filters with band widths that vary in time [30,31]. EEMD is a truly noise-assisted data analysis (NADA) method [32].

The IMFs are calculated from the signals such way that they fulfil two conditions: (i) every IMF has the same number of extrema and zero crossings and (ii) each IMF is symmetric with respect to the local mean. The EMD calculation process (called the 'sifting process') is the following [28, 33–35]: (1) All local minima and maxima of the given signal $x(t) = \{x(t_i)|i = 1, 2, \ldots, N\}$ are identified, (2) the upper $e_u(t)$ and lower $e_l(t)$ envelopes of the signal are calculated by interpolating the local minima and maxima by a cubic spline function, (3) the mean of the two envelopes $m_i(t) = [e_l(t) + e_u(t)]/2$ is then subtracted from $x(t)$ which gives the first component: $h_i(t) = x(t) - m_i(t)$. The steps (1)–(3) are performed again on $h_i(t)$ until $h_i(t)$ is a function that fulfils the two described conditions defining an IMF.

If $h_i(t)$ fulfils the conditions, $h_i(t)$ is an IMF denoted as $c_i(t)$. The residual $r_i(t) = x(t) - c_i(t)$ is then treated as a new signal and the sifting process is applied on it.

Finally, the original signal $x(t)$ is given as a sum of the IMFs and the residual:

$$x(t) = \sum_{i=1}^{M} c_i(t) + r_N(t),$$

where $c_i(t)$ is the $i$-th IMF, $M$ the total number of IMFs, and $r_N(t)$ the final residual.

Since, during the sifting process, high-frequency components are firs extracted, the high-order IMFs represent fast variations, and low-order IMFs characterize slow oscillations.

In comparison to EMD, EEMD also performs the sifting process but with the elaboration that the following additionally steps are performed: (1) white noise (with a given amplitude) is added to the input signal, (2) the sifting process is performed to the new signal (raw signal + white noise), (3) steps (1) and (2) are repeated with different realizations of white noise, and (4) the ensemble mean of the corresponding IMFs of the decompositions is calculated [32]. This procedure improves EMD by avoiding the mode mixing problem (not optimal decomposition of the input signal, leading to IMFs that not represent the true oscillations component of the input signal) that can appear by applying EMD [32]. When using EEMD, two parameters are needed to be set: (i) the amplitude of the added white noise in relation to the standard deviation of the input signal ($a_{std}$), and (ii) the ensemble number ($n$). The ensemble number refers to the number of repeated sifting processes.

For the present study, an ensemble number of $n = 100$ was used by applying EEMD to the three input signal (D/Pd, $T$ and $P$). The parameters $a_{std}$ were empirically chosen for every signal so that the daily oscillation could be extracted optimally. The following values are used: $a_{std}(D/Pd) = 0.5$, $a_{std}(T) = 2$, and $a_{std}(P) = 1$.

After decomposing of each signal (D/Pd, $T$ and $P$) into IMFs, we tested whether each IMF is a really a physically meaningful oscillation or only noise. The method proposed by Wu and Huang [36,37] was used. It calculated for each IMF whether it contains statistically significant information or not. For this statistical test, the rescaled energy of each IMF is calculated and compared with the theoretical white noise level.

2.5. Power spectral analysis

Power spectral analysis was applied to the signals by performing a $n$-point discrete Fourier transform (DFT) using the fast Fourier transform (FFT) method. For having a good frequency resolution, we choose $n = 500$.

## 2.6. Correlation analysis

The correlation between the signals was quantified by calculating the Pearson correlation coefficient $r$, which measures the linear dependency between two variables, resulting in a value in the range [–1, 1], with $r = 0$ implying that there is no linear correlation and $r = –1$ or $r = 1$ that the relationship between the two variables is perfectly described by a linear equation. The statistical significance of the correlations was computed using a $t$-test.

## 2.7. Phase synchronization analysis

In order to gain insights into how well the signals are in phase, a phase synchronization analysis was performed. The phase synchronization for two signals $x(t)$ and $y(t)$ can be calculated by a three step process [38,39]. First, the analytical signals of $x(t)$ and $y(t)$ are calculated using the Hilbert transform:

$$\psi_1(t) = x(t) + i\tilde{x}_1(t) = A_1(t)\,e^{i\,\varphi_1(t)} \text{ and } \quad \psi_2(t) = y(t) + i\tilde{y}_2(t) = A_2(t)\,e^{i\,\varphi_2(t)},$$

where $A_1(t)$ and $A_2(t)$ are the instantaneous phases, $\varphi_1(t)$ and $\varphi_2(t)$ the instantaneous frequencies, and $\tilde{x}_1$ and $\tilde{x}_2$ the Hilbert transforms of $x(t)$ and $y(t)$, respectively. In general, the Hilbert transform of a signal $z(t)$ is given as

$$\tilde{z}(t) = \frac{1}{\pi}PV\int\limits_{-\infty}^{\infty} z(\tau)\frac{1}{t-\tau}\mathrm{d}\tau,$$

where $PV$ refers to the Cauchy principal value.

In the next step, the instantaneous phase difference $\Delta\varphi(t)$ of the two signals $x(t)$ and $y(t)$ is calculate according to $\Delta\varphi(t) = \varphi_2(t) - \varphi_1(t)$.

Finally, the synchronization index $\gamma(t)$ is calculated by $\gamma(t) = \left|e^{i\Delta\varphi(t)}\right|$. All values of $\gamma(t)$ are in the range [0, 1] where $\gamma = 1$ refers to a perfect synchronization and $\gamma = 0$ to no synchronization between the signals.

## 3. Results

### 3.1. Waveforms

Figure 1 shows the raw signals, the selected time span and the filtered version of the signals. The waveform analysis revealed that the waveforms of the daily oscillations where different in the three signals (see Fig. 2). The amplitudes of the $T$ and $P$ signals had a negative maximum where the waveform of D/Pd had a positive amplitude maximum. The average values for the amplitudes $A$ of the oscillations where $A(\text{D/Pd}) \approx 2\%$, $A(T) \approx 2\,\text{K}$ and $A(P) \approx 0.06\,\text{atm}$.

### 3.2. EEMD and IMFs

The results of the signal decompositions are depicted in Fig. 3. It was found that for all the three signals, the second IMF was statistical significantly above the theoretical white noise level ($p = 0.05$) (see Fig. 3(d–f)). Therefore, for the further analysis the second IMF (see Fig. 3(g–i)) was used from each of the three signals.

### 3.3. Power spectra

The calculation of the power spectra revealed that the statistical significant oscillation (the second IMF) of the signals is a daily oscillation with a frequency of $1\,\text{d}^{-1}$ (see Fig. 4(a–c). In order to see the effect of the filtering, the spectra where also calculated using the raw data for comparison (see Fig. 5). The additional peaks in the spectra are clear;
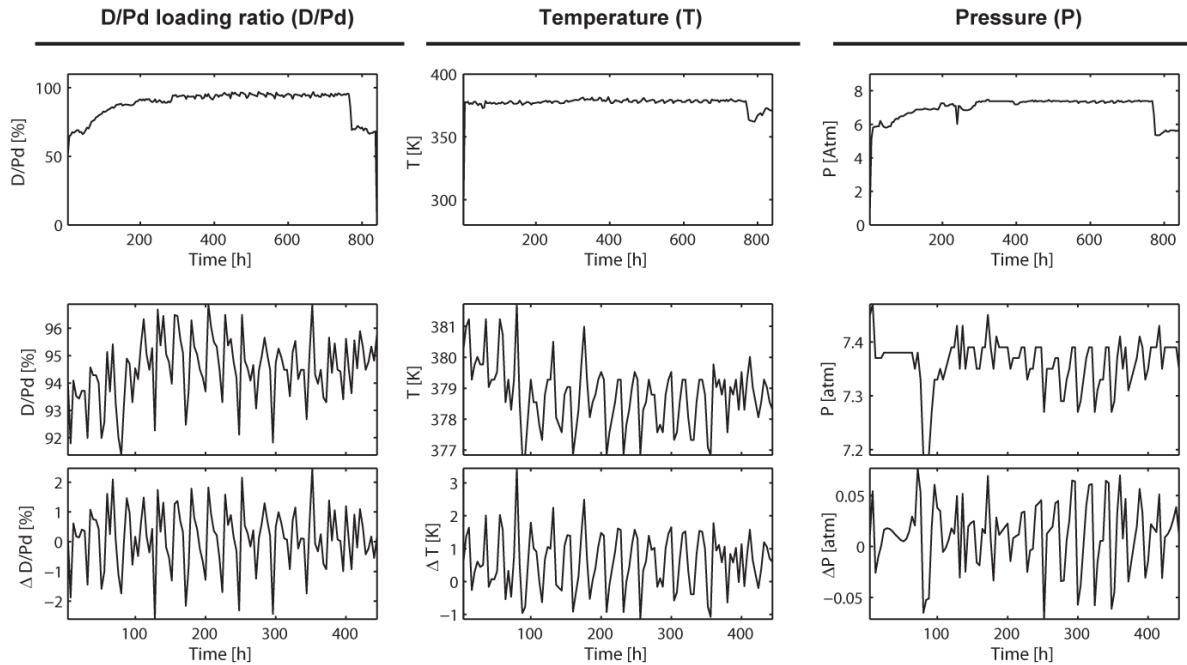
**Figure 1.**   Raw signals (a–c), selected intervals (d–f) and results of the FIR-filtering (g–i).
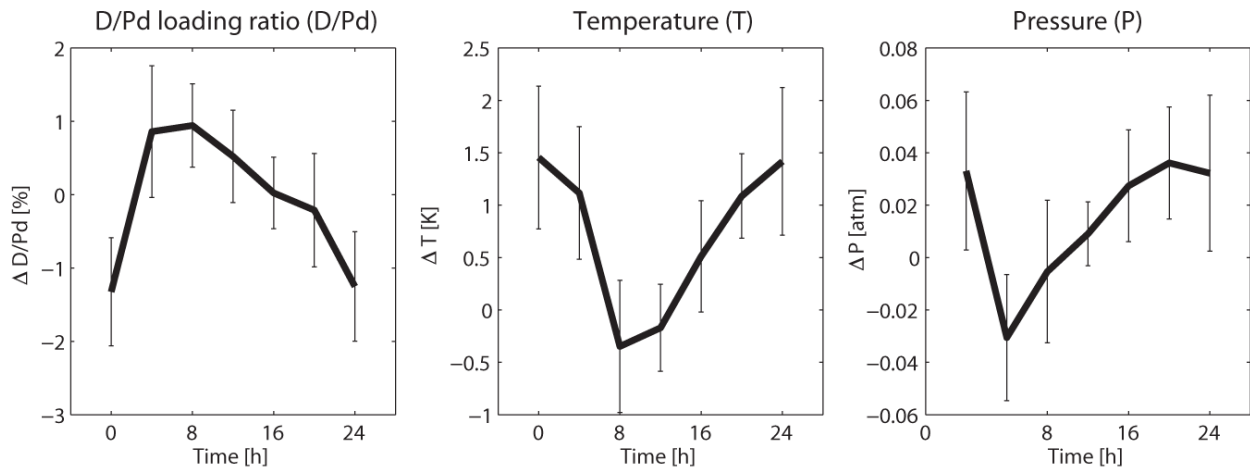


**Figure 2.**   Block averages of the consecutive time intervals with a duration of 24 h from the three measured signals. *Bold line*: mean, error bars: ± standard deviation.

they appear at the frequencies of approx. $2$ and $3\,\mathrm{d}^{-1}$ as well as in the low-frequency (LF) band ($< 0.5\,\mathrm{d}^{-1}$). Only the daily oscillations where significant (as the statistical test of the IMFs indicated). Hence, one can conclude that (i) the

oscillations of 2 and 3 $d^{-1}$ are harmonics in the power spectra that are caused by the non-sinusoidal waveforms and are not own oscillations present in the signals, (ii) the LF components are non-linear trends in the signal that also do not represent a physically meaningful oscillation component of the signal.
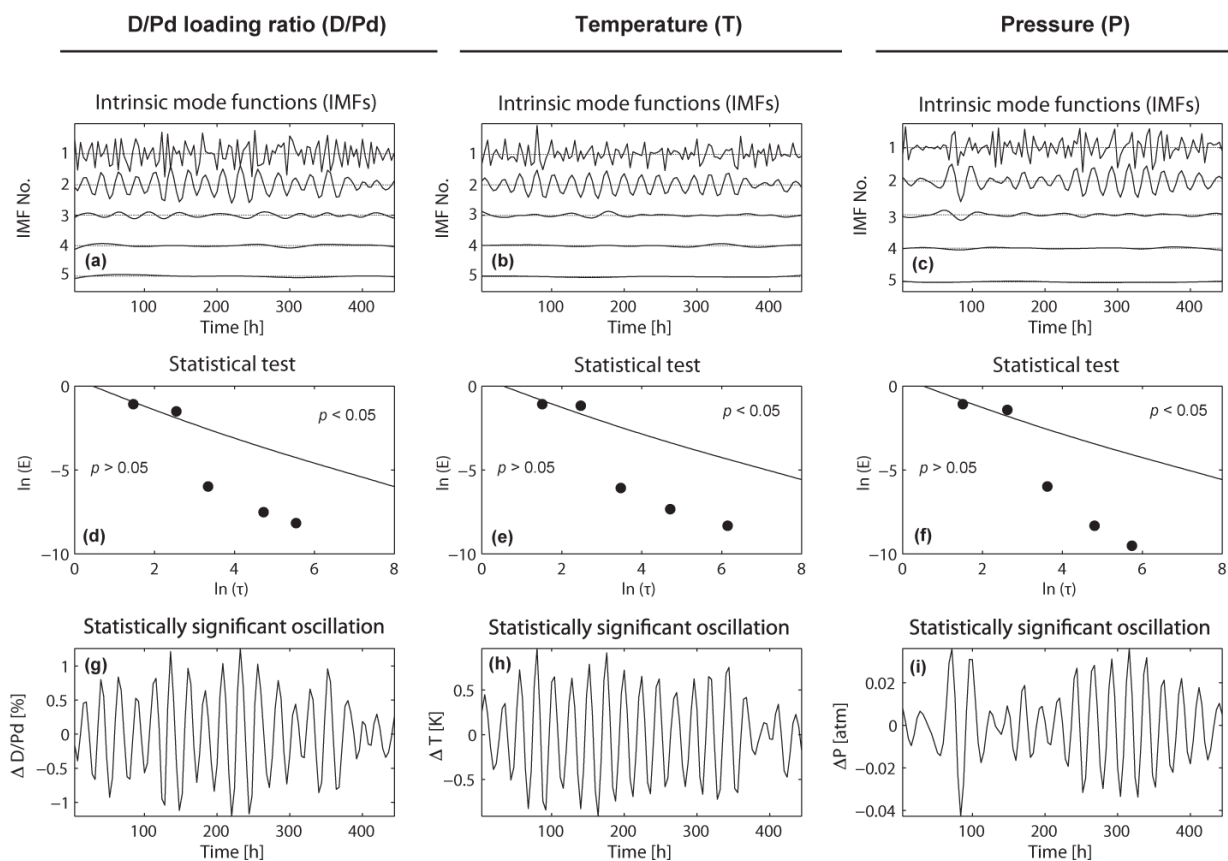


**Figure 3.**   Results of the EEMD signal processing. IMFs (a–c), results of the statistical test (d–f) and statistically significant oscillations (g–i). The lines in the subplots (d–f) are the theoretical white noise levels with correspond to the 5% significance level ($p = 0.05$).

### 3.4.   Correlations

As the correlation analysis showed, D/Pd and $T$ as well as D/Pd and $P$ were significantly negatively correlated ($r = -0.7693$,  $p < 0.001$ and $r = -0.4324$,   $p < 0.001$) while the correlation between $T$ and $P$ was significantly positive ($r = 0.307$, $p < 0.001$) (see Fig. 4(d–f)).

### 3.5.   Phase synchronization

The analysis of the phase synchronization between the signals showed that all signals are synchronized during the whole time where the strongest synchronization was detectable between D/Pd and $T$ (see Fig. 4(g–i)).
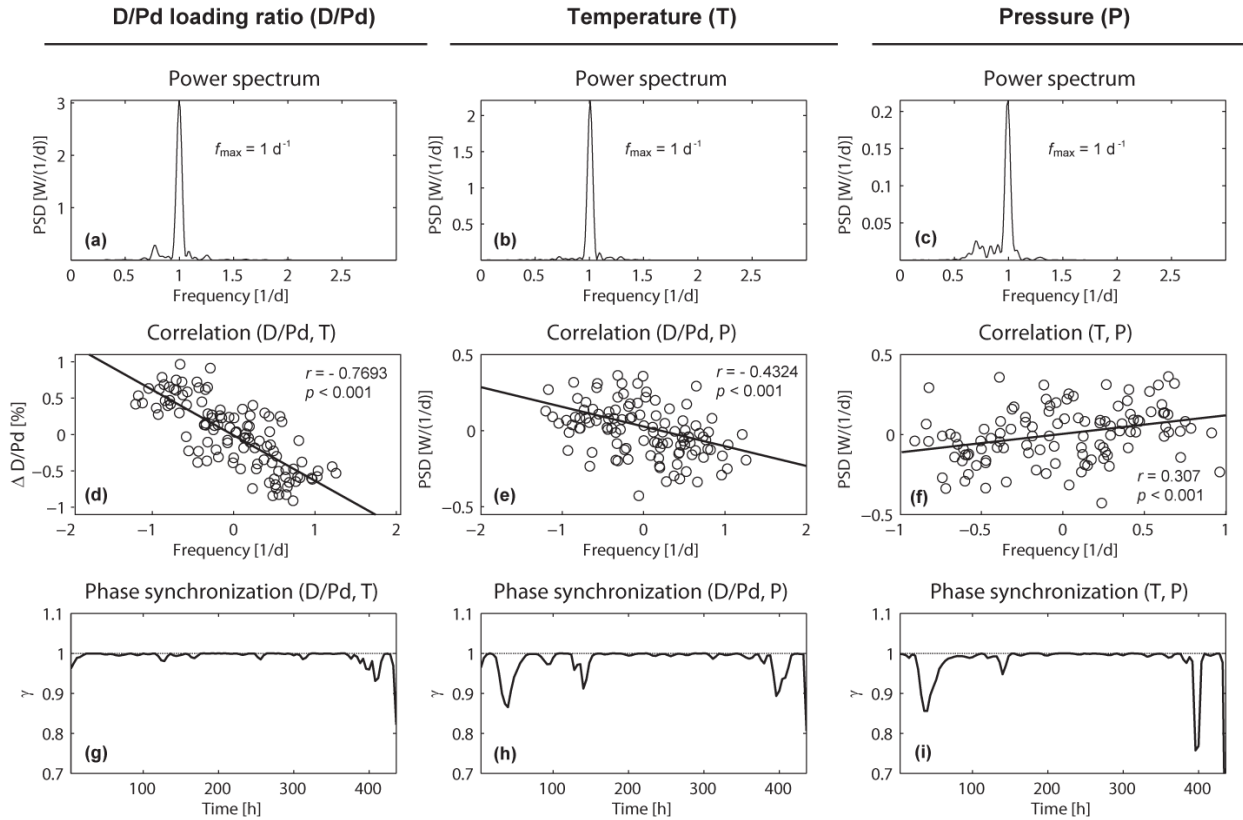
**Figure 4.**   Power spectra (a–c), correlations (d–f) and time variations of the phase synchronizations (g–i).

## 4.  Discussion, Conclusions and Outlook

The different methods of signal analysis performed in the present study revealed that (i) in all three signals (D/Pd, *T* and *P*) a clear daily oscillation was present (confirmed with statistical testing of the IMFs, power spectral analysis and
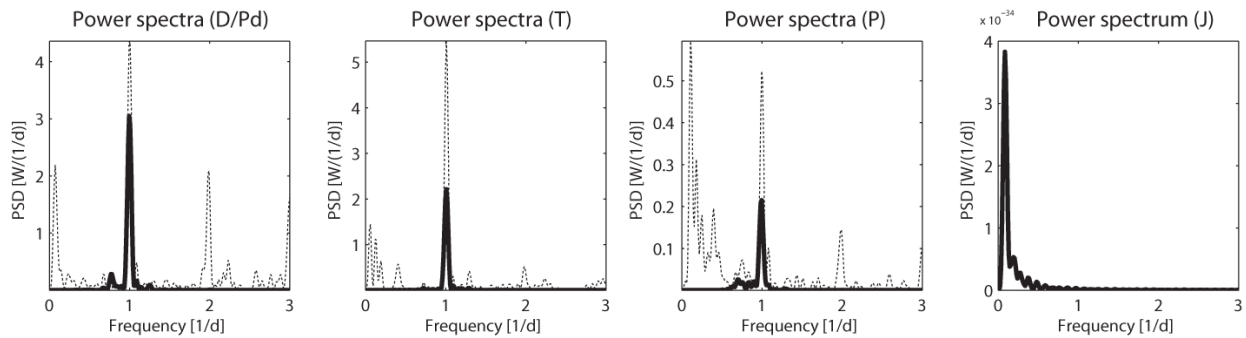


**Figure 5.**   Power spectra calculated with the raw and filtered signals.

waveform analysis) while the current density $J$ did not showed such an oscillation, (ii) the daily oscillation in $T$ and $P$ had similar waveforms and where anti-correlated to the oscillation in D/Pd, (iii) D/Pd and $T$ had the highest correlation ($r = 0.7693$), (iv) all three signals exhibited phase synchronization over the whole signal length, with the strongest phase synchronization between D/Pd and $T$.

Concerning the possible cause of the daily oscillation one can conclude from the obtained results that it is not probably that a daily variation in the current density $J$ caused the daily oscillations in the three other signals. That is, the power supply was stable independent over time. Also, there might be a causal relationship between D/Pd and $T$ (since they are the best correlated). The direction of causality could not be analyzed since of the poor sampling frequency. Having an higher sampling frequency would allow performance of a causality analysis, such as the Granger causality test [40] for example.

In general, the factor causing the daily oscillation could be an internal or external one.

An internal factor could be that the electrochemical LENR dynamics exhibit characteristics of a nonlinear physiochemical oscillator, driven by the thermodynamic non-equilibrium and the composition of the reactants. Such self-oscillations where found to occur in different chemical and physiochemical reactions [41–45], where the Belousov–Zhabotinsky reaction [46] is the most famous one.

The observed daily variation could also be caused by an external factor. The most obvious factors could be a meteorological variable such as atmospheric temperature, atmospheric pressure or relative humidity. Daily oscillations are present in the fluctuations of atmospheric temperature [47], atmospheric pressure [48] and relative humidity [49]. Also the concentration changes of $NO_2$, $O_2$, $O_4$ [50], $CO_2$ [51,52] and radon [53,54] exhibit a daily oscillation.

Other external factors could be of geophysical (e.g. changes of the geomagnetic field strength and orientation) or of cosmophysical origin (e.g. changes in cosmic ray intensity and solar wind strength). Periodic geo- and cosmophysical influences were reported for different physiochemical processes. For example, Piccardi et al. [55] observed daily, annual and long-term variations in chemical reaction rates. Similar effects where found in crystallisation processes [56]. They were explained as originating mainly from low-frequency oscillations of the earth magnetic field.

Unexpected daily oscillations were also found in a world-wide network of physical random number generators [57], in the frequency drift of two quartz resonators [58] and even in the value of the gravitational constant measured using a torsion balance [59].

Interestingly, unexpected oscillations with different periods where also registered in nuclear decay process. Oscillations with daily [60–63], monthly [60,61,63] and yearly [61,63–72] periods where found. In addition, even an oscillation with a period in the range of 11–12 years could be identified [70,73] (maybe corresponding to the 11-year solar cycle).

In order to evaluate whether one of the mentioned internal and external factors caused the observed daily oscillation in this LENR experiment, further analysis has to be done. One good start would be to replicate the original LENR experiment of Mizuno et al. [5] and to optimize the experimental setup and measurement with respect to:

(1) Increasing the duration of the experiment and the measurements (suggestion: > 1 month).
(2) Increasing the sampling frequency (suggestion: 1 Hz).
(3) Improving the experimental setup so that there could not be any effect from temperature, pressure and humidity on the LENR process in the flask.
(4) Continuous measuring temperature, pressure and humidity inside and outside the flask, as well as in the room where the experiment takes place.
(5) Continuous measuring of the magnetic field strength and the strength of electromagnetic radiation in different frequency bands.
(6) Performing the experiment at different global locations in order to evaluate whether the daily oscillation is dependent on the geographical location.

(7) Simultaneously performing the experiment on different locations and analyzing the time correlation of the measured parameters.

(8) Applying different kinds of shielding (e.g. lead, aluminium, mu-metal) to the experimental setup.

(9) Intentional variation of the potential influencing parameters (temperature, pressure, humidity, magnetic field strength, etc.) and analyzing their impact on the occurrence and characteristic of the daily oscillation.

(10) Performing a causality analysis between all measured parameters to determine their relationships.

(11) Measuring the D/Pd ratio with two different methods (gas and resistance method) and evaluating whether the daily oscillation is present in both parameters or not.

In conclusion, the present study investigated the observed phenomenon of a daily oscillation in an LENR experiment. No clear answer could be given regarding the origin of the daily oscillation. However, a promising signal processing framework was demonstrated. It could be employed in further analysis using data from proposed experiments, which extend the original experiment regarding the duration of the experiment and the recording of internal and external parameters. Thus, further analyses might indicate the origin of the daily oscillations in nuclear reaction rates.
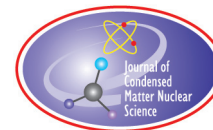
## References

[1] G.H. Miley, Characteristics of reaction product patterns in thin metallic films experiments, in *Asti Workshop on Anomalies in Hydrogen/Deuterium Loaded Metals*, Rocca d' Arazzo, Italy, 1997.

[2] G.H. Miley et al., Quantitative observations of transmutation products occuring in thin-film coatedmicrospheres during electrolysis, in *6th Int. Conf. on Cold Fusion*. 1996. Tokyo, Japan.

[3] G.H. Miley and J.A. Patterson, Nuclear transmutations in thin-film nickel coatings undergoing electrolysis, *J. New Energy* **1**(3) (1996) 5–39.

[4] T. Mizuno, Experimental confirmation of the nuclear reaction at low energy caused by electrolysis in the electrolyte. in *Symposium on Advanced Research in Energy Technol. 2000,* Hokkaido University, 2000.

[5] T. Mizuno, Transmutation reactions in condensed matter, in *Low-Energy Nuclear Reactions Sourcebook, American Chemical Society Symposium Series,* J. Marwan and S.B. Krivit (Eds.), DC, Oxford University Press, 2008, pp. 271–294.

[6] D.W. Mo et al., The evidence of nuclear transmutation phenomena in Pd-system using NAA, Vancouver, B.C., Canada: ENECO, University of Utah Research Park, 1998.

[7] T. Ohmori et al., Transmutation in a gold-light water electrolysis system, *Fusion Technol.* **33** (1998) 367–382.

[8] Y. Iwamura, M. Sakano and T. Itoh, Elemental analysis of Pd complexes: effects of $D_2$ gas permeation, *Japanese J. Appl. Phys.* **41** (2002) 4642–4648.

[9] J. Warner and J. Dash. Heat production during the electrolysis of D20 with titanium cathodes. in *8th Int. Conf. on Cold Fusion*, Bologna, Italy, 2000.

[10] M. Bernardini et al., Anomaleous effects induced by $D_2O$ electrolysis at titanium. in *8th Int. Conf. on Cold Fusion,* Bologna, Italy, 2000.

[11] R.T. Bush and R.D. Eagleton, Evidence for electrolytically induced transmutation and radioactivity correlated with excess heat in electrolytic cells with light water rubidium salt electrolytes, *Trans. Fusion Technol.* **26**(4T) (1994) 344.

[12] J. Divisek, L. Fuerst and J. Belej, Energy balance of $D_2O$ electrolysis with a palladium cathode. Part II. Experimental results, *J. Electroanal. Chem.* **278** (1989) 99.

[13] D. Cirillo and V. Iorio, Transmutation of metal at low energy in a cinfined plasmain water, in *11th Int. Conf. on Cold Fusion,* Marseilles, France, 2004.

[14] R. Notoya, Low temperature nuclear change of alkali metallic ions caused by electrolysis, *J. New Energy* **1**(1) (1996) 39.

[15] V.A. Romodanov, Tritium generation during the interaction of plasma glow discharge with metals and a magnetic field, in *10th Int. Conf. on Cold Fusion,* Cambridge, USA, 2003.

[16] V. Violante et al., X-ray emission during electrolysis of light water on palladium and nickel thin films, in *9th Int. Conf. on Cold Fusion,* Beijing, China, 2002.

[17] V. Violante et al., Analysis of Ni-hybride thin film after surface plasmons generation by laser technique, in *10th Int. Conf. on Cold Fusion,* Cambridge, USA, 2003.

[18] Y. Iwamura, T. Itoh and M. Sakano, Nuclear products and their time dependence induced by continous diffusion of deuterium through multi-layer palladium containing low work function material, in *8th Int. Conf. on Cold Fusion*, Bologny, Italy, 2000.

[19] J. Dash and S. Miquet, Microanalysis of Pd cathodes after electrolysis in aqueous acids, *J. New Energy* **1**(1) (1996) 23.

[20] S. Miguet and J. Dash, Microanalysis of palladium after electrolysis in heavy water, *J. New Energy* **1**(1) (1996) 23.

[21] F. Celani et al., Thermal and isotopic anomalies when Pd cathodes are electrolyzed in electrolytes, in *10th Int. Conf. on Cold Fusion*, Cambridge, USA, 2003.

[22] Y. Iwamura et al., Detection of anomaleous elements, X-ray and excess heat induced by continous diffusion of deuterium through multi-layer cathose (Pd/CaO/Pd), in *7th Int. Conf. on Cold Fusion,* Vancouver, Canada, 1998.

[23] T. Ohmori et al., Transmutation in the electrolysis of light water - excess energy and iron production in a gold electrode, *Fusion Technol.* **31** (1997) 210.

[24] T. Ohmori and M. Enyo, Iron formation in gold and palladium cathodes, *J. New Energy* **1**(1) (1996) 39.

[25] T. Mizuno, T. Ohmori and M. Enyo, Anomalous isotopic distribution in palladium cathode after electrolysis, *J. New Energy* **1**(2) (1996) 37.

[26] T. Mizuno, T. Ohmori and M. Enyo, Isotopic changes of the reaction products induced by cathodic electrolysis in Pd, *J. New Energy* **1**(3) (1996) 31–45.

[27] D.J. Nagel, T. Mizuno and D. Letts, Diurnal variations in LENR experiments, in *15th Int. Conf. of Low Energy Nuclear Reactions,* Roma, Italy, 2010.

[28] N.E. Huang et al., The empirical mode decomposition and the Hilbert spectrum for nonlinear and non-stationary time series analysis, *Pro. Roy. Soc. London Ser. a-Math. Physical and Eng. Sci.* **454** (1971) 903–995.

[29] I. Magrin-Chagnolleau and R.G. Baraniuk, Empirical mode decomposition based time-frequency attributes, in *69th SEG Meeting,* Houston, TX, USA, 1999.

[30] P. Flandrin, G. Rilling and P. Goncalves, Empirical mode decomposition as a filter bank, *IEEE Signal Process. Lett.* **11**(2) (2004) 112–114.

[31] S. Assous, A. Humeau and J.P. L'Huillier, Empirical Mode Decomposition applied to laser doppler flowmetry signals: Diagnosis approach, *27th Annual Int. Conf. of the IEEE Engineering in Medicine and Biology Society*, Vols. 1–7, 2005, pp. 1232–235.

[32] Z.H. Wu and N.E. Huang, Ensemble empirical mode decomposition: a noise assisted data analysis method, *Adv. Adaptive Data Analysis* **1**(1) (2009) 1–41.

[33] N.E. Huang, An adaptive data analysis method for nonlinear and nonstationary time series: The empirical mode decomposition and Hilbert Spectral Analysis, *Wavelet Analysis and Applications*, 2007, pp. 363–376.

[34] N.E. Huang, Review of empirical mode decomposition, *Wavelet Applications VIII* **4391** (2001) 71–80.

[35] N.E.Huang, A new method for nonlinear and nonstationary time series analysis: Empirical mode decomposition and Hilbert spectral analysis, *Wavelet Applications VII* **4056** (2000) 197–209.

[36] Z.H. Wu and N.E. Huang, A study of the characteristics of white noise using the empirical mode decomposition method, *Pro. Roy. Soc. London Series, a-Math. Physical and Eng. Sci.* **460** (2006) 1597–1611.

[37] P.X. Gao, H.F. Liang and W.W. Zhu, Periodicity of flare index revisited using the Hilbert-Huang transform method, *New Astronomy* **16**(3) (2011) 147–151.

[38] M.G. Rosenblum, A.S. Pikovsky and J. Kurths, Phase synchronization of chaotic oscillators, *Phy. Rev. Lett.* **76**(11) (1996) 1804–1807.

[39] M. Winterhalder et al., Sensitivity and specificity of coherence and phase synchronization analysis, *Phys. Lett.* A **356**(1) (2006) 26–34.

[40] C.W.J. Granger, Investigating causal relations by econometric models and cross-spectral methods, *Econometrica* **37**(3) (1969) 414–438.

[41] F. Rossi and M.L.T. Liveri, Chemical self-organization in self-assembling biomimetic systems, *Ecological Modelling* **220**(16) (2009) 1857–1864.

[42] S. Kiatiseviand and S. Maisch, Study of the oscillation and luminol chemiluminescence in the $H_2O_2$–KSCN–$CuSO_4$–NaOH system, *Chemical Phys. Lett.* **499**(1–3) (2010) 173–177.

[43] V.I. Nekorkin et al., Polymorphic and regular localized activity structures in a two-dimensional two-component reaction–

diffusion lattice with complex threshold excitation, *Physica D-Nonlinear Phenomena* **239**(12) (2010) 972–987.

[44] J. Horvath, I. Szalai and P. De Kepper, Pattern formation in the thiourea–iodate–sulfite system: Spatial bistability, waves, and stationary patterns, *Physica D-Nonlinear Phenomena* **239**(11) (2010) 776–784.

[45] R. Yoshida et al., Self-oscillating gel as novel biomimetic materials, *J. Controlled Release* **140**(3) (2009) 186–193.

[46] A.M. Zhabotinsky, Periodic oxidizing reactions in liquid phase, *Doklady Akademii Nauk Sssr.* **157**(2) (1964) 392–395.

[47] K.Y. Vinnikov, A. Robock and A. Basist, Diurnal and seasonal cycles of trends of surface air temperature, *J. Geophysical Research-Atmospheres* **107**(D22) (2002).

[48] V.V. Ivanov, Seasonal and diurnal variations in atmospheric pressure, *Izvestiya Atmospheric and Oceanic Phys.* **43**(3) (2007) 323–337.

[49] A. Dai et al., Diurnal variation in water vapor over North America and its implications for sampling errors in radiosonde humidity, *J. Geophysical Research-Atmospheres.* **107**(D10) (2002) ACL 11.1–11.14.

[50] G.S. Meena and D.B. Jadhav, Study of diurnal and seasonal variation of atmospheric $NO_2$, $O_3$, $H_2O$ and $O_4$ at Pune, India, *Atmosfera* **20**(3) (2007) 271–287.

[51] S.B. Idso, C.D. Idso and R.C. Balling, Seasonal and diurnal variations of near-surface atmospheric $CO_2$ concentration within a residential sector of the urban $CO_2$ dome of Phoenix, AZ, USA, *Atmospheric Environment* **36**(10) (2002) 1655–1660.

[52] Y.S. Wang et al., Trend, seasonal and diurnal variations of atmospheric CO2 in Beijing, *Chinese Sci. Bulletin* **47**(24) (2002) 2050–2055.

[53] J.P. Rydock, A. Naess-Rolstad and J.T. Brunsell, Diurnal variations in radon concentrations in a school and office: implications for determining radon exposure in day-use buildings, *Atmospheric Environment* **35**(16) (2001) 2921–2926.

[54] V.R.K. Murty et al., Indoor and outdoor radon levels and its diurnal variations in Botswana, *Nucl. Inst.Methods Phys. Res.* A **619**(1–3) (2010) 446–448.

[55] G. Piccardi, *The Chemical Basis of Medical Climatology,* Springfield, Charles C. Thomas, 1962.

[56] E.A. Baranovsky, V.P. Tarashchuk and B.M. Vladimirsky, Effect of solar activity and geophysical disturbance on physical-chemical processes in liquid medium: Preliminary analysis of storm-glass activity, *Izvestiya Atmospheric and Oceanic Phys.* . **46**(8) (2010) 925–934.

[57] S.E. Shnoll and V.A. Panchelyuga, Cosmo-physical effects in the time series of the GCP network, arXiv:physics/0605064v1 [physics.gen-ph], 2006.

[58] N.V. Klochek, L.E. Palamarchuk and M.B. Nikonova, Preliminary results of investigation of the influence of cosmophysical radiation of non-electromagnetic nature on physical and biological systems, *Biofisika* **40**(4) (1995) 889–896.

[59] M.L. Gershteyn et al., Experimental evidence that the gravitational constant varies with orientation, *Gravitation and Cosmology* **8**(3) (2002) 243–246.

[60] Y.A. Baurov et al., Experimental investigations of changes in the rate of beta decay of radioactive elements, *Phys. Atomic Nuclei.* **70**(11) (2007) 1825–1835.

[61] S.E. Shnoll, K.I. Zenchenko and N.V. Udaltsova, Cosmo-physical effects in structure of the daily and yearly periods of change in the shape of the histograms constructed by results of measurements of alpha-activity Pu-239, arXiv:physics/0504092v1 [physics.space-ph], 2005.

[62] Y.V. Deshcherevskaya et al., Spectral analysis of macroscopic fluctuations in experimental time series, *Biofizika* **40**(5) (1995) 1113–1116.

[63] A.G. Parkhomov, Researches of alpha and beta radioactivity at long-term observations, arXiv:1004.1761v1 [physics.gen-ph] 2010.

[64] D.E. Alburger and G. Harbottle, Half-Lives of Ti$^{44}$ and Bi$^{207}$, *Phy. Rev.* C **41**(5) (1990) 2320–2324.

[65] K.J. Ellis, The effective half-life of a broad beam (pube)-Pu-238 total-body neutron irradiator, *Phys. Medicine and Biology* **35**(8) (1990) 1079–1088.

[66] H. Siegert, H. Schrader and U. Schotzig, Half-life measurements of europium radionuclides and the long-term stability of detectors, *Appl. Radiation and Isotopes* **49**(9–11) (1998) 1397–1401.

[67] E.D. Falkenberg, Radioactive decay caused by neutrinos? *Apeiron* **8**(2) (2001) 32–45.

[68] D.E. Alburger, G. Harbottle and E.F. Norton, Half-life of $^{32}$Si, *Earth and Planetary Sci. Lett.* **78**(2–3) (1986) 168–176.

[69] P.A. Sturrock et al., Power Spectrum Analysis of Physikalisch-Technische Bundesanstalt Decay-Rate Data: Evidence for Solar Rotational Modulation, *Solar Phys.* **267**(2) (2010) 251–265.

[70] D. Javorsek et al., Power spectrum analyses of nuclear decay rates, *Astroparticle Phys.* **34**(3) (2010) 173–178.

[71] J.H. Jenkins et al., Evidence of correlations between nuclear decay rates and Earth-Sun distance, *Astroparticle Phys.* **32**(1) (2009) 42–46.

[72] J.H. Jenkins, D.W. Mundy and E. Fischbach, Analysis of environmental influences in nuclear half-life measurements exhibiting time-dependent decay rates, *Nucl. Instr. Methods Phys.* A **620**(2–3) (2010) 332–342.

[73] P.A. Sturrock et al., Power spectrum analysis of BNL decay rate, *Astroparticle Phys.* **34**(2) (2010) 121–127.

Research Article

# Correlation Between Surface Properties and Anomalous Effects in F&P Experiments

E. Castagna, S. Lecci, M. Sansovini, F. Sarto and V. Violante RdA*

*ENEA, Unità Tecnica Fusione, C. R. Frascati, Via Enrico Fermi, 45 - 00044 Frascati (Rome) Italy*

## Abstract

The reproducibility of anomalous excess heat production during electro-chemical deuterium permeation of Pd cathodes has been recently observed[1] to be strongly correlated with the palladium surface properties (easy loading at low current, crystal grain distribution, crystallographic orientation, and surface morphology). The understanding of the physical mechanism that is responsible for such observed correlation is very challenging and it is complicated further by the fact that the different features are not, in principle, independent each from the other. In this work, the experimental results concerning the correlation of the excess heat production with the cathode surface properties are reviewed and some possible connections of the observed effects with the deuterium kinetics inside the palladium and the electromagnetic interactions at the metal/electrolyte interface are discussed.
© 2012 ISCMNS. All rights reserved. ISSN 2227-3123

*Keywords:* Atomic force microscopes, Electron states at surfaces and interfaces, Optical properties of surfaces

## 1. Introduction

The reproducibility of excess heat production in palladium/deuterium systems is a critical problem that, more than any other issue, has been feeding the criticisms against the reliability of the experimental evidences of this effect. In order to evaluate correctly the reproducibility of any experiment, it is necessary to define the system under study, as well as possible, getting the control over those experimental parameters which are expected to mainly affect it. In the case of anomalous excess heat production, being still lacking an exhaustive theoretical frame, the definition of these parameters is very difficult and it risks to be incomplete.

In the last years, an increasing amount of experimental evidence has been reported, pointing out the correlation between the material properties of the palladium cathodes used in the excess heat experiments and the reproducibility of the effect [1–3]. Replication of calorimetric results in different laboratories was achieved according to the fact that the cathodes had undergone the same manufacturing process and were belonging to the same commercial Pd lot [4]. Some cathodes features have been preliminarily identified to be relevant to the occurrence of the effect, in particular the polycrystalline structure and the surface morphology on micrometer scales.

---

*E-mail: emanuele.castagna@enea.it

Recently, a systematic study has been carried out by the authors, aimed to characterize the surface properties of the cathodes and to correlate them with the excess heat occurrence [2]. The results support the preliminary observations, showing further evidence of the dependence of the anomalous heat effect on the crystallographic orientation, impurity contamination and microscopic features of the cathodes' surface.

As concerning the metallurgical properties, their correlation with the excess heat production can be partially adduced to their effect on the maximum hydrogen/palladium ratio achievable during the experiment, which is well known to correlate with the heat production through a threshold behavior [4]. Actually, the crystal grain size distribution and grain boundary shape can strongly affect the deuterium/hydrogen solubility in palladium, by controlling the diffusion processes and stress fields developed during hydrogenation [5].

The crystal orientation as well as the presence of impurities can strongly affect the result of chemical etching on the surface morphology of polycrystalline materials [6]. Both these material properties may have also a non-negligible role on electrode kinetics during electrolysis [7,8], then influencing the deposition/dissolution processes of the cathode surface, and, consequently, its local morphology.

Cathode's surface morphology seems to be a crucial parameter in controlling the excess heat reproducibility. In this article, we investigate some possible effects, through which surface features and the excess heat production could be related. Before going through the discussion, we briefly review the experimental results and setup concerning the surface characterization of the cathodes.

## 2. Experimental Results

### 2.1. Cathode manufacturing

The Pd samples used as cathodes in electrolysis experiments were obtained from different commercial lots of pure Pd, having nominal purity above 99.95%. They have been processed by mechanical, thermal and chemical treatments, well described elsewhere [2], in order to reduce foil thickness and to improve metallurgical properties and surface morphology. The typical manufacturing procedure consists in the following steps: (1) cold rolling of the raw 1 mm thick material to produce foils thinner than 50 $\mu$m; (2) annealing at temperatures ranging from 800 to 900°C for about 1 h, to relax defects and induce re-crystallization into a proper polycrystalline structure, optimized for achieving maximum deuterium loading; wet chemical etching by nitric acid and aqua regia, to remove impurities and native oxide, and to produce a specific surface roughening.

### 2.2. Characterization of cathodes' surface

The samples were analyzed by different microscopic technique before and after being electrolyzed. Scanning electron microscopy and electron backscattered diffraction spectroscopy were used to inspect crystal grain distribution and orientation.

Surface morphology was better investigated also by Atomic Force Microscopy (AFM). AFM gives a direct measurement of the tri-dimensional (3-D) surface height profile. This is different from images acquired by other microscopic techniques, such as scanning electron microscopy or optical microscopy, in which the contrast is not directly related to the changes in height profile, and 3-D profile reconstruction requires stereoscopic methods or numerical elaboration. For each sample, several images have been taken at different points on the surface, excluding grain boundaries. Details of the AFM instrument used can be found elsewhere [3]. To make easier the comparison between different samples, the images were acquired on the same length scale (typically $24 \times 24$ $\mu$m$^2$) and with the same number of pixels (typically $257 \times 257$). Scanning of the same sample zone on different scale was also performed, in order to select the magnification factor more convenient to observe the surface features of typical samples.

**Table 1.** Summary of max PSD intensity in the range 1–4 $\mu\text{m}^{-1}$ and excess heat data. The second column indicates the excess to input power ratio, the third column indicates the ratio between the number of samples giving excess heat and the total number of experimented samples of the same lot.

| Sample | Excess heat (%) | Reproducibility | Max PSD intensity ($\times 10^{-32}$ m$^4$) |
|--------|-----------------|-----------------|---------------------------------------------|
| #64    | 80–100          | 2/2             | 9.5                                         |
| L5     | 25–60           | 2/4             | 0.7                                         |
| ET-US3 | 25              | 1/1             | 0.6                                         |
| L46    | 12              | 1/1             | 0.06                                        |

The height profiles of the investigated samples were generally characterized by random fluctuations superimposed on periodic or quasi-periodic patterns. These surface features are hard to recognize in direct space, but can be effectively revealed in reciprocal space of the spatial frequencies *(kx, ky)*, by computing the Power Spectral Density (PSD) of the height profile, that provides a decomposition of the surface profile into its spatial wavelength. Although the computation of the PSD is a quite common practice in isotropic random surface characterization, because of the anisotropic texture of our samples, we have defined a dedicated set of (1-D) PSD functions, which were more appropriate to extract the more relevant patterns embedded in the surface profiles, without missing the information relative to surface anisotropy. Details of image processing and analysis can be found in previous publication [3].

In Figs. 1–4, the PSD spectra of samples giving or not anomalous excess heat production were compared; the results showed the maximum intensity of the spectra is quite correlated with the percentage of heat in excess and its reproducibility (see Table 1), but it is much lower in the spectra of samples which did not produce excess heat.

A similar correlation does not appear to be evident in the specific surface area values, which are shown in Table 2I and which are scattered less than 10% around the same mean value.

## 3. Electromagnetic Field Enhancement at PD/Electrolyte Cathode Interface

It is well known that nano-metric surface features of a metal/dielectric interface can induce local oscillations of the electronic charge (surface plasmons), which can be associated to strong amplification of the local electromagnetic field [9].

It has been suggested that the presence of oscillating electromagnetic (EM) field of suitable frequency and intensity may affect the collision dynamics of two deuterons moving in a PdD lattice [10]. In that theoretical investigation, the bulk collective oscillation of the conduction electron was considered as the EM field source. Based on these premises, it could make sense to argue that the observed correlation between the surface morphology of Pd cathodes and the reproducibility of anomalous excess heat production may involve such surface plasmon oscillations and electromagnetic field enhancement effect. In order to explore this hypothesis, we try to get an estimate of the contribution of such a mechanism to the local EM field which is expected to build up at the cathode/electrolyte interface. In particular, we focalize on the role played by the surface morphology in the effect of EM field enhancement.

**Table 2.** Effective surface area of the studied samples, computed from the AFM $24\times24$ $\mu\text{m}^2$ images by the free GNU GPL software Gwyddion.

| Sample | L46 | ET-US3 | L5 | #64 | L47 | L51 | L53 |
|--------|-----|--------|-----|-----|-----|-----|-----|
| Effective area ($\mu\text{m}^2$) | 588 | 634 | 653 | 684 | 631 | 640 | 602 |
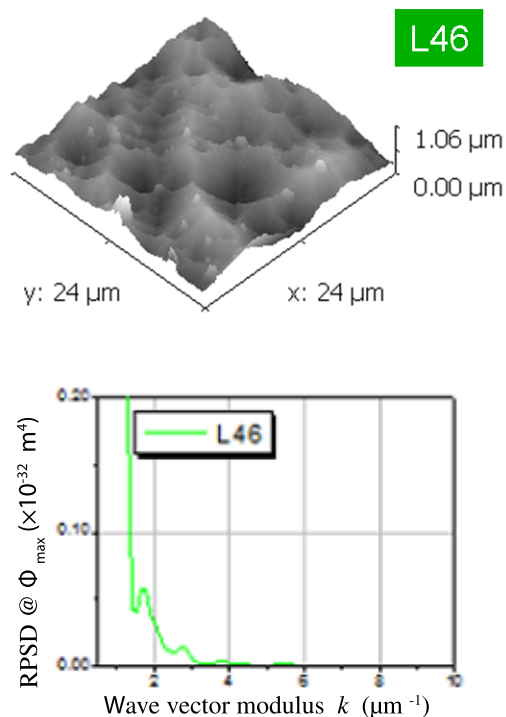
**Figure 1.**  Top:  3-D AFM images of samples L46, which gave excess heat during electrochemical deuterium loading; Bottom:  Maximum Power Spectral Density curves computed from the AFM images shown on the bottom.

## 3.1.  Theoretical approach to EM field enhancement calculations

The theory of EM field enhancement at metallic interfaces has been developed deeply in connection with the study of surface enhanced Raman spectroscopy since about forty years [11] and it is based on the application of Maxwell's equations and linear material dispersion assumptions.

Surface plasmons polaritons (SPP) are eigen-states of the *conducting electron* gas, consisting in collective oscillations of the electronic charge at a metal/dielectric interface.  These excited modes can be activated by an external EM field impinging on the interface, under some conditions specified below.  In practice, the metal electron charge respond to the external excitation by such collective fluctuations, which induce in turn an EM field; the resulting total EM field distribution is spatially localized around the interface and its amplitude is strongly enhanced accordingly to energy conservation.

Depending on the particular geometry of the interface, the SPP may be characterized by different spatial EM distribution and amplitude amplification.

Although the rigorous calculation in the case of a "*real*" surface is a very complicate task, depending on the model adopted to describe the surface profile, some particular ideal cases have been extensively studied and analytically approached, from which physical insight can be extracted.  Numerical simulations may also be a powerful tool in such

a kind of calculations, but their results are hardly extendable to real physical situations because of the complexity of the real surface profile in the direct space. Parametric studies could be instructive, although time consuming.

A widely studied configuration, which could resemble our experimental case of not- engineered polycrystalline Pd surfaces such as those shown in Figs. 1–4, is that of a randomly rough metallic surface. Under the assumption that the average amplitude of the height profile fluctuation (roughness, $\sigma$) is small respect to the wavelength of the EM field, the linear theoretical approach can provide a very simple picture of the SPP effect [12,13]. In this scheme, the surface profile ($z(x, y)$) scanned by AFM is described as the superposition of several sinusoidal diffraction gratings; because of the linear hypothesis described above, the interaction of the EM field with the metallic surface is reduced to the superposition of the single interactions from each single sinusoidal grating. This interaction can produce the excitation of a SPP mode, that consists of in a longitudinal oscillation of the electronic charge confined close to the metal/dielectric interface, whose amplitude depends on the height of the grating, if the wave-vector of the incident field and the pace of the grating satisfy a proper matching condition [14].

The result of such theoretical formulation is an analytical expression describing the EM field enhancement due to SPP excitation, in which the effect of the metal surface properties is expressed only through the power spectral density of
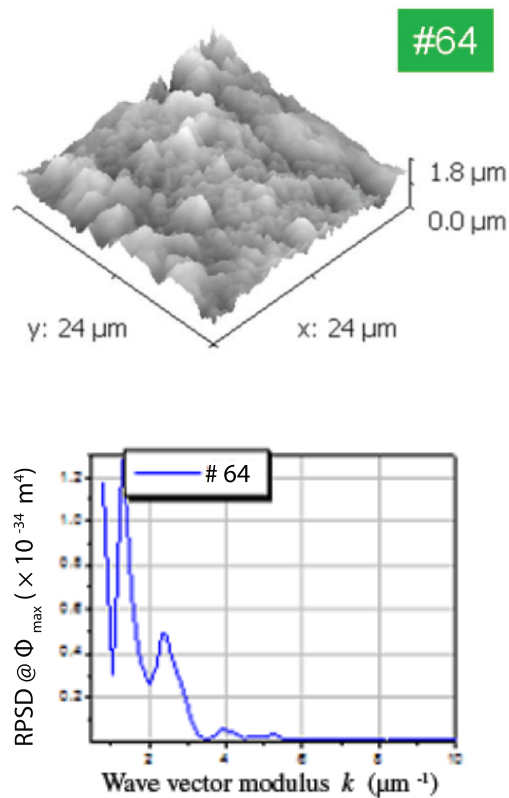


**Figure 2.** Top: 3-D AFM images of samples #64, which gave excess heat during electrochemical deuterium loading; Bottom: Maximum Power Spectral Density curves computed from the AFM images shown on the bottom.
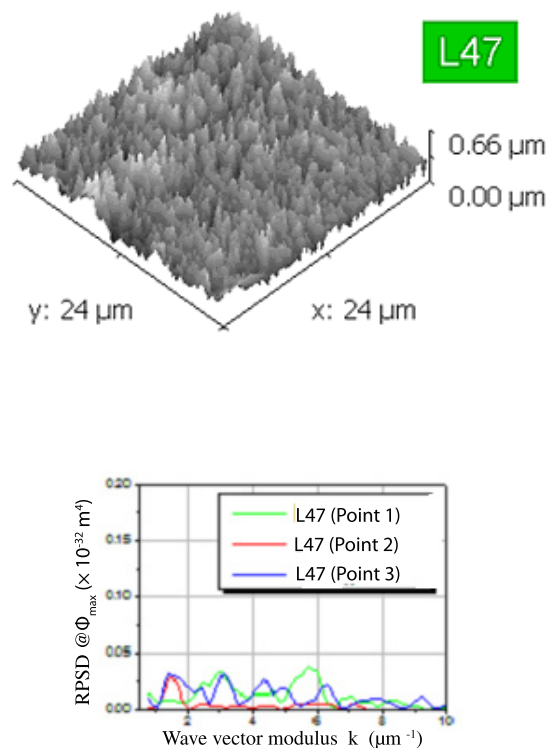
**Figure 3.** Top: 3-D AFM images of samples L47, which did not give excess heat during electrochemical deuterium loading; Bottom: Maximum Power Spectral Density curves computed from the AFM images shown on the top; in case of sample L47 the curves obtained by the analysis of three different sample points are also shown.

the surface profile and the dielectric constant of the metal. In particular, this model, describing the interaction between an electromagnetic field and a corrugated metal surface, finds out that the local amplification of the electromagnetic field, due to the presence of a particular surface morphology, is dependent on the intensity of the PSD spectrum of the considered surface profile.

This dependence of the field enhancement on the PSD profile, together with the experimentally observed correlation between the PSD profile of the cathode surface and the anomalous excess heat production, supports the idea that *this effect* may involve surface plasmon oscillations and electromagnetic field enhancement phenomena.

### 3.2. Predictions of the linear theory

To get a more quantitative feeling of how much such effects may be relevant, we have evaluated the ratio between the maximum amplitude of the SPP electric field and that of the incident one, by following the analytic approach of the linear theory described above, starting from the PSD spectra of the surface profiles of some PdH cathodes.

In Fig. 5, we have reported the results of the calculation of some samples used in excess heat experiment, but each
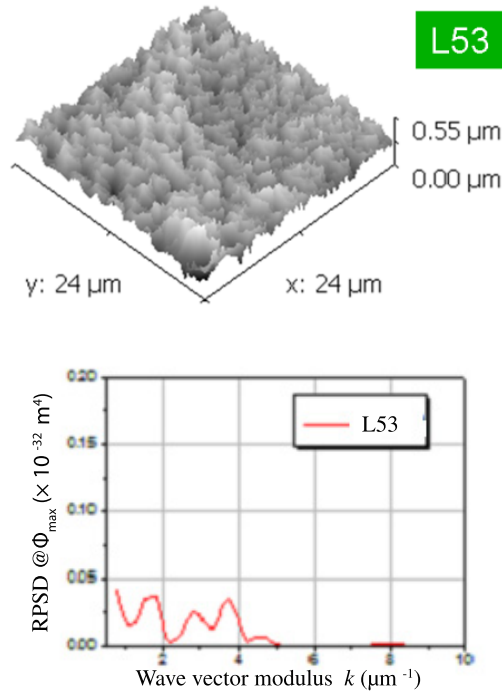
**Figure 4.** Top: 3-D AFM images of samples L53, which did not give excess heat during electrochemical deuterium loading; Bottom: Maximum Power Spectral Density curves computed from the AFM images shown on the top.

giving a different amount of heat as reported in Table 1. The pictures show a quite good correlation between the two effects, although the maximum values of the enhancement factor are not extraordinary high. Note that the results have to be considered as an upper limit of what can be obtained by a more accurate calculation, because of the approximations made in the computation. In particular, the imaginary part of the dielectric constant of palladium hydride has been assumed negligible; this implies that the damping of the electromagnetic field due to the absorption of the material has been neglected; the effect of neglecting the damping is the reduction of the maximum intensity of the amplified electromagnetic field. The other working hypothesis of the used theoretical approach consist in neglecting nonlinear interactions between the surface profile corrugation and the electromagnetic field; this hypothesis is valid for samples having a small roughness. If the sample roughness is not so small to satisfy the requirement of the linear approximation, the nonlinear contributions to the interactions between the surface profile corrugation and the electromagnetic field should be considered into the computation; the effect of these nonlinear contributions is to decrease the maximum intensity of the amplified electromagnetic field, as in the case of the first approximation mentioned above. Then, both the assumptions made lead to over-estimate in the simulation the effect of the electromagnetic field enhancement, so that the reported results should be considered as an upper limit of what can be obtained by a more accurate calculation [15].

### 3.3. The modification of the dielectric constant of PdH

We have already mentioned above that, beside the surface morphology, the other surface property of the cathode on which the SPP field enhancement depends is the dielectric constant of the metallic material. This property is strongly modified during the electrolysis, because of the chemical modification of the material due to the hydride formation and also because of the electric charging of the metal surface, produced by the building up of the electrolysis double layer. Calculations of the electronic density of states of palladium hydride at different H/Pd ratios have been performed by *ab-initio* methods [16]; comparison with experimental data is available in the literature only in the case of thin films of PdH, up to a loading ratio of 0.82 [17], showing the reduction of the modulus of both the real and imaginary part of the dielectric constant, in agreement with the lower electron density at the Fermi level induced by hydrogen. The measurement of the dielectric constant in bulk (i.e. some microns thick) samples at high loading ratios is difficult because of the high optical absorption of the metal, which prevents the use of plasmonic methods based on the attenuated total reflection configuration, and of the instability of the stoichiometric hydride at room temperature.
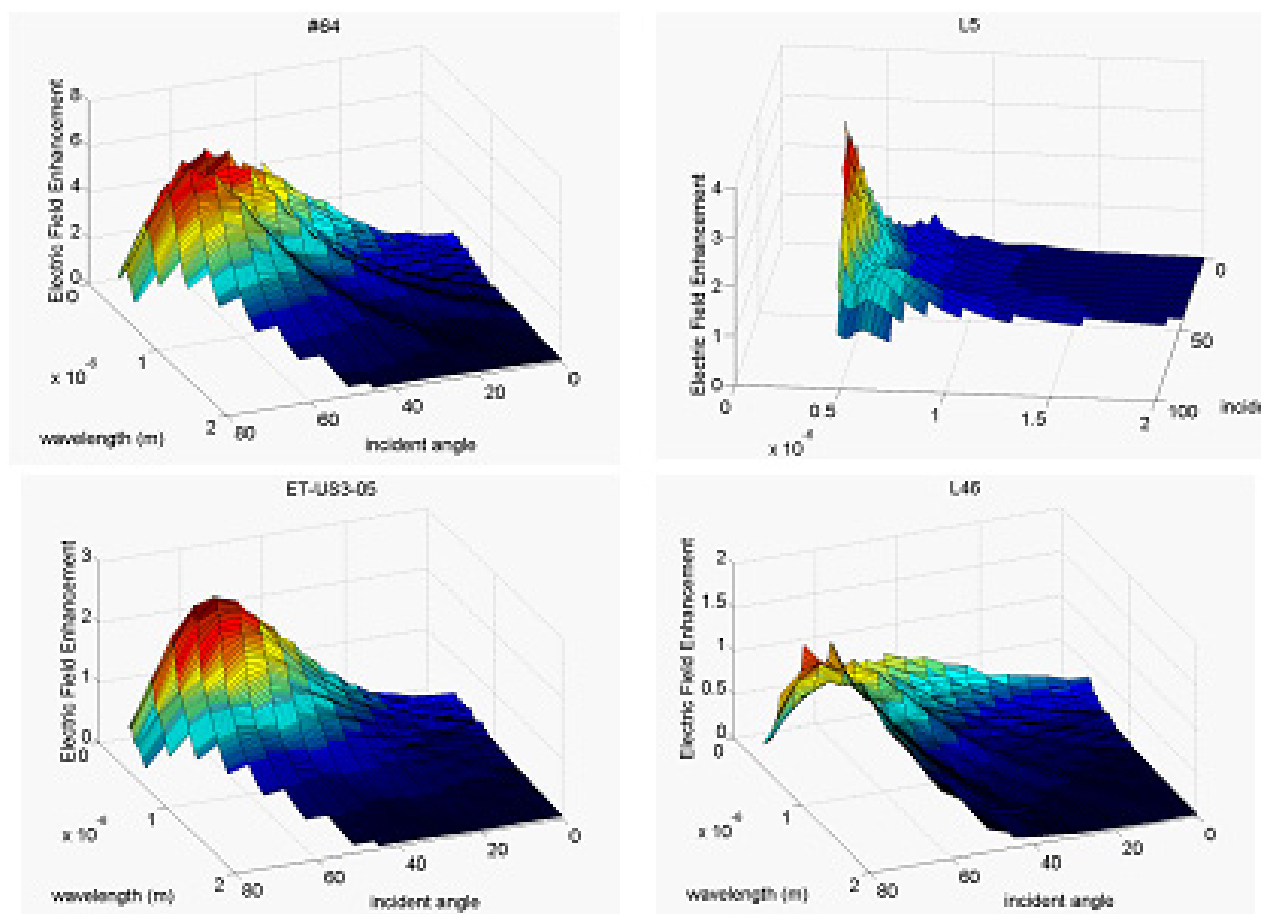


**Figure 5.** Calculation of the electric field enhancement factor of samples #64, L5, #ET-US3-05 and L46, according to the theoretical approach described in text.

As concerning the effect of the electrolysis double layer, in Ref. 17 the authors have applied to PdH the theoretical approach used in the literature to model surface plasmon polariton resonance sensing experiments with gold electrodes [18]. In this theoretical frame, the dielectric constant of the electrode material is assumed to be determined by the electronic charge density (Drude model). Because of the charging of the electrode due to the electrolysis, the electronic charge density of the electrode is modified, producing, consequently, the change of the dielectric constant of the electrode material [19]. The change of the electron density due to this mechanism depends on the electric charge accumulated at the electrode surface, which can be estimated by the Stern model of the double layer and depends on the electrolysis parameters [20]. Figure 6 shows the results of the calculation of the dielectric constant of the PdH electrode, with and without the application of the additional electric charge due to the building –up of the electrolysis double layer, according to the model described above. The results indicate that, the real part of the dielectric constant (see Fig. 6, top) moves towards more negative values, which are typical of the metallic behavior, while the imaginary part of the dielectric constant, that is indicative of the optical absorption of the material, remains quite un-changed (see Fig. 6, bottom).
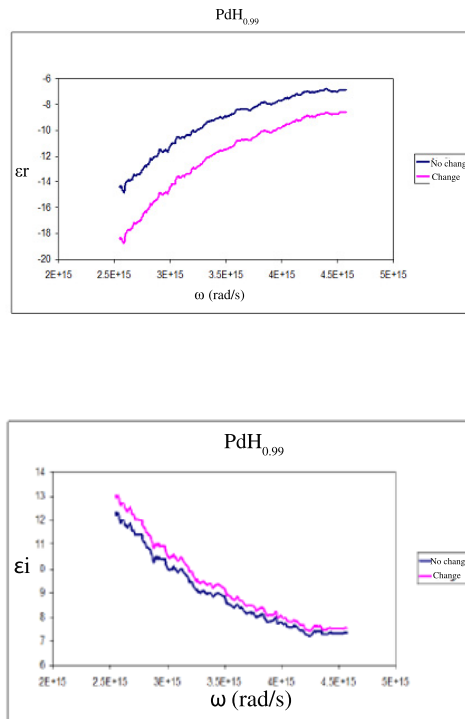


**Figure 6.**   Real (Top) and imaginary (bottom) parts of the dielectric constant of palladium hydride cathode with and without cathodic polarization.

### 3.4. The effect of a dynamic interface

The analysis performed is for a static case but the electrochemical loading condition with electrons going to the surface and D atoms moving in (and out) through the surface is highly dynamic. Treating this mathematically is well beyond the scope of this paper. However, we try in this paragraph to speculate on how this dynamic might affect the above scenario.

The change in time regarding the metal-electrolyte interface system mostly concerns the variation of:

(1) double layer charge, whose time scale is the related to the rate of the external charge fluctuation and its screening by the metal free electrons;
(2) hydrogen/deuterium concentration inside the metal lattice, which follows the local dynamic of hydrogen/deuterium ions across the metal interface;
(3) surface morphology, which depends on mechanisms of corrosion and deposition at the metal surface.

In the proposed scenario of SPP excitation, both the double layer charge and the deuterium/hydrogen concentration enter into the process through their effect on the dielectric constant of the metal, while the surface morphology directly affects the power spectral density of the surface profile.

Given $\tau_\omega$ the time period of the electromagnetic incident radiation and $\tau_{change}$ the time period relative to the system modification rate, if $\tau_{change} \gg \tau_\omega$ then we can assume to be valid the adiabatic approximation in which the external electromagnetic field and the system are mostly independent and the interaction scheme developed for the static condition still holds. Then, the effect of such a "slow" variation of the interface on the total field distribution will result in a corresponding "slow" change of the parameters entering the SPP resonance matching condition, i.e. the wavelength and incidence angle of the external radiation respect to the metal surface. Anyway, it's worth noting that, in the case in which the main source of interface variation is due to points 1 and 2, the expected modifications are quite small, as computation showed that there are not huge changing in the dielectric function with the double layer charge (see Fig. 6 in the paper). On the other hand, the effect of the changing of the surface morphology (point 3) can result in a change of the SPP resonance wave vector that can be also quite different from which found for the static case, according to the shape and size of the modified surface shape.

The condition $\tau_{change} \ll \tau_\omega$ is quite far from our experimental conditions, as the frequency of the incident radiation is quite high, typically in the range of the visible electromagnetic spectrum. However, in such a condition, a linear approximation vs. time, similar to the one applied vs. space in this paper to treat the interaction of the radiation with the "rough" surface, can be applied, under the hypothesis that the amplitude of the time variations was not to high. Within such a frame, the system could be considered to be as static, by considering the time average value of the dielectric function instead of the time varying one, and including as a new variable the time autocorrelation function of the surface fluctuations, with a role similar to that played by the power spectral density function within the static scenario.

Finally, if $\tau_\omega \sim \tau_{change}$, the linear response assumptions break down, since the time response of the system is no more linearly related to the external electric field. The system can still be described by the Maxwell's equations, but the time-harmonic solution will be no more valid because of the time dependence of the dielectric constant. Such a time dependence can be interpreted, in the frequency domain, as being responsible for the generation of additional frequency components of the total electromagnetic field, giving rise to a "multi-harmonic" nonlinear system.

## 4. Conclusions

The cathode's surface morphology seems to be a crucial parameter in controlling the anomalous excess heat reproducibility. Different mechanisms can be imagined to explain the experimentally observed dependence of the excess heat results on the cathode surface status. The possible effect of local electro-magnetic field enhancement at the metal/dielectric interface has been investigated. First order electromagnetic theory has been applied to simulate the enhancement of

the EM field, starting by the experimental surface profile data acquired by AFM microscopy. The results support the idea that this effect can be involved in the correlation between the surface morphology and the excess heat production, although the expected maximum enhancement is not very high. This mechanism should be taken into account when the electrochemical kinetics at the cathode is considered, in particular in the case of nano-structured cathode surfaces.

### References

[1]   V. Violante, F. Sarto, E. Castagna, M. Sansovini, S. Lecci, D.L. Knies, K.S. Grabowski, G.K. Hubler, Material Science on Pd-D System to Study the Occurrence of Excess Power, to be published in Proceedings of ICCF-14 International Conference on Condensed Matter Nuclear Science, Washington, DC (2008).

[2]   E. Castagna, M. Sansovini, S. Lecci, A. Rufoloni, F. Sarto, V. Violante, D.L. Knies, K.S. Grabowski, G. K. Hubler, M. McKubre, and F. Tanzella, Metallurgical characterization of Pd electrodes employed in calorimetric experiments under electrochemical deuterium loading, to be published in Proceedings of ICCF-14 International Conference on Condensed Matter Nuclear Science, Washington, DC (2008).

[3]   F. Sarto, E. Castagna, M. Sansovini, S. Lecci, V. Violante, D.L. Knies, K.S. Grabowski, and G.K. Hubler, Electrode Surface Morphology Characterization by Atomic Force Microscopy, to be published in Proceedings of ICCF-14 International Conference on Condensed Matter Nuclear Science, Washington, DC (2008).

[4]   M. McKubre, F. Tanzella, I. Dardik, A. El Boher, T. Zilov, E. Greenspan, C. Sibilia, and V. Violante, Replication of Condensed Matter Heat Production, ACS Proceedings of ACS National Meeting (2007).

[5]   V. Violante, A. De Ninno, and A. La Barbera, *Phys. Rev. B* **56** (1997) 2417–2420.

[6]   M.A. Gosàlvez and R.M. Nieminen, *New J. Phys.* **5** (2003) 100.

[7]   M. Eiswirth, M. Lubke, K. Krischer, W. wolf, J.L. Hudson, and G. Ertl, *Chem. Phys. Lett.* **192** (1992) 254–258.

[8]   M.T. Spitler, *Electrochimica Acta* **52** (2007) 2294–2301.

[9]   A.V. Zayats, I.I. Smolyaninov, A. A. Maradudin, *Phys. Reports* **408** (2005) 131–314.

[10]   V. Violante, A. Torre, G. Selvaggi, and G. Miley, *Fusion Technol.* **39** (2001) 266–281.

[11]   Hora Metiu and Purna Das, *Ann. Rev. Phys. Chem.*, **35** (1984) 507–536.

[12]   A. Marvin, F. Toigo, V. Celli, Phys. Rev. B, **11** (1975) 2777.

[13]   W.H. Weber and G.W. Ford, Optics Lett. **6** (1981) 122.

[14]   H. Raether, in *Surface Plasmons on Smooth and Sough Surfaces and on Gratings*, edited by Springer-Verlag, Berlin Heidelberg New York London Paris Tokyo (1986), Cap. 6.

[15]   F. Toigo, A. Marvin, V. Celli, and N.R. Hill, *Phys. Rev. B* **15** (1977) 5618.

[16]   D.A. Papaconstantopoulos, B.M. Klein, and J.S. Faulkner, *Phys. Rev. B* **18** (1978) 2784–2791.

[17]   W.E. Vargas, I. Rojas, D.E. Azofeifa, and N. Clark, *Thin Solid Films* **496** (2006) 189–196.

[18]   E. Castagna, S. Lecci, M. Sansovini, F. Sarto, and V. Violante RdA, Interaction of the Electromagnetic Radiation with the Surface of Palladium Hydride Cathodes, submitted to be published in Proceedings of ICCF-15 International Conference on Condensed Matter Nuclear Science, Rome, Italy (2009).

[19]   V. Lioubimov, A. Kolomenskii, A. Mershin, D.V. Nanopoulos, and H.A. Schuessler, *Applied Optics* **43** (2004) 3426–3432.

[20]   H. Ohshima and K. Furusawa, *Surf. Sci. Ser.* **76** (1998) 1–17.

Research Article

# The Study of the Fleischman and Pons Effect through the Materials Science Development

V. Violante,* F. Sarto, E. Castagna, S. Lecci and M. Sansovini

*ENEA, Unità Tecnica Fusione, CR Frascati, Via Enrico Fermi, 45-00044 Frascati (Rome) Italy*

## M. McKubre and F. Tanzella

*SRI International Menlo Park, CA, USA*

**Abstract**

The state of the palladium metal has been identified on the basis of statistical data to play fundamental roles in producing the Fleischman–Pons excess heat effect. The deuterium loading dynamics and its equilibrium concentration are mostly controlled by the metallurgy; a minimum threshold loading (D/Pd $\sim$ 0.9) is necessary to observe the excess. The crystallographic orientation is also correlated with the phenomenon such that mainly $\langle 100 \rangle$ oriented samples gave the highest reproducibility. A specific cathode surface morphology, identified by means of the power spectral density function, represents an additional identified condition to observe the effect. Materials specimens respecting the characteristics described above have been used to obtain a transportable reproducibility. Designed materials giving excess power have been produced but the amplitude of the signals and full reproducibility are not yet achieved. Other features of the material such as the nature and content of impurities and defects seems to be crucial in obtaining the required palladium characteristics.
© 2012 ISCMNS. All rights reserved. ISSN 2227-3123

*Keywords:* Calorimetry, Chemical potential, Diffusion coefficient, Dimensionless transport equation, Gorsky effect

## 1. Introduction

Since 1996 at ENEA, the metallurgy was identified to be responsible for the loading of hydrogen or deuterium into palladium cathodes [1]. Loading is, in general, not homogeneous and concentration gradients produce a stress field that modifies the chemical potential of hydrogen dissolving into the lattice, as a consequence the diffusion dynamics change and the hydrogen or deuterium equilibrium concentration may be reduced. A metallurgy able to minimize the concentration gradients is required in order to achieve the loading threshold considered to be a necessary condition to observe the production of excess heat.

---

*E-mail: emanuele.castagna@enea.it

A process has been defined to have a metallurgy enhancing mass transfer by reducing the hydrogen (deuterium) concentration gradients and then the stress field into the sample.

The focus of our research activity was mainly on:

(1) Extended material science also involving the study of the surface and crystallography to increase both, reproducibility and signals.
(2) Calorimetric experiments conceived to have an appropriate signal/noise ratio.
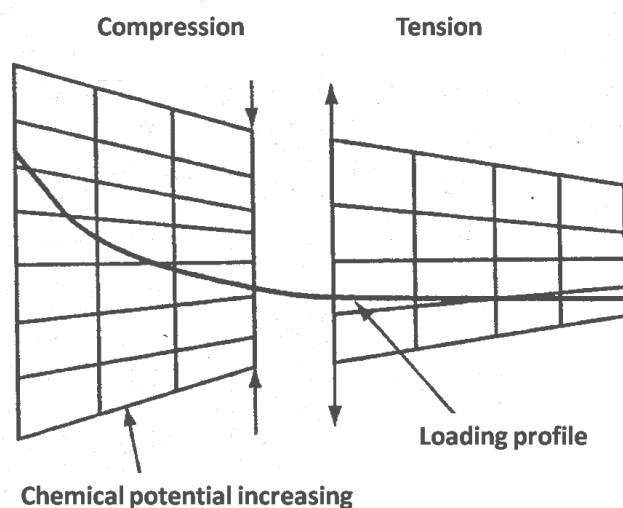


**Figure 1.**    The effect of the hydrogen concentration profile on the stress field.

(3) Theoretical work to identify methods to trigger the effect.

## 2. Stress Field Limiting Hydrogen (Deuterium) Solubility in Palladium

The dissolution of hydrogen isotopes into a metal lattice is not only a problem of thermodynamic equilibrium between the hydrogen inside the lattice and the hydrogen in the external phase (gas or liquid) but is also a problem of disequilibrium because of the occurrence of a transport process. Both aspects of this phenomenon are correlated since the equilibrium concentration of the solute is achieved when the chemical potentials of the hydrogen in both phases are equal and because the transport process inside the metal lattice is driven by the gradient of the chemical potential.

The migration of interstitials in a metal under an applied external bending is well known as Gorsky effect [2]. The deformation field produces the defects migration toward the expanded areas. Lewis and co-workers [3–5] showed that internal stresses are generated during insertion and diffusion of interstitial hydrogen and that the resulting strain production represents an opposing force to the flux produced by the concentration gradient.

The study of the stress as limiting factor in achieving the deuterium loading threshold in palladium to generate excess power production is carried out in the following. The chemical potential of the hydrogen in solid solution in a metal lattice is strongly influenced by force fields, like the stress field, modifying the free energy of the system.

The hydrogen isotopes atoms dissolving into the metal (i.e. palladium) occupy interstitial sites, and thereby the lattice expands. This process generates a stress field when significant concentration differences (strong gradient or coexistence of different phases) are created.

The situation is quite similar to the stress produced by a temperature gradient as shown in Fig. 1.

In the following we show how to approach the solution to this problem in order to have an analytical tool to estimate the effect of the stress field on the loading and to identify the metallurgical conditions that can reduce this effect and hence allowing the increase of the amount of hydrogen dissolved in the metal.

Chemical potential of hydrogen diffusing into the metal lattice, in presence of a stress field, becomes [6]:

$$\mu_s = \mu_s^* - \frac{\bar{V}_s}{3}\left(\sigma_{xx} + \sigma_{yy} + \sigma_{zz}\right) = \mu_s^* - \bar{V}_s \operatorname{tr}\bar{\bar{\sigma}} \equiv \mu_s^* - \bar{V}_s\sigma_h, \tag{1}$$

where $\mu_s^*$ is the chemical potential of hydrogen diffusing into the lattice without stress, $\bar{V}$ is the partial molar volume of the solute and $\sigma_h$ the trace of the stress tensor.

## 2.1. Flux equation with a stress field

A diffusive flux of hydrogen within an homogeneous and solid media is created by a gradient of the chemical potential and by the field of the applied forces so that the expression for the flux is

$$\bar{J} = -Mc\frac{\partial\mu}{\partial c}\frac{\partial c}{\partial x} + Mc\bar{F}, \tag{2}$$

where $M$ is the mobility, $c$ the solute concentration, $\bar{F}$ the vector given by the sum of the applied forces acting on the hydrogen interstitially dissolved in the solid.
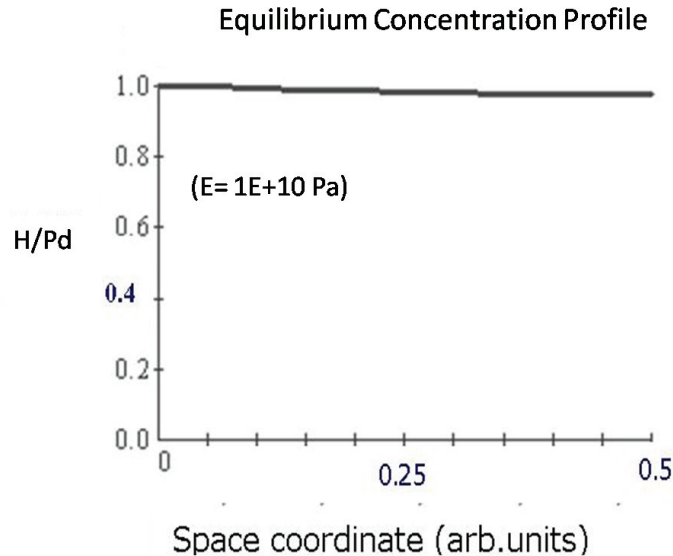


**Figure 2.** Equilibrium H concentration profile within a Pd foil with Young module $= 1$ E+10 Pa.
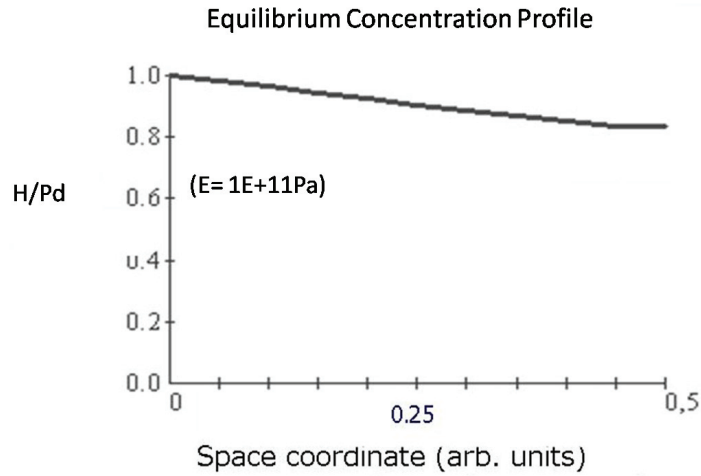
**Equilibrium Concentration Profile**

H/Pd

(E= 1E+11Pa)

Space coordinate (arb. units)

**Figure 3.** Equilibrium H concentration profile within a Pd foil with Young module $= 1E+11$ Pa.

By replacing the relationship between diffusion coefficient and chemical potential, $D = Mc(\partial\mu/\partial c)$, into Eq. (2) it follows:

$$\bar{J} = -D\nabla c + \frac{D\bar{F}c}{c(\partial\mu/\partial c)}.$$
(3)

**R/Ro in Pd foil: high H solubility
Calculated evolution**

R/Ro

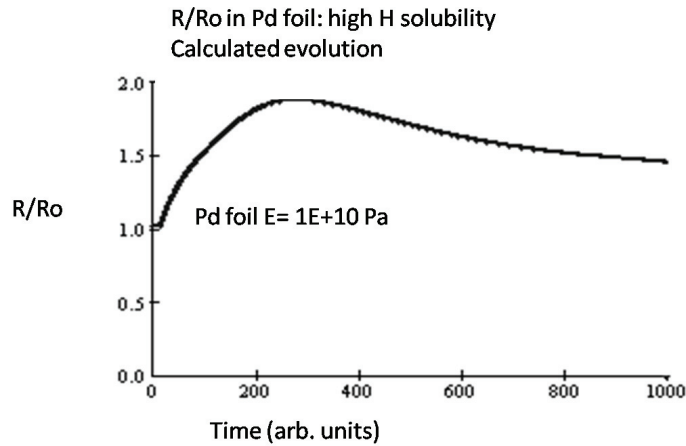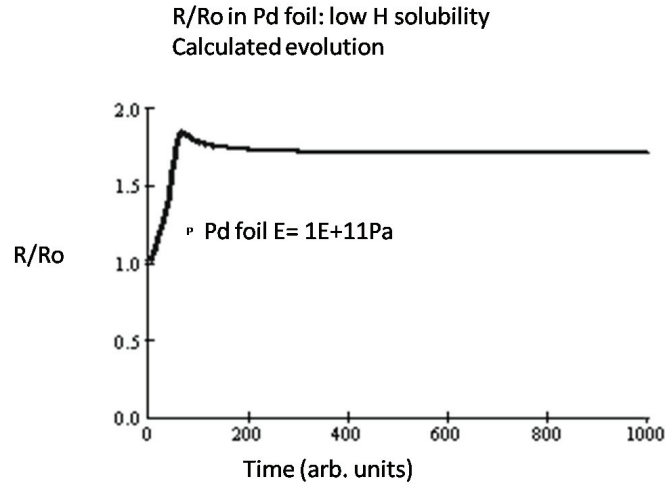Pd foil E= 1E+10 Pa

Time (arb. units)

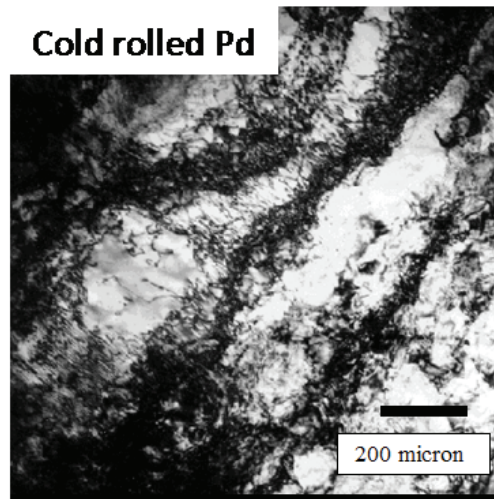**Figure 4.** Calculated evolution of $R/R_o$ for high solubility (reduced stress) material.

**Figure 5.** Calculated evolution of $R/R_0$ for low solubility (high stress) material.

A little of algebra leads to

$$\bar{J} = -D\nabla c + D\frac{\bar{F}}{RT}c. \tag{4}$$

For a stress field the flux equation becomes:

$$J = -D\left(\nabla c - \frac{c\bar{V}}{RT}\nabla\sigma_{\text{loc}}\right), \tag{5}$$



**Figure 6.** Cold rolled sample.
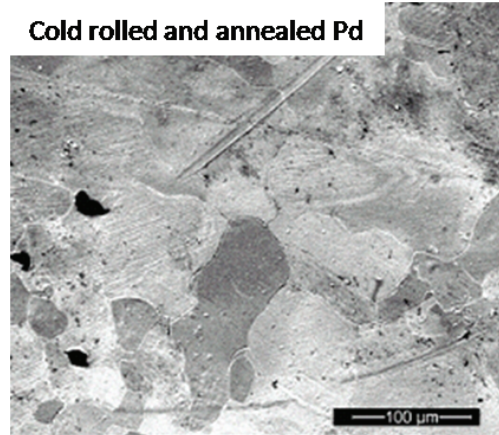
**Figure 7.** Cold rolled and annealed (850°C) sample.

where $\sigma_{loc}$ is the local stress.

Equation (5) shows that a zero flux condition can be achieved even if a non-zero concentration gradient exists (i.e. when the two terms have the same value).

Therefore, the loading process may be inhibited by a stress gradient, for instance behind the external surface, where



**Figure 8.** Schematic view of the flow calorimetric system and of the closed electrochemical cell.

**Figure 9.**    Input, output and excess power in experiment L14.



**Figure 10.**    Increasing of the electrolyte temperature during the production of excess of power.
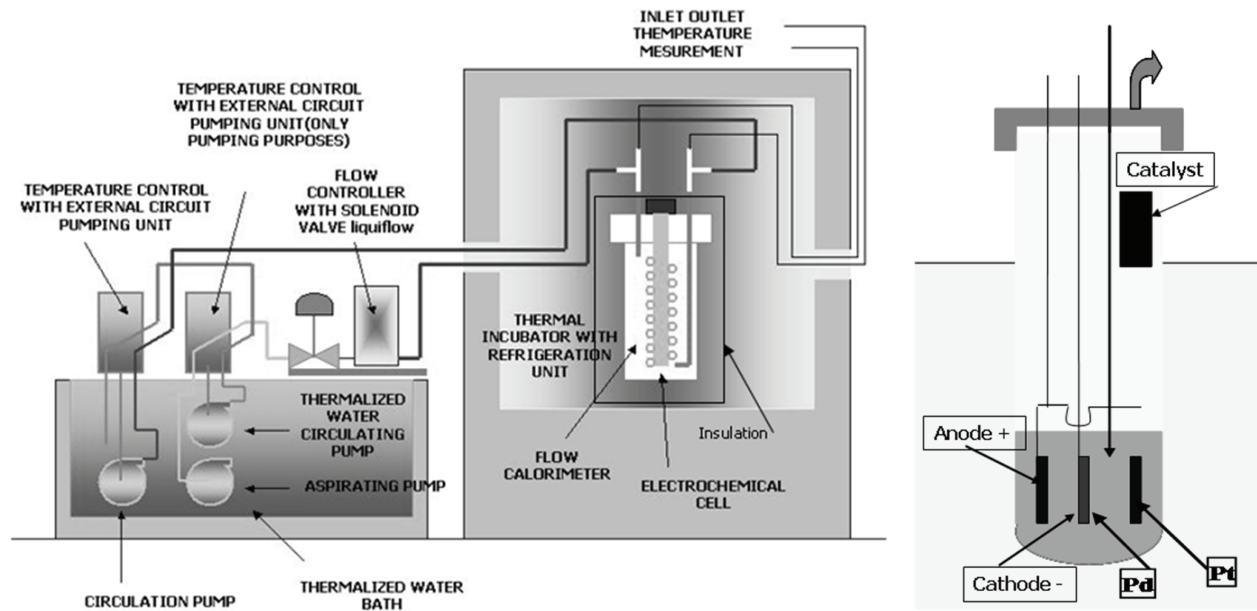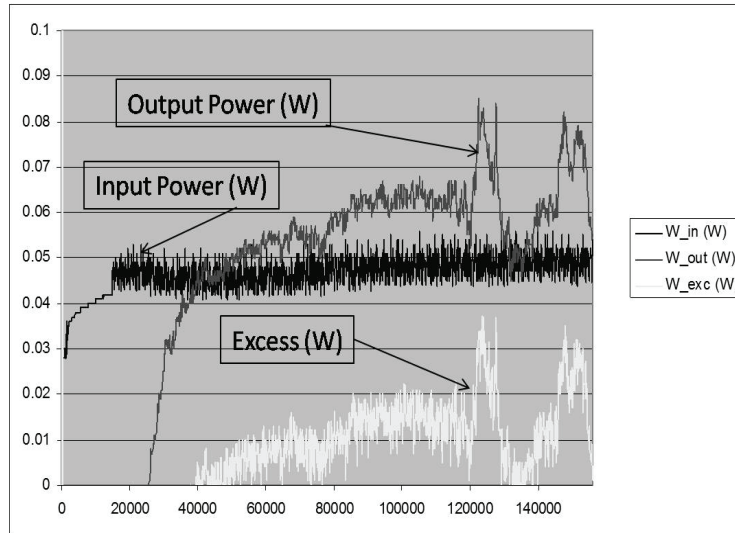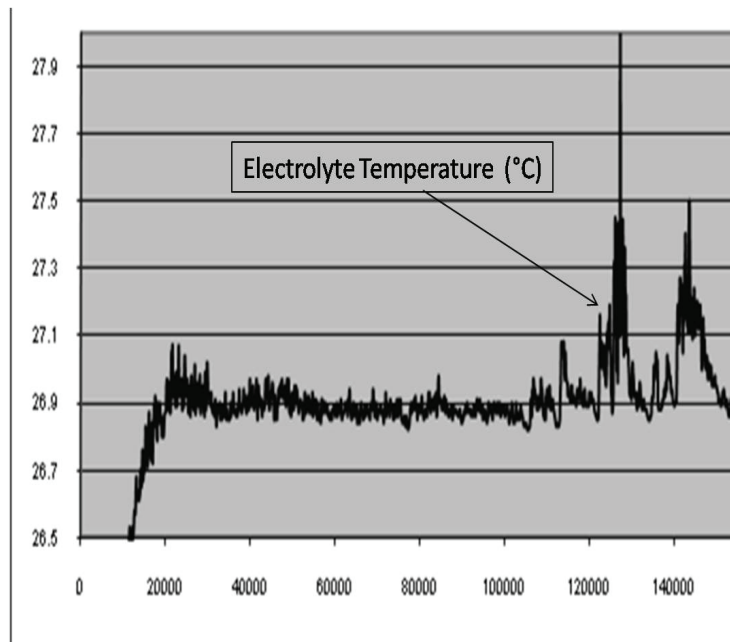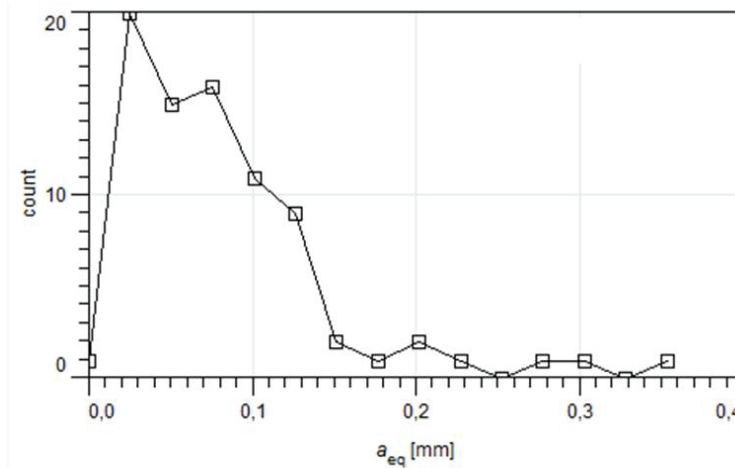
**Figure 11.**   First lot grain-size distribution.

the effect is traceable to the effect of a strong temperature gradient. Thus, in the zone at high concentration, compressed by the zone at low concentration, the chemical potential of the solute increases and the loading can be inhibited.

The analysis allows us to study the mass transfer problem when the stress field is created during the loading. In the following, we consider a system where the diffusion is well described by one-dimensional time dependent model (foil, membrane or wire).

By introducing the fraction of relaxed stress $\eta(x)$ into the flux equation it follows:

$$J^d = D \left( -\frac{\partial c}{\partial x} + (1 - \eta) \frac{\bar{V}}{RT} c \frac{\partial \sigma}{\partial x} \right).$$   (6)

A mass balance on a foil leads to:

$$\frac{\partial c}{\partial t} = D \frac{\partial}{\partial x} \left( \frac{\partial c}{\partial x} - (1 - \eta) \frac{\bar{V}}{RT} c \frac{\partial \sigma}{\partial x} \right).$$   (7)
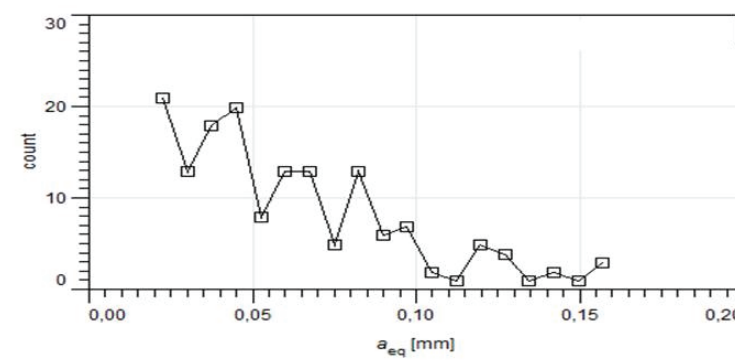


**Figure 12.**   Second lot grain-size distribution.
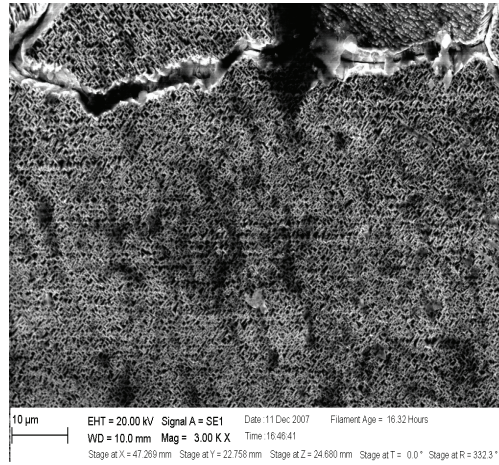
**Figure 13.**    Microscopy of #64 sample surface.

Let us consider the well known stress ($\sigma$) strain ($\varepsilon$) relationship:

$$\sigma = E\varepsilon, \tag{8}$$

where $E$ is the Young's modulus. The relationship between strain and concentration for the Pd beta phase (assuming that it may be extrapolated up to a loading atomic fraction close to one) can be expressed as

$$\varepsilon(\bar{c}) = [1 + b(\bar{c} - \bar{c}_{\beta\,\min})], \tag{9}$$

where $\bar{c}_{\beta\,\min}$ is the hydrogen concentration value for the $\alpha + \beta$ phases coexistence limit, $b = 0.044$ and $\bar{c} = c/c_0$ the dimensionless concentration ($c_0$ is the metal atoms concentration). Let us introduce the following dimensionless
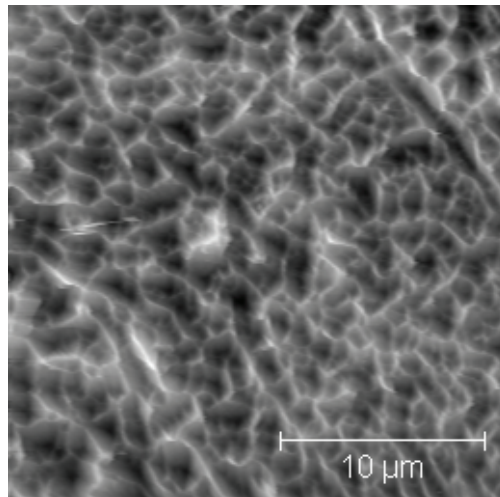


**Figure 14.**    Microscopy of L25 sample surface.
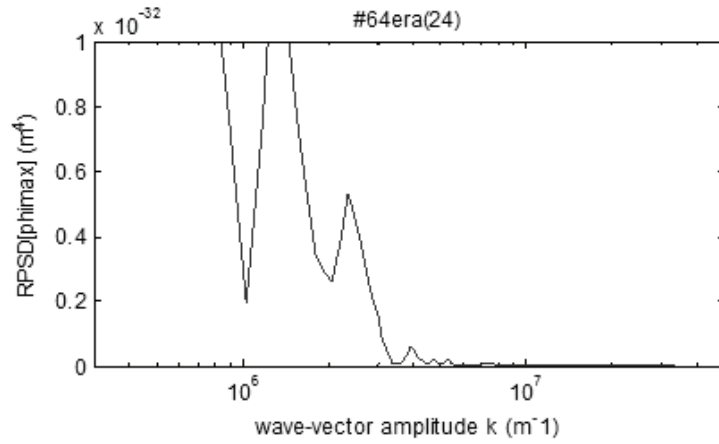
**Figure 15.** PSDF of #64 sample.

parameters

$$\bar{x} = {}^{x}\!/_{L}; \quad \tau = {}^{L^2}\!/_{D}, \tag{10}$$

$L$ is the characteristic length of the system (typically the thickness or the radius).

A mass balance across a differential control volume leads to the following dimensionless transport equation:

$$\frac{\partial \bar{c}}{\partial \tau} = \frac{\partial^2 \bar{c}}{\partial \bar{x}^2} - (1 - \eta)b\frac{\bar{V}E}{RT}\left(\frac{\partial \bar{c}}{\partial \bar{x}}\right)^2 - (1 - \eta)b\frac{\bar{V}E}{RT}\bar{c}\frac{\partial^2 \bar{c}}{\partial \bar{x}^2} - b\frac{\bar{V}E}{RT}\frac{\partial \eta}{\partial \bar{x}}\bar{c}\left(\frac{\partial \bar{c}}{\partial \bar{x}}\right), \tag{11}$$



**Figure 16.** PSDF of L25 sample.
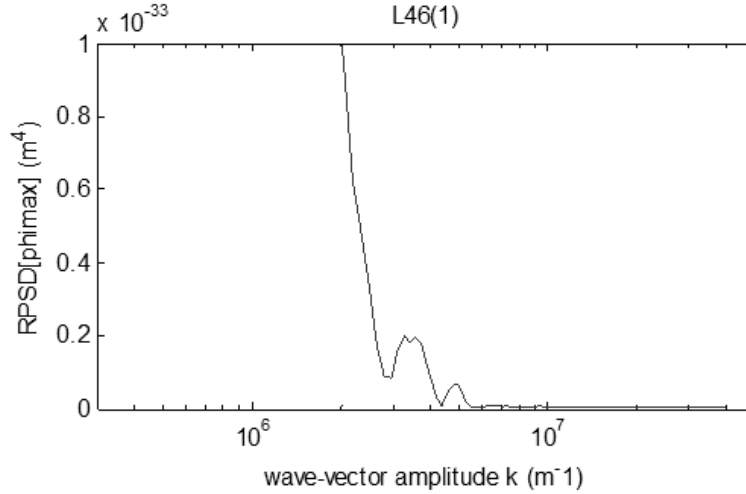
**Figure 17.** PSDF of a material designed to produce excess of power.

where we introduced above $\eta(x)$ as a parameter giving the percentage of stress that is released by plastic deformation or by dislocation slipping:

$$\eta = \frac{\sigma_{\text{loc}}}{\sigma_{sn}}$$

$\sigma_{sn}$ yield strength.

When the release of the stress is complete ($\eta = 1$ and constant along the domain), Eq. (11) reduces to the Fick's law.

Equation (11) describes the interstitial diffusion of hydrogen into the metal (e.g. palladium) under a stress field. The effect of stress at steady state conditions results in a different concentration profile, hence in different loading characteristics that depend on the properties of the material such as the Young module.

The transport equation (11) is numerically solved with the boundary and initial conditions $\bar{c} = 1$, $\bar{x} = 0 (\forall\, t)$ and $\partial \bar{c} / \partial \bar{x} = 0$, $\bar{x} = L/2$, $\bar{c} = 0$, $t 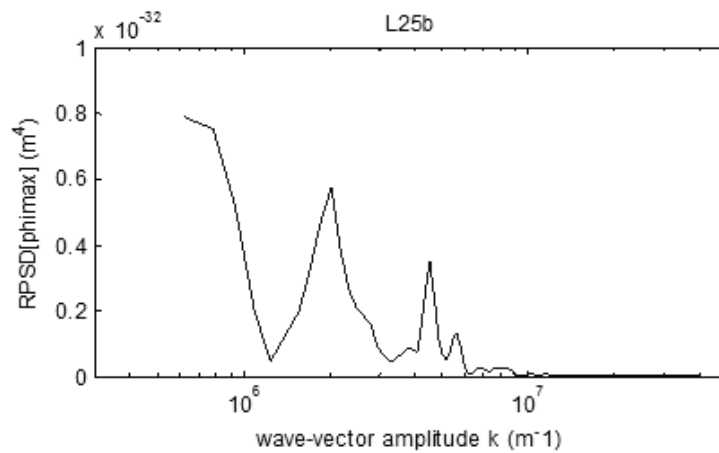= 0$ and includes the calculation of the relaxed stress on the basis of the mechanical properties of the material ($\sigma_{\text{r}}$). Some calculations have been done by using indicative values of the Young module in order to clearly show the effect. Figures 2 and 3 present the equilibrium concentration profile, from the external side up to the symmetry plane, for two palladium foils with different Young modules. In the first case the value of the Young module is $1.0 \times 10^{10}$ Pa whereas in the second case the value is $1.0 \times 10^{11}$ Pa (these values are chosen to better enforce this effect). It is clear that the loading reduces when the Young module increases. The calculation of the concentration profile evolved has been used to also calculate the evolution of the $R/R0$ ratio by assuming the foil to be as a parallel of the electric resistance and by considering the well-known literature data on palladium hydride (deuteride) resistance. Figures 4 and 5 show the evolution of the $R/R_0$ ratio for the two considered loading conditions described above.

Figures 4 and 5 represent typical situations that one may observe experimentally.

(1) *High loading*: $R/R_0$ reduces to 1.4 and to 1.6, after achieving the maximum, for both H and D, respectively.
(2) *Low loading*: $R/R_0$ shows a small reduction, after achieving the maximum, since the dissolution of H or D stops because of the stress field (surface contaminants are in control at the same level during the loading process).

The model allows us to seek for a material that shows homogeneous loading characteristics able to minimize the concentration gradient and hence the stress field. Some treatment processes, based on cold rolling and annealing steps are shown to optimize the metallurgical structure of the materials in order to increase the H(D) loading. The raw material is a palladium foil (1 mm thick) able to reach a loading ratio of about 0.8 (hydrogen atomic ratio). The treatment has been done in two steps:

(1) Cold rolling of the raw material leading to a Pd foil of 50 $\mu$m thickness.
(2) Annealing at different temperatures (ranging from 700 and 1100°C) at different time intervals.

Figure 6 shows a simple cold worked sample. Figure 7 shows the effect of the annealing after the rolling treatment procedure.

A H/Pd ratio of 0.97 has been obtained in the sample, cold worked and annealed at 850°C for 1 h.

The tests described above have shown a satisfactory reproducibility.

## 3. Calorimetry: Experimental Results

The calorimetric set-up was conceived to directly measure the output power by means of a mass flow calorimeter. The electrochemical loading was performed in a closed electrochemical cell equipped with a catalytic fixed bed to recombine the gas produced during electrolysis. The mass flow calorimetric system is composed of a Memmert thermostatic box ($\pm 0.05$°C), Haake thermostatic bath for coolant water, Bronkhorst high precision mass flow meter and controller ($0.3-0.1$ cm$^3$/s), read by the data acquisition system in order to precisely measure the output power. Inlet and outlet temperature of the coolant are measured using two Pt 100 thermometers (four wires measurement). The closed electrochemical cell is equipped with a recombiner (Sued-Chemie Pd on alumina catalyst). Cell power supply is provided by the AMEL galvanostat. Output power is measured by means of the mass flow rate and coolant temperature, $R/R_0$ measurement is done by means of an HP- 4284 (four wires measurement). Figure 8 shows a schematic view of the flow calorimetric system.
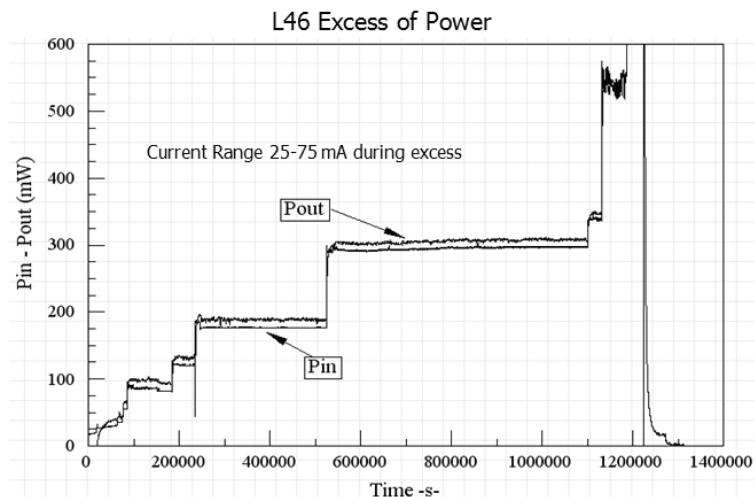


**Figure 18.** Excess of power produced by the designed material.
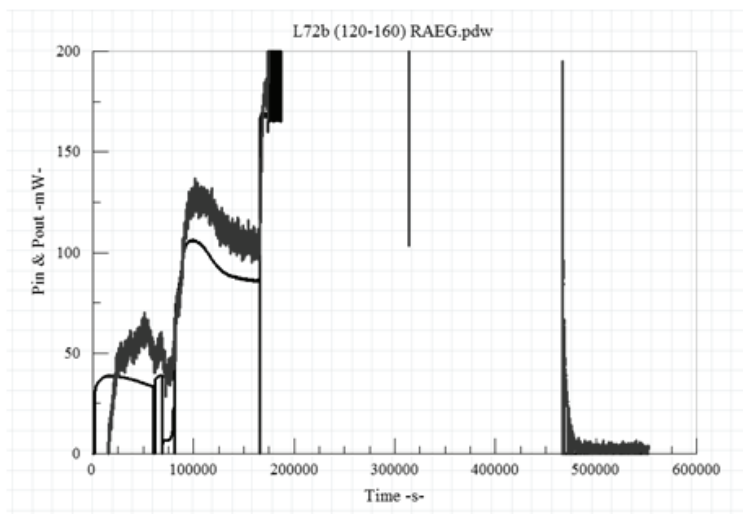
**Figure 19.** Excess of power produced by a designed sample.

Several (reference) experiments in light water (LiOH 0.1 M electrolyte) were carried out, and with this a calorimeter efficiency of 97.5% was obtained (the difference between input and output power is due to heat loss). Using light water during electrolysis, we did not observe any release of excess power, despite the fact that a very high loading ratio (H/Pd = 0.97) was always achieved.

Different behavior was observed using Pd cathodes loaded in deuterium containing solutions, concentration threshold (at. frac.) D/Pd of 0.9:

(1) High-power gain during the excess,
(2) low-power gain during excess,
(3) no excess.

Differences in two palladium lots received from the same producer have been identified, both lots were 99.95% pure Pd. The first lot gave a reproducibility larger than 60% with signal amplitudes well above 100%, Fig. 9 shows the input, output and excess power in the experiment L14, Fig. 10 shows the increasing of the electrolyte temperature in this experiment during the excess production. The reproducibility reduces under 20% with the second lot and the excess amplitude was always below 25% of the input power.

## 4. Material Characteristics

Such evidence led to a systematic effort to improve knowledge about the status of the material that is required to have the effect.

The experimental work highlighted that high loading is a necessary, but not sufficient condition to have the production of excess of heat, for such a reason the focus was moved on other features of the samples correlated with the occurrence of the effect.

The first observation correlated to the different calorimetric behavior of these two lots was the different spectrum of contaminants.

It is well known from physics metallurgy that contaminants may have several effects on the metal characteristics:

Contaminants may act on: Grain size, Crystal orientation, Grain boundary.

The effect on grain size distribution can be seen in Figs. 11 and 12, where the typical grain size distribution of samples obtained from the first and second lot is shown. The microscopy images have been analyzed by using GWYDDION software.

Samples belonging to the first and the second lot showed a different crystallographic orientation: the first lot was mainly oriented $\langle 100 \rangle$ while the second lot was $\langle 100 \rangle$ and $\langle 100 \rangle$ 50% oriented. Excess of power was observed with samples having a dominant $\langle 100 \rangle$ orientation.

The difference in the spectrum of contaminants produced also a different effect of the chemical etching because of the different reactivity of the surface. This may be explained as a micro-corrosion process. The consequence was a different surface morphology between samples belonging to the two lots.

The second lot required a current density higher than the one used for the first lot to achieve the same loading. This is indicative of a different mass transfer regime.

The Power spectral density was selected as merit figure to identify the status of the surface.

Figures 13 and 14 show the surface microscopy of samples #64 (experienced at Energetics) and L25 respectively; both gave a significant excess of power production but the effect was stronger for lot #64. Figures 15 and 16 show the power spectral density function for lot #64 and for lot L25 respectively.

One may observe that the structures of the Power Spectral Density Function (PSDF) are quite similar but the larger the amplitude of the PSDF peaks the larger the produced excess of power. This correlation was also found in other measurements.

## 5. A Designed Material

The experimental evidence led us to produce a material having characteristics close to the ones described.

A Pd lot having a spectrum of contaminants similar to lot 1 underwent treatment leading to a dominant $\langle 100 \rangle$ orientation and appropriate metallurgy.

We have identified some metallurgical differences between samples and we know from the physical metallurgy that these differences can be produced by contaminants. The preliminary analysis work [7] revealed a different spectrum of contaminants in the considered lots. The role of the individual contaminant is under study.
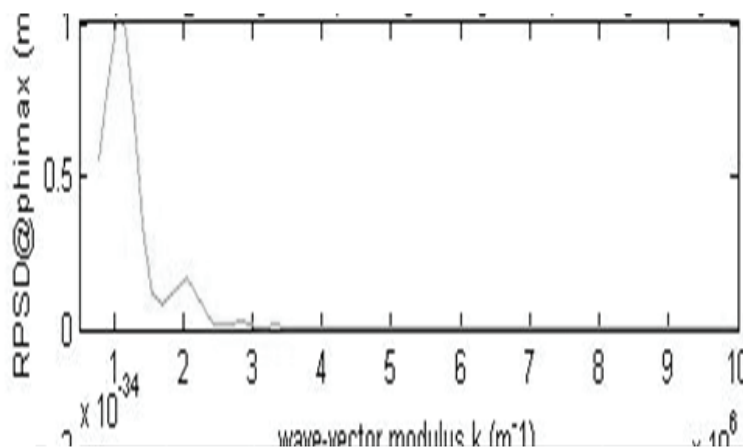


**Figure 20.** PSDF of a designed material.

The chemical etching treatment on the surface produced a morphology quite similar to the ones of #64 and L25. The PSDF for such a sample, shown in Fig. 17, reproduces the shape of samples #64 and L25 even if with peaks of lower amplitude. A small excess was expected from such a sample. The experimental behavior was in agreement with the expectation. Fig. 18 shows the produced excess of power up to 12% of the input.

This is giving an additional evidence that a proper surface morphology is an additional condition for having the excess of power. The rebuilding of a material designed to have excess of power production was replicated successfully by using the approach described above. Figures 19 and 20 show the excess of power and the PSDF for another designed sample.

The results show an increased control of the effect even if not yet satisfactory, in particular if one looks at the amplitude of the signals.

## 6. Conclusions

Some characteristics have been identified that give cathodes different behavior. Enhanced probability for having an excess of power is observed when:

Loading is easy at a relatively low current density due to proper metallurgy.

⟨100⟩ Crystal orientation.

Identified surface morphology.

Some samples demonstrating the three conditions were realized, and production of excess of heat was observed. Work is in progress to identify other correlations and, on the basis of the material characteristics, the mechanisms producing the effect.

## References

[1]   V. Violante et Al., Consequences of Lattice Expansive Strain Gradients on Hydrogen Loading in Palladium, *Phys. Rev.* B **56**(5) (1997) 2417–2420.
[2]   H. Wipf, *J. Less-Common Met.* **49** (1976) 291.
[3]   F.A. Lewis, J.P. Magennis, S.G. McKee and P.J.M. Sebuwufu, *Nature* (London) **306** (1983) 673.
[4]   F.A. Lewis, B. Baranowski and K. Kandasamy, *J. Less Common Met.* **134** (1987) L27.
[5]   F. A. Lewis, X. Tong, K. Kandasamy, R. V. Bucur and Y. Sakamoto, *Electrochem. Acta* **218** (1993) 57.
[6]   R.A. Oriani, *Trans. Fusion Technl.* **26** (1994) 235–266.
[7]   V. Violante et al., Material Science on Pd–D system to study the occurrence of excess power, in I*CCF-14 Int. Conf. on Condensed Matter Nuclear Science proceedings*, 2008. Washington, DC.

Research Article

# Model for Electromagnetic pulsed BEC Experiments

Roger S. Stringham *

*First Gate Energies, PO Box 1230 Kilauea, HI 96754, USA*

## Abstract

Sonofusion experiments, which incorporate transient Bose Einstein condensates, BEC, have recently focused on related sono-superconductivity. Cavitation jets implant high-density deuteron clusters into a target foil. Clusters are then squeezed by accelerated charges that form dense transient EM pulses. Cavitation and the associated sonoluminescence phenomena, used as a measuring tool, helps develop and explain related experimental results. Two outcomes, sonofusion and sono-superconductivity both produce $D^+$ clusters in reactors of different geometries. MHz reactor No. 1 is driven by a disk piezo and has produced excess heat, $Q_x$, using the foil target and other products, including $^4$He. The new MHz reactor No. 2 is driven by a cylindrical piezo low power with a concentric wire target with transient cluster steady state concentration near the wire surface. The target's steady state cluster coverage may satisfy a sono-superconductivity subsurface cluster connectivity during the MHz's 100 ns collective sonoluminescence pulse. It was anticipated that ambient sono-superconductivity was possible but so far has proved difficult to measure. Cavitation $D_2O$ bubbles in both reactors were controlled by three main parameters for the two reactors: temperature, pressure of Ar gas over $D_2O$, and acoustic watt input; $T_i$, $P_i$, and $Q_a$. The $z$-pinch jets' contents of deuterons and electrons were implanted, with an induced picosecond transient charge separation. This charge separation produced an electromagnetic, EM, cluster compression pulse that formed a high-density BEC environment, as the EM pulse pressure overwhelmed repulsive deuteron cluster pressure for that picosecond. This model used unique attributes of the high-density transient deuterons to produce sonofusion in reactor No. 1 and sono-superconductivity in reactor No. 2 near ambient temperature. The measurements showed the presence of sonoluminescence pulses, implanted plasma, and heat pulse ejecta sites.

*Keywords:* BEC, Deuteron, Sonoluminescense, Superconductivity, *z*-pinch

## 1. Introduction

The presented model can explain experimental results of 23 years of cavitation and sonoluminescence investigation of sonofusion. Cavitation piezo frequencies ranged from 20 kHz to 2.5 MHz, and showed definite advantages at the higher frequencies. The naturally selected cavitation resonant bubbles produced by a MHz feedback oscillator were very small 0.2 $\mu$m for the initial radius, $R_i$. The resonance control parameters of circulating $D_2O$ were temperature, $T_i$, the pressure of Ar over the $D_2O$, $P_i$, and acoustic watt input, $Q_a$ or Ap. These were all adjusted experimental

*E-mail: firstgate@earthlink.net; Tel.: 808 826 7530

conditions [1]. The small selected bubbles starting with a radius $R_i$ of 0.2 $\mu$m, expanded isothermally to a maximum radius of 2.0 $\mu$m, $R_o$ (see Fig. 1). This was followed by a sub-microsecond adiabatic collapse in the positive pressure zone of the acoustic wave to the final radius of 0.02 $\nu$m, $R_f$, about a 0.1 $\nu$s inertial compression process. This bubble is transient cavitation bubble that produces a high-energy density terminal bubble, radius $R_f$. The internal kinetic energy density of the transient cavitation bubble is KE/m$^3$ = $10^{-11}/R_f^3$ in J/m$^3$. Sonoluminescence pulses in reactor No. 1 with an acoustic input, $Q_a$, of 2 W was not detected, while in reactor No. 2, an acoustic watt input, Ap, of 2 W was near saturation. The MHz devices, with reactor volumes 0.3–1 cm$^3$, a reactor mass of 20–50 g, and mass flow rate of D$_2$O of 0.55 cm$^3$/s produced the same excess heat, $Q_x$, as the 46 and 20 kHz systems and were 1000 times larger [x]. High frequencies also produced a more intense sonoluminescence pulse, which was used to monitor the sonofusion process and its partial dense plasma. Cavitation systems followed a natural process, and with some control of parameters, $T_i$, $P_i$, and $Q_a$, were guided to produce usable power. During the bubble selection process only a fraction of the bubbles had the $R_i$ that would couple to the frequency of the piezo resonator. The rest of the bubbles within the piezo influence had little involvement with the sonofusion process. (*Note*: The transient cavitation bubble in the model existed for one acoustic cycle.) Sonoluminescence was used as a tool to gauge the relative number of deuterons in the high density excited state in the bubble's final radius, $R_f$, of the pseudo adiabatic collapse (Fig. 2). The collapsing bubble produced at the same moment, the sonoluminescence pulse (Multi Pixel Photon Counting, MPPC), and a high-density $z$-pinched plasma jet with its contents squeezed by the EM pressure and implanted into a nearby target at a velocity of about 30 km/s [2–4].

## 2. General Set-up for Reactor Nos. 1 and 2

It was necessary for the SL pulse measurements that monitored the MHz piezo operation to be made in a black felt lined light box cooled by a small fan circulating outside air that removed heat from the box [5] (see Fig. 3). Calorimetry could be performed on reactors using the flow through type of calorimeter. A Measurement Computing USB 1608 HS collected data from an Ohio Semiconductor PC5 103CX5 that measured the total watts in, $Q_i$, and several type K thermocouples measured temperatures. A pressure device measured Ar pressure over the D$_2$O. A variac controlled the
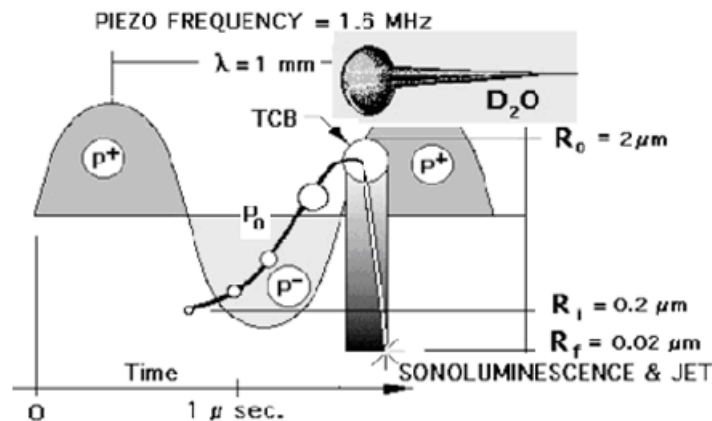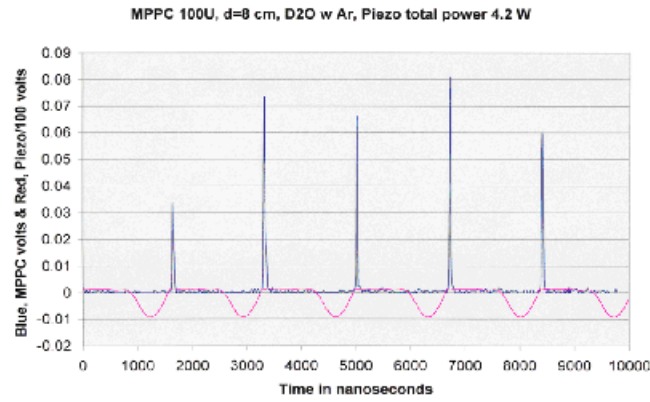


**Figure 1.** The 1.6 MHz TCB cycle .

**Figure 2.** The MPPC SL pulse and MHz piezo volts.

power to the transformer that was measured by a watt meter and powered a feedback oscillator that drove the MHz piezo with the acoustic watt input, $Q_a$, of reactor No. 1 or $Ap$ of reactor No. 2 [4]. The $D_2O$ circulation loop of the reactors connected components with 1 mm inside diameter tubing. $D_2O$ was circulated by an FMI metering pump, model QV, into a circular tubing heat exchanger, then a 10 μm particle filter at a flow rate of 0.55 cm$^3$/s At the reactor ports DT, $T_{in}$ - Tout, and the flow of $D_2O$ was measured through the reactor volume. The flow progressed to a flow meter and a bubbler where Ar gas pressure was monitored, and then back to the pump completing the calorimetry of the $D_2O$ cycle (Figs. 3 and 4). Temperatures, pressures, power, and flow rates were collected from the reactors for processing. The 50 W, 120 V at 60 cycles variable power supply powered a feedback type oscillator that sensed any change in reactor temperature, and amplified that signal as the acoustic watt input, $Q_a$ or $A_p$, at its resonance frequency. $Q_a$ and $Ap$ MHz signals were pulsed at 120 cycles/s, an envelope for the MHz signal. Reactor No. 2 used the same set-up (Figs. 3 and 4).

## 3. General Calorimetry

Calorimetry was a flow through type calorimetric measurement of $\Delta T = T_{out} - T_{in}$ with several thermocouples. Equally important was the $D_2O$ flow per second measurement of mass flow, MF. DT*MF*4.669 equals the measured output watts, $Q_o$; this was the basic calorimetry. 4.669 was a scaling factor for converting heated $D_2O$ from calories to joules. $Q_o - Q_a = Q_x$ [2]. The acoustic input, $Q_a$, was 0–16 W. A wattmeter measured $Q_i$ and an efficiency factor of 0.30 converted $Q_i$ to $Q_a$, $0.3Q_i = Q_a$. The amount of $Q_x$ measured was the difference between the measured total heat out, $Q_o$, minus $Q_a$ the acoustic watts input. The relationship between these three, sonoluminescence, $Q_i$, and $Q_x$, were plotted (Fig. 5).

## 4. General $^4$He Measurement

The circulation of $D_2O$ through the reactor provided easy access to the ejecta that included the fusion products heat and $^4$He. The $^4$He fusion product was circulated in the $D_2O$ and could be collected at any time using standard gas expansion into evacuated gas sampling volumes for measurement. Helium four was measured from a stainless steel 50 cm$^3$ gas sample from circulating $D_2O$ in the low frequency, 20 kHz, reactor. The gases were analyzed using the mass

spectroscopy facilities of the DOE's laboratory at the Rocketdyne Corp. in Southern California where Brian Oliver measured $^4$He at 552 ppm at a $\sigma \pm 1$ ppm [6]. The 65 W of $Q_x$ was measured by calorimetry over a 19 hour period.

## 5. Reactor No. 1 Set-up

The reactor was in a light box, and the DC electric input $Q_i$, powered the MHz oscillator and the piezo acoustic input, $Q_a$ and the sonoluminescence photomultiplier, Hamamatsu $^3$He 125, along with the Systron-Donner counter/timer that was used for measurements. The $D_2O$ circulation system powered by an FMI pump in line with a filter circulated the $D_2O$ at a constant rate to the reactor $T_{in} - T_{out} = \Delta T$. $D_2O$ flow continued to the two liter $H_2O$ bath and 2 mm $\times$ 3 m stainless steel cooling coil and through the flow meter to a bubbler and back to the pump. Reactor No. 1 used a larger acoustic input, $Q_a$, to the PZT piezo disk, 2 mm thick and 22 mm in diameter. $Q_a$ was distributed over the disk's central 1/3 surface area while measuring excess heat production, $Q_x$. The disk was clamped at its periphery. The geometry was a 1 cm$^2$ $\times$ 100 $\mu$m thick target foil located 1 mm from the piezo surface, with circulating $D_2O$ passing between the disk and the target. A small resistance heater placed in reactor No. 1's $D_2O$ flow-through volume was used for calibration purposes. Figures 1 and 3 show the transient cavitation bubble evolution and time line that resulted in the SL pulse and $z$-pinch jet. The $R_f$ bubble energy density produced by the pseudo adiabatic collapse launched the dense plasma jet at about 30 km/s accelerating to the target lattice. The photon pulses were made up of millions of individual sonoluminescence 100 ns bubble emissions, from each of the thousands of collapsing transient cavitation bubbles during 1 acoustic cycle, $10^{-6}$ s. $z$-Pinched deuterons and electrons of the jet plasma were implanted into a target
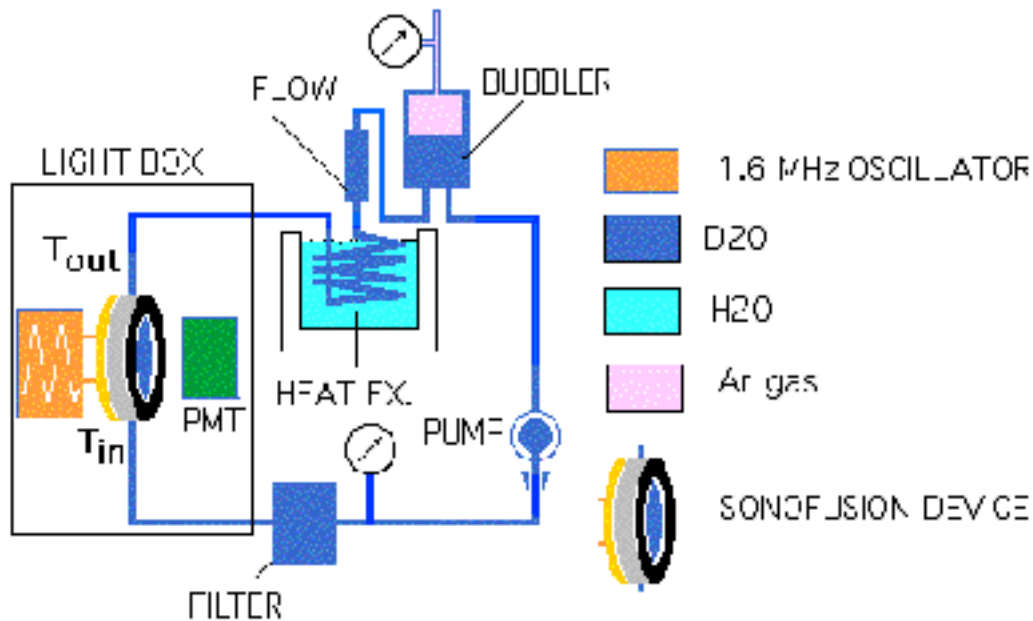


**Figure 3.** Reactor No. 1, sonofusion set-up.
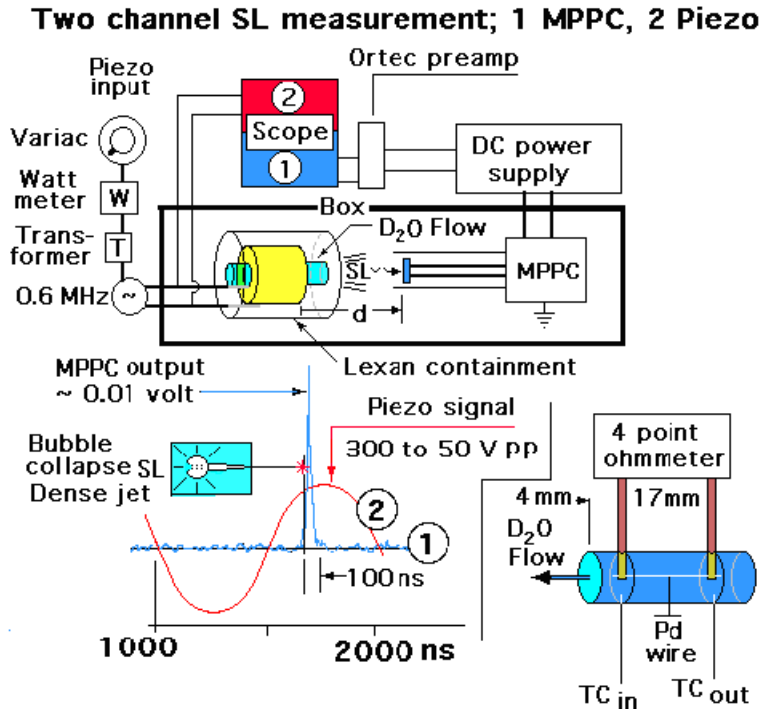
**Figure 4.** Reactor No. 2 superconductivity set-up with MPPC.

producing a femto-second electron deuteron charge separation. Accelerated electrons compressed deuterons into BEC clusters via a picosecond EM pulse. An example of $Q_x$ heat from DD fusion generation from reactor No. 1 is shown in Fig. 5. The picosecond time line for the compression pressures and evaporative deuteron cooling with the increasing repulsive escape pressure allowed for a low temperature and high density DD fusion event much like muon fusion (see Figs. 6 and 8). No $^4$He measurements were made of gases in MHz reactors. The measurement of excess heat, $Q_x$, from calorimetric measurements, showed no measurable amount of radiation. Ejecta sites originating from fusion heat pulses were measured by SEM surveys of target foil surfaces showing their frequency differences and correlate to $Q_x$ [2]. The low piezo frequencies, 20 and 46 kHz, had a broad size distribution and produced many multi-fusion events. MHz piezos had a 50 nm diameter ejecta site indicating a single fusion event per cluster of about 20 MeV in magnitude [2,7]. The sequence of producing and compressing deuteron BEC clusters also applies to reactor No. 2 systems.

## 6. Reactor No. 1, MHz Experiment

The 1.6 MHz experimental system produced the data shown in Fig. 5. The advantage to using the low-mass system was the time, about 60 s, for a 90% temperature response to its steady state temperature – heating and cooling curves. The $D_2O$ residence circulation time was about 1 s in the 1 cm$^3$ reactor volume at a flow rate of 0.55 cm$^3$/s The external pressure, $P_i$, for these runs was 1–2 atm of argon. In the calibration mode the sonofusion device used a joule heater replacing $Q_a$ , and $Q_x = 0$. To guard against radio-frequency interference, all DT measurements were made during the off mode of the piezo, no $Q_a$ [4]. The heat capacity of reactor No. 1 was measured and surface convection was
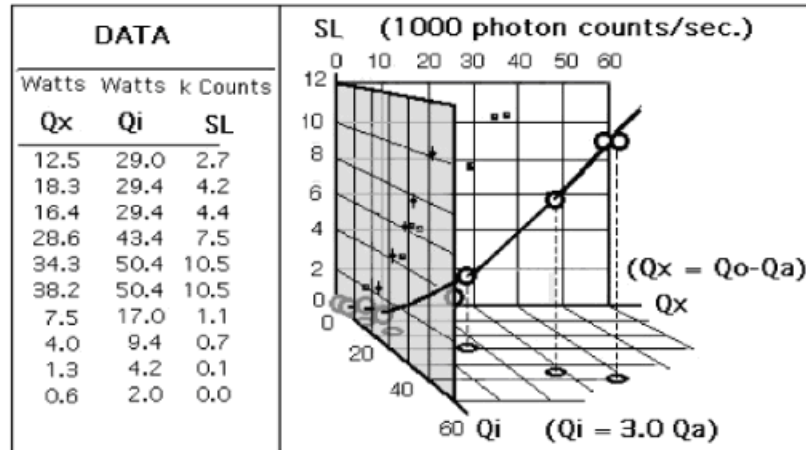
**Figure 5.**   Reactor No. 1, sonofusion results of model BEC clusters.

estimated to be small at these low DTs. The calibration mode demonstrated the heat characteristics of reactor No. 1. At these flow rates about 90% of heat is removed by $D_2O$ circulation. Figure 5 depicts one of many short experiments that showed $Q_x$ where the input power, $Q_i$, was varied via a power variac into (low mass) reactor No. 1. The output power, $Q_o$, was measured as reactor No. 1 approached its steady state temperature [2,4,5].
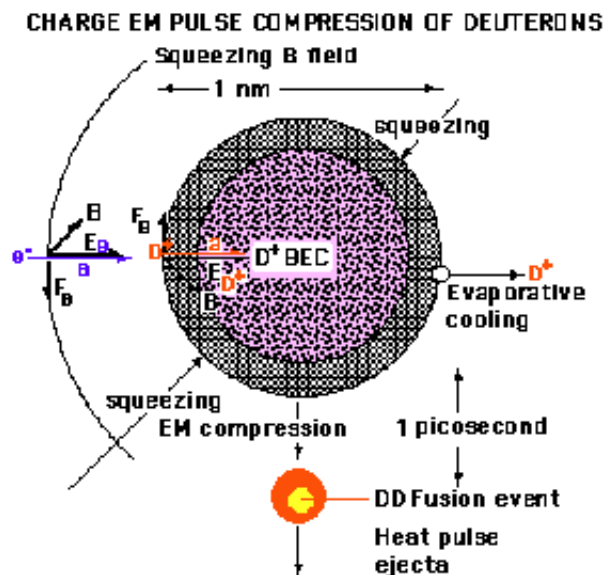


**Figure 6.**   The cluster fusion of deuterons.
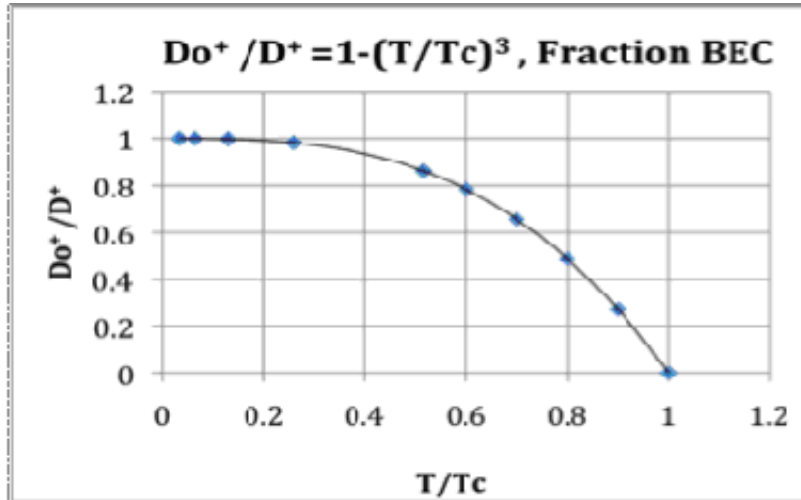
**Figure 7.** A smaller $T/T_c$ drives cluster into a BEC.
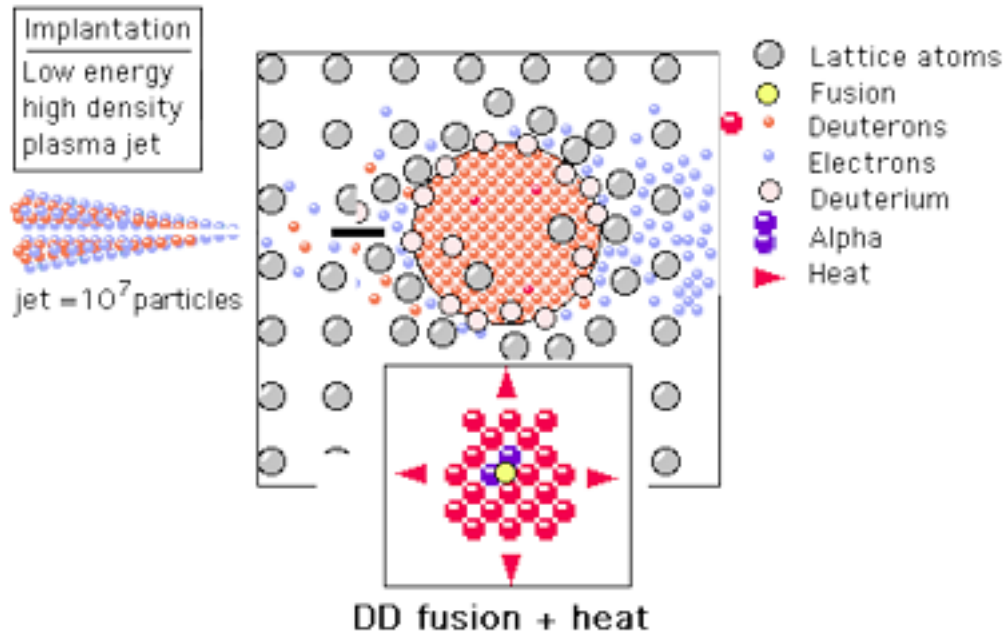


**Figure 8.** *Z*-Pinch jet implantation and BEC SF cluster.
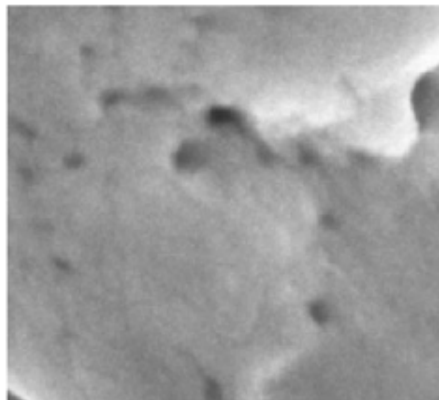
**Figure 9.**    100 $\mu$m thick Pd SEM 1 sq, $\mu$m at 46 kHz.

## 7.  General Cluster

The following is directed towards sonofusion's $Q_x$, heat of fusion of 2D$^+$ (Figs. 6–8).  Immediately after the implant of the Coulombically squeezed $z$-pinch jet's dense plasma of electrons and deuterons into the lattice foil, the trapped deuterons attract the mobile electrons.  The accelerating electrons compressed the deuterons with a collective EM pulse for a picosecond [3].  The 1 cm$^2$ and 100 $\mu$m thick Pd target lattice contained the compressing clusters, each with the potential characteristics of an inertial confined fusion system.  The picosecond pulse pressures of EM compression were initially far greater than the constant escape pressure of Coulombic repulsion of the cluster deuterons.  The BEC compressing environment of the cluster existed for that picosecond.  These opposing pressures reversed their position after a picosecond and all the particles were dispersed, but in the case of reactor No. 1 DD fusion conditions were reached.  Continuous evaporative cooling of the surface of escaping deuterons during this picosecond controlled the
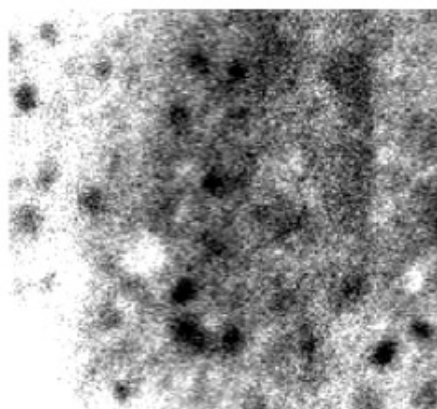


**Figure 10.**    100 $\mu$m thick Pd SEM 1 sq, $\mu$m at 1.6 MHz.
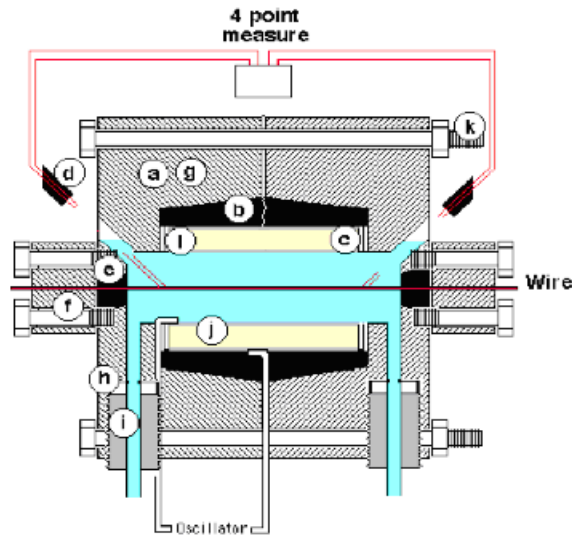
**Figure 11.** Reactor No. 2 – $D_2O$ flow and piezo squeeze.

environment cooling the remaining cluster deuterons. Over this picosecond as many as one-half of the cluster deuterons evaporated as surface deuterons and removed heat from the BEC cluster. It was important for the BEC cluster's stability for it to remain as cool as possible as the cluster's energy density increased. The BEC cooling mechanism helped to maintain the unique properties of the BEC cluster. The deuterons are compressed to extreme densities by the EM pressure pulse focused on the cluster contents during the picosecond of electron acceleration. In low-frequency kHz systems both single and multiple DD fusion events occur in the cluster's BEC environment. $Q_x$ heat pulse and ejecta sites in the 1 $\mu m^2$ area SEM survey photo are shown in Fig. 9. At a MHz, only single DD fusion events were found in the SEM Pd target foil photo (Fig. 10). The single events, $4 \times 10^{-12}$ J/event, produced 50 nm ejecta sites in a $\mu m^2$ 100 $\mu m$ . SEM Figs. 9 and 10 are by Jane Wheeler, Evans Lab., Sunnyvale, CA. Figure 9 shows that the 46 kHz ejecta sites are fewer and have a much wider size distribution having multiple fusion events where the MHz system (Fig. 10) has more ejecta sites per $\mu m^2$, all about the same ejecta size [2].

The heat pulse generated by the DD fusion event approached, during a picosecond, densities of a white dwarf star and muon DD fusion. The heat of DD cluster fusion was distributed to the BEC's cluster deuteron population before a gamma could be formed. Then the heat from the cluster was passed on to the target lattice as a heat pulse. Ejecta vapor that included the fusion products and target lattice atoms from the expanding DD fusion heat pulse were ejected into the circulating $D_2O$ where fusion products were collected and measured. One more important question on this path to DD fusion was the critical temperature, $T_c$, of the BEC cluster, and how it could be so high. The answer is the absence of electrons. The nuclear dissociation of a deuteron is 2.23 MeV. The deuteron has no accessible energy levels before its dissociation. The cluster is nuclear, not chemical and has none of the usual atom associated electrons. This difference is important. A BEC of atoms forms at ground state well below its next energy level, which is a small fraction of an eV. The neutron–proton boson is nuclear with no energy levels other than ground state. The cluster's high-density compression occurred in a collection of deuteron bosons with no electrons. There was a change of phase as the cluster density increased and the temperature decreased via $D^+$ evaporation. As $D^+$ bosons were compressed in the BEC, in the $D_O^+$ cluster, nearly all $D^+$ were in the condensed phase (Fig. 7). The deuteron cluster, free of electrons for a
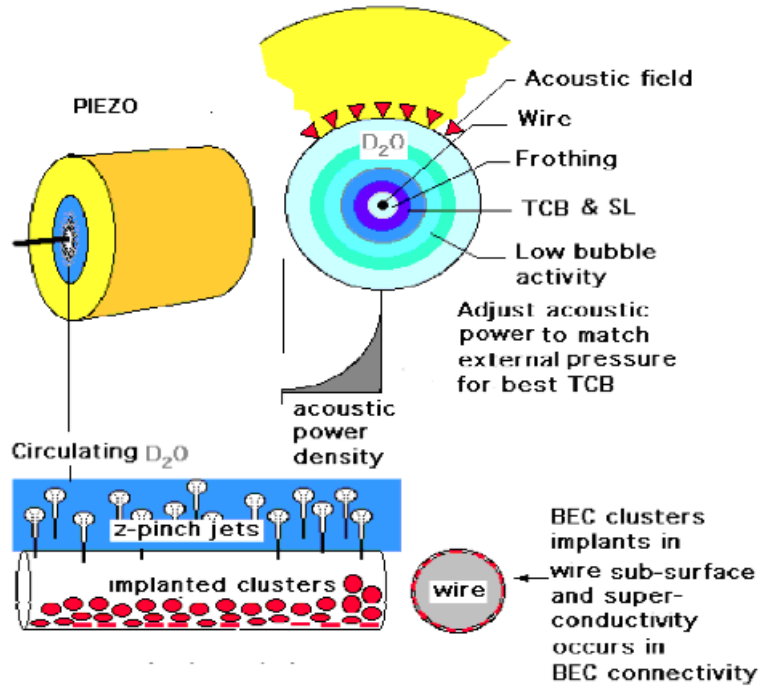
**Figure 12.**    Reactor No. 2 – Piezo and target wire.

picosecond, had a particularly high critical temperature, $T_c$. The cluster temperature, $T$, of several eV was well below its nuclear $T_c$. The cluster $D^+$ population ratio, $D_O^+/D^+ = 1 - (T/T_c)^3$, changes with decreasing $T$. The compressing and cooling cluster's BEC phase moved the bulk of the cluster's deuterons into the BEC phase, $D_o^+$. Normally BECs, ultra cold boson atoms, not nuclei, have atomic energy levels at a small fraction of an MeV. Normally boson atoms
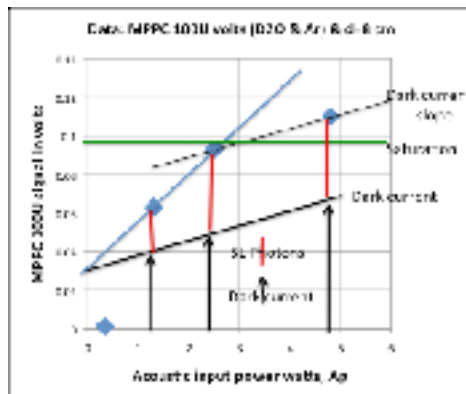


**Figure 13.**    The MPPC photon measurement.
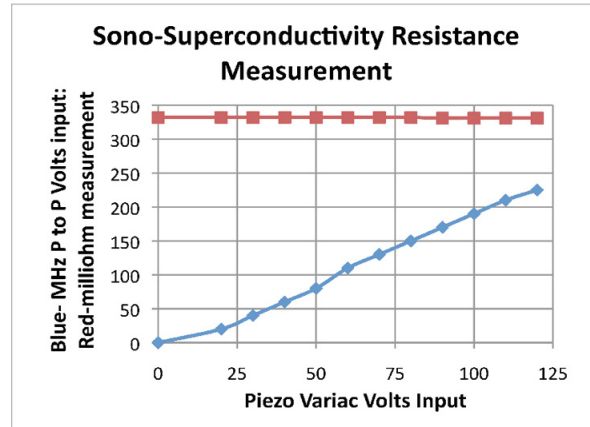
**Figure 14.** Reactor No. 2, superconductivity non-results.

must have low $T_c$ temperatures and low pressure for their bosons to form a BEC phase based on their energy levels. The nuclear energy levels for light nuclei like the deuteron in the Shell and Collective models are large, MeV, compared to atomic energy levels of light boson atoms, a fraction of an eV. The BEC phase for the deuteron in the model was close to 100% when the cluster was at 4000 K (Fig. 7). The EM compression pulses easily met the conditions of a BEC cluster via the Shell Model. The picosecond time line for the compression pressures and evaporative deuteron cooling with the increasing repulsive escape pressure allowed for a low temperature and high-density DD fusion event much like muon fusion (see Figs. 6 and 8).

## 8. Reactor No. 2 and Set-up

The terms $Q_a$ and $Ap$ are equivalent for measurements of acoustic watt inputs driving piezos in reactors Nos. 1 and 2. The $Ap$ of the cylindrical piezo converts its displacement to acoustic pressure wave that focuses at the center of the $D_2O$ flow. Figure 12 shows the bubble collapse, $z$-pinch, implantation, and cluster compression. Reactor No. 2 depends on the increasing focused acoustic energy density at the wire surface. This allows for very small acoustic inputs $Q_a$ in the order of 1 W to produce sonoluminescence. The objective is to implant a higher density of sub-surface BEC clusters that will network at a steady state concentration. New oscilloscope voltage measurements in this environment hopefully will show the model's superconductivity

Reactor No. 2 has its PZT piezo outer surface clamped with a surrounding hard rubber sheath while circulating $D_2O$ at a rate of 0.55 cm$^3$/s through its 0.3 cm$^3$ volume. See clamping bolts ($k$) in Fig. 11. The target was a fine wire, 100 $\mu$m Pd, and the objective was finding an ambient temperature superconductivity path associated with the BEC cluster model. The Hamamatsu MPPC S10362-11- series of multi pixel photon counters with a DC power supply, HP 6034 A, was used to measure the sonoluminescence photons (Fig. 2). The driving piezo had a cylindrical geometry 1.7 mm in length, 12 mm OD, and 5 mm ID. The MPPC DC volt output signal was processed by an ORTEK VT120A preamp. This cylindrical piezo concentrated energy along its central axis. The sonoluminescence measurements in reactor No. 2 were difference measurements, piezo on – piezo off in the light box. The MPPC signal data was passed through the ORTEK preamp to the oscilloscope. The absolute value of this photon difference signal included the dark current, other interference, and counted photons (Figs. 2 and 13). The oscilloscope measured two channels of data.
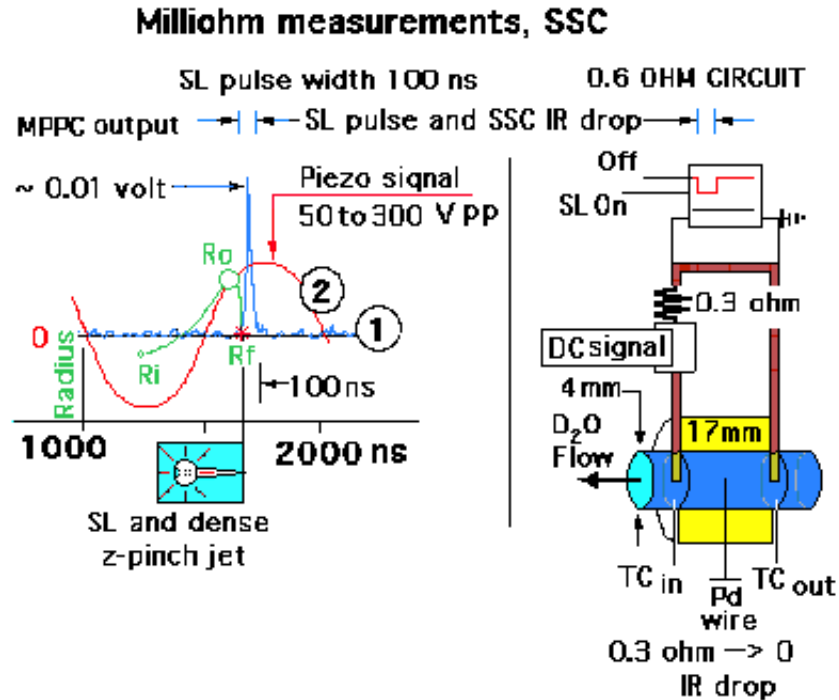
**Figure 15.**   A piezo driven TCB collapse and the measurement of a Pd wire SSC.

One channel measured the acoustic watts input, Ap, at its resonant frequency, and the other the MPPC signal voltage (Fig. 4). The MPPC millivolt signal output generated from an $Ap$ acoustic watt input a sequence of piezo five cycles and shows the resulting coupled sonoluminescence (Fig. 2). The data average of several different $Ap$ values is shown (Fig. 13). The original MPPC signal made up of dark current, other interference, and sonoluminescence photon count was separated into its component parts as the increasing $Ap$ broke its straight line at the MPPC saturation point, $Ap = 2.4$ W, shown in Fig. 13. The break occurs as individual sensing pixels were saturated with photons producing a constant photon count when the 100 pixels of the MPPC are recovering from a photon count, a period of 300 ps. Saturation across the bulk of the MPPC's 1 mm$^2$ sensing surface area of 100 pixels caused this change of slope in the measured $Ap$ signal.

The photon count was based on the photon saturation point of the MPPC. A number of measurements used the MPPC set at a distance, $d = 8$ cm and $d = 16$ cm (Fig. 4). Varying the $Ap$ watts input from 0.5 to 4.8 W show in Fig. 13 the change in slope reverting to the dark current slope at the MPPC's sonoluminescence saturation point. There were several graphs using different types of MPPC devices and distances that had graphs similar to Fig. 13. The MPPC recovery time was listed as 0.3 ns for all devices. The maximum number of times a pixel could be exposed between saturations, during the 100 ns sonoluminescence pulse duration is 100 ns/0.3 ns = 333 pseudo pixel ratio (Fig. 2). At saturation all pixels are at steady state so the photon count is constant. The MPPC photon counting device sensing area is 0.01 cm$^2$. The 8 cm distance produces a radiance surface area ratio of $8 \times 10^4$. So the total number of photons was about $(8 \times 10^4) \times (333) \times 100 = 2.7 \times 10^9$ photons at MPPC saturation. The MPPC photon measurements centered at 450 nm with an 1 spread of 350–900 nm, and therefore did not measure the majority of the UV and VUV photons, but a

relative number of photons; so the actual number may be $10^{10}$ photons at this 2.4 W $Ap$ saturation setting.

## 9. Reactor No. 2 Experiment

Superconductivity experiments are ongoing. $Ap$ is used when referring to the acoustics of reactor No. 2 system. Several Hamamatsu MPPC photon detectors that improved photon measurements in reactor 2 devices measured the sonoluminescence. The geometries of the two reactors to accommodate the flow-through calorimetry and piezos were different. The target configurations were different. The general conditions and set-up were the same for both reactors. The temperatures, flow rates, the reactor materials, and argon and $D_2O$ were the same. Jack Forman machined both reactors from polycarbonate blocks. The purpose of these wire experiments was sono-superconductivity, SSC, measurements

The experiment circulated $D_2O$ through a cylindrical 0.3 cm$^3$ volume at the rate of 2.5 reactor volumes per second of a cylindrical focusing piezo No. 2. The wire was centered and placed in a vertical position, minimizing bubble collection. Piezo measurements involved off and on modes made by the 4 point milliohm meter, to measure any drop in the resistance (Fig. 14). The 17 mm long 100 $\mu$m Pd target wire had a resistance 0.332m$\Omega$ with electrical contacts using heavy 2 mm diameter copper wire leads of negligible resistance

In the light box, where the wire resistance was measured, red line, no resistance differences were noted (Fig. 14). A varied voltage, 0–120 V, produced a wattmeter input measurement to the oscillator, $Q_i$, ranging from 0 to 16.4 W and $Ap = 0.3Q_i$ so $Ap$ acoustic input watts varied from 0 to 4.8 W and drove the piezo at its resonance frequency. The red line showed no difference between the piezo off and on mode as the $Ap$ input watts was increased, shown as the blue line. A better measurement technique is shown for sono-superconductivity in Fig. 15. The same basic set-up will use a scope for a quick response to 100 ns looking for an IR that signifies a superconductivity measurement. The 100 $\mu$m diameter Pd wire, was part of the measuring circuit and the implantation target, lower right of Fig. 15. The cavitation in $D_2O$ produced an adiabatic collapsing transient cavitation bubble that produced a $z$-pinch jet and sonoluminescence emission of photons. The implantation process via EM pressure pulse condensed into the dense BEC phase as cluster density maintained a connectivity for 100 ns. The superconducting property depended on the concentration of these sub surface transient BEC elements during the 100 ns period of the sonoluminescence pulse. The left-hand side of Fig. 15 shows the bubble growth, green, and the SL pulse, blue (1), coupling to the piezo acoustic wave resonance, red (2). The right-hand side of Fig. 15 shows the piezo with the flow of circulated $D_2O$ and the low-resistance superconducting measuring circuit, brown, and the oscilloscope measurement of the expected superconducting signal IR drop, red, at every resonance cycle of the piezo. The scope measurement at the top, right box, shows the expected sono-superconducting IR drop, red, during the period of the sonoluminescence. Photon emission measured, 100 ns/acoustic cycle, by the multi pixel photon counter, MPPC.

The sonoluminescence pulse is coupled to 1 MHz resonance of a 17 mm long cylindrical piezo. The 100 $\mu$m diameter Pd wire of 0.3 $\Omega$ resistance in $D_2O$, forming the bottom half of the circuit, is in series with 0.3 $\Omega$ resistor, black, in a simple circuit powered by a 1 V, DC signal. Any repeating in phase IR drop in the scope total resistance value is a positive response to superconductivity presence. A 1 MHz 100 ns voltage pulse coupled to the piezo resonance frequency can be explained as a BEC steady state concentration level that supports sono-superconductivity and sonofusion. These are ongoing and current experiments

## 10. Discussion and Summary

The number of transient cavitation bubbles associated with each piezo oscillation, and the geometric differences between reactors Nos. 1 and 2 show that $Q_a$ and $Ap$, the respective acoustic watt inputs, were different in their bubble distribution and high acoustic bubble densities. $Q_a$ was three times higher in power than $Ap$. The acoustic watt input, $Q_a$ , of a

cavitating disk piezo at a MHz in $D_2O$ in reactor No. 1, with an energy density, $Q_a$ /m$^3$, did not change much in a linear piezo acoustic field at small distances, about a millimeter between the disk and the target foil. In reactor No. 2 the acoustic watt input, $Ap$, of a focused cylindrical piezo acoustic field, with an energy density, $Ap$/m$^3$, increased at the wire target surface. $Ap$/m$^3$ was inversely proportional to the distance from the active piezo inside surface to the target wire surface (the inside piezo radius). As the $Ap$ acoustic wave moved to the piezo center, the acoustic power density, $Ap$/m$^3$, increased. For reactor No. 1 acoustic energy density, $Q_a$/m$^3$, at the target foil was proportional to the activity at the Pd foil target surface producing BEC clusters. The sonoluminescence photon and ejecta site counts quantified the transient cavitation bubble's collapse that formed sonoluminescence pulses, $z$-pinch jets, and BEC cluster formation. The measured ejecta sites support the fact that very small but energetic sources, sub-nanometer in diameter BEC clusters, were produced beneath the target lattice surface. The model shows a correspondence between calorimetric measurements of $Q_x$, the excess heat and heat of fusion [5], and ejecta sites that can be explained by radiation free DD fusion measured products.

Sonoluminescence pulses and high-density $z$-pinch jets were produced at the transient cavitation bubble collapse process in the final bubble collapsing radius [9,10]. Some of these $z$-pinch jets were close enough to implant their high-density deuteron electron plasma into a target. The lattice picosecond implantation and charge separation produced a dynamic EM compression pulse pressure that overwhelmed the Coulombic repulsion escape pressure, and led to a picosecond DD cluster compression fusion environment. The final density of the cluster in this picosecond should have approached $10^{36}$ deuterons/m$^3$ for a compressing and cooling environment, promoting DD fusion. The implanting $z$-pinch jet may form many clusters of various sizes with one fusion event per cluster in the MHz sonofusion devices. Calorimetric measurements were made in reactor No. 1; about 38 W of $Q_x$ were measured (Fig. 5). Here $10^{13}$ DD fusion events per second produced about 40 W of $Q_x$ from single fusion ejecta sites. A determination by an ejecta site SEM survey could easily support this $Q_x$ measurement. In the MHz reactor No. 2, it was reasonable that the MPPC measurement of $10^{16}$ photons/s, mostly in UV and VUV range, could also produce the same 40 W $Q_x$. Sonoluminescence measurements were improved using the MPPC device.

The primary compression pressure was the acceleration of charges to the cluster's center producing an EM pressure pulse surrounded by the electron's magnetic field lines parallel to the cluster surface that cinched down on the shrinking compressing nm cluster, like the nova birth of a white dwarf star. The electron EM pulse formed a cavity enclosing the collapsing deuteron cluster, a pseudo Meissener effect. Except during this picosecond there were moving deuteron charges toward the cluster center. Its strong collapsing magnetic field opposed the direction of the external electron's magnet field. The deuteron's electric field was part of the EM compression pulse also directed to the cluster's center. For a picosecond a dense cluster of $D^+$ were squeezed together in a BEC (4000 K) with superfluid and superconducting properties (Fig. 6). Energy of fusion in the deuteron BEC was transformed into $^4$He and heat; $Q_x$ excess heat was produced before the expected 24 MeV gamma mechanism was in place in the BEC environment (gamma production cycle was about $6 \times 10^{-21}$/s). In the BEC environment the simplest path for a DD fusion event was to the products of heat, $Q_x$, and $^4$He [2]. The deuteron BEC cluster assumed the properties for a picosecond of a high-density liquid for the instantaneous transfer of energy to heat. The $^4$He and heat products should be favored for this and other implied reasons.

One can add to the cluster's compression by way of the cluster's surface deuteron evaporation that cools the remaining cluster contents via its momentum exchange. The loss of the cluster's surface deuterons cooled the BEC during its compression. The escaping deuterium ion moved into the surrounding Pd target lattice as an ion and its exchange momentum removed heat and added to the compression. After a picosecond, the Coulombic repulsion escape pressures overwhelmed the increasing cluster's compression pulse pressures. In reactor No. 1, sonofusion DD products, deuterons, and vaporized target foil were ejected into the circulating $D_2O$. Reactor No. 2 produced few fusion products and would be on the path to its BEC superconductor distribution, and denser cluster surface implantation. To strengthen these ideas are theories that predict attractive pressures between dense like charges and Cooper pairs [11],

in a collection of high-density deuterons [12]. These theories might lengthen the picosecond lifetime stability of an implanted positively charged deuteron cluster.

The $T_c$ for a normal ultra cold BEC is a degree or so above absolute zero. The 2.23 MeV, nuclear dissociation energy of the deuteron, fused neutron and proton, could be associated with its unique dissociation of 2.23 MeV. Absence of electrons makes it the lightest elemental boson ion that exists (except [$^1$H$^+$$^1$H$^+$]). It appears that the deuteron's, $D^+$, $T_c$ is exceptionally high for its two nucleons, and has the lowest binding energy of any polynuclear nucleus. In the picosecond environment of reactor No. 1 a pair of deuterons fuse. The heat of fusion produced a sub-surface $Q_x$ heat pulse in the cluster that erupts from the target lattice as an ejecta site in the target foil. These sites were observed and surveyed in SEM photos, as evidence of cluster DD fusion and $Q_x$ [2,5]. The clusters' fusion products were ejected along with lattice vapors into the circulating $D_2O$ and then measured. The cluster compression sequence was similar to that of a white dwarf star nova and muon fusion [13]. The cluster was destroyed by the fusion event, a single pair of fusing deuterons in a picosecond EM pulse. The cluster's remnants recombined into $D_2O$, $D_2$ and DOOD at steady state concentrations. Reactor Nos. 1 and 2 were density driven systems like muon fusion [14]. If the input acoustic watts, $Ap$, was adjusted correctly, it allowed for the measured resistance of the transient superconductor using a 4-point milliohm-meter, but the sequence of events was too fast for this measurement system. Because of its transient nature the superconductor resistance could be measured via an oscilloscope keyed to the 100 ns sonoluminescence pulse (Fig. 15).

This model is a good fit for sonofusion's experimental products of $^4$He and heat of fusion, $Q_x$, with no gammas. It fits other systems that may have incidental bubbles. The BEC has a possible wider distribution in nature, astrophysically, directed towards dark matter. Several multi-million dollar projects are searching for the axion boson resonance and their connection to dark matter. Under the correct conditions axions will convert to micro-wave photons and back. These will be revealed in the experiments at the University of Washington in the ADMX device. So, some thinking of sonoluminescence pulses and other photon sources and a possible connection to axions is worth consideration [15].

## Acknowledgements

## References

[1] M.P. Brenner, S. Hilgenfeldt and D. Lohse, Single bubble sonoluminescence, *Rev. Modern Phys.* **74**(2) (2002) 425–484.
[2] R.S. Stringham, *ACS Book, LENR Sourcebook*, J. Marwan and S. Krivit (Eds), Vol. 2, 2009.
[3] R.S. Stringham, *ICCF-14 Proceedings*, D. Nagel and M. Melich (Eds.), Washington DC, USA, 411, Oct. 5–9, 2008.
[4] R.S. Stringham, *ICCF-11 Proceedings*, J.P. Biberian (Ed.), Marseilles, France, Oct.31–Nov. 5, 2004, pp. 238–252.
[5] R. Stringham, *ICCF-10 Proceedings*, P.L. Hagelstein and S.R. Chubb (Eds.), Cambridge, MA, USA, August 24–29, 2003, p. 233.
[6] 17. Brian Oliver; DOE MS analysis of $^4$He and $^3$He form EQuest Sciences, report, 1995; Helium Analysis of Gas Samples. B.M. Oliver, Rockwell International, Canoga Park, CA, 91309, 2005.
[7] R. Stringham, *ICCF-8 Proceedings*, F. Scaramuzzi (Ed.), Lerici, LaSpezia, Italy, May 21–26, 2000, pp. 299–304.
[8] R. Stringham, *ICCF-9 Proceedings*, Xing Z, Li (Ed.), *Int. Convention Center*, Tsinghua, Beijing, China, May 19–24, 2002, p. 323.
[9] R.S. Stringham, *JCMNS* **5**(13) (2010), to be published.
[10] Y. Tomita and A. Shima, High speed photographic observations of laser induced cavitation bubbles in water, *Acoustica 71* (1990) 161. P.M. Felix and A.T. Ellis, Laser-induced liquid breakdown – a step by step account, *Appl. Phys. Lett.* **19** (1971) 484. W. Lautterborn and J. Bolle, Experimental investigations of cavitation – bubble collapse in the neighborhood of a solid boundary, *Fluid Mech.* **723** (1975) 91.

[11]  E. Muller, Mueller Research Group, Cornell, http://people.ccmr.cornell.edu/ emueller/becbcs.html (2009).
[12]  N.L. Lawandy, *Appl. Phys. Lett.* **95**  (2009) 234101.

[13]  J.D. Jackson, *Phys. Rev.* **106** (1957) 330.
[14]  S. Badiei, P. Andersson and L. Holmlid, *Int. J. Hydrogen Energy* **34** (2009) 487–495.
[15]  Wikipedia, http://en.wikipedia.org/wiki/Axion (2011).

Research Article

# Low-energy Subbarrier Correlated Nuclear Fusion in Dynamical Systems

V.I. Vysotskii*

*Electrodynamics Laboratory "Proton-21", Kiev, Ukraine*

S.V. Adamenko

*Kiev National Shevchenko University, Kiev, Ukraine*

## Abstract

In the work the method of formation of a correlated coherent states of nuclei in the nuclear-synthesis systems and application of the method for essential optimization of low-energy nuclear interaction are considered. The relation of the correlation coefficient of these nuclei to the probability of their passage through a Coulomb barrier in order to realize a nuclear reaction is studied. We have determined the form of such an optimum dependence of the correlation coefficient on time, at which the formation of a maximally correlated states of particles and the attainment of the maximum variance of their coordinates under a parametric pumping of a harmonic oscillator are possible. The conditions allowing the choice of those possible laws of variations of the frequency of a harmonic oscillator, which cause the formation of a correlated state, are established. The possible type of a parametric pumping which induces the fast asymptotic formation of the completely correlated state of a particle with giant increasing variance of the coordinate under the parabolic barrier and similar increasing of nuclear reactions probability are determined.
© 2012 ISCMNS. All rights reserved. ISSN 2227-3123

*Keywords:* Coherent correlated states, Schrodinger–Robertson uncertainty relation, Subbarrier low-energy reactions

## 1. Introduction

It is well known that the total probability for nuclear reactions to run with the participation of charged particles at a low or middle energy (for $E \ll Ze^2/R$) is defined, in the first turn, by the action of a Coulomb barrier $Ze^2/R$ and, as a result, is bounded by a very small probability of the tunnel effect. This fundamental limitation complicates sharply the solution of the problem of nuclear synthesis and stimulates the use of fast particles in the composition of a hot thermonuclear plasma, which leads at once to the necessity to solve the extremely complicated technological problems related to the formation and confinement of such a plasma. The experience of studies performed in various countries for 50 years showed that the perspectives to realize the large-scale power-releasing thermonuclear synthesis

*E-mail: vivysotskii@gmail.com

remain to be unclear and unfavorable for the time being even for lightest particles (d and t). It is also obvious that the choice of the "thermonuclear" way makes any attempt to use, under the terrestrial conditions, the reactions of synthesis on the base of isotopes heavier than deuterium or tritium (they, in their turn, are not optimum candidates) to be absolutely unreal. For example, much more optimum is the synthesis on the basis of the ecologically safe reaction $^{11}B + p = 3\,^4He$ with the participation of heavier nuclei $^{11}B$. This reaction is not accompanied by both the appearance of neutrons and an additional radioactivity, but none of the promising thermonuclear-energy projects considers this reaction due to a significantly less probability of the tunnel effect.

Together with these "classical" and extremely expensive thermonuclear studies, whose efficiency is very small now and is not proportional to the undertaken efforts and the financial expenditures, many different disconnected experiments were carried out, where the nuclear synthesis ran at a low energy and under clearly "nonthermonuclear" conditions with the probability incomparably greater than those limitedly small values which must be revealed on the basis of the tunnel effect.

Convincing results were obtained at the Electrodynamics Laboratory "Proton-21" in Kiev for last 12 years in the experiments, where a state and a composition of needle-like targets were changed under the spatially symmetric action of nanosecond pulses of the current of an electron beam with the amplitude $J_0 \approx 50$–$70$ kA at the energy of accelerated electrons of about 300–400 keV. In all the experiments, the current pulse energy of a beam did not exceed 200–300 J. In these experiments (their total number in 12 years is at least 18 000, we observe the various effects related to the fundamental transformations of elements and isotopes of the initial chemically pure targets. In particular, after each of the experiments, we registered the synthesis products with the extremely wide spectrum of isotopes (from hydrogen to transuranium elements). As a distinctive peculiarity of the experiments, we mention the very high efficiency of nucleosynthesis. It corresponded to the transformation of about $N_n \approx 10^{19}$–$10^{21}$ nucleons per one cycle of the pulse action with the total duration of at most 50 ns. In addition, we registered a great number of protons with their energy in the interval from several keV to several MeV and greater, many fast deuterons, very intense X-rays, and gamma emission in each of the experiments. The scales of nuclear transformations corresponded to a change of the total binding energy $\Delta Q_{\text{bind}} \approx 30 - 50$ MJ or about $\Delta Q_{\text{bind}}/N_n \approx 1$ Mev/nucleon, i.e., it was by many orders higher that the mean specific energy of an electron driver (at most 1 eV/ nucleon). The more complete data on the results of these studies are presented in Refs. 1–4, à their detailed description is given on the Web-page of the Electrodynamics Laboratory "Proton-21" [5].

Various isotopic anomalies under clearly "nonthermonuclear" conditions were observed (though on considerably smaller scales) also in experiments performed by other groups.

The essential change of the isotope composition of the structural materials (mainly, Fe and Ti, for which the variations were at the level of 3–5%) of switching elements which realized the rapid commutation of hard currents (1–50 kA) and high voltages (up to 5 kV under idling conditions) was observed in industrial hard-current nets after the long-term operation [6]. Of importance is the circumstance that an electric arc (plasma) appeared at the time moment of the breaking of a hard current in all the studied facilities, where the isotope anomalies were registered.

Other experiments [7] have demonstrated the considerable variations of the isotope composition (about 5–7%) on the explosion of wires and foils immersed in a liquid under the action of millisecond hard-current pulses with the total energy of 20–30 kJ.

The transformations of nuclei, whose efficiency was close to that of the above-mentioned experiments, were observed in Ref. 8. On the passage of powerful submicrosecond electric pulses through an aqueous solution of $ZnSO_4$, a significant decrease in the zinc concentration was registered.

Of great interest are the experiments on the registration of neutrons escaping from a volume of cold gaseous deuterium positioned in a strong magnetic field with variable amplitude [5]. In these experiments, the emission of intense bunches of neutrons was registered only under very specific conditions, namely on the cooling (!) of gaseous deuterium down to the temperature of liquid nitrogen ($-196°C$) and for a very short time interval at once after the

change of the strong magnetic field with intensity of at least 8–10 kOe! These experimental results contradict directly the basic postulates and the very ideology of thermonuclear synthesis on the basis of tunnel effects, according to which the probability of the nuclear synthesis must exponentially decrease on a decrease in the temperature and increase on its growth.

The essential change in the isotope and element compositions was observed in studies [10,11] of the isotope composition of microbiological cultures rapidly growing in specially prepared nutrient media. The duration of the growth stage under study was several days. These media were impoverished by one of the vitally necessary chemical elements (in particular, by natural iron), but they contained the additional isotopes of other elements (in particular, concentrated heavy water $D_2O$ and $^{55}Mn$ as an admixture or, respectively, light water $H_2O$ and admixtures of $^{23}Na$ and $^{31}P$). The elementary analysis shows that the simple addition of these isotopes allows one (in principle) to ensure the synthesis of the absent element, because the reactions $^{55}Mn + d = {}^{57}Fe$ and $^{23}Na + {}^{31}P = {}^{54}Fe$ are characterized by the positive energy of the reaction and satisfy all the conservation laws. The detailed combined mass-spectrometric and Mössbauer analyses of the composition of the grown microbiological cultures showed that they turned out, indeed, to be enriched by these isotopes. In this case, their increment was by many orders more, than this could be explained on the basis of the probability of the tunnel effect. We also mention the experiments on the synthesis of $^{57}Fe$, where a synthrophic association of various types of microbiological cultures, which was stable under the action of depressing toxins and products (wastes) of the own metabolism, was used, rather than "pure" strains. In these experiments, not only the increase in the relative and absolute concentrations of isotope $^{57}Fe$, but approximately the same decrease in the absolute concentration of the initial isotope $^{55}Mn$ were surely registered!

All the above-mentioned experiments executed by the independent scientific groups at the nuclear centers of various countries have demonstrated the large-scale nuclear transformations under such clearly "nonthermonuclear" subthreshold conditions, when their efficiency calculated within the standard model of the tunnel effect must be by many orders less than that determined in the experiments. This circumstance becomes else more obvious if we take into account that the majority of experiments involved the isotopes with the charge of nuclei $Z \ll 1$ which participated in the process of nuclear transformations. For such isotopes, the probability of the tunnel effect at a low temperature is extremely small, and the number of events with nuclear transformations must be by many orders lower than the registration threshold.

Of course, the certain attempts to substantiate a specific mechanism, which would promote specific reactions with the participation of nuclei with $Z \gg 1$, were made on the interpretation of the mentioned experiments. But such substantiations involve, most frequently, only the qualitative arguments [6–8] or are generally absent [9]. A sufficiently grounded quantitative theory of the observed global nuclear transformations on the basis of the conception of self-controlled collapse in the volume of a target was proposed only in the works devoted to the analysis of the experiments executed at the Electrodynamics Laboratory "Proton-21" [1–4].

In addition, we note that all the above-considered experiments, despite the basically different ideologies, equipments, methods, and scales of observed processes, are joined by the fact that the success was associated only with those experiments, in which the perturbation stimulating the nuclear transformations was nonstationary or corresponded to a transient mode. In this case, the following empiric rule was fulfilled in the successful experiments: the optimum duration of the relaxation of a perturbation is inversely proportional to the amplitude of this perturbation.

Below, we consider a general and sufficiently universal mechanism of the stimulation and optimization of nuclear reactions running at a low energy. This mechanism ensures the large probability of the nuclear reactions under conditions, where the ordinary tunneling effects (including resonant tunneling effect) obviously "does not work", and can be applied with the same efficiency to very different experiments (both the executed and planned ones).

## 2. Correlated Coherent States of Particles and Schrödinger–Robertson Uncertainty Relation

The presence of wave properties and the possibility of the tunnel effect for microparticles are ones of the basic distinctive peculiarities of the quantum-mechanical description of the Nature. In the concentrated form, these properties are expressed in the form of the uncertainty relations which determine, in fact, the limit of the applicability of the classical and quantum descriptions of the same object.

Atomic and nuclear physics use widely the well-known Heisenberg uncertainty relation,

$$\sigma_q \sigma_p \geqslant \hbar^2/4, \tag{1}$$

which connects the variances and mean square errors,

$$\sigma_q \equiv (\delta q)^2 = \langle (q - \langle q \rangle)^2 \rangle, \ \sigma_p \equiv (\delta p)^2 = \langle (p - \langle p \rangle)^2 \rangle, \tag{2}$$

of the coordinate $q$ and the corresponding component of the momentum of a particle $p$.

The connection of this relation and similar ones to the commutativity of the operators of corresponding quantities in the form of the generalized uncertainty relation

$$\sigma_A \sigma_B \ \geqslant \ |\langle \widehat{A}\widehat{B} \rangle|^2/4, \tag{3}$$

was discovered by Robertson in 1929 for dynamical variables $A$ and $B$, whose commutator $\widehat{A}\widehat{B}$ is nonzero.

Relation (1) can be used for quantitative estimation of the tunnel transparency of a potential Coulomb barrier of a nucleus $V(q)$ with width $L(E)$ on the identification of the quantity $\delta p$ with the mean square effective radial momentum of a particle with energy $E$,

$$\delta p = \sqrt{2M \langle V(q) - E \rangle}, \tag{4}$$

in the subbarrier region defined by the conditions $V(q) \leqslant E, \ R \leqslant q \leqslant L(E)$.

In particular, if the condition $L(E) \ll \hbar/2\delta p$ is satisfied, then the transparency coefficient of the Coulomb barrier surrounding the nucleus is close to 1.

In the opposite case where $L(E) \gg \hbar/2\delta p$, the transparency of the barrier $D$ will be extremely small:

$$D = \exp\{-W(E)\} \ll 1,$$

$$W(E) = (2/\hbar) \int\limits_{R}^{R+L(E)} \sqrt{2MV(q) - E}\,dq = 2\,\delta p_q\,L(E)/\hbar \gg 1. \tag{5}$$

The very low transparency of the barrier is the main argument which is used in the proof of the impossibility (or the extreme inefficiency) for nuclear reactions to run at a low energy of colliding particles, which corresponds to a very large width of the barrier $L(E)$.

We note that the condition of smallness of the energy $E \ll \langle V(q) \rangle$ is a minor argument in the proof of the inefficiency of a reaction as compared with the main argument, namely the presence of a great width of the potential barrier at a low energy: $L(E) \gg \hbar/2\delta p$. This is related to the fact that the quantity $W(E)$ in (5) for the transparency of the barrier is proportional to the barrier width and depends on the energy only as a square root.

Not denying the obvious importance of the made estimates, we note that the particular (1) and general (3) Heisenberg uncertainty relations are not such universal laws as, for example, the energy conservation law. Their applicability is

limited, as it is easy to prove, to only those quantum states, where the quantities $A$ and $B$ are mutually noncorrelated. We recall briefly the most strict derivation of the basic relation (3). It follows from the requirement that the expression

$$G = \int\limits_{-\infty}^{\infty} |\alpha u(q) + i v(q)|^2 \mathrm{d}q \geqslant 0 \qquad (6)$$

be nonnegative for any value of the parameter $\alpha$ and for any functions $u(q)$, $v(q)$. Relation (3) was obtain on the basis of the direct analysis of (6) under the conditions that $\alpha$ is any real parameter, and $u(q)$, $v(q)$ are the functions related to the variances:

$$u = \Delta \widehat{A} \psi(q) \equiv (\widehat{A} - \langle A \rangle) \psi(q),$$
$$v = \Delta \widehat{B} \psi(q) \equiv (\widehat{B} - \langle B \rangle) \psi(q),$$
$$\sigma_A = \int |u(q)|^2 \mathrm{d}q, \ \sigma_B = \int |v(q)|^2 \mathrm{d}q \ . \qquad (7)$$

In 1930, Schrödinger and Robertson independently generalized the Heisenberg idea of the quantum-mechanical uncertainty of different dynamical quantities $A$ and $B$ on the basis of the more correct analysis of (6). If we remove the ungrounded limitation that the parameter $\alpha$ is purely real, then (6) yields the more universal condition

$$\sigma_A \sigma_B \geqslant |\langle \widehat{A} \widehat{B} \rangle|^2 / 4(1 - r^2) \qquad (8)$$

called the Schrödinger–Robertson uncertainty relation [12, 13]. In this relation, the quantity

$$r = \sigma_{AB} / \sqrt{\sigma_A \sigma_B} \qquad (9)$$

is the correlation coefficient which determines the degree of cross correlation of the quantities $A$ and $B$ in a specific state described by the wave function $\Psi(q)$. Respectively, the expression

$$\sigma_{AB} = \langle \{\Delta \widehat{A}, \Delta \widehat{B}\} \rangle / 2 = (\langle \widehat{A} \widehat{B} + \widehat{B} \widehat{A} \rangle)/2 - \langle \widehat{A} \rangle \langle \widehat{B} \rangle \qquad (10)$$

is the mean value of the anticommutator of the operators of errors $\Delta \widehat{K} = \widehat{K} - \langle K \rangle$ of the quantities $A$ and $B$. By analogy with $\sigma_A$ and $\sigma_B$, the quantity $\sigma_{AB}$ can be called the cross variance of these quantities.

The Schrödinger–Robertson uncertainty relation (8) is an obvious generalization of the Heisenberg uncertainty relation (3) to the case of partially or completely correlated states. It clarifies the interrelation between the quantities $A$ and $B$, by defining the lower bound for the product of variances.

In the case of completely mutually noncorrelated quantities $A$ and $B$, we have $\sigma_{AB} = 0$, $r = 0$ and (8) is reduced to (3), which corresponds to the minimization of the product of variances $\sigma_A \sigma_B$. In this case, it is possible to form such coherent superposition (a packet) of the eigenfunctions of a particle in a specific potential well, for which $(\sigma_A \sigma_B)_{\min} = \hbar^2/4$. This superposition is called a coherent state (CS), and the last equality is the condition of its realization. In the presence of a partial correlation of these quantities, $\sigma_{AB} \neq 0$, $0 < |r|^2 < 1$, and $(\sigma_A \sigma_B)_{\min} > \hbar^2/4$. Respectively, on their full correlation, we have $|r|^2 \to 1$ and

$$(\sigma_A \sigma_B)_{\min} \to \infty \qquad (11)$$

Such correlated coherent state (CCS) can be created only on the basis of another coherent superposition of the same functions, for which the condition of maximization of the quantity $|\sigma_{AB}|$ is fulfilled.

For the correlated states, the specific uncertainty relations of type (1) are also changed and take the form

$$\delta q \, \delta p_q \geqslant \hbar/2\sqrt{1 - r^2}, \quad \delta E \, \delta t \geqslant \hbar/2\sqrt{1 - r^2}. \qquad (12)$$

From the formal viewpoint, the influence of the correlation of dynamical quantities can be taken into account by the introduction of the modified Planck constant $\hbar^* = \hbar/\sqrt{1-r^2}$ in the formulas for the tunnel effect probability. In addition to the purely formal equivalency, such a substitution well reflects also the sense of these changes, because just the Planck constant defines the boundary separating the regions of adequacy of the classical and quantum-mechanical descriptions of the processes. It is obvious that the presence of a cross correlation of different processes extends significantly the region, where only the quantum-mechanical description is valid, and this fact corresponds directly to an increment of the Planck constant.

For particles in the completely correlated states, the barrier transparency will be always large ($D \to 1$ at $r^2 \to 1$) at any energy (including $E \ll V_{\max}$), which breaks at once the universality of the assertion on the inefficiency of nuclear reactions at a low energy for any states of charged particles interacting at a low energy. It is seen that this assertion is valid only for uncorrelated particles. In view of this conclusion, it is obvious that the question about the possibility and the conditions of a realization of the correlated states of particles with $r^2 \to 1$ becomes central.

### 3. Conditions of the Formation of a Correlated Coherent State of a Particle

From the formal viewpoint, the problem of the formation and the stability of a correlated state of particles is reduced to solving the inverse problem of quantum mechanics, i.e., to finding such a state of a specific particle in the given force field, for which the maximum value of the cross variance modulus $\sigma_{AB}$ (10) of different physical characteristics of this particle is realized. The necessary properties can be inherent only in the superpositional function defining a phased superpositional state of a particle in the given force field. One of the simplest methods of the formation of the correlated coherent states of a particle under a parametric pumping of a nonstationary harmonic oscillator, being firstly in the ground state, is considered in Refs. 14–18.

The system of normed eigenfunctions $\Psi_\alpha(q, t)$, which describe the behavior of a particle in the field of a nonstationary harmonic oscillator with variable frequency $\omega(t)$ at an arbitrary time moment, can be found from the solution of a nonstationary Schrödinger equation and has the form

$$\Psi(q,t) = \int b(\alpha)\Psi_\alpha(q,t)\mathrm{d}\alpha,$$

$$\Psi_\alpha(q,t) \equiv= \frac{1}{\sqrt[4]{\pi\varepsilon^2}}\exp\left\{\left[\frac{i\xi^2}{\omega_0}\frac{\mathrm{d}\varepsilon}{\mathrm{d}t} + \alpha\xi\sqrt{8} - \alpha^2\varepsilon^* - \varepsilon|\alpha|^2\right]\bigg/2\varepsilon\right\}. \tag{13}$$

Here, $\zeta = q/q_0$ is the coordinate normed by the quantity $q_0 = \sqrt{\hbar/M\omega_0}$, $\omega_0 = \omega(t=0)$ is the base frequency of the harmonic oscillator at the time moment of the switching of a perturbation, $\alpha$ is any constant complex-valued number, and $\varepsilon(t)$ is a complex-valued solution of the classical equation of motion of the oscillator with variable frequency $\omega(t)$,

$$\frac{\mathrm{d}^2\varepsilon}{\mathrm{d}t^2} + \omega^2(t)\varepsilon = 0, \quad \varepsilon(0) = 1, \quad \frac{\mathrm{d}\varepsilon}{\mathrm{d}t}\bigg|_0 = i, \quad \omega(0) = \omega_0. \tag{14}$$

The direct calculation of the correlation coefficient (8) with the use of the wave function (13) yields

$$r = \mathrm{Re}\left\{\varepsilon^*\frac{d\varepsilon}{dt}\right\}\bigg/\left|\varepsilon^*\frac{d\varepsilon}{dt}\right|, \quad r^2 = 1 - \omega_0^2\bigg/\left|\varepsilon^*\frac{d\varepsilon}{dt}\right|^2. \tag{15}$$

Formulas (13)–(15) show that wave function (13) of a correlated state can be written as

$$\Psi_\alpha(q,t) = \frac{1}{\sqrt[4]{2\pi\sigma_q}}\exp\left[-\frac{q^2}{4\sigma_q}\left(1 - \frac{ir(t)}{\sqrt{1-r(t)^2}}\right) + \frac{\alpha q}{\sqrt{\sigma_q}} - \frac{1}{2}(\alpha^2 + |\alpha|^2)\right], \tag{16}$$

$$\langle q \rangle = 2\sqrt{\sigma_q} \, Re\alpha, \qquad \langle p \rangle = \frac{\hbar}{\sqrt{\sigma_q}} \left\{ Im\alpha + \frac{r}{\sqrt{1-r^2}} Re\alpha \right\}$$

Here, $\alpha$ is a parameter determining the symmetry of the system and the direction of the drift of the coherent correlated state. In a symmetric nonstationary parabolic potential well with $\alpha = 0$, $\langle q \rangle = 0$, and $\langle p \rangle = 0$, the wavefunction of the correlated state of a particle has the form

$$\Psi_0(q) = \frac{1}{\sqrt[4]{2\pi\sigma_q}} \exp\left[ -\frac{q^2}{4\sigma_q} \left( 1 - \frac{ir}{\sqrt{1-r^2}} \right) \right]. \tag{17}$$

Based on relations (14)–(17), we obtain the connection between the given change of the correlation coefficient $r(t)$ and the necessary law of variations in the actual frequency $\omega_r(t)$ of the harmonic oscillator [17]:

$$\omega_r(t) = A\sqrt{\frac{1}{(g(t))^2(1-r^2)} \left\{ 1 - \frac{g(t)}{\omega_0\sqrt{1-r^2}} \frac{dr}{dt} \right\}},$$

$$g(t) = \frac{r(t)}{|r(t)|} + 2\omega_0 \int_0^t \frac{r(\tau)d\tau}{\sqrt{1-r(\tau)^2}}. \tag{18}$$

The coefficient $A$ can be found from the condition $\omega_0 = \omega(t = 0)$. In particular, we have $A = \omega_0$ under the initial conditions

$$r(0) = 0, \quad dr/dt|_{t=o} = 0. \tag{19}$$

Equations (14)–(19) determine a solution of the problem of the formation of a correlated coherent state on the basis of the parametric swinging of a harmonic oscillator.

Relation (18) for $g(t)$ implies that the sign of the function $g(t)$ is defined by the sign of the correlation coefficient $r(t)$ and the product $g(t)(dr/dt)$ is a positive value increasing with the correlation coefficient modulus $|r(t)|$. In this case, it follows from the explicit formula (18) for $\omega_r(t)$ that an increase in the correlation degree ($dr/dt > 0$) corresponds always to a decrease in the frequency of a parametric pumping $\omega_r(t)$.

Formula (18) yields also easily the explicit form of the law of variations of the frequency of a parametric pumping

$$\omega_{r_0}(t) = \omega_0/(1 + 2\omega_0|r_0|t/\sqrt{1-r_0^2}) \tag{20}$$

for which the correlation coefficient remains constant and is equal to $r_0$. In particular, in order that the system be all the time in a state close to that with maximum correlation (for $|r_0| \approx 1$), it is necessary that the resonant frequency of the oscillator vary by the law

$$\omega_{r_0}(t) \approx \sqrt{1-r_0^2}/2t, \qquad |r_0| < 1. \tag{21}$$

These results have a great heuristic meaning. In particular, we can make the following important conclusion on their basis. In order that $|r(t)|$ will grow, it is necessary that the frequency $\omega_r(t)$ will decrease faster than $\omega_{r_0}(t)$ (21) with increase in time.

There is additional condition for creation of optimal correlated state of the particle.

The final correlated state with $r(t)$ cannot be attained for an arbitrarily small time interval. This corresponds to the fact that the derivative $|dr(t)/dt|$ should not be large at all the time moments. Formally, this condition follows

immediately from solution (18) defining the law of variations of the frequency of a parametric swinging. This frequency cannot become imaginary, which yields the condition

$$\frac{\mathrm{d}r(t)}{\mathrm{d}t} \leqslant \omega_0\sqrt{1-r(t)^2} \bigg/ \left\{ 1 + 2\omega_0 \int_0^t \frac{r(\tau)\mathrm{d}\tau}{\sqrt{1-r(\tau)^2}} \right\}. \tag{22}$$

This condition corresponds to the requirement for the process of variation of the frequency $\omega_r(t)$ to be adiabatic. One of the possible solutions [17], that satisfy the condition of adiabaticity and ensure the fulfillment of the condition $|r(t \to \infty)| \to 1$ has the form

$$r(t) = \frac{t/\tau}{\sqrt{F(t) + (t/\tau)^2}}, \quad F(t \to 0) \to \infty, \quad F(t \to \infty) \to \text{const},$$

$$\tau = T_{1/2}\sqrt{2/F(T_{1/2})} \tag{23}$$
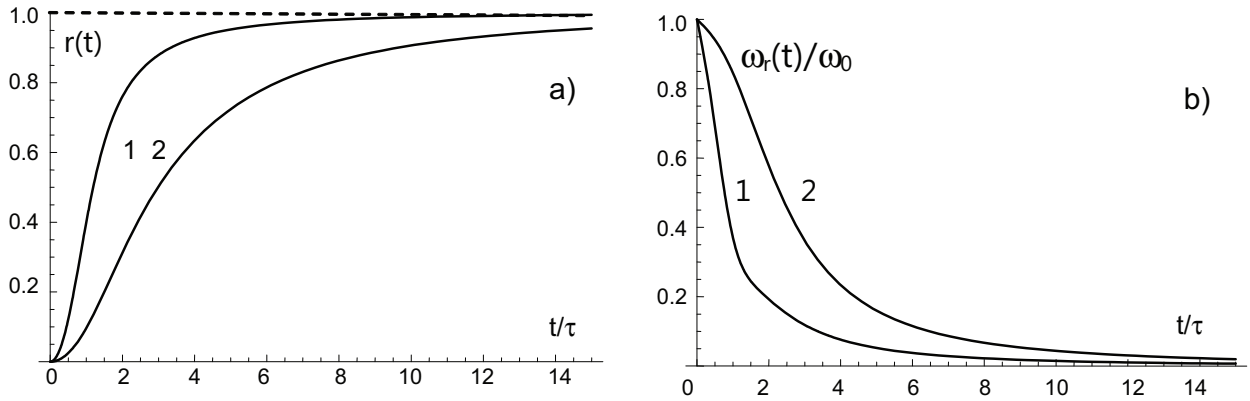
for any monotonously decreasing function $F(t)$.

In Fig. 1, the temporal dependence of the optimum frequency $\omega_r(t)$ of a parametric pumping of a harmonic oscillator and the correlation coefficient $r(t)$ for a function

$$F(t) = c^2 1/c + (\tau/t)^{32/3} \tag{24}$$

is presented.

The physical reason for the increase of the probability of tunneling effect is related to the fact that the formation of a coherent correlated state leads to the cophasing and coherent summation of all fluctuations of the momentum $\Delta\vec{p}(t) = \sum_n^N \Delta\vec{p}_n(t)$ for various eigenstates forming the superpositional correlated states (16), (17). This leads to a very great dispersion of the momentum

$$\sigma_p = \langle\left\{\sum_n^N \Delta\vec{p}_n(t)\right\}^2\rangle = N\left\langle(\Delta\vec{p}_n)^2\right\rangle + N^2\langle\Delta\vec{p}_n\Delta\vec{p}_m\rangle \tag{25}$$



**Figure 1.** Change of correlation coefficient $r(t)$ of the particle in nonstationary harmonic oscillator (a) connected with the change of frequency $\omega_r(t)$ of the oscillator (b) for function $F(t) = c^2 1/c + (\tau/t)^{32/3}$, $c = 2$ (case 1), $c = 10$ (case 2).

# Uncorrelated state

# Correlated state



**Figure 2.**   Formation of total (superpositional) fluctuating momentum of a particle in potential well in uncorrelated and correlated states.

correlated state, very great fluctuations of kinetic energy

$$\langle \Delta T \rangle = \langle \Delta \vec{p}(t)^2 \rangle / 2M = N^2 \langle \Delta \vec{p}_n \Delta \vec{p}_m \rangle / 2M + N \left\langle (\Delta \vec{p}_n)^2 \right\rangle / 2M \sim N^2 \tag{26}$$

of the particle in the potential well and increasing of potential barrier penetrability. This situation is presented in symbolic form in Fig. 2.

## 4. Change of the Probability of the Barrier Transparency for Particles in Coherent Correlated State

Let us consider simple model [17] which allows to demonstrate the process of barrier transparency increase during the increase of correlation coefficient $r(t)$.

   Let us suppose that the particle are presented in the one-dimensional deforming parabolic well, and the characteristic frequency $\omega_r(t)$ of that well decreased to the value $\omega_0$ to the moment $t = 0$ in a specific way, and at that moment the particle state was characterised by the correlation coefficient $r_s$. After that moment (at $t > 0$) well-deformation stops.

   For such one-dimensional Cartesian system we have (see (17))

$$\Psi_{\text{corr}}(x, r_s, t = 0) = \frac{1}{\sqrt[4]{2\pi \sigma_x}} \exp \left[ -\frac{x^2}{4\sigma_x} \left( 1 - \frac{i r_s}{\sqrt{1 - r_s^2}} \right) \right]. \tag{27}$$

From the other hand the standard wave function of the particle in stationary parabolic well in any time (including $t \geqslant 0$ is

$$\Psi(x, r_s, t \geqslant 0) = \sum_n B_n(r_s) \varphi_n(x) e^{-i E_n t / \hbar}, \quad \varphi_n(x) = C_n H_n(x) e^{-x^2 / 2x_0^2}, \tag{28}$$

$$C_n = \frac{1}{\sqrt{x_0 2^n n \sqrt{\pi}}}, \quad x_0 = \sqrt{\hbar / M \omega_0}, \quad E_n = \hbar \omega_0 (n + 1/2), \quad x_0^2 = 2\sigma_{x0}. \tag{29}$$

Population coefficients

$$B_n(r_s) = \int\limits_{-\infty}^{\infty} \Psi_{\text{corr}}(x, r_s, t = 0) \varphi_n^*(x) \mathrm{d}x \tag{30}$$

can be find from the condition of continuity for the total wave function at $t \leqslant 0$ and $t \geqslant 0$.

The resulting expression for the full wave particle function in partially correlated state with $r_s$ in the stationary well at $t \geqslant 0$ has the form

$$\Psi(x, r_s, t \geqslant 0) = \sum_n \left\{ \int_{-\infty}^{\infty} \Psi_{\text{corr}}(x', r_s, t = 0)\varphi_n^*(x')\mathrm{d}x' \right\} \varphi_n(x) \exp(-i E_n t/\hbar). \tag{31}$$

The results of calculations of probability density $|\Psi(x, r_s, t \geqslant 0)|^2 = \rho$ of particle localization within a parabolic well at any moment of time $t \geqslant 0$ depending on the correlation coefficient $r_s$ are presented below.

Figure 3 shows the results of calculation of this probability density for the localization of the particle in the parabolic well $V(x, t \geqslant 0) = (\hbar\omega_o/2)(x/x_0)^2$.

Figure 4 shows periodic modulation of probability density $|\Psi(x, r_s, t \geqslant 0)|^2 = \rho$ for states with different coefficient of correlation for different values of transversal coordinates.
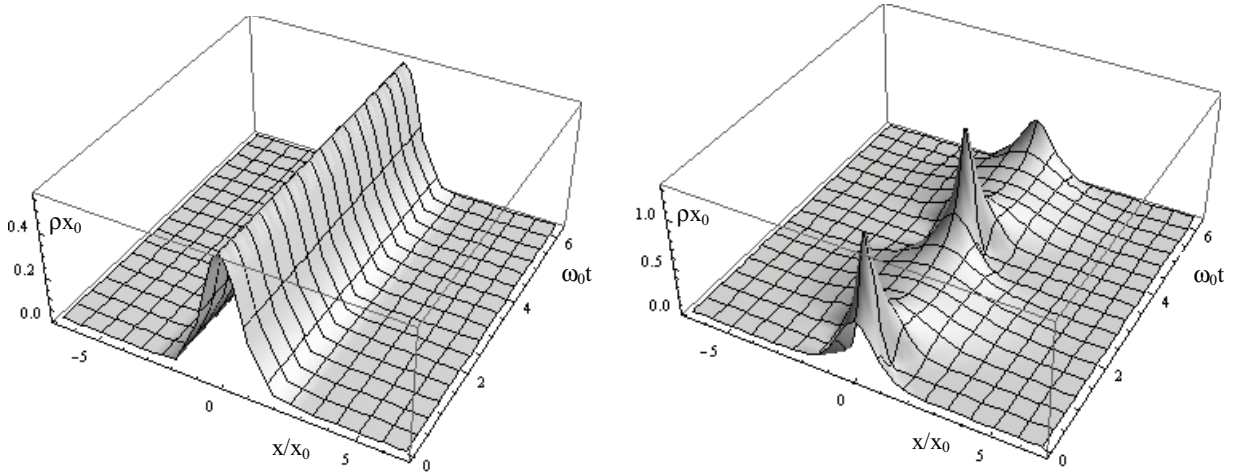
The dispersion of the coordinate for an uncorrelated state remains unchanged and equal to the initial value $\sigma_{x0}$. The probability of penetration of the particle in the subbarrier region for $|x| \gg x_0$ is very low. It can be seen from the results of calculation that the value of the probability density in the subbarrier region (at $|x| > 2x_0$) for correlated states in the delocalization phase considerably exceeds the steady-state value for uncorrelated states.

It can be seen from the figure that the very sharp increase in the coordinate dispersion of a particle and in the probability of its subbarrier penetration for the correlated state in the delocalization phase (see Fig. 4c) is not compensated and is much larger than the decrease in these parameters in the localization phase.

The results of averaging of function $|\Psi(x, r_s, t \geqslant 0)|^2 = \rho$

$$\langle\rho\rangle \equiv \langle|\Psi(x, r_s, t \geqslant 0)|^2\rangle_t = \frac{1}{T} \int_t^{t+T} |\Psi(x, r_s, t \geqslant 0)|^2 \mathrm{d}t, \quad T = 2\pi/\omega_0 \tag{32}$$

for various values of the initial correlation coefficient in the same well are presented in Fig. 5.



**Figure 3.** Changes of the cross structure of the distribution $|\Psi(x, r_s, t \geqslant 0)|^2 = \rho$ in an uncorrelated state $r_s = 0$(a) and in a state with the coefficient of correlation $r_s = 0.9$(b) in the course of time.
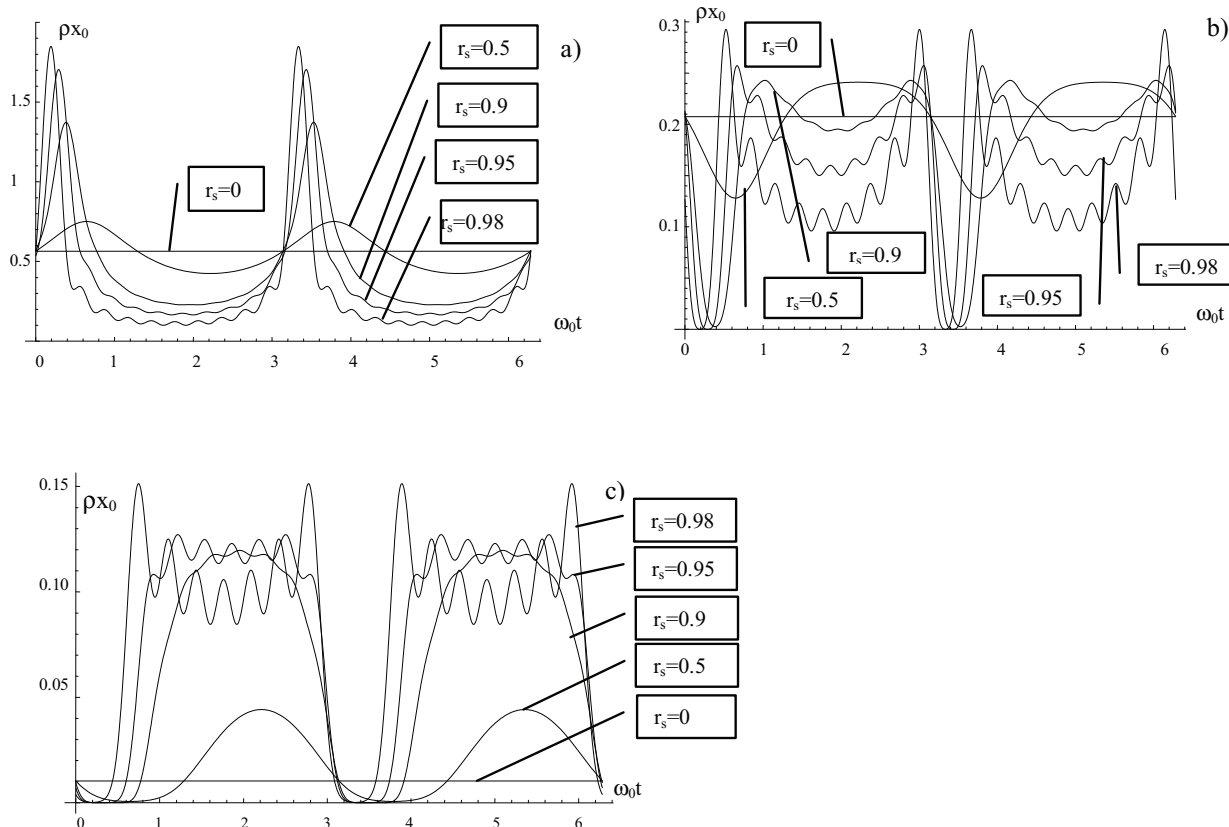
Figure 6 shows the resultant change (increase) in the averaged probability density of particle localization (tunneling probability $D$) $D = \langle |\Psi(x, r_s, t \geqslant 0)|^2 \rangle_t = \langle \rho(x, r_s) \rangle$ for various values of the correlation coefficient in the interval $r_s = [0, 0.988]$ and for coordinate $x = 10x_0$ in the region under the same potential barrier $V(x)$.

It can be seen that the tunneling probability for correlated states always increases considerably; the variation in the tunneling probability deep in the subbarrier region (e.g. for $r_s = 0.988$ and $x = 10x_0 \approx 14\sqrt{\sigma_{x0}}$ it increases by 30–40 orders of magnitude in relation to the uncorrelated state!).

The rate of nuclear synthesis (probability of reaction per unit of time for one pair of interacting nuclei situated at $x = 0$ and $x = x^{(n)}$) is equal

$$\lambda_{r_s} = \Lambda \langle |\Psi(x^{(n)}, r_s, t)|^2 \rangle_t. \tag{33}$$

Here, $\Lambda = S(E)\hbar/\pi M e^2$ is the constant of nuclear synthesis for a specific pair of nuclei; $S(E)$ is the astrophysical nuclear factor depending on a matrix element of the interaction energy of nuclei. $S(E)$ is the slowly changing function of energy, which with low relative energy of interacting particles in the case of non-resonance nuclear reactions, is constant $S(E) = S_0$ For example, $S_0 \approx 0.11$ Mev $bn$ and $\Lambda_{dd} \approx 1,5 \times 10^{-16}$ cm$^3$s$^{-1}$for a non-resonance dd-fusion.



**Figure 4.** Periodic modulation of probability density $|\Psi(x, r_0, t \geqslant 0)|^2 = \rho$ for states with the coefficient of correlation $r_s$ =0; 0.5; 0.9; 0.95; 0.98 in the same potential well for different values of transversal coordinates $x$ in the channel $V(x)$: (a) $x = 0$; (b) $|x| = x_0$; (c) $|x| = 2x_0$.

The "giant" increasing of the barrier transparency $\langle|\Psi(x^{(n)}, r_s, t)|^2\rangle_t$ leads to the similar increasing the probability (33) of nuclear reaction with participation of nearest nuclei situated at the same distances $x^{(n)}$.

## 5. Conclusions

Presented results clearly demonstrate the "giant" increases (by many order of magnitude) of localization density under the potential barrier and also the possibility of very effective under the barrier penetrations of particles at the increase of correlation coefficient. The regime of potential well deformation (parametric buildup of a harmonic oscillator) ensuring the most optimal adiabatic mode of the increase in the correlation factor that approaches its limiting value $|r| \rightarrow 1$ is determined, and this leads to an unlimited increase in the dispersion of the particle coordinate and to complete penetrability of the potential barrier.

One more nontrivial result seems to be important.

At increase of the correlation coefficient $|r| \rightarrow 1$ the giant increase the dispersion of the nucleus coordinate takes place. At such condition the mean square uncertainty $\delta x = \sqrt{\sigma_x}$ of the of this nucleus coordinate can significantly exceed the mean distance between nuclei $\langle a \rangle$. In this case, the volume of the three-dimensional region, where a nucleus in the correlated state is localized, will contain
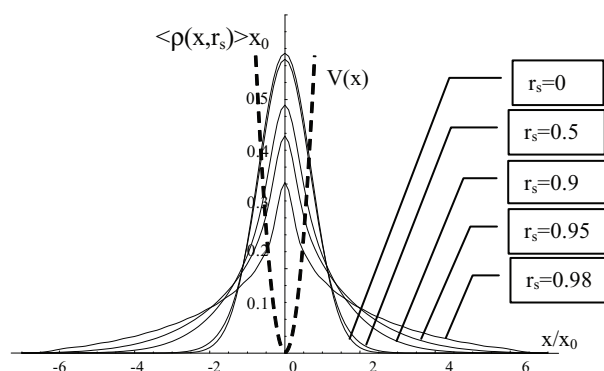
$$N_c \approx (\sqrt{\sigma_x}/\langle a \rangle)^3 \gg 1 \tag{34}$$

nearest nuclei, with which a nuclear reaction is possible.

This result opens the way to the possibility for correlated collective many-nucleus reactions to run. The probability of such reactions increases by $N_c$ times as compared with the probability of the running of binary reactions in the absence of a correlation.

These effects may play the important role in processes of controlled nuclesynthesis in different potential holes and systems with nonstationary action on active systems (e.g. in experiments with high-current electron driver in Kiev Laboratory "Proton-21" and in experiments on nuclear transmutation in biological systems).

The same effect of giant increasing of subbarrier transparency (by $10^{40} - 10^{60}$ and more times!) takes place during the increase of correlation coefficient at special high-frequency periodic action on quantum system. Such effects take



**Figure 5.** Averaged distributions of the probability density $\langle|\Psi(x, r_s, t \geqslant 0)|^2\rangle_t = \langle \rho(x, r_s) \rangle$
for a particle in the same potential well in an area under the barrier for correlated and uncorrelated states of particles with $r_s = 0$; 0.5; 0.9; 0.95; 0.98
.

**Figure 6.** Change of the averaged barrier transparency (tunneling probability $D$) $D = \langle|\Psi(x, r_s, t \geqslant 0)|^2\rangle_t = \langle\rho(x, r_s)\rangle$ for selected coordinate $x = 10x_0$ under the same parabolic barrier V(x) for different coefficients of correlation.
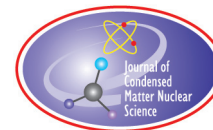
place in different nonstationary CF experiments with release of energy (including action of ultrasound and the method of "SuperWave" [19]. These result will be presented in our next papers.

## References

[1] S.V. Adamenko, A.S. Adamenko, and V.I. Vysotskii, Full-range Nucleosynthesis in the Laboratory – Stable Superheavy Elements: Experimental Results and Theoretical Description, Infinite Energy **9**(54) (2004) 23–30.
[2] S.V. Adamenko and V.I. Vysotskii, Mechanism of synthesis of superheavy nuclei via the process of controlled electron-nuclear collapse, *Found. Phys. Lett.* **17**(3) (2004) 203–233.
[3] S.V. Adamenko and V.I. Vysotskii, Evolution of annular self-controlled electron-nucleus collapse in condensed targets, *Found. Phys.* **34**(11) (2004) 1801–1831.
[4] S.V. Adamenko and V.I. Vysotskii, Neutronization and protonization of nuclei – two possible ways of the evolution of astrophysical objects and the laboratory electron-nucleus collapse, *Found. Phys. Lett.* **19**(1) (2006) 21–36.
[5] Web Page http://www.Proton-21.org.ua
[6] A.S. Agapov, V.A. Kalensky, Ch.B. Kaitusov, A.V. Malyshev, C.V. Ryabov, A.V. Steblevsky, L.I. Urutskoev, and D.V. Filippov, *Proc. of the 13th Russian Conf. on Low Energy Nuclear Transmutation of Chemical Elements*, P. 34, Dagomys,2004 (2005).
[7] L.T. Urutskoev, V.I. Liksonov, and V.G. Tsinoev , *Annales de la Foundation Louis de Broglie* **27** (2002) 701.
[8] V.V. Krymsky and V.F. Balakirev, *DAN RAEN* **385** (2002) 786.
[9] T. Mizuno, T. Akimoto, A. Takahashi, and C. Francesco, Neutron emission from $D_2$ gas in magnetic fields under low temperature, *Condensed Matter Nuclear Science, Proceed. of 11th ICCF Conference*, Marseilles, France, 31 Oct. – 5 Nov. 2004, World Scientific, Singapore, pp. 312–323 (2006).
[10] V.I. Vysotskii and A.A. Kornilova, *Nuclear Fusion and Transmutation of Isotopes in Biological Systems* (MIR, Moscow, 2003).
[11] V.I. Vysotskii and A.A. Kornilova, *Nuclear Transmutation of Stable and Radioactive Isotopes in Biological Systems* (Pentagon Press, India, 2010).
[12] E. Schrödinger, *Ber. Kgl. Akad. Wiss., Berlin* S.296–S303 (1930).
[13] H.P. Robertson, *Phys.Rev. A* **35** (1930) 667.
[14] V.V. Dodonov and V.I. Man'ko, *Trans. FIAN (Russia)* **183** (1988) 71–175.

[15] V.V. Dodonov, A.V. Klimov, and V.I. Man'ko, *Trans. FIAN (Russia)* **200** (1991) 56–105.

[16] V.V. Dodonov and V.I. Man'ko, *Phys. Lett. A* **79**(2/3) (1980) 150–152.

[17] V.I. Vysotskii and S.V. Adamenko, Correlated states of interacting particles and problems of the Coulomb barrier transparency at low energies in nonstationary systems, *Technical Phys.* **55**(5) (2010) 613–621.

[18] V.I. Vysotskii, *Quantum Mechanics and its Application in Applied Physics* (Kiev National Shevchenko University Publishing House, Kiev, 354 p., 2008).

[19] I. Dardik, T. Zilov, H. Branover, A. El-Boher, E. Greenspan, B. Khachaturov, V. Krakov, S. Lesin, and M. Tsirlin, Excess heat in electrolysis experiments at energetics technologies, *Condensed Matter Nuclear Science, Proceed. of 11*[th] *ICCF Conference*, Marseilles, France, 31 Oct. – 5 Nov. 2004, World Scientific, Singapore, pp. 84–101 (2006).

# Quantum-correlated Fluctuations, Phonon-induced Bond Polarization, Enhanced Tunneling, and Low-energy Nuclear Reactions in Condensed Matter

## K.P. Sinha

*Physics Department (Emeritus), Indian Institute of Science, 560012 Bangalore, India*

## A. Meulenberg *

*NAv6 Centre, Universiti Sains Malaysia, 11800 Penang, Malaysia*

## Abstract

In heavily (deuterated or hydrogenated) palladium, some of the crystallinity is lost. As a consequence, the localized phonon modes of the crystal/damaged-region interface have a much higher frequency than the host. These high-frequency modes create electrostatic fields that interact strongly with electrons of the local atoms. A resulting instantaneous potential inversion, from polarization, leads to the formation of lochons (local charged bosons–electron pairs in the singlet state, perhaps isolated from the Pd d-orbital energy levels) and of an associated $H^+$ or $D^+$ ion (with its two shared electrons instantaneously isolated into the adjacent Pd d-levels). The Coulomb repulsion between the nuclei of these pairs is greatly reduced by strong screening from the lochons that can even generate an attractive polarization potential. Furthermore, the mutual tunneling penetration probability of the Coulomb barrier is enhanced by correlated fluctuations. This arises from the generalized uncertainty relations, $\Delta x \, \Delta p_x, \, \Delta E \, \Delta t \geq (n + 1/2)h/(1 - \rho^2)^{0.5}$, where $n$ may be on the order of 10–100 and where results from two models are combined. The integer n values represent excitations in the phonon modes of the H or D sub-lattice and $\rho$ is the correlation coefficient with $0 < \rho < 1$. Higher values of $n$ and $\rho$, for a particle in a potential well, imply less localization and greater uncertainties in location (i.e., extending its probability distribution further into the barrier). These periodic fluctuations into the barrier are an interference effect similar to that of beat frequencies.
© 2012 ISCMNS. All rights reserved. ISSN 2227-3123

*Keywords:* Bond polarization, Correlated fluctuations, Lattice-assisted tunneling, LENR, Phonons

## 1. Introduction

As noted earlier, low-energy nuclear reaction (LENR) occurs in $PdD_x$ (or $PdH_x$) after considerable loading by D or H [1]. This loading produces degradation of crystallinity or amorphization of the alloy [2]. When extreme, this degradation is known to suppress LENR by allowing $H_2$ or $D_2$ to escape from the interior of the crystal along fractures. On the

---

*E-mail: mules333@gmail.com; Tel.: 011-604-6534632

other hand, disorder at a lower level may provide some of the necessary conditions for LENR. With this in mind, one has to consider not just the bulk material, but, also its external surfaces, its defects, and its internal crystallite and grain boundaries [3]. Of particular interest at these boundaries are the defects and the interface phonon modes. Associated with the boundary, interface, and defect states is the effect of nanoparticle (NP) surfaces relative to those of bulk or even thin-film material. The large surface to volume ratio of the NPs, relative to Pd thin films and bulk, alters the Pd-lattice size and its response to hydrogen loading [2]. At least in this recent study, the $PdH_x$ beta phase in NPs appears to be dominant at exposure to 2% H gas, but not until 10% H gas for thin films. Thus, both surface and subsurface effects depend on the nature of the interfaces. Linear defects have been addressed earlier [4]. The present paper examines another aspect of these interfaces.

## 2. Generalized Uncertainty Relation

The wave amplitude of interface phonon modes (in particular, longitudinal-optical modes) decays away from the interface junction. Thus, solutions of the wave equation correspond to localized modes near the interface. Further, these phonons produce electrostatic fields that strongly couple with the electrons and ions confined to the layer in a manner that may differ from that in the bulk. The effect of these fields in introducing paired-electron states (lochons – local charged bosons) has been discussed in detail in earlier papers [5,6]. Here we also explore the local-interface-state phonons as distinct from the bulk phonons.

The frequencies ($\omega_1$) of these localized modes are much higher than those of the phonon modes of the pure (host) lattice [7].In addition to the higher frequency (energy) of the local-state phonons, we will explore the effects of the phonon populations and of their correlations. Since we are concerned only with these localized-longitudinal-lattice modes, we will just use $\omega_1 = \omega$ in the equations below.

The expectation values of the number of these phonons at a particular frequency $\langle n_{r,\omega} \rangle$ about an interface D* or H* sub-lattice atom (or ion) and the expectation values of their amplitudes $\langle A_{r,\omega} \rangle$ are related [7].

$$\langle n_{r,\omega} \rangle = 2M\omega \langle A_{r,\omega} \rangle^2 / \hbar, \tag{1}$$

where $M$ is the mass of the atom. For $M_D =\sim 3.3 \times 10^{-24}$ g, $\omega \simeq 5 \times 10^{14}$ to $10^{15}$ s$^{-1}$ and $\langle A_{r,\omega} \rangle =\sim 3 \times 10^{-9}$ cm, $\langle n_{r,\omega} \rangle$ is of the order of tens of phonons. Why do we choose this value for $A$? If the spacing between the interstitial D site and the lattice barrier containing the deuterium is on the order of $10^{-8}$ cm, then a quadratic potential well, with a broad minimum would allow motion within its walls that would be dependent on the square root of the energy, e.g., on the number of phonons in a given direction and frequency (defining a mode). With many variables determining the actual average motions (temperature, direction, etc.), a ball-park value is the best that can be suggested. While the room-temperature mean-squared displacement [8] is $\sim 0.09$ au $= \sim 5 \times 10^{-10}$ cm, the transitory displacement into preferred directions (e.g., between Pd atoms and with another polarized deuterium atom approaching from the adjacent cell) will be significantly greater. The lattice-assisted nuclear reaction, LANR, depends on this increased displacement and the 'additional effects' mentioned below.

In the context of the present problem, we have to consider the time ($t$) energy ($E$) uncertainty relation as generalized by Schrodinger [9] and Robertson [10] and extended by Roy and Singh and others [11–13]. Since the maximum energy in phonons of a given mode is equal to the sum of the n phonons plus the zero-point energy ($\hbar\omega/2$) of the mode ($\omega$), and each phonon has $E = \hbar\omega$, and the cycle time is inversely proportional to ($\omega$), then:

$$\Delta x \, \Delta p_x \text{ and } \Delta E \, \Delta t \geq (n_{r,\omega} + 1/2)h. \tag{2}$$

Accordingly, the fluctuation-enhanced uncertainty in energy (the dynamic portion of the phonon that goes through zero twice a cycle) turns out to be:

$$\Delta E > (n_{r,\omega} + 1/2)h/\Delta t =\sim 2M_D\omega \langle A_{r,\omega} \rangle^2 / \Delta t. \tag{3}$$

It now becomes important to determine the appropriate value of $\Delta t$. Since $E$ varies between 0 and $E_{\max}$ in 1/4 of a cycle, the time of that maximum uncertainty should also be 1/4 of a cycle. With $\omega = 2\pi\upsilon > 0.5 - 1 \times 10^{15}$ rad/s, we can assume a period of $T = \sim 10^{-14}$ s and $\Delta t = \sim 2 \times 10^{-15}$ s. With values of the other parameters given above, we have $\Delta E = 1.5 - 3 \times 10^{-11}$ ergs $= \sim 10 - 20$ eV. This energy is very high for phonons and even for plasmons. However, when we take into account the polarization-induced dynamic, short-range, attractive forces (Eq. (A.4) in the Appendix) of the deuterium and the Pd atoms near the collision point of the lattice barrier, the value is more realistic. Furthermore, this is close to the $\sim 40$ eV associated with the plasma frequency of the Pd electron cloud [14].

If the preferred directions are along a linear harmonic chain (spacing $= a$), then with only nearest-neighbor interaction, oscillations $\omega(k) = \omega_0 |\sin(ka/2)|$ result, where $\omega_o$ is the resonance frequency. The phonon density of this level (density of normal modes) [15] is given by $g(\omega) = 2/\pi a (\omega_0^2 - \omega^2)^{1/2}$. ghe number of phonons in this 'van Hove singularity' is limited by many things; but, populations in resonant states can still be high. By increasing the local fields and displacement amplitudes, such resonance may greatly enhance the polarization potential $V_{\mathrm{pp}}(r)$ [16].

Tunneling probabilities in the classically forbidden region will have the form

$$P(E) = \exp[(-2/\hbar) \int (2M(V(r) - E))^{1/2} \mathrm{d}r_i]. \tag{4}$$

Taking the above polarization and fluctuation into account, the factor $(V(r) - E)$ changes to

$$V(r) + V_{\mathrm{pp}}(r) - \Delta E(\rho) - E, \tag{5}$$

where $V_{\mathrm{pp}}(r) = -|\alpha|^2/2r^4$ is an attractive short-range potential (Appendix). Even for low-energy situations, where $E$ is almost negligible compared to $V(r)$, the phonon-induced $\Delta E(\rho)$ can rise to the tens-of-eV range. The difference between this and the $\sim 26$ meV of room temperature energy, generally considered in such problems, may increase the tunneling probability of D–D fusion by many tens of orders of magnitude.

It is interesting that this result, when combined with the low energy, zero angular momentum corrections [4] to the normal Gamow tunneling-cross-section equation, corresponds roughly to those results predicted by the high values of $\Delta E$ ($\sim 400$ eV) determined by low-energy deuteron-beam experiments and the uncorrected Gamow equation [17]. The researchers involved in such experiments attribute the result to screening of the D–D interactions by electrons of the embedding material. *However, theoretical calculations for conventional screening effects are only one-quarter to one-half of these experimental values.* Screening effects, addressed in the next section, are not included in these calculations above.

## 3. Correlated Fluctuation

Phonons, as bosons, are self-correlating when in the same mode. That is why their ability to transfer energy is additive. However, any lattice has many modes. Not being in the same state as in other modes, most phonons do not necessarily add. However, if they are correlated, they can phase lock because of the non-linearities within a lattice and become coherent. A subset of these correlated phonons, the longitudinal-optical mode, is of particular interest to us.

An example of the consequences of this coherence is pictured by considering the probabilities of deuterons penetrating the lattice barrier if their periodic motion is in phase with a periodic motion of the Pd atoms. If the phases are such that the Pd atoms are further apart [18] at the time that the D atoms are approaching the barrier, the penetration will be much greater than if either phase were reversed. If these particular phonon frequencies of the Pd and D lattices are equal, or harmonic, then the number of deep penetrations for in-phase motion is increased relative to that of non-resonant phasing.

To carry this picture into the real world, assume the motion modes are not independent. This is likely, since real potentials are not truly simple harmonic oscillators (as generally assumed in QM). The anharmonicity or non-linearity of

the modes may allow them to couple to other modes (or result from such coupling). Even anharmonic correlation of the modes will create periodic fluctuations large enough to permit fusion under the right circumstances. Such events would just happen less often than they would with harmonic correlations. If the modes are of equal or multiple frequencies, the coupling can grow and reach a folding point (something breaks). Does this apply to the LANR experiments? Two examples described below indicate that this may be so.

Experiments with laser stimulation of deuterium sub-lattice phonon modes (using beat frequencies of laser pairs to get into the correct frequency range [19]) have demonstrated enhanced heat output at specific ranges. This is expected from any model based on lattice barrier penetration by deuterons. However, stimulation of PdD by lower frequencies, e.g., those produced by complex acoustic stimulation [20] (deliberately constituted to create high-frequency overtones) and even high-frequency electrical stimulation [21] have also shown positive results.

These lower frequencies could stimulate the Pd-lattice resonant modes and thereby enhance the motion that could permit the deuterons greater access to adjacent sub-lattice sites. They could also stimulate the much higher deuteron phonon harmonic frequencies that are many multiples of the Pd-phonon and source frequencies. However, the sub-lattice frequencies that are most critical may be harmonics generated by non-linearities of the Pd phonon modes and would then have both the correct frequencies and phase relationship for enhanced deuteron transport into and across the lattice barriers.

What are the quantitative consequences of this coherent-correlation effect? Given a correlation factor $\rho$, where $0 \leq \rho < 1$, that increases with correlation, we find an effect on the uncertainty relation such that

$$\Delta E \, \Delta t = \Delta x \, \Delta p_x \geq \hbar/2(1 - \rho^2)^{0.5}. \tag{6}$$

This means that as correlation increases, the fluctuations in energy, time, position, or momentum increase as well. For highly correlated states in which $\rho \Rightarrow 1$, the fluctuations in position or momentum can be quite high. If the states are also coherent, then these fluctuations can seldom occur or can occur all of the time (every cycle or $n^{th}$ cycle) depending on the phase and harmonic. If we couple the phonon effects with the correlated-coherence effects, then Eq. (2) becomes:

$$\Delta E \, \Delta t = \Delta x \, \Delta p_x \geq (n_{r,\omega} + 1/2)\hbar/(1 - \rho^2)^{0.5}. \tag{7}$$

If $n$ is of order 10 and $\rho$ is 0.9, the fluctuations in energy, relative to standard calculations, can increase by $\sim 20\times$. This value can be larger and readily enhanced. Specifically, the effects of proper laser stimulation of phonon modes can greatly increase $n_{r,\omega}$ and the selection, modifications, and chance correlation of material properties can be explained and shown to contribute greatly to the energy of the deuteron fluctuations within a Pd lattice.

## 4. Additional Effects

There are combined effects that might go beyond the non-linearities that can couple orthogonal modes. For example, if the optical modes of the Pd lattice allow the lattice barrier to be lowered at a time when the deuteron pair is approaching it, the amplitude of oscillation in that particular deuteron lattice mode may be significantly increased. The increased amplitude does not necessarily mean that the number of phonons increases in this case (Eq. (8)). The effective mass of the deuterons could be altered by the motion of the Pd lattice. Barrier penetration attributed to stochastic extremes [22] could, in fact, be a result of these coherent-correlated effects. There are so many variables in this problem that it is unlikely that theory alone will be able to determine which is most important (until experimental results point the way).

Beside the mechanical resonances that are obviously important, there are electric field effects of the phonons that may be even more important for the heat versus fragmentation balance in any resulting D–D fusion. Palladium, as a metal, clearly has many or most of its lattice atoms ionized. Hydrogen, with its much deeper ground-state energy levels, would not be ionized much, if any, of the time. However, it shares its electron with the adjacent ionized-Pd atoms. The Pd ion(s) also shares d-orbital electrons with the H atom. This results in a covalent bond sharing the H ground-state

orbital and yet leaving it with a net positive charge in the lattice [23,4]. The polarized covalent bond between the H and Pd atoms raises the average H energy level (Appendix) and population of the Pd valence electrons and therefore increases the conductivity of the material as H is added (nearly up to saturation, at $x = 1$ in PdD$_x$). Pd-ion and PdD-dipole phonon modes will generate oscillating electric fields. These fields interact with the H or D electrons, thereby polarizing the deuteron pairs colliding (at a Pd lattice barrier) in the longitudinal optical-phonon modes. The phonon-induced colliding motion of the H (or D) atomic pairs in the sub-lattice, means that the bound electrons, attracted to the opposing D nucleus will do more work ($W$ = Force × distance, T. Barnard, http://www.ichaphysics.com/the-science-of-cold-fusion] than they could without the phonon assist.[a]

An aspect of this $E$-field interaction that ties in with the correlated-coherent phonon modes and the deep orbit is the Extended Lochon Model [24]. This model makes use of these fields to create stable hydrogen–electron pairs in an s-orbital that is momentarily, but cyclically, much below the Pd d-orbitals. This periodically decouples the D–Pd covalent bonds and creates a D$^-$ ion within the lattice. Similarly, the fields can momentarily polarize valence electrons away from an adjacent lattice and sub-lattice location. This means that the shared Pd and D electrons shift more toward the Pd atoms leaving these D atoms/ions with a greater net positive charge. The result is a D$^+$D$^-$ pair that is attractive and aids in the collision process by reducing the Coulomb barrier in size and magnitude. Thus, coupled-phonon modes, which might not appear to have any mechanical connection with the deuterons' motion toward the lattice barrier, may have a major role simply by altering the electron concentration/polarization in the right place at the right time.

The above examples provide physical intuition for the theoretical papers on coherent-correlated-enhancement[12] and anharmonic-fluctuation effects. These dynamic resonance and non-linear effects are seldom treated well in QM because they are so dependent on material properties. Therefore, it is an open question as to which is more likely to succeed in determining the best materials and conditions for LENR and LANR, theory or experiment. Here-to-fore, experiment has provided the only basis for moving forward. Only now, is there a glimmer that theory can help guide in the selections.

## 5. Strong-screening Contribution

In our earlier papers [3–6], we have invoked the concept of strong-screening and attraction as a result of the doubly negative lochon being present in a tight orbit about a deuteron. The advantage of this concept is that the electron effective size and orbits shrink as the colliding deuterons approach on another. They shrink for two reasons. First, the long-range Coulomb fields of the electrons and protons cancel each other more completely as they approach one another. The screened long-range monopole charge field becomes a short-range dipole field. Second, if the electrons do work on bringing the deuterons together, they move deeper into the potential well converting potential energy into kinetic energy and work. This lowers the orbit radius. At the sub-atomic level, shrinking the average electron distance from the nuclei, which determines the 'effective size' of the electron, has the greatest effect on tunneling probability by reducing the length of the nuclear-Coulomb barrier..

There is a point to our considering that electrons reduce their average distance from a nucleus just by doing work. It allows them to reach the postulated deep-electron location (at least a metastable or resonance state), which is not accessible by normal means, i.e., photon emission [25]. It is also expedient to consider that a strong-screening effect of these tightly bound electron pairs is created assuming a lochon in this deep orbit.

The local screening effect may be represented by an equation normally used to describe an 'effective charge' of a unit charge in a plasma or free electron environment:

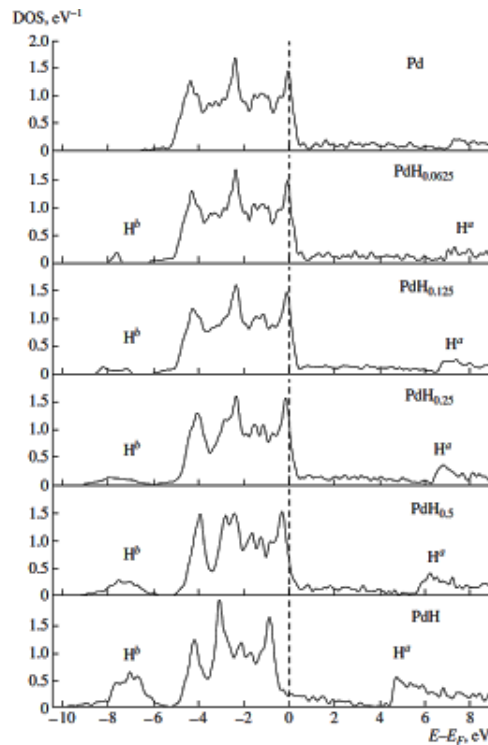$$e^2 \rightarrow (e_{\text{eff}})^2 = e^2 \exp(-\alpha_s), \tag{8}$$

---

[a]Without phonon assist, the electrons move in the atomic Coulomb potential, not the nuclei; thus, the work they do is generally negligible. If the phonons move the nuclei, then the work done by the electrons can be significant.

where $\alpha_s$ is the dimensionless screening parameter [26]. This $\alpha_s$ is not the same as the polarizability $\alpha$ in the appendix; however, it is very similar in both nature and effect. Values of $\alpha_s = 1, 2$, which give $e_{eff} =\sim e/2$, provide screening sufficient to raise the energy level of a bound hydrogen electron pair beyond their binding energy. In the presence of the electron pair's bound double-negative charge, what is the effective charge of the deuterium nucleus as seen by another charge. Since $H^-$ in the lattice is instantaneously stable, the paired electrons must be in a much deeper orbit or at least not provide the same value of $e_{eff}$ as would a free-electron density giving $\alpha_s = 1.2$. However, since the lochon model requires close proximity of the second deuteron to bring the lochon to a deep orbit, the paired deuterons must already be very close together. For even instantaneous stability at this point, the new screening parameter, $\alpha'_s$, is once again on the order of 1 and the effective charge of one of the deuterons (as seen by the other) is $e_{eff} =\sim 0.6e$.

For the $H^-$ and $D^-$ lochon cases, our estimated value of $\alpha'_s (\sim 1)$, gives $e^2 \exp(-\alpha_s) = 23 \times 10^{-20} \times 0.37 =\sim 8 \times 10^{-20}$ esu. Thus, to reach a micro-molecule orbit (e.g., $\sim 2 \times 10^{-11}$ cm) at which point fusion occurs rapidly, the nuclei have to climb a Coulomb barrier of energy:

$$V(R) = e^2 \exp(-\alpha_s)/R =\sim 8 \times 10^{-20} \text{ esu}/2 \times 10^{-11} \text{ cm} = 4 \times 10^{-9} \text{ erg} = \sim 3 \text{ keV}. \tag{9}$$

This is compared to the $\sim 10$ keV at which D–D colliding beam experiments start seeing measurable deviations from the Gamow tunneling model. The actual attraction and repulsion of the electron charges with the protons and each other must be examined in this context, since the protons will screen the electrons as well.



**Figure 1.** Density-of-states, DOS, in pure Pd and in PdH$_x$ solid solutions for different H concentrations $x$. H$^b$ and H$^a$ are peaks corresponding to bonding and antibonding states of Pd–H ( [28] with permission).
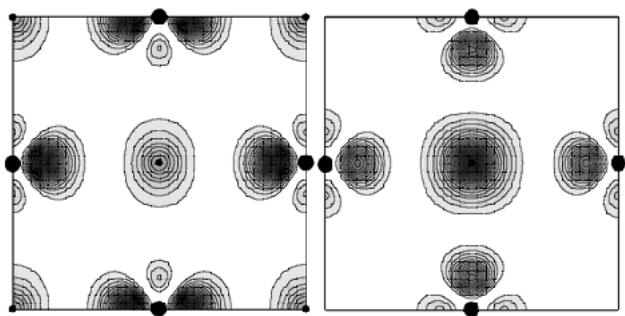
.

## 6. Conclusions

It is seen that no single mechanism can account for the D–D fusion observed in cold-fusion experiments. However, a combination of effects can explain some of the results. Individual phonons are below the 100 meV range; however, as bosons, they seek the same states and can increase the effective energy of their combined action by more than an order of magnitude. Random fluctuations of the lattice-barrier height can permit deuterons to penetrate the barrier, if they are at the right place at the right time. This is unlikely for truly random fluctuations. Therefore, it is important to seek correlated and coherent motions of the deuterons and Pd atoms within the lattice.

If the motions (phonon-induced) are both coherent and correlated, then resonance effects can greatly amplify the deuteron motions within the sub-lattice. If Pd lattice phonons are also coherent and correlated (at least harmonically) with the sub-lattice phonons, then the lattice barriers can be greatly lowered at the correct times for barrier penetration by the deuterons.

Even if the motions of the deuterons and the Pd lattice are correct for barrier penetration, the deuterons cannot overcome their nuclear Coulomb barrier without other mechanisms. The phonon electric fields can provide one of these by cyclically polarizing the deuteron electrons relative to the colliding deuterons. As a result, if the different phonon modes of both the lattice and sub-lattice allow coherent-correlated action, the bound electrons can move deeper into the nuclear-Coulomb-potential well for hundreds of orbits and shrink their orbital radius during a portion of the phonon cycle. This action leads to a strong-screening effect, or actual attraction between the deuterons, that reduces the effective charge of the nuclei and allows them to penetrate through their mutual Coulomb barrier to the attractive nuclear potential well within.

The LENR results, both from the unconventional 'Cold Fusion' community and the 'conventional' keV D–D collision work, cannot be explained by standard mechanisms. The cumulative effects on the energy barrier proposed in this paper are still small compared to those effects from standard calculations, 10s of eV vs ∼100 eV for screening, that can enhance fusion results. And these, in turn, are small compared to the experimental values attributed to screening to explain fusion rates for low-energy (> keV) D–D collision experiments [17]. Therefore, there must be a difference between the random nature of screening and the actual cause of the high fusion rates observed. Reducing the randomness and 'focusing' the effects of the low energies available in the system appear to be key to the observed LENR results. Even these contributing factors are not likely to be sufficient unless some other mechanism is, or can be, triggered by the additional energies and mechanisms. The ability of the electron pairing (formation of the lochon), to not just overcome



**Figure 2.**  Maps of electron probability-density distributions for H-–Pd bonding and anti-bonding states in PdH (*left panel*) and PdH 0.25 (*right panel*). The four large dots in each frame represent Pd atoms and the 5, or 1, small dots represent H atoms. ([28] with permission)

the Coulomb barrier problem but to create an attraction between deuterons under the proper conditions, would appear to be the mechanism that can explain the observed fusion rates. This mechanism also leads to answers [24] of the arguments against LENR based on known high-energy nuclear physics.

**Acknowledgement**

**Appendix A. Polarization and Electron-sharing Effects**

In the situation of Pd loading by D (or H), one must take into account the polarizability of atoms, covalently bonded molecules, and clusters of atoms. Polarization leads to an attractive (induced-dipole) [27] potential:

$$V_{\text{pp}}(r) = -\alpha e^2/2r^4, \tag{A.1}$$

where $\alpha$ is the polarizability having the dimension of volume. This will act: against the linear, hard-core, repulsive potential $V(r) = e^2/r$, between the nuclei of two interacting atoms (ions); and against the lattice barrier(s).

The tunneling probability in the classically forbidden region has the form

$$P(E) = \exp\left[-2/\hbar\right) \int_r^R \sqrt{2M(V(r) - E)} \, dr\right], \tag{A.2}$$

where $E$ is the energy of the deuteron and $r_o$ and $R$ denote the beginning and the end of nuclear-Coulomb potential barrier. For low-energy situations, $E$ is almost negligible. However, when we consider the lattice, the situation is much more complicated. $E$ now includes the minimum lattice barriers $V_l(r)$ and maximum energies. The average lattice energy may be at room temperature; but, with correlated motion and fluctuations (phonons and plasmons, etc.) arising from the generalized uncertainty, instantaneous energies $\Delta E(\rho)$ can be many eV. These energies can reduce the Coulomb barrier of the nuclei and lattice (assumed to be quadratic) and contribute to bringing adjacent deuterium atoms in the lattice closer together. Localized charge distributions increase the polarization potential $V_{pp}(r)$; and the factor $(2M(V(r) - E)^{0.5}$ for free-space is now modified to:

$$2M(V(r) - E)^{0.5} \Rightarrow (2M(V_1(r) + V_{\text{pp}}(r) - \Delta E(\rho)))^{0.5}. \tag{A.3}$$

The values of $V(r)$, $V_l(r)$, and $V_{pp}(r)$ are compared (Table 1) for $r$ values (distance between the H atoms approaching a common point of the lattice barrier) from $\sim 1.4 \times 10^{-8}$ to $7 \times 10^{-9}$ cm. However, even with detailed modeling [8], predictions of potentials at $< 1.6 \times 10^{-8}$ cm are not considered to be reliable. Assuming unit charges and a value of deuterium polarizability to be $\alpha = 0.68 \times (10^{-8})^3$ − not generally valid in the solid state – an approximation gives Table 1.

**Table 1.** Comparison of potentials in Eq. ( A.3)

|  | $V(r)$ (eV) | $V_l(r)$ (eV) | $V_{\text{pp}}(r)$ (eV) |
|---|---|---|---|
| $r = 1.4 \times 10^{-8} \Rightarrow$ | $\sim 7$ | $\sim 4$ | -1.2 |
| $r = 10^{-8}$ | $\sim 14$ | $\sim 4$ | -5 |
| $r = 7 \times 10^{-9}$ | $\sim 28$ | $\sim 4$ | -20 |

All of the potentials $V(r)$, $V_l(r)$, and $V_{pp}(r)$ and $\Delta E$ are cyclic, but generally at different frequencies. In this region, they are similar in amplitude as demonstrated by the ability of hydrogen to diffuse in a Pd lattice and for plasmon-induced ionization to move throughout the lattice [29].

The attractive polarization potential gives rise to forces with which the interacting atoms (ions) move towards each other.

$$F_{pp} = 2\alpha e^2/r^3. \tag{A.4}$$

With heavy loading, there is breakdown of crystallinity resulting from the amorphization of the alloy along with cluster formation. This can further increase the polarization and decrease the minimum distance of approach between deuterons.

Loading the Pd lattice with hydrogen, introduces an electron s-band below the Pd d-band (Fig. 1) [28]. Hybridization of these levels satisfies the atoms by 'filling' both the H s-orbitals and the Pd d-orbitals. However, the electrons are more tightly bound to the H atoms, and the result is a net negative charge on the H atoms relative to the Pd atoms. But, because of the loss of electrons to the conduction band, there is positive charge on both the Pd and H atoms. This relative charge difference produces a polarizable charge dipole that responds to both plasmon and photon fields. Because of the additional covalently-bonded electron in the hydrogen orbits, its induced polarizability is also greater.

As the H content increases with loading and the Pd d-orbitals fill, the Fermi level rises. Conduction eventually (at PdH) takes place only in the Pd 5s-orbital. While H does not 'lose' electrons in PdH, it shares electrons in a covalent bond with Pd atoms in a manner that makes it more positive than neutral atoms. Figure 2 displays the electron configurations about the Pd atoms (large dots) and H atoms (small dots) for PdH and for $PdH_{0.25}$. The electron density about the H atoms in $PdH_{0.25}$ (no H in corners) is greater than that in the PdH because, in the PdH lattice, there are fewer Pd electrons for each H to share.
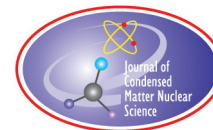
Another explanation for the change in electron density about the hydrogen atoms is based on lattice strain. Until the Pd lattice is stressed by being filled, the hydrogen 1s- and the Pd 4d-orbitals do not spread sufficiently for them to overlap and share their electrons. Thus, the electrons are more confined than they are when the lattice is full.

A phonon-induced electric field can shift the shared electron(s) from one Pd or H atom (or pair of atoms) to another. Thus, H can change from bonding, $H^b$, to anti-bonding, $H^a$, states (Fig. 2). Since the charge densities differ about the $H^b$ and adjacent $H^a$ atoms, they will become polarizable as pairs and respond to the local fields. The $H^a$ sites are dominant plasmon centers [29] and, if resonant with longitudinal optical-phonon modes, can have correlated-coherent effects that would greatly enhance the H–H or D–D fusion probability.

## References

[1] M.C.H. McKubre and F.L. Tanzella, Cold Fusion, LENR, CMNS, FPE, One perspective on the state of the science based on measurements made at SRI, *J. Condensed Matter Nucl. Sci.* **4** (2011) 32–44.
[2] Manika Khanuja et al., Hydrogen induced lattice expansion and crystallinity degradation in palladium nanoparticles: Effect of hydrogen concentration, pressure, and temperature, *J. Appl. Phys.* **106** (2009) 093515-1to 8.
[3] K.P. Sinha and A. Meulenberg, Laser stimulation of low-energy nuclear reactions in deuterated palladium, *Current Sci.* **91**(7) (2006) 907–912 (arXiv:cond-mat/0603213).
[4] K.P. Sinha and A. Meulenberg. A model for enhanced fusion reaction in a solid matrix of metal deuterides, in *Proc. ICCF-14 Int. Conf. on Condensed Matter Nucl. Sci.* Aug. 2008, Washington, DC, D.J. Nagel, M. E. Melich, R. W. Johnson, S. R. Chubb, and J. Rothwell (Eds.), http://www.iscmns.org/iccf14/ProcICCF14b.pdf. ISBN: 978-0-578-06694-3.
[5] K.P. Sinha, *Infinite Energy* **29** (2000) 54 (arXiv:0705.0595v1).
[6] K.P. Sinha and A. Meulenberg, Lochon catalyzed D–D fusion in deuterated palladium in the solid state, *Nat. Acad. Sci. (India) Lett.* **30**(7,8) (2007) 243–245 (arXiv:0705.0595v1).
[7] L. Mihaly and M.C. Martin, *Solid State Physics*, Wiley-VCH, Weinhein, 2004.
[8] A. Shabaev, D.A. Papaconstantopoulos, M.J. Mehl and N. Bernstein, First-principles calculations and tight-binding molecular dynamics simulations of the palladium–hydrogen system, *Phy. Rev.* B **81** (2010) 184103.

[9] E. Schrodinger, *Ber. Kgl. Akad. Wiss, Ion*. (Berlin) **24** (1930) 296.

[10] H.P. Robertson, A general formulation of the uncertainty principle and its classical interpretation, *Phy. Rev.* **35** (1930) 667; An indeterminacy relation for several observables and its classical interpretat, *Phy. Rev.* **46** (1934)794–800.

[11] V.V. Dodonov, E.V. Kurmystev and V.I. Manko, Generalized uncertainty relation and correlated coherent states, *Phy. Lett.* A **79** (1980) 150.

[12] V.I. Vysotskii and S.V. Adamenko, Correlated States of Interacting Particles and Problems of the Coulomb Barrier Transparency at Low Energies in Nonstationary Systems, *Tech. Phys.* **55** (2) (2010) 613–621, ISSN 1063_7842, © Pleiades Publishing, Ltd., 2010; V.I. Vysotskii and S.V. Adamenko, *Zhurnal Tch. Fiz.* **80** (2010) 23.

[13] S.M. Roy and V. Singh, Generalized coherent states and the uncertainty principle, *Phy. Rev.* D **25** (12) (1982) 3413.

[14] S. Feng, Enhancement of cold fusion rate by electron polarization in palladium deuterium solid, *Solid State Communi.* **72**(2) (1989) 205–209.

[15] N.W. Ashcroft and N.D. Mermin, *Solid State Physics*, Holt, Rinehart and Winston, New York, 1976.

[16] K.D. Bonin and V.V. Kresin, *Electric-Dipole Polarizabilities of Atoms, Molecules, and Clusters,* World Scientific, Singapore, 1997.

[17] K. Czerski, A. Huke, P. Heide and G. Ruprecht, Experimental and theoretical screening energies for the $^2$H(d, p)$^3$H reaction in metallic environments, *Eur. Phys. J.* A **27** (2006) s1.83–s1.88.

[18] E. Simanek, Quantum tunneling through a fluctuating barrier: enhancement of cold-fusion rate, *Physica* A **164** (1990) 147–168.

[19] D. Letts, D. Cravens and P.L. Hagelstein, Dual Laser Stimulation and Optical Phonons in Palladium Deuteride, *Low-Energy Nuclear Reactions and New Energy Technologies Sourcebook:* Vol.2, Marwan, Jan and Krivit, Steven B. (Eds.), American Chemical Society/Oxford University Press, Wash., D.C., 2009, pp. 81–93, DOI: 10.1021/bk-2009-1029.

[20] I. Dardik et. al., Ultrasonically-excited electrolysis experiments at energetics technologies, in *Proc. ICCF-14 Int. Conf. on Condensed Matter Nucl. Sci..* Aug. 2008, Washington, DC, D.J. Nagel, M.E. Melich, R.W. Johnson, S.R. Chubb and J. Rothwell, http://www.iscmns.org/iccf14/ProcICCF14b.pdf, ISBN: 978-0-578-06694-3,

[21] R.E. Godes, Quantum fusion hypothesis, in *Proc. ICCF-14 Int. Conf. on Condensed Matter Nucl. Sci.,* Aug. 2008, Washington, DC, D.J. Nagel, M.E. Melich, R.W. Johnson, S.R. Chubb and J. Rothwell (Eds.), http://www.iscmns.org/iccf14/ProcICCF14b.pdf, ISBN: 978-0-578-06694-3

[22] S. Habib, Quantum diffusion, *Proc. 4th Drexel Symposium on Quantum Nonintegrability*, 1994 (arXiv:hep-th/9410181).

[23] W. Sanger and J. Voitlander, Comparison between the magnetic susceptibilities of Pd$_{1-x}$, Ag, and single phase PdH, The 3:2 split of added electron $\Rightarrow$ unbalanced covalent bond (s–d) *J. Magnetism Magnetic Materials* **71** (1987) 111–118.

[24] A. Meulenberg and K.P. Sinha, Tunneling beneath the $^4$He* fragmentation energy, *J. Cond. Matter Nucl. Sci.* **4** (2011) 241–255.

[25] A. Meulenberg and K.P. Sinha, From the naught orbit to He* excited state, this issue, *J. Cond. Matter Nucl. Sci.* **5** (2012).

[26] S. Ichimaru, *Statistical Plasma Physics, Vol. II, Condensed Plasma*, Chapter 3, Addison–Wesley, New York, 1994.

[27] J.S. Brown, Enhanced low energy fusion rate in metal deuterides due to vibrational deuteron dipole–dipole interactions and associated resonant tunneling between neighbouring sites *J. Condensed Matter Nucl. Sci.* **2** (2009) 45–50.

[28] I.P. Chernov, Yu.M. Koroteev, V.M. Silkin and Yu.I. Tyurin, Evolution of the electron structure and excitation spectrum in palladium as a result of hydrogen absorption, *Doklady Phys.* **53**(6) (2008) 318–322, ISSN 1028-3358. © Pleiades Pub. Ltd., 2008. Original Russian Text published in *Doklady Akademii Nauk* **420**(6) (2008) 758–762.

[29] Yu.I. Tyurin and I.P. Chernov, Nonequilibrium escape of atomic hydrogen from metals exposed to radiation, *Dokl. Phys.* **44** (1999) 427–431 [*Dokl. Akad. Nauk* **367** (1999) 328].

Research Article

# Electrochemistry and Calorimetry of Ruthenium Co-deposition

## Melvin H. Miles*

*Dixie State College, St. George, Utah 84770, USA*

## Abstract

The electrochemical co-deposition of ruthenium (Ru) proved challenging due to the numerous possible oxidation states of this metal. Ruthenium (III) nitrosylnitrate, $Ru(NO)(NO_3)_3$, was investigated in the $NH_4Cl + NH_4OH/H_2O$ and $ND_4Cl + ND_4OD/D_2O$ electrolytes. The ruthenium solution had an intense red color that remained unchanged during extensive electrolysis at constant currents of 6, 10, 20 and 100 mA. However, at a constant current of 400 mA, the solution became completely clear overnight with a black deposit of ruthenium metal covering the copper cathode. The collapsed cyclic voltammetric trace indicated a large electrode capacitance (1–2 F) and a large ruthenium surface area ($10^5$ cm$^2$) similar to the previous observations for palladium co-deposition in this ammonia system. Extensive calorimetric studies using a constant current of 200 or 300 mA produced no measureable excess power in $H_2O$ or $D_2O$ for this ruthenium system. The very stable calorimetry allowed the determination of the effect of the electrolyte level on the cell constant at 0.0008 W/K mL for both the $Ru/H_2O$ and the $Ru/D_2O$ systems. The mean cell constants were $0.1318 \pm 0.0025$ W/K for the $Ru/H_2O$ study and $0.1312 \pm 0.0025$ W/K for the $Ru/D_2O$ experiment. There was no chemical excess power or shuttle reactions due to the nitrate ions present in these ruthenium solutions. In contrast to the palladium co-deposition studies, there was no detection of chlorine or nitrogen trichloride formation in any ruthenium co-deposition study. Based on out-gassing observations when the current was turned off, there was no absorption of hydrogen or deuterium within the bulk of the deposited ruthenium metal. Preliminary results are also reported for co-deposition studies of rhenium (Re), iridium (Ir), and nickel (Ni). Based on these new experiments with various metals, both palladium and $D_2O$ are essential for excess power in co-deposition studies.
© 2012 ISCMNS. All rights reserved. ISSN 2227-3123

*Keywords:* Absorption, Capacitance, Cell constants, Oxidation states, Vacancies

## 1. Introduction

Previous co-deposition calorimetric experiments in the $ND_4Cl + ND_4OD/D_2O$ electrolyte have focused solely on the Pd/D system [1,2]. However, if the anomalous excess power is due to near surface effects or vacancies, then other metals may also be active in producing excess power in co-deposition experiments. The use of other metals will also allow for the testing of the calorimetric system under conditions similar to those for the Pd/D co-deposition system. Ruthenium was selected because this metal was previously investigated as a supercapacitor material [3]. It has been proposed

that the large electrochemical capacitance effects observed for ruthenium may involve hydrogen ion absorption into the metal as well as adsorption at the surface [3]. Similar to platinum and palladium, ruthenium is also an excellent catalyst for water electrolysis, fuel cells and other processes. Ruthenium has the electronic configuration $[Kr]4d^7 5s^1$ and exhibits various oxidation states in its compounds. The most common oxidation state is 3+ as found for $Ru(NO)(NO_3)_3$. This is explained by the loss of two electrons from the 4d level and one electron from the 5s level to give the more stable electronic configuration $[Kr]4d^5 5s^0$. Other oxidation states for ruthenium are 4+ as illustrated by $RuO_2$, 8+ as found for the toxic $RuO_4$, as well as 2+, 5+, 6+, and 7+ oxidation states [4]. The seven oxidation states for ruthenium are tied with osmium as the most for any metal [4]. Another major reason for this ruthenium experiment is that it may serve as a control regarding possible chemical excess heat due to shuttle reactions in the $ND_4Cl + ND_4OD + D_2O$ co-deposition system [5–7]. This study will also provide a comparison between the similarities and differences encountered in palladium and ruthenium co-deposition systems.

## 2. Experimental

Calorimetric studies used a new isoperibolic design as previously reported [8,9]. Electrochemical experiments such as cyclic voltammetry (CVA) and electrochemical impedance spectroscopy (EIS) were performed using the Princeton Applied Research PARSTAT 2272 with the appropriate software as described elsewhere [6]. The deuterated chemicals used were Cambridge Isotope Laboratories $D_2O$ (99.9 atom % D), ACROS $ND_4Cl$ (98 atom% D), and ACROS $ND_4OD$ (99 atom% D). Alfa-Aesar ruthenium (III) nitrosylnitrate, $Ru(NO)(NO_3)_3$, was used for the electrochemical deposition of ruthenium metal. The actual solution concentrations were 0.02534 M $Ru(NO)(NO_3)_3$, 0.1468 M $ND_4Cl$, and 0.45 M $ND_4OD$ for the Ru/$D_2O$ study and 0.02158 M $Ru(NO)(NO_3)_3$, 0.1502 M $NH_4Cl$, and 0.45 M $NH_4OH$ for the Ru/$H_2O$ study.
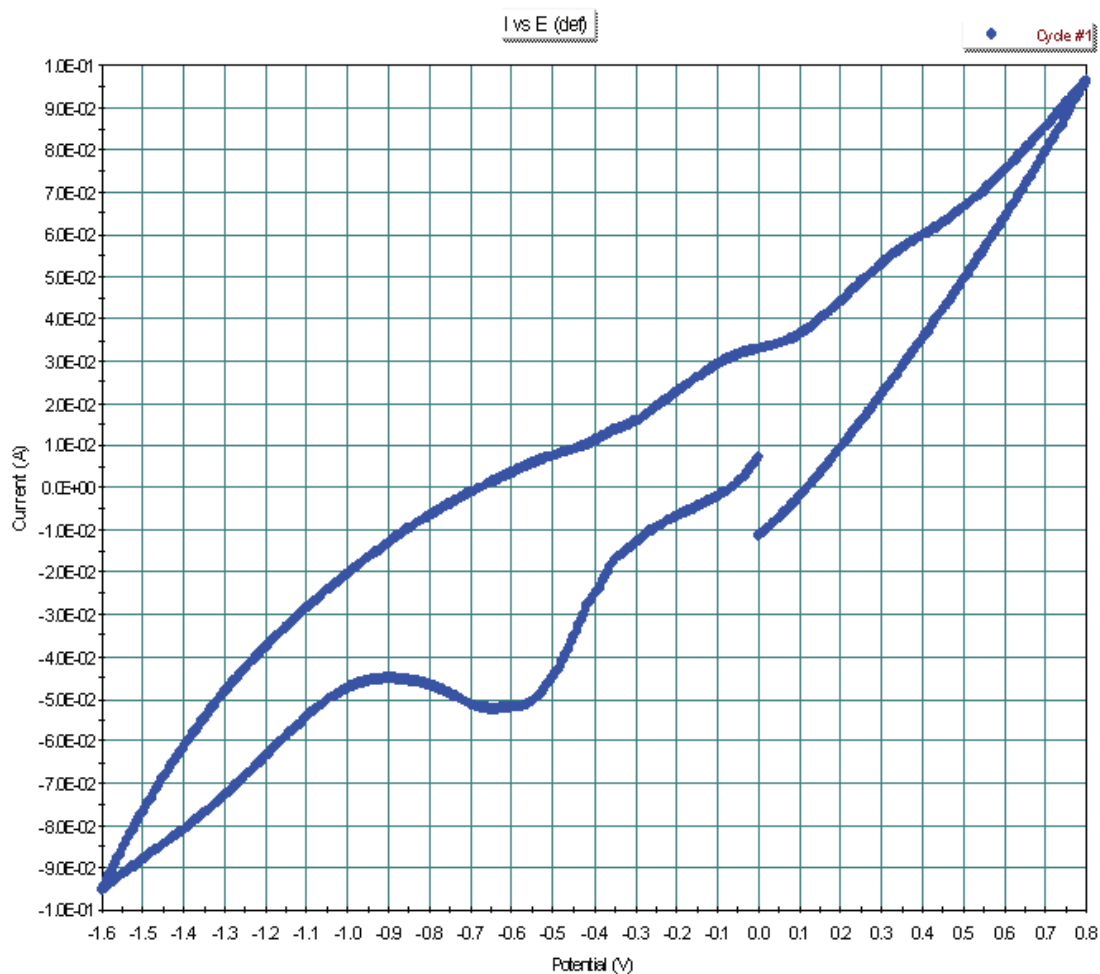
## 3. Results

### 3.1. Electrochemical deposition of ruthenium

The electrochemical deposition of ruthenium from the $Ru(NO)(NO_3)_3 + NH_4Cl + NH_4OH/H_2O$ solution proved to be much more difficult than the deposition of palladium from this ammonia system. This was likely due to the multiple of oxidation states for ruthenium. The $NH_4Cl + Ru(NO)(NO_3)_3$ dissolved readily in $H_2O$ to form a dark red solution with pH = 2.53. This acidic ruthenium solution was stable towards displacement reactions for all metals that were tested (Cu, Ni, Co, Al, Ta, Mo, Hf, Ag and Pt). Therefore, metal ion impurities due to chemical reactions should not be a concern in these ruthenium solutions. The addition of 0.15 M $NH_4OH$ did not produce the expected precipitate, thus the $NH_4OH$ concentration was increased to 0.45 M. The solution remained dark red and gave no precipitate with the pH = 9.67. The intense red color of the ruthenium solution remained unchanged during extensive electrolysis at constant currents of 6, 10, 20 and 100 mA. Finally, at a constant current of 400 mA, the ruthenium solution became completely clear overnight with a robust deposit of black ruthenium metal covering the copper cathode. The measured pH of the solution also decreased to pH = 2.02. This is similar to the pH effects observed for palladium co-deposition [6]. The acidic solution produced (pH = 2.02) is due to the cell reaction

$$2Ru^{+++} + 3H_2O \rightarrow 2Ru + 3/2O_2 + 6H^+, \tag{1}$$

where each $Ru^{+++}$ ion deposited is replaced by three hydrogen ions to maintain charge neutrality. Furthermore, the electrolysis gases at high currents drive off the ammonia. There was no detection of chlorine evolution or the related formation of nitrogen trichloride, $NCl_3$, as previously observed for palladium deposition in this ammonia electrolyte [5,6]. However, this $Cl_2/NCl_3$ phase may have been passed through quickly overnight at 400 mA. Based on the initial $Ru^{+++}$ concentration in $H_2O$ (0.02158 M), the expected final pH would be 1.19. The higher measured pH = 2.02 could
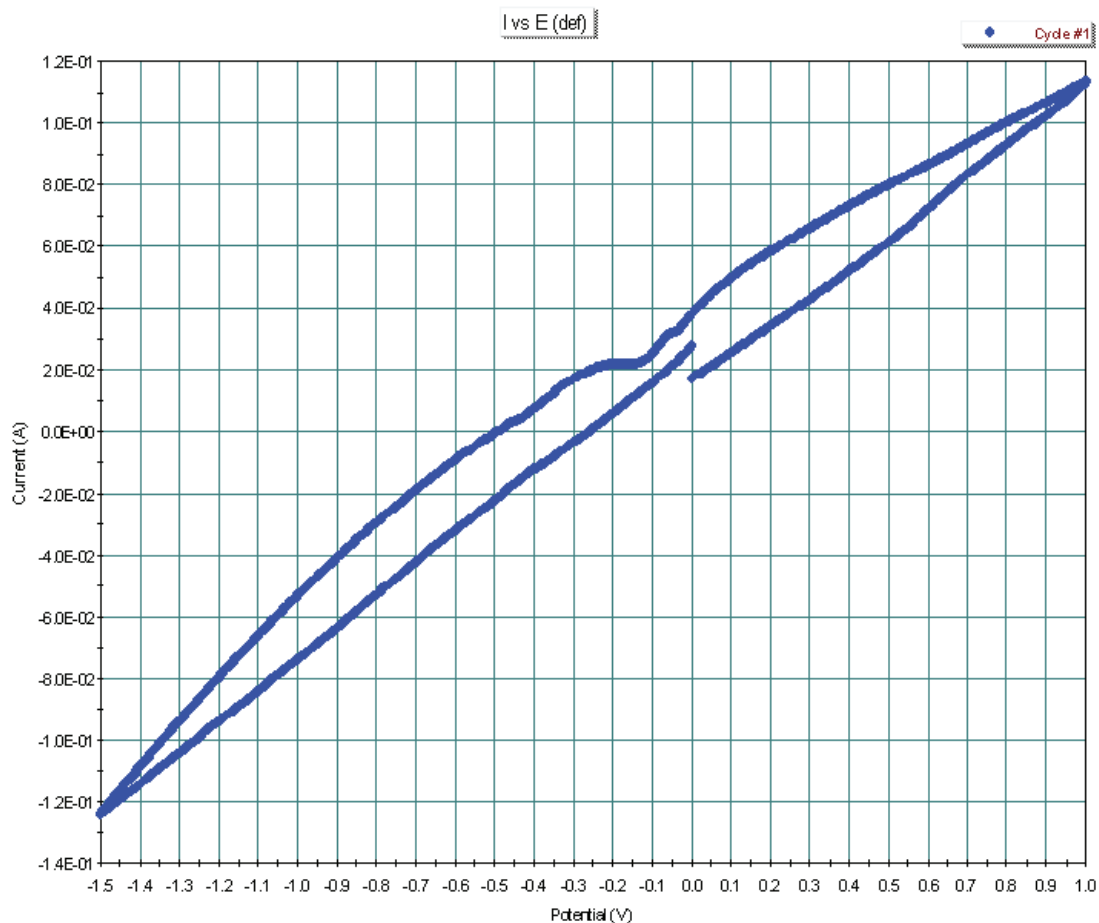
**Figure 1.**    Cyclic voltammetric study prior to the completed ruthenium deposition. The potential sweep rate was 50 mV/s.

be due to some chlorine evolution. Another possibility is the oxidation of small amounts of ruthenium ions to form the volatile and toxic $RuO_4$ that may exit the cell.

### 3.2. Electrochemical investigations

The cyclic voltametric study of the cathode before the completed ruthenium deposition is shown in Fig. 1. The solution was still dark red in color, but the copper cathode was completely black due to the partial ruthenium deposition. This study was made following the application of a constant current of 100 mA for 24 h. The reduction peak at $-0.63$ V may be due to the reduction of $Ru^{+++}$ ions to $Ru^{++}$ or Ru metal. The small oxidation partial peak at $-0.05$ V could be due to $Ru^{++}$ oxidation back to $Ru^{+++}$. However, this cyclic voltammogram appears to be partially tilted and collapsed
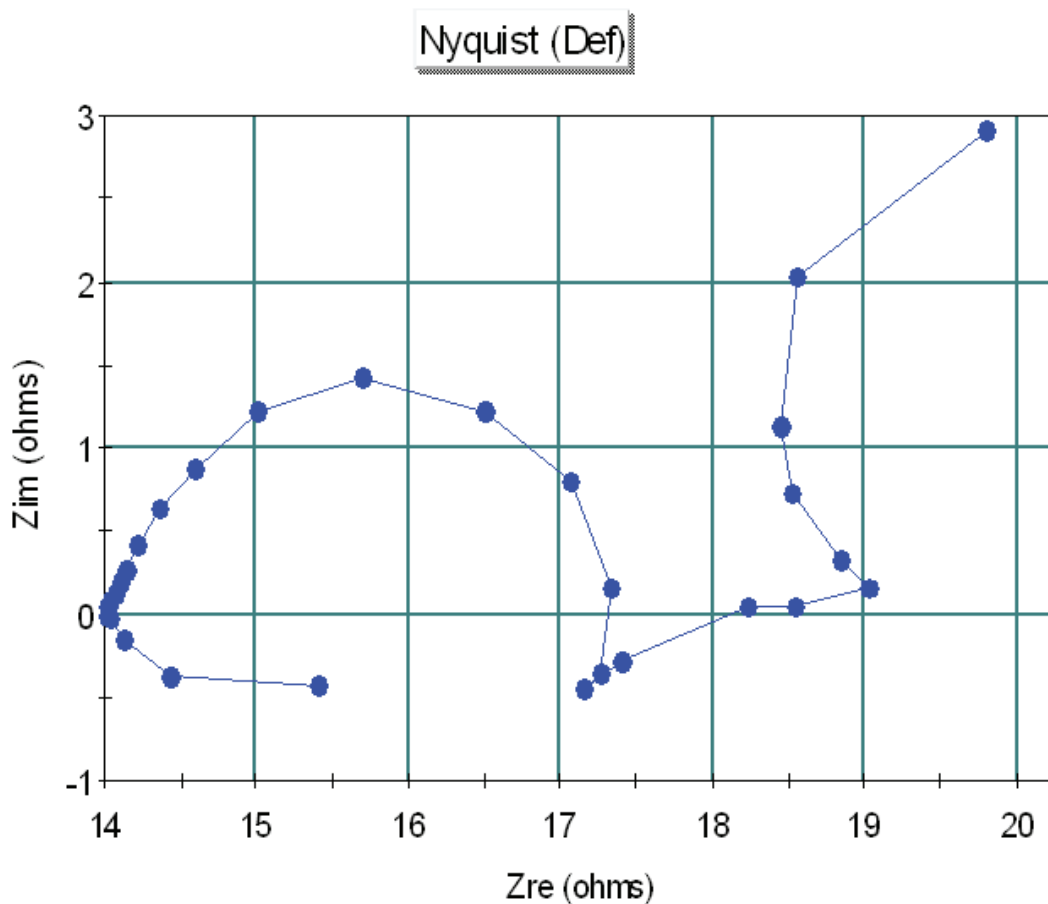
**Figure 2.**    Collapsed and tilted cyclic voltammetric trace following the complete deposition of ruthenium (50 mV/s).

towards Ohm's law behavior due to a large capacitance effect as previously reported for palladium deposition [5]. A reasonable cell resistance of 8.312 $\Omega$ can be calculated from the cell currents and voltages at the end points.

Figure 2 presents the cyclic voltammetric study following the complete deposition of ruthenium at a constant current of 400 mA. The cyclic voltammogram is now almost completely tilted and collapsed into a featureless Ohm's law behavior as found for palladium deposition [5,6]. A cell resistance of 10.52 $\Omega$ is calculated from the end points for the cell currents and voltages using Ohm's law. This result indicates a capacitance of about 1–2 F for the ruthenium cathode and a surface area of about $10^5$ cm$^2$ (Refs. [3,5]).

Figure 3 presents the Nyquist plot for an EIS study after further electrolysis at 50 mA over the weekend. A reasonable semicircle is observed followed by the beginning of a larger semicircle at lower frequencies. The EIS results suggest good electrode kinetics due to the larger surface area and also provides an accurate value of 14.25 $\Omega$ for the cell resistance. From the measured charge transfer resistance ($R_{ct}$) of 3.30 $\Omega$, an exchange current of $4 \times 10^{-3}$ A is calculated for the electrode reaction at open circuit.
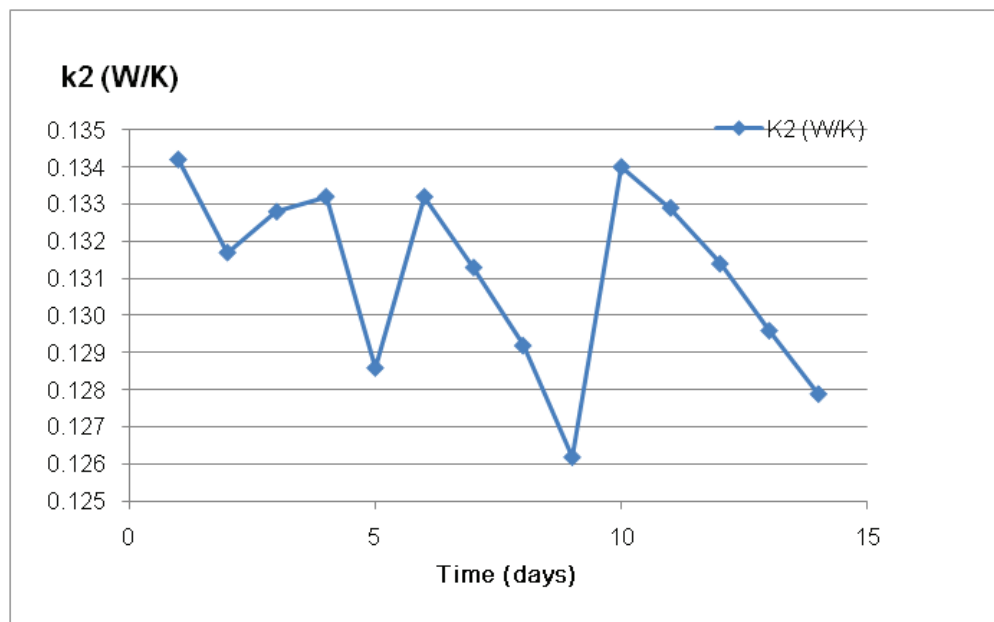
**Figure 3.** Nyquist plot for an EIS study after further electrolysis. The frequency range was from 100 kHz to 10 mHz.

### 3.3. Calorimetry

The simplest starting point for calorimetric measurements is (Refs. 8–10)

$$P_x = (k_C - k_C')\Delta T, \tag{2}$$

where $P_x$ is the excess power, $k_C$ is the true conductive heat transfer coefficient, $k_C'$ is the lower bound conductive heat transfer coefficient obtained by assuming $P_x = 0$. Obviously $k_C$ and $k_C'$ would be identical if there were actually no excess power. The advantage of this simple equation is that all other calorimetric power terms cancel in this derivation [8–10]. For the calorimeter used in this study, the true conductive heat transfer coefficient has been established as 0.1340 W/K when the electrochemical calorimetric cell is filled with 50.0 mL of electrolyte. This cell constant will decrease as the electrolyte level decreases during electrolysis.

**Figure 4.** Calorimetric lower-bound conductive heat transfer coefficient ($k_2$) versus time for the Ru/$H_2O$ experiment in the NH$_4$Cl + NH$_4$OH/$H_2O$ electrolyte.

Figure 4 presents the lower-bound conductive heat transfer coefficient ($k_2$) measured using Thermistor 2 for the Ru/$H_2O$ experiment in the ammonia (NH$_4$Cl + NH$_4$OH/$H_2O$) electrolyte.

This calorimetric study at a constant current of 300 mA shows only the expected changes of the cell constant due to changes in the electrolyte level. The peaks show where make-up $H_2O$ was added to the cell. These results are for Thermistor 2 used in the calorimeter. A second thermistor (Thermistor 4) positioned on the opposite side of the electrochemical cell provided results ($k_4$) similar to those of Fig. 4.

Figure 5 shows the lower-bound heat transfer coefficient ($k_2$) for the Ru/$D_2O$ experiment in the ND$_4$Cl + ND$_4$OD/$D_2O$ electrolyte. This cell started with an over-filled electrolyte level of about 55 mL, thus the cell constant ($k_2$) is higher at the beginning. Also, lower currents of 200 and 250 mA were used during the first few days. Nevertheless, the results in Fig. 5 are very similar to those shown in Fig. 4. Both the Ru/$H_2O$ and the Ru/$D_2O$ studies were run longer than normal between cell re-filling in order to measure the effect of the electrolyte level in these stable calorimetric experiments. Much smaller changes in $k_2$ would occur with the normal cell filling every 1 or 2 days.

As shown in Figs. 4 and 5, there are no significant differences between the Ru/$H_2O$ and the Ru/$D_2O$ experiments because neither study produced excess power. In fact, the mean calorimetric cell constants are almost identical. For Ru/$H_2O$, the mean cell constant is $\langle k_2 \rangle = 0.1318 \pm 0.0030$ W/K while $\langle k_2 \rangle = 0.1312 \pm 0.0025$ W/K for Ru/$D_2O$. These mean cell constants are less than the true value of 0.1340 W/K because the mean electrolyte level is less than the initial filled volume of 50.0 mL. The error ranges given for $\langle k_2 \rangle$ reflect the larger than normal changes in the electrolyte volume rather than actual calorimetric errors. The calorimetric stability for these ruthenium studies allowed the measurements of the effect of the electrolyte level on the cell constant, $\Delta k_2/\Delta V$. For both Ru/$H_2O$ and Ru/$D_2O$, the results were measured as $\Delta k_2/\Delta V = 0.0008 \pm 0.0001$ W/K mL.
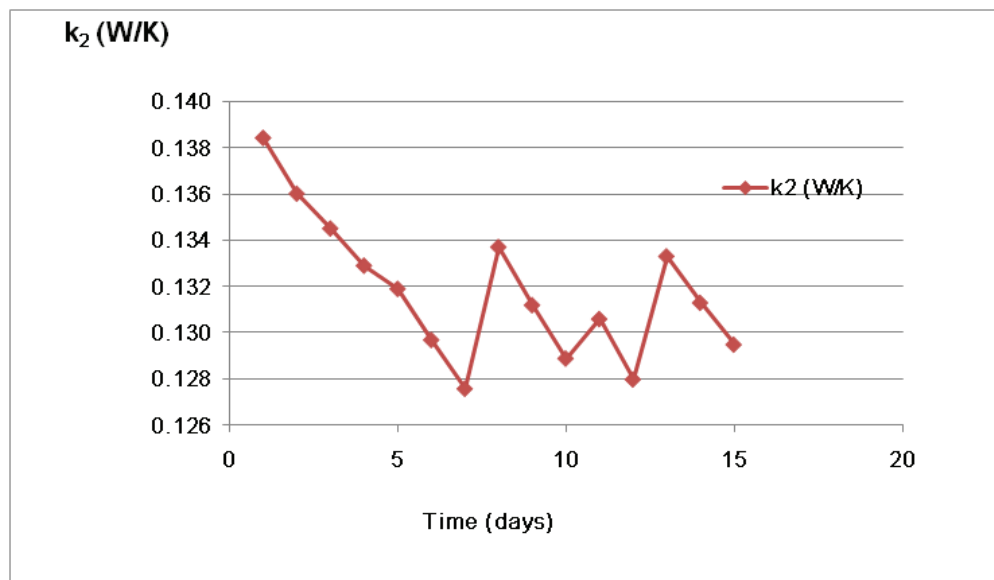
### 3.4. Consumption of $H_2O$ and $D_2O$

The $H_2O$ or $D_2O$ consumption has been measured in every co-deposition study using the ammonia system. These measured amounts are then compared with the theoretical calculations based on Faraday's law using $-9.03$ mL/F for $H_2O$ electrolysis and $-9.07$ mL/F for $D_2O$ electrolysis where $F = 96,485$ C/eq (C = A s). Previous results are presented elsewhere [6]. In these experiments, the $Ru/H_2O$ study gave a measured $H_2O$ consumption of 45.5 mL versus the theoretical value of 40.7 mL. For the $Ru/D_2O$ study, the measured consumption of $D_2O$ was 43.0 mL versus the theoretical value of 41.8 mL. The ratio of measured/theoretical is 1.12 for $Ru/H_2O$ and 1.03 for $Ru/D_2O$. This is consistent, within error limits, of previous studies [6]. Including these ruthenium results with six previous palladium studies [6] yields a mean measured/theoretical ratio of $1.083 \pm 0.099$. None of these consumption measurements suggest any significant recombination of the electrolysis gases or any significant shuttle reactions [6]. This measured/theoretical ratio is expected to be somewhat larger than unity due to $H_2O$ or $D_2O$ evaporation where the vapor exits the cell with the electrolysis gases [10]. The exact value of this ratio is largely determined by the temperature of the vapor at the glass exit tube.

## 4. Discussion

### 4.1. Ruthenium red

The difficulty of the electrochemical deposition of ruthenium and the deep red solution color is likely due to the formation of the inorganic dye "Ruthenium Red" [4]. This substance, $[(NH_3)_5–Ru-O-Ru(NH_3)_4-Ru(NH_3)_5]^{6+}$ is produced by the treatment of "$RuCl_3$" with aqueous ammonia in air [4]. These conditions were certainly present in these experiments using the ammonia and ammonium chloride electrolyte and the production of oxygen at the anode. Two Ru atoms are in the 3+ oxidation and one is in the 4+ oxidation state in this substance. High over-voltages produced by high currents are likely needed to break up this stable substance and reduced the "Ruthenium Red" ruthenium ions to the metal. This



**Figure 5.** Calorimetric lower-bound heat transfer coefficient ($k_2$) versus time for the $Ru/D_2O$ experiment in the $ND_4Cl + ND_4OD/D_2O$ electrolyte.

is very different from the palladium co-deposition system where the reduction of palladium ions occurs readily at low currents.

### 4.2. Nitrate ions

The 0.025 M $Ru(NO)(NO_3)_3$ dissolves to form 0.075 M $NO_3^-$ in $H_2O$ or $D_2O$ solutions. It has been proposed that nitrate ions may form from the $NH_4Cl + NH_4OH$ solutions and undergo shuttle reactions that give an excess power effect [5–7]. The lack of any excess power effect in these studies despite the presence of nitrate ions provides further evidence against proposed shuttle reactions in this ammonia based co-deposition systems [5,6].

### 4.3. Electrolyte level effect

The ruthenium experiments that gave the electrolyte level effect of $\Delta k_2 / \Delta V = 0.0008$ W/K mL involved the usual 50.0 mL of the heat conducting fluid (Mobile-1 oil) surrounding the glass electrochemical cell within the calorimeter [8]. This heat conducting fluid was, therefore, always above the electrolyte level in the cell. In the next experiment with rhenium, only 35.0 mL of the heat conducting fluid was added. This simple change reduced the electrolyte level effect by about a factor of four to yield 0.0002 W/K ml. Maintaining the electrolyte level above the level of the heat conducting fluid maintains a constant surface area for the main heat transfer pathway from the electrolyte across the heat conducting fluid and cell insulation to the water bath. This principle is similar to the Fleischmann–Pons Dewar cell that is silvered at the top in the region of the electrolyte level to maintain a constant surface area for radiative heat transfer [10]. When properly filled, the electrolyte level is at the mid-point of the silvered region for the Dewar cell [10]. The silvered region does not support radiative heat transfer in the Dewar cell. Similarly, the regions filled with air or electrolysis gases in this copper calorimeter are not nearly as effective as the liquid phases for heat transfer by conduction. Providing a constant surface area for heat transport is an important feature for accurate isoperibolic calorimeters.

### 4.4. Role of vacancies

Metal vacancies created in co-deposition experiments may be important for the excess power effect [11]. The creation of vacancies during the co-deposition of metals mainly requires the absorption of hydrogen or deuterium into the metal lattice to give a high H/M or D/M ratio where M represents a metal [11]. Based on this study, ruthenium produces very little absorption of H or D into the metal. Unlike palladium, the outgassing of hydrogen from ruthenium stopped abruptly when the current was switched off. This observation agrees with ruthenium studies at high hydrogen pressures (90 kbar) that gave only very small ratios of H/Ru = 0.03 [12]. Therefore, the low level of acceptability of hydrogen into the ruthenium lattice and the resulting low level of vacancies may explain why there was no measurable excess power for the Ru/D co-deposition system.

### 4.5. Preliminary results for the co-deposition of other metals

Initial studies for the co-deposition of rhenium (Re), iridium (Ir), and nickel (Ni) have been completed using the same ammonia electrolyte as used for palladium and ruthenium. No measurable excess power was detected in the calorimetric studies. The compounds used were $ReCl_3$, $IrCl_3$, NiO, and $NiCl_2 \cdot 6\,H_2O$. Low cell currents (6–10 mA) were used for Re and Ir deposition as well as for the study using NiO. However, a much larger deposition current of 200 mA was used for the $NiCl_2 \cdot 6\,H_2O$ experiment. None of these metals showed any significant hydrogen absorption based on out-gassing observations. In fact, iridium is one of the most resistive metals to hydrogen absorption with H/Ir = 0.005 even at 90 kbar (90,000 atm) hydrogen pressure at 250°C [12].

It should be noted that the complete deposition of the metal was achieved in all studies except for the iridium solution where a black precipitate remained. However, about half of the iridium was deposited onto the cathode in the usual black form. The statistical analysis of all 19 co-deposition experiments involving Pd, Ru, Re, Ni and Ir in $H_2O$ and $D_2O$ yields a probability of greater than 99.9999% that the anomalous excess power effect in these co-deposition studies requires the presence of both palladium metal and $D_2O$. The probability that these results showing excess power only for the Pd/D co-deposition systems could be due to random errors calculates to be less than one in a million.
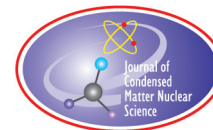
## 5. Summary

The electrochemistry and chemistry of the ruthenium co-deposition system varied markedly from the palladium system. However, the black metallic deposit, the high surface capacitance, the high electrode area produced, the $H_2O$ and $D_2O$ consumption, and the large changes in the solution pH were similar. However, no excess power was observed for the Ru/D system. This is likely due to the low level of acceptability of hydrogen or deuterium into the ruthenium metal lattice. The very stable calorimetry for the ruthenium co-deposition system permitted accurate measurements of the electrolyte level effect on the calorimetry.

## References

[1]  S. Szpak, P.A. Mosier-Boss, and M.H. Miles, Calorimetry of the Pd + D Co-Deposition, *Fusion Technol.* **36** (1999) 234.
[2]  S. Szpak, P.A. Mosier-Boss, M.H. Miles, and M. Fleischmann, Thermal behavior of polarized Pd/D electrodes prepared by co-deposition, *Thermochimica Acta* **410** (2004) 101.
[3]  M.H. Miles, T.J. Groshens, and C.E. Johnson, Examination of linear potential sweep methods in determining the capacitance of hydrous ruthenium oxide materials, in *Batteries and Supercapacitors*, edited by G.A. Nazri, E. Tekeuchi, R. Koetz and B. Scrosati, PV 2001, The Electrochemical Society Inc., Pennington, NJ, pp. 602–609 (2001).
[4]  N.N. Greenwood and A. Earnshaw, *Chemistry of the Elements*, Pergamon Press, Oxford, U.K., First Edition, pp. 1242–1274 (1984).
[5]  M.H. Miles, Investigations of co-deposition systems, *Proceedings of ICCF-15*, ENEA, Rome, Italy, 2009, pp. 33–37.
[6]  M.H. Miles, Investigations of possible shuttle reactions in co-deposition systems, *Proceedings of ICCF-16*, Chennai, India, 2011 (submitted).
[7]  D. Knies, Personal Communication (2009).
[8]  M.H. Miles and M. Fleischmann, New approaches to isoperibolic calorimetry, *ICCF-15 Proceedings*, ENEA Rome, Italy, 2009, pp. 22–26.
[9]  M.H. Miles and M. Fleischmann, Measurements of excess power effect in Pd/$D_2O$ systems using a new isoperibolic calorimeter, *J. Condensed Matter Nuclear Sci.* **4** (2011) 45–55.
[10]  M.H. Miles, M. Fleischmann, and M.A. Imam, *Calorimetric Analysis of a Heavy Water Electrolysis Experiment Using a Pd-B Cathode*", Report Number NRL/MR/6320-01-8526, Naval Research Laboratory, Washington, DC, March 26 (2001).
[11]  P. Hagelstein, *E-mail Communications*, June (2011).
[12]  V.E. Antonov, I.T. Belash, V.Yu. Malyshev, and E.G. Ponyatovsky, The Solubility of Hydrogen in the Platinum Metals Under High Pressure, *Int. J. Hydrogen Energy* **11**(3) (1986) 193.

Research Article

# Nuclear Signatures to be Expected from Rossi Energy Amplifier*

Jacques Dufour [†]

*CNAM Laboratoire des sciences nucléaires, 2 rue Conté 75003 Paris, France*

**Abstract**

The nuclear signatures that can be expected when contacting hydrogen with fine nickel powders are derived from thermal results recently obtained (Rossi energy amplifier). The initiation of the reactions (either by proton or neutron capture) is not discussed and considered as true. Proposals are made to check the process either by radiation emission measurements or by elemental analysis (ICP-MS)

© 2012 ISCMNS. All rights reserved. ISSN 2227-3123

*Keywords:* Energy production, Hydrogen, Nickel, Nuclear reaction, Radiations

## 1. Introduction:

In a recent paper [1], results are presented on vast amounts of energy (kWh) generated by contacting Hydrogen at pressures of tens of bars and temperatures round 400°C, with nickel powder (with an unspecified additive). No harmful radiations were measured, which is attributed to the presence of a lead shield absorbing $\gamma$ emission occurring during the run and to the very short period of the instable species formed during the run and decaying after shut down. The efficiency of the process is very high ($E_{out}/E_{in}$ up to 400). These levels of energy production strongly points to a nuclear origin. The proposed process [1] would be proton capture by the nickel nuclei.

The coulomb barrier problem is suggested to be solved by the strong screening of the electrons. Another solution has been proposed [2]: virtual neutrons formation, reacting with the Nickel nuclei. This solution is also proposed in [3] with a very elaborate justification.

In this paper, the capture of a neutron or a proton by a nickel nucleus is accepted as real. The consequences of these captures are analyzed (using very well documented nuclear chemistry data [4,5] and proposals are made for precise verification of the process invoked.

---

*A first version of this paper has been published in *J. Nucl. Phys.* on 6 May 2010. This improved version may slightly differ from the first one.
[†]E-mail: 3jdufour@laposte.net

**Table 1.** Neutron capture

| Ni parent isotopic composition | Ni parent nucleus | Mass parent or daughter Ni nucleus | Energy (MeV) released | Excited intermediate nucleus | Decay intermediate nucleus ground state | End s table nucleus | Natural copper isotopic composition |
|---|---|---|---|---|---|---|---|
| 0.68007 | $^{58}$Ni | 57.935346 | 8.22 | $^{59}$Co | EC, 7.5 $10^4$ y, 1.07 | $^{59}$Co | |
| | $^{59}$Ni | 58.934349 | | | | | |
| 0.26223 | $^{60}$Ni | 59.930788 | 7.04 | $^{61}$Ni* | | $^{61}$Ni | |
| 0.0114 | $^{61}$Ni | 60.931058 | 9.82 | $^{62}$Ni* | | $^{62}$Ni | |
| 0.03634 | $^{62}$Ni | 61.928346 | 6.06 | $^{63}$Ni* | $\beta^-$, 100 y, 0.066 | $^{63}$Cu | 0.6917 |
| | $^{63}$Ni | 62.929669 | | | | | |
| 0.00926 | $^{64}$Ni | 63.927968 | 5.32 | $^{65}$Ni* | $\beta^-$, 2.52 h, 2.14 | $^{65}$Cu | 0.3083 |
| | $^{65}$Ni | 64.930086 | | | | | |

## 2. The Neutron or Proton Capture by Nickel :

The reactions paths for these 2 routes finally ends up to the same stable products ($^{59}$Co, $^{61}$Ni, $^{62}$Ni, $^{63}$Cu and $^{65}$Cu) and are summarized in Tables 1 and 2.

The energy release (see Table 3) occurs mostly by de-excitation through $\gamma$ emission of the intermediate excited Ni* compound nucleus. The characteristics of this $\gamma$ emission (depending upon the levels of the excited nucleus). are very well known [4]. This represents (on average) some 8 MeV (balance after deduction of the energy required for the "virtual neutron" formation, i.e 0,782 MeV). The remaining comes from the decay of the ground states of the radioactive intermediate species formed ($^{59}$Ni, $^{63}$Ni and $^{65}$Ni). Data for intermediate radioactive species are from [5]. In the column "Decay intermediate nucleus ground state" $3^{rd}$ figure is the energy of the emitted radiation (MeV).

The energy is released in a way very similar to the neutron capture route, with a lower release from the de-excitation of the intermediate excited Cu* compounds nucleus (some 4 MeV, see Table 3). The remaining half comes from the decay of the ground states of the radioactive intermediate species formed ($^{59}$Cu, $^{59}$Ni, $^{61}$Cu and $^{62}$Cu). Data for intermediate radioactive species are from [5].

**Table 2.** Proton capture

| Ni parent isotopic composition | Ni parent nucleus | Mass of parent Ni nucleus | Mass of daughter Cu nucleus | Energy (MeV) released | Excited intermediate nucleus | Decay intermediate nucleus ground state | End s table nucleus | Natural copper isotopic composition |
|---|---|---|---|---|---|---|---|---|
| 0.68007 | $^{58}$Ni | 57.935346 | | | $^{59}$Cu* | $\beta^+$, 82s, 4.8 | $^{59}$Ni=$^{59}$Co | See note |
| | $^{59}$Ni | | 58.939503 | | | | | |
| 0.26223 | $^{58}$Ni | 59.930788 | | 4.8 | $^{59}$Cu* | $\beta^*$, 82s, 4.8 | $^{59}$Ni= $^{59}$Co | See note |
| 0.0114 | $^{60}$Ni | | 4.8 | | $^{61}$Cu* | $\beta$, 3.41 h, 2.34 | $^{61}$Ni | |
| | 59.930788 | | | | | | | |
| 0.03634 | $^{62}$Ni | 6.928346 | 61.932586 | 6.12 | $^{63}$Cu | | $^{63}$Cu | 0.6917 |
| | $^{63}$Ni | | 62.929598 | | | | | |
| 0.00926 | $^{64}$Ni | 63.927968 | | 7.45 | $^{65}$Cu | | $^{65}$Cu | 0.3083 |
| | $^{65}$Ni | | 64.927793 | | | | | |

*Note*: $^{59}$Ni from $^{59}$Cu decays to $^{59}$Co by electron capture (life time $7.5 \times 10^4$ years).

**Table 3.**  Energy released (MeV)

|  | Neutron capture | Proton capture |
|---|---|---|
| De-excitation | 7.82 | 3.94 |
| Decay | 0.02 | 3.92 |
| Total | 7.84 | 7.86 |

## 3. Evaluation of the Reaction Rates

One experiment (Type B) presented in [1] has yielded 3768 kWh for an energy input of 18.54 kWh (between March 5, 2009 and April 26, 2009). This is a net power produced of some 3 kW during a time $T$ of some $4.5 \times 10^6$ s. The rate of production of the by-products will be determined using this net produced power, according to the proton and the neutron reaction scheme. The time $T$ will be used to calculate the amount of reaction products present at the end of the experiment.

From Tables 1 and 2, the energy released per Ni atom (averaged by the isotopic composition of the Nickel) has been calculated under following hypothesis:

(1) The captures (proton or neutron) have the same probabilities whatever the Ni isotope is. This is a first approximation. For the neutron capture route, following cross sections (barn) are measured: $^{58}$Ni:4.6, $^{60}$Ni:2.9, $^{61}$Ni:2.5, $^{62}$Ni:15 and $^{64}$Ni:2.9).
(2) The subsequent reactions with formed products are not taken into account (too low concentration to have a ny significant effect).
(3) Decay energy of nucleus with half life time much longer than the experiment duration have been ignored ($^{59}$Ni for the proton route and $^{59}$Ni, $^{63}$Ni for the neutron route).

Table 3 is thus obtained.

As expected, the two routes give similar amounts of energy, mainly de-excitation for the neutron route and half de-excitation, half decay for the proton route.

The proton or neutron capture rate can thus be evaluated as

$$r = \frac{3000}{7.85 \times 1.6 \times 10^{-13}} = 2.4 \times 10^{15} \text{ s}^{-1}$$

for both routes

## 4. Evaluation of the $\gamma$ Emission Rates

The de-excitation of a compound nucleus resulting from neutron capture is very well documented [4]. For nickel, one capture gives rise to 2.66 emission of $\gamma$ photon, with an energy repartition $f_i$ given in Table 4.

For the proton capture route, less data are available. To get a first order of magnitude of the $\gamma$ emission coming from the de-excitation of the primary nucleus formed, the same number of photons per proton capture with the same energy repartition as for the nickel has been taken into account, with of course an average value half the one for nickel (1.79 MeV compared to 3.58). The second half of the energy comes (in the form of $\gamma$ photons) from the short live $\beta+$ emitters: associated $\gamma$ emission, bremsstrahlung of the positron and annihilation radiation. The average energy of these photons is taken to be in the 0.75 MeV range, thus less penetrating. The energy repartitions $f_i'$ (Table 5) have been evaluated according to the photon production rate in the proton capture route given below.

**Table 4.** Neutron capture

| $\gamma$-Energy (MeV) | Repartition ($f_i$) | Absorption coefficient, $\mu$ (cm$^{-1}$) |
|---|---|---|
| 0.5 | 0.32 | 0.578 |
| 1.5 | 0.15 | 0.045 |
| 2.5 | 0.09 | 0.0229 |
| 4 | 0.09 | 0.024 |
| 6 | 0.13 | 0.0398 |
| 8 | 0.22 | 0.079 |
| Mean value | 3.58 | 1.0 |

Finally, the $\gamma$ photon production rate $r_\gamma$ for both routes has been evaluated as follows:

(a) Neutron capture route $(r_\gamma)_N = 2.66r$

(b) Proton capture route $(r_\gamma)_p = 2.66r \left(0.5 + \frac{0.5 \times (E_\gamma)_{\beta+}}{2.66 \times 0.75}\right) = 2.66r(0.5 + 0.9825)$

$(E_\gamma)_{\beta+}$ being the mean energy released by $\beta+$ emissions (3.92 MeV).

## 5. Effect of Lead Shielding on Expected $\gamma$ Emission

For a poly-energetic beam of photons, the attenuation $l/l_0$, resulting from a thickness $d$ of lead, is

$$l/l_0 = \sum_i f_i \exp(-d\mu_i)$$

is the fraction of the beam of energy $E_i$ and $\mu_i$ $f_i$ the absorption coefficient for photons of energy $E_i$ (cm$^{-1}$) and $d$ (cm).

In [6], the quantity $\mu/\rho$ (cm$^2$/g) is given for photon energies from 1 eV to 20 MeV. This gives for lead ($\rho = 11.34$ g/cm$^{-3}$), the absorptions coefficients $\mu_i$ (Tables 4 and 5).

Finally, following relations were used to evaluate the attenuation of the beam for increasing values of

**Table 5.** Proton capture

| $\gamma$-Energy (MeV) | Repartition ($f_i'$) | Absorption coefficient, $\mu$ (cm$^{-1}$) |
|---|---|---|
| 0.25 | 0.18 | 1.136 |
| 0.75 | 0.51 | 0.139 |
| 1.25 | 0.05 | 0.058 |
| 2 | 0.05 | 0.045 |
| 3 | 0.07 | 0.061 |
| 4 | 0.14 | 1.111 |
| Mean value | 1.79 | 1.0 |

$d$ ( $f_i$ from Table 5)

$$\text{Neutron capture route} \qquad \frac{l}{l_0} = \sum_i f_i \exp(-\mu_i d),$$

$$\text{Proton capture route} \qquad \frac{l}{l_0} = \sum_i f_i \exp(-\mu_i d).$$

As expected, the lead shielding is more efficient in the proton capture route. Even in that case and for 40 cm of lead, the transmitted activity is still $10^6$ s$^{-1}$. The corresponding value is $3 \times 10^{10}$ s$^{-1}$ in the neutron capture route.

An important point must be stressed: in the above calculation, the emitting nuclear source is considered to be concentrated in one single point, which is of course not the case. To get a realistic evaluation of the expected flux of photons, it is supposed that the Nickel powder is contained in a cylindrical reactor, diameter 2 cm and length 100 cm (outer surface 628 cm$^2$). At 1 m from this tube, shielded by 40 cm of lead, the photons flux (number of particles emitted in the solid angle under which the source is seen from the point where the flux is evaluated), is thus $\approx 1$ s$^{-1}$cm$^{-2}$ for proton capture and $\approx 5 \times 10^3$ s$^{-1}$cm$^{-2}$ for neutron capture.

## 6. Final Products and Residual Activity after Shut Down

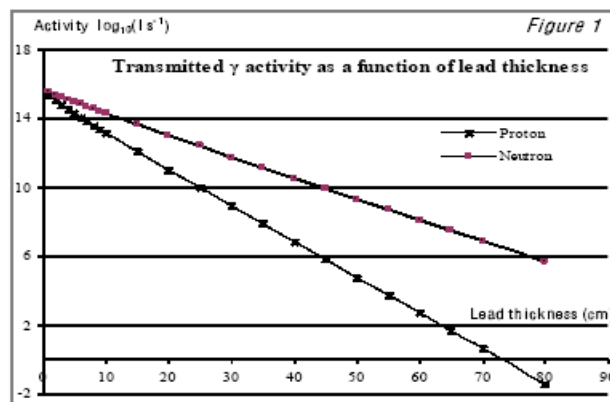The number of stable atoms $i$ formed at the end of the experiment (time $T$) is

$$N_i(T) = r_i T = r x_i T.$$

For radioactive atoms with a disintegration constant $\lambda_i$, the number of atoms formed at $T$ is

$$N_i(T) = \frac{r x_i}{\lambda_i}(1 - e^{-\lambda_i T})$$

For short life atoms ($^{59,61 \text{ and } 62}$Cu-proton capture- $^{65}$Ni-neutron capture-), the asymptotic limit is reached well before $T$ and the number of atoms at $T$ is

$$N_i(T) = \frac{r x_i}{\lambda_i}.$$



**Figure 1.** Gives the transmitted $\gamma$ activity (as $\log_1 0(I.s^{-1})$), as a function of the lead thickness $d$.

For long life atoms ($^{59 \text{ and } 63}$Ni-neutron capture and $^{59}$Ni-proton capture), the final product at T can be considered to be $^{59 \text{ and } 63}$Ni on the one hand and $^{59}$Ni on the other.

Tables 6 and 7 summarize the various atoms formed at the experiment shut-down.

The figures indicated in the last column of Tables 6 and 7 are for an energy production of 3 kW during time $T$ (see Section 3).

## 7. Residual Activity after Shut Down

For both routes, short live species are formed: $^{65}$Ni for neutron capture and $^{59,61}$ and $^{62}$Cu for proton capture (see Tables 1,2,6 and 7). Their concentrations at shut down Ni(T) are given in Tables 6 and 7. The number of short live species decreases as $N_i(t) = N_i(T)e^{\lambda_i t}$ ($t = 0$ at shutdown) and their residual activity decreases exponentially with time $t$ after shut down as

$$\frac{dN_i(t)}{dt} = -\lambda_i N_i(T)e^{\lambda_i t} (s^{-1}).$$

Table 8 gives Ni(T) at shutdown (after duration $T$ of the experiment) and the remaining atoms at $t = 7200$ s (2 h after shut down) $N(7200) = N_i(T)e^{-7200O\lambda_i}$ and hence the zero residual activity at that time

$$\frac{dN_i(7200)}{dt} = -\lambda_i N_i(7200) (s^{-1}).$$

The numerical value is given for $t = 7200$ s, this value providing sufficient time to dismantle the experiment after shut-down.

Tables 8 and 9 give the residual activity 2 hours after shutdown. The energy of the main characteristic gammas are given in keV and the branching ratios in % (between brackets).

It can be seen from Table 8 (neutron capture), that 2 h after shutdown, the activity of $^{65}$Ni is still $1.3 \times 10^{13}$ s$^{-1}$. For proton capture (Table 9) the corresponding activity of $^{61}$Cu is still $4.2 \times 10^{14}$ s$^{-1}$.

As for the emission during the run, the emitting nuclear source is considered to be concentrated in one single point, which is of course not the case. If, as supposed previously, the Nickel powder is contained in a cylindrical reactor, diameter 2 cm and length 100 cm, the total weight of nickel is some 1260 g (apparent density 4, volume 300 cm$^3$). If 3 cm$^3$ of the powder is placed against a germanium detector, the activity would be reduced to some $10^{11}/10^{12}$ s$^{-1}$ and characteristic radiations could be measured (annihilation radiation for $^{61}$Cu and characteristic gammas (see Table 8) for $^{65}$Ni). Note that if the actual mass of nickel used is m, all results indicated in Tables 6–9 are to be multiplied by m/1260)

**Table 6.** Neutron capture

| Ni parent composition ($X_i$) | Intermediate ground state nucleus | Disintegration constant $\lambda (s^{-1})$ | Intermediate ground state atoms at $T$ | First (or final) daughter nucleus | Stable atoms formed at $T$ ($^{59}$Ni and $^{63}$Ni are "quasi-stable": they decay slowly to $^{59}$Co and $^{63}$Cu) | |
|---|---|---|---|---|---|---|
| 0.68007 | $^{59}$Ni | $2.90 \times 10^{-13}$ | $7.32 \times 10^{21}$ | $^{59}$Co | $^{59}$Ni | $7.32 \times 10^{21}$ |
| 0.26223 | $^{61}$Ni | | | | $^{61}$Ni | $2.82 \times 10^{21}$ |
| 0.0114 | $^{62}$Ni | | | | $^{62}$Ni | $1.23 \times 10^{20}$ |
| 0.03634 | $^{63}$Ni | $2.20 \times 10^{-11}$ | $3.91 \times 10^{20}$ | $^{63}$Cu | $^{63}$Ni | $3.91 \times 10^{20}$ |
| 0.00926 | $^{65}$Ni | $7.64 \times 10^{-5}$ | $2.90 \times 10^{17}$ | $^{65}$Cu | $^{65}$Cu | $9.97 \times 10^{19}$ |

**Table 7.** Neutron capture

| Ni parent composition ($X_i$) | Intermediate ground state nucleus | Disintegration constant $\lambda(s^{-1})$ | Intermediate ground state atoms at $T$ | First (or final) daughter nucleus | Stable atoms formed at $T$ ($^{59}$Ni and $^{63}$Ni are "quasi-stable": they decay slowly to $^{59}$Co) | |
|---|---|---|---|---|---|---|
| 0.68007 | $^{59}$Cu | $8.45 \times 10^{-3}$ | $1.93 \times 10^{17}$ | $^{59}$Ni | $^{59}$Ni | $7.30 \times 10^{21}$ |
| 0.26223 | $^{61}$Cu | $5.65 \times 10^{-5}$ | $1.11 \times 10^{19}$ | $^{61}$Ni | $^{61}$Ni | $2.82 \times 10^{21}$ |
| 0.0114 | $^{62}$Cu | $1.19 \times 10^{-3}$ | $2.3 \times 10^{16}$ | | $^{62}$Ni | $1.22 \times 10^{20}$ |
| 0.03634 | $^{63}$Cu | | | | $^{63}$Cu | $3.90 \times 10^{20}$ |
| 0.00926 | $^{65}$Cu | | | | $^{65}$Cu | $9.94 \times 10^{19}$ |

## 8. Transmuted Products Formed

If the total amount of nickel supposed to be processed is some 1260 g, corresponding to 21.7 mol or $1.30 \times 10^{25}$ atoms, a tentative mass balance can be made.

For both routes, the isotopic composition of the Nickel is not significantly altered. For both routes, a sizeable amount of "quasi-stable" $^{59}$Ni is produced, that represent more than 500 ppm atoms of the starting nickel. This is far beyond the precision of Mass spectrometry and could thus be easily detected. In the neutron capture route, "quasi-stable" $^{63}$Ni could also be detected (50 ppm atoms).

As regards the isotopic ratio of copper $^{63}$Cu/$^{65}$Cu $= 2.244$, it should increase in the proton capture route (the copper produced has a ratio of 3.92). It should decrease in the neutron capture route (no $^{63}$Cu is produced). The copper produced represents some 7 ppm atoms in the neutron route and some 37 ppm atom in the proton route. Starting from Nickel powder containing around 1 ppm Copper should give reliable indications of the process.

## 9. Conclusion

Strong nuclear signatures are expected from the Rossi energy amplifier and it is hoped that this paper can help detect them.

It is of interest to note that in [3] a mechanism is proposed, that strongly suppresses the gamma emission during the run (it is the same mechanism that creates very low energy neutrons, subsequently captured by the nickel. This does not suppress the emission after shut-down, which should be observed, together with the transmutations described above.
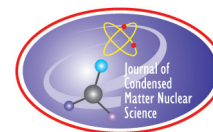
**Table 8.** Neutron capture

| Ni parent composition ($X_i$) | Intermediate ground state nucleus | Disintegration constant $\lambda(s^{-1})$ | Ni($T$)(atoms) | Ni(7200)(atoms) | Acivity after 2 h $dNi/dt$ ($s^{-1}$) | Main gamma photons (keV) (%) |
|---|---|---|---|---|---|---|
| 0.68007 | $^{59}$Cu | $8.45 \times 10^{-3}$ | $1.93 \times 10^{17}$ | $7.13 \times 10^{-10}$ | $6.03 \times 10^{-12}$ | 511, (196) |
| 0.26223 | $^{61}$Cu | $5.65 \times 10^{-5}$ | $1.11 \times 10^{19}$ | $7.41 \times 10^{18}$ | $4.19 \times 10^{14}$ | 511, (122) |
| 0.0114 | $^{62}$Cu | $1.19 \times 10^{-3}$ | $2.3 \times 10^{16}$ | $4.46 \times 10^{12}$ | $5.3 \times 10^{9}$ | 511, (196) |
| 0.03634 | $^{63}$Cu | | | | | |
| 0.00926 | $^{65}$Cu | | | | | |

**Table 9.** Proton capture

| Ni parent composition ($X_i$) | Intermediate ground state nucleus | Disintegration constant $\lambda(s^{-1})$ | Ni($T$)(atoms) | Ni(7200)(atoms) | Acivity after 2 h d$Ni$/d$t$ ($s^{-1}$) | Main gamma photons (keV) (%) |
|---|---|---|---|---|---|---|
| 0.68007 | $^{59}$Cu | $8.45 \times 10^{-3}$ | $1.93 \times 10^{17}$ | $7.13 \times 10^{-10}$ | $6.03 \times 10^{-12}$ | 511, (196) |
| 0.26223 | $^{61}$Cu | $5.65 \times 10^{-5}$ | $1.11 \times 10^{19}$ | $7.41 \times 10^{18}$ | $4.19 \times 10^{14}$ | 511, (122) |
| 0.0114 | $^{62}$Cu | $1.19 \times 10^{-3}$ | $2.3 \times 10^{16}$ | $4.46 \times 10^{12}$ | $5.3 \times 10^{9}$ | 511, (196) |
| 0.03634 | $^{63}$Cu | | | | | |
| 0.00926 | $^{65}$Cu | | | | | |

## References

[1] S. Focardi and A. Rossi, A new energy source from nuclear fusion, *J. Nucl. Phys.*, http://www.journal-of-nuclear-physics.com, February 28 2010

[2] L. Daddi, Virtual neutrons in orbital capture and neutron synthesis, *J.Nucl. Phys.* http://www.journal-of-nuclear-physics.com, March 18 2010

[3] Widom Larsen, Theoretical Standard Model rates of proton to neutron conversions near metallic hydride surfaces, *New Energy time Widom-Larsen portal*.

[4] A. Bauer, Protection contre les rayonnements, Commissariat à l'énergie atomique ISBN 2-7272-0102-8.

[5] IAEA. ENSDF. Nuclear data service, 2009. http://www-nds.iaea.org/.

[6] -NISTX-Ray-Mass-attenuation-Coefficients-Lead
http://physics.nist.gov/PhysRefData/XrayMassCoef/ElemTab/z82.html

Research Article

# New analysis of MIT Calorimetric Errors

## M.H. Miles*

*Dixie State College, St. George, UT 84770, USA*

## P.L. Hagelstein

*Research Laboratory of Electronics, MIT, Cambridge, MA 02139, USA*

### Abstract

Accurate isoperibolic calorimetry requires a well-defined heat transfer pathway from the calorimetric cell to a constant temperature water bath. The MIT isoperibolic calorimetric results published in 1990 had a major impact in convincing scientists, as well as US Patent officials, that the anomalous excess enthalpy reported in 1989 by Fleischmann and Pons in Pd/D systems was due to various calorimetric errors. Additional information about the MIT calorimetry has allowed a more detailed analysis. The major new finding is that the walls of the MIT calorimetric cell were so well insulated with glass wool (2.55 cm thickness) that the major heat transfer pathway was out of the cell top into the room air rather from the cell into the constant temperature water bath. This helps to explain the reported sensitivity of 40 mW for the MIT calorimetry versus the sensitivity of 0.1 mW achieved for the Fleischmann–Pons Dewar calorimetry. The evaluation of calorimetric designs, accuracy of temperature measurements, electrolyte level effects, calorimetric equations, and data analysis methods leads to the clear conclusion that the Fleischmann–Pons calorimetry was far superior to that of MIT. Therefore, the results of the MIT calorimetry cannot be used as a refutation of the Fleischmann–Pons experiments.
© 2012 ISCMNS. All rights reserved. ISSN 2227-3123

*Keywords:* Accuracy, Heat, Insulation, Temperature, Work

## 1. Introduction

The calorimetric results of MIT [1], Caltech [2], and Harwell [3] reported in 1989–1990 had a major impact in convincing most scientists that the anomalous excess enthalpy reported by Fleischmann and Pons [4,5] in Pd/D electrolysis systems was due to calorimetric errors. However, there were major errors in the Caltech, Harwell and MIT calorimetry that have been documented in a previous publication [6]. Critical experimental data was lacking in the initial MIT publication [1] that was later provided in a MIT report [7]. This additional information has allowed a more detailed analysis of the MIT calorimetry. The need for a new analysis of the MIT calorimetry even after 20 years was illustrated by a last minute book cancellation in 2010 by the American Institute of Physics (AIP) because someone apparently did not like the subject matter [8]. Furthermore, the US Patent office continues to block applications that mention the word cold

---

*E-mail: melmiles1@juno.com

fusion. Finally, the scientific journal access for Low Energy Nuclear Reactions (LENR) or cold fusion remains severely limited by the editors of refereed publications. This is all a lingering effect from the 1989 to 1990 reports from MIT, Caltech, and Harwell. A previous study concluded that the MIT calorimetric methodology was flawed and that this flawed MIT publication may be the single most widely quoted work used by the critics of cold fusion to dismiss the phenomena [9].

## 2. MIT Calorimetric Errors

### 2.1. Thick glass wool insulation

The major MIT calorimetric error is that the walls of the calorimeter were so well insulated with glass wool (2.55 cm thickness) that the major heat transport pathway was out of the cell top into the room temperature air rather than from the cell into the constant temperature water bath. The walls of any heat conduction calorimetric cell could be insulated to the point that almost all heat flow would be out of the cell top. Design calculations should be made prior to the calorimetric cell construction to determine the optimum amount of insulation to be used.

The dimensions of the MIT calorimeter were 7.60 cm in diameter and 15 cm in length while the glass cell had a diameter of 2.50 cm [1,7]. This leaves a space of 2.55 cm thickness that was filled with the glass wool insulation. For the radial heat flow from the cell, across the insulation, to the water bath, it can be shown [10] in terms of power ($P$) that

$$P = 2\pi k_i L(T_a - T_b)/\ln(r_b/r_a) = k_{\text{wall}}(T_c - T_b), \tag{1}$$

where $k_i$ is the thermal conductivity of the glass wool ($0.040 \text{ Wm}^{-1}\text{K}^{-1}$), $L$ the length (0.15 m), $r_b$ the radius of the calorimeter (3.80 cm), $r_a$ the radius of the glass cell (1.25 cm), $T_a = T_c$ the temperature inside the glass cell, and $T_b$ is the temperature of the water bath. Therefore, the conductive heat transfer coefficient for the cell wall [7] is

$$k_{\text{wall}} = 2\pi k_i L/\ln(r_b/r_a) = 0.034 \text{ W/K}. \tag{2}$$

Based on the MIT experimental data reported [1,7] $T_c = 46.0°C$, $T_c - T_b = 20.0°C$, and $P = 1.76$ W, thus the cell wall transports only 0.68 W of power under these conditions

$$P = k_{\text{wall}}\Delta T = (0.034 \text{ W/K})(20 \text{ K}) = 0.68 \text{ W} \tag{3}$$

and only 39% of the total power (1.76 W) can be transferred across the cell wall due to the thick glass wool insulation. The MIT cell schematic shows about the same thickness of glass wool at the cell bottom, hence only about 0.06 W of power can be transferred across the cell bottom. The remainder of the power (1.76 W–0.68 W–0.06 W = 1.02 W) must be transferred across the cell top to the room temperature air. In summary, only 39% of the power for the MIT calorimeter is transferred across the cell wall to the water bath while 58% of the cell power is transferred across the cell top to the room temperature air. The remainder (3%) is transferred across the cell bottom. This undesirable result is due to the use of too much glass wool insulation.

Individual heat transfer coefficients can be calculated for the heat transfer across the cell top, across the cell walls, and across the cell bottom. Thus $k_{\text{top}} = 0.051$ W/K, $k_{\text{wall}} = 0.034$ W/K, and $k_{\text{bottom}} = 0.003$ W/K. The sum of these three pathways gives the total heat transfer coefficient for the MIT calorimetric cell as $k_{\text{total}} = 0.088$ W/K. This rather low value reflects the effect of the thick glass wool insulation that was used.

The use of a glass wool thickness of about 0.5 cm instead of the 2.55 cm thickness would have given much better results for the MIT calorimeter. This would have allowed a much higher percentage of the heat transfer to occur across the cell walls to the constant temperature water bath. For this 0.5 cm thickness of glass wool, $k_{\text{wall}}$ would increase to 0.112 W/K and allow most of the cell power to be transported across the cell walls to the constant temperature water bath.

From the reported cell voltages and currents used in the MIT experiment, the electrochemical input power ($P_{EI}$) was only about 0.26 W. This means that about 1.50 W of heat power ($P_H$) was required to maintain a cell temperature of 46.0°C. It is unusual to use a cell heater power that is significantly larger than the applied electrochemical power, and this would make the detection of any excess power more difficult. For example, excess power is often only 10–20% of the input electrochemical power. The normally expected excess power would, therefore, be in the range of 26–52 mW. Considering the calorimetric error for the MIT system, such small excess power effects would have been difficult to detect. The small electrochemical input power of 0.26 W in the MIT experiments is due to the use of 0.25 M LiOD [1] rather than 0.10 M LiOD as in the Fleischmann–Pons experiments.

## 2.2. Room-temperature variations

Because most of the heat transfer is out of the cell top in the MIT calorimeter, the effect of room temperature variations will be greatly magnified. From the reported room temperature variations of $\pm 2$°C (Ref. 7), this error can be calculated as

$$\Delta P = k_{\text{top}} \Delta T = (0.051 \text{ W/K})(\pm 2\text{K}) = \pm 0.102 \text{ W}. \tag{4}$$

The MIT analysis of errors caused by room temperature variations gives a smaller error of $\pm 0.044$ W [7]. A simple method to minimize this error would be the use of less insulation for the cell walls to allow greater heat flow into the water bath. Furthermore, insulation could be added at the cell top to block the heat transfer to the room. In addition, accurate isoperibolic calorimetry requires much better control of the room temperature than reported by MIT. For example, a second thermal impedance unit can be used surrounding the cell and bath with a temperature control of better than $\pm 0.2$ K. These methods have proven to be successful in other calorimetric designs [1–14].

## 2.3. Temperature measurements

The reported accuracy of temperature measurements for the MIT calorimeter was $\pm 0.1$°C[1,7]. In contrast, the accuracy of temperature measurements in the Fleischmann–Pons Dewar cells was $\pm 0.001$°C[13,15]. This accuracy required careful internal calibrations of the thermistors. The electrochemical cells behave as well-stirred tanks, and the ultimate accuracy of the calorimeter is limited by the accuracy of the temperature measurements [13,15]. Thus, the temperature measurement accuracy of the Fleischmann–Pons calorimetric cells offers a one hundred fold increase in accuracy over the MIT calorimetric cell. This is consistent with the reported sensitivity of 40 mW for the MIT calorimetry [1,7] versus the sensitivity of 0.1 mW achieved for the Fleischmann–Pons Dewar calorimetry [15,16].

Temperature measurement errors can produce large errors in the power term for the calorimetric system or cell

$$P_{\text{calor}} = C_p M \, dT_c / dt, \tag{5}$$

where $C_p M$ is the heat capacity of the calorimetric system (J/K) and $dT_c/dt$ is the rate of change (K/s) of the temperature of the cell [12,13]. From the reported size of the MIT cell [1,7] it is estimated that $C_p M = 300$ J/K, thus making a measurement every 300 s with a temperature error of $\pm 0.1$ K, could produce an error in $P_{\text{calor}}$ of (300 J/K)($\pm 0.1$ K)/300 s $= \pm 0.100$ W. In contrast, for the Fleischmann–Ponns cell with $C_p M = 450$ J/K, the temperature measurement error of $\pm 0.001$ K would produce an error in $P_{\text{calor}}$ of only $\pm 0.0015$ W. The data averaging and integration methods used by Fleischmann reduces the total error to $\pm 0.1$ mW [15,16].

## 2.4. Effect of electrolyte level

It was reported for the MIT calorimetric cell that the addition of 5.0 mL of $D_2O$ to the cell required an increase of 0.15 W in heater power to maintain the same cell temperature [7]. Therefore, the change in the conductive cell heat transfer

coefficient with change in the electrolyte volume for the MIT calorimeter can be calculated as

$$\Delta k_c / \Delta V = 0.15 \text{W}/(5.0 \text{ mL})(20 \text{ K}) = 0.0015 \text{ W/K mL} \tag{6}$$

with $T_c - T_b = 20$ K. This effect of the electrolyte level for the MIT cell is significantly larger than measured for other calorimetric cells with the same diameter. This large electrolyte level effect for the MIT cell is due to the large heat flow out of the cell top rather than to the constant temperature water bath.

Recent measurements on a calorimetric cell with the same diameter as the MIT cell (2.50 cm), but with ample insulation at the cell top has given a much smaller value of $\Delta k_c / \Delta V = 0.0002$ W/K mL [14]. The change in power per mL of electrolyte volume is given by $\Delta P = (\Delta k_c / \Delta V)(T_c - T_b)$. For the MIT calorimeter where $T_c = 46.0°$C, $T_b = 26.0°$C, $\Delta P = 0.030$ W/mL. For our calorimeter with this same cell diameter and at the same temperatures $\Delta P = 0.004$ W/mL. The Fleischmann–Pons Dewar calorimeter at the same temperatures and cell diameter yields $\Delta P = (\Delta k_r / \Delta V)(T_c^4 - T_b^4) = 0.004$ W/mL. Kelvin temperatures to the fourth power are required for Dewar cells because the main heat transfer pathway is by electromagnetic radiation as expressed by the Stefan–Boltzmann law rather than by heat conduction as in the MIT calorimeter. Thus, the large heat flow out of the top of the MIT calorimeter produces an electrolyte level effect that is 7.5 times larger than other calorimeters of the same diameter.

The heat flow out of the cell top is also affected by the change in the thermal conduction path length ($L$) with change in the liquid level [7]. This can be expressed as [7]

$$P_{\text{top}}(t) = k_j A(T_c - T_{\text{top}})/L(t), \tag{7}$$

where $k_j$ is the thermal conductivity of gases and other materials above the liquid level and $A$ is the cross sectional area. It should be obvious that insulation at the cell top to block this heat flow pathway can greatly minimize this effect. Even if the heat flow out of the cell top were completely blocked, a small electrolyte level effect will remain for electrochemical calorimetric cells. This is due to the fact that the thermal conductivity of the gas phase is always smaller than that for the liquid phase within the cell. This can be expressed as

$$k_c = k_L(V_L/V_T) + k_G(V_G/V_T), \tag{8}$$

where $k_c$ is the conductive heat transfer coefficient, $k_L$ is the contribution for the liquid phase and $k_G$ is the contribution of the gas phase. The volume of the liquid ($V_L$) and gas phases ($V_G$) can be used because their ratios to the total cell volume ($V_T$) are the same as the ratio of surface areas for all cells of the same diameter. Experimentally, it has been found that $k_G = 0.70 \, k_L$ for cells with a diameter of 2.50 cm [13,14]. From Eq. (8), we obtain

$$dk_c/dV_L = k_L/V_T - k_G/V_T = (k_L - k_G)/V_T = k_L(1 - 0.70)/V_T, \tag{9}$$

where $dV_L = -dV_G$. Because $k_L > k_G$, there will always be a non-zero value for $dk_c/dV_L$ even with zero heat flow out of the cell top. This effect, however, can be minimized by maintaining a constant surface area for the main heat transfer pathway from the cell electrolyte to the water bath. This is achieved in our present calorimeter by a secondary compartment containing a heat transfer fluid level that is always below the electrolyte level [14]. If the heat transfer fluid is always above the electrolyte level, experimental measurements yield $\Delta k_c / \Delta V = 0.0008$ W/K mL [14]. This is reduced to $\Delta k_c / \Delta V = 0.0002$ W/K mL by using a smaller amount of the heat transfer fluid such as its level is always below the electrolyte level. From Eq. 9, we calculate $dk_c/dV = 0.0006$ W/K mL for our cell where $k_L = 0.147$ W/K and $V_T = 70.0$ mL. The Fleischmann–Pons Dewar cell provides a constant radiative heat transfer area by silvering the top portion of their cell such that the electrolyte level is maintained within the silvered region [13,14]. Although the electrolyte level effect is not eliminated by these methods, it is certainly minimized. In contrast, the poor design of the MIT calorimetric cell maximizes the effect of the electrolyte level.

2.5. Missing calorimetric terms

The correct modeling of isoperibolic calorimetric systems involves eight different power terms [5,6,13–17]. These are the rate of changes of the enthalpy content of the calorimetric system ($P_{calor}$), the rate of enthalpy input due to the applied electrochemical current ($P_{EI}$), any applied heater power ($P_H$), excess power if present ($P_X$), the rate of enthalpy carried out of the cell by conduction ($P_c$) and by electromagnetic radiation ($P_R$), the rate of enthalpy transport out of the open cell due to the loss of the electrolysis gases and water vapor ($P_G$) and the rate of any work performed ($P_W$). Therefore, the first law of thermodynamics for the calorimetric system expressed as power can be stated as [16,17]

$$P_{calor} = P_{EI} + P_H + P_X + P_C + P_R + P_G + P_W, \tag{10}$$

where $P_{EI}$, $P_H$, and $P_X$ are positive terms (rate of enthalpy added to the cell) and $P_c$, $P_R$, and $P_G$ and $P_W$ are negative terms (rate of energy transported from the cell to the surroundings). The power for the thermodynamic calorimetric system is represented by $P_{calor}$ and defined by Eq. (5), thus Eq. (10) represents a differential equation. Exact expressions for each of these terms are presented elsewhere [5,6,13–16]. The expression for the rate of work done by the electrochemically generated gases ($P_W$) has not always been used [16,17], but this term is small and may often be neglected (see the Appendix).

The MIT calorimetric analysis [1] discusses the input power to the cell ($P_{EI}$), the heater power ($P_H$), the conductive thermal transport power ($P_c$) and excess power ($P_X$). There is no mention of the terms $P_{calor}$, $P_R$, $P_G$, and $P_W$. However, the missing $P_R$, $P_G$, and $P_W$ terms would likely be small considering the low cell temperature (46.0°C and rather low cell current (195 mA). If the cell temperature had been maintained exactly constant, the $P_{calor}$ term (Eq. (5)) would have been zero. However, the MIT temperature measurement error of $\pm 0.1$ K could produce a large error of $\pm 0.100$ W as discussed previously. The actual display of cell temperatures by MIT (Ref. 1, Figs. 4 and 5), shows a temperature error range of $\pm 0.25$ K for the $H_2O$ cell and a gradual increase of 0.5 K for the $D_2O$ cell. Nevertheless, the MIT calorimetric analysis [1] certainly is better than the Caltech [2] or the Harwell [5] work in correctly identifying some of the more important terms needed for isoperibolic calorimetry.

## 3. Summary

A rather large error of 40 mW was reported for the MIT calorimetry. This large error is due mainly to the thick glass wool insulation that surrounded the walls of the MIT cells. As a result, the desired heat flow pathway from the cell to the constant temperature water bath was severely blocked, thus a major portion of the heat flow was through the cell top to the room temperature air. This created a large error source due to the large room temperature variations. Other contributing sources of error were the error in temperature measurements ($\pm 0.1$ K), a large electrolyte level effect, and missing calorimetric terms in the MIT calorimetric analysis. In contrast, the Fleischmann-Pons Dewar calorimetric cells provided for a constant radiative heat transfer pathway directly from the cell to the constant temperature water bath, much more accurate temperature measurements ($\pm 0.001$ K), a minimized electrolyte level effect due to a constant radiative heat transfer surface area, and the use of all required calorimetric terms in their data analysis. In addition, extensive data averaging and numerical integration of the calorimetric data in the differential equation was used to obtain an accuracy of $\pm 0.1$ mW [13,15]. For any unbiased scientist, it should be clear that the Fleischmann–Pons calorimetry was far superior to that reported by MIT. Therefore, the MIT calorimetric results cannot be used as a refutation of the Fleischmann–Pons reports of anomalous excess energy in Pd/D systems.

## A. Appendix

A.1. Role of work in electrochemical calorimetry

The First Law of Thermodynamics is expressed in terms of energy ($U$), heat ($q$) and work ($w$) where

$$\Delta U = q + w \tag{A.1}$$

For pressure–volume ($P - V$) work done by the electrogenerated gases on the surroundings at constant pressure ($P$), $w = -P\Delta V$. From the Ideal Gas Equation, $PV = nRT$, the volume change is given by $\Delta V = \Delta nRT/P$, thus the work done by the electrolysis gases ($D_2$, $O_2$) is

$$w = -P(\Delta nRT/P) = -\Delta nRT. \tag{A.2}$$

The electrolysis of $D_2O$, $0.5\,D_2O \rightarrow 0.5\,D_2 + 0.25\,H_2$, produces 0.75 mol of $D_2$ and $O_2$ gases per Faraday (F). Therefore $\Delta n = 0.75\ It/F$, and the work done on the surroundings is given by

$$w = -0.75\ It\,RT/F. \tag{A.3}$$

In terms of power ($P_W$), this becomes

$$P_W = -0.75\ IRT/F. \tag{A.4}$$

Normally, this $P_W$ term is small and could be included in the heat transfer coefficient by the calibrations. For example, at a current of $I = 0.100$ A, and a cell temperature of 50°C (323.15 K), $P_W = -0.0021$ W. Nevertheless, there could be an error if the cell is calibrated at $I = 0.100$ A, and the current is later increased to $I = 0.500$ A to give $P_W = -0.0105$ W at 50°C. Because of such possible changes in $P_W$, this term has been included in calorimetric equations in several previous publications [16,17]. This would account for the puzzling negative enthalpy ($-436$ J/day) reported for the Pd-B experiment on Day 61 when the cell current was increased to $I = 1.000$ A [13].

The use of enthalpy ($H$) in the calorimetric equations does not eliminate the need for the $P_W$ term. Enthalpy is defined as

$$H = U + PV. \tag{A.5}$$

Thus at constant pressure, $\Delta H = \Delta U + P\Delta V$. If the only work is $P - V$ work, then $\Delta U = q$ - $P\Delta V$ and
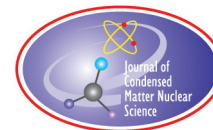
$$\Delta H = q - P\Delta V + P\Delta V = q. \tag{A.6}$$

This is the well-known thermodynamic expression that $\Delta H$ at constant pressure equals the heat, $q$. The enthalpy change for the electrolysis reaction is used in calculating the thermoneutral potential, $E_H$, given by $E_H = -\Delta H/nF$. This thermoneutral potential is used in the term for electrolysis power, $P_{EI} = (E - E_H)I$. Although the $-E_H I$ term accounts for the rate of the chemical heat energy ($q$) present in the $D_2$ and $O_2$ electrolysis gases that leave the cell at constant pressure, it does not account for the rate of the work done by these gases on the surrounding atmosphere. This power term for work is given by Eq. (A.4).

## References

[1]  D. Albagli et al., Measurements and analysis of neutron and gamma-ray emission rates, other fusion products, and power in electrochemical cells having Pd cathodes, *J. Fusion Energy*  **9** (1990) 133–148.

[2]  N.S. Lewis et al., Searches for low-temperature nuclear fusion of deuterium in palladium, *Nature* **340** (1989) 525–530.

[3]  D.E. Williams et al., Upper bounds on cold fusion in electrolysis cells, *Nature* **342** (1989) 375–384.

[4]  M. Fleischmann and S. Pons, Electrochemically induced nuclear fusion of deuterium, *J. Electroanal. Chem.* **261** (1989) 301–308.

[5]  M. Fleischmann, S. Pons, M.W. Anderson, L.J. Li, and M. Hawkins, Calorimetry of the palladium–deuterium–heavy water systems, **287** (1990) 293–348.

[6]  M.H. Miles, B.F. Bush, and D.E. Stilwell, Calorimetric principles and problems in measurements of excess power during Pd–$D_2O$ electrolysis, *J. Phys. Chem.* **98** (1994). 1948–1952

[7]  S.C. Luckhardt, Technical Appendix to D. Albagli, et al. *J. Fusion Energy* (1990), Calorimetric Error Analysis, PFC/RR-92-7, Plasma Fusion Center, MIT, Cambridge, Massachusetts 02139, pp. 1–22, May (1992).

[8]  The American Institute of Physics (AIP) book on Low Energy Nuclear Reactions (LENR) was cancelled as this book was going to press in October, 2010. The executive director of AIP, H. Frederick Dylla, was involved with this decision. The papers for this book are now scheduled to be published electronically by the *J. Condensed Matter Nuclear Sci.* **4** (2011) 45–55.

[9]  M.R. Swartz, R-Examination of a Key Cold Fusion Experiment: Phase-II Calorimetry by the MIT Plasma Fusion Center, *Fusion Facts*, p. 27, August 1992.

[10] F.W. Sears, M.W. Zemansky, and H.D. Young, University Physics, $6^{th}$ Edition, Addison-Wesley, Reading, Massachusetts, pp. 317–318 (1982).

[11] M.H. Miles and M. Fleischmann, Measurements of Excess Power Effects in Pd/$D_2O$ Systems Using a New Isoperibolic Calorimeter, American Chemical Society, New Energy Technology Symposium, Abstract No. 53, San Francisco, California, March 21 (2010).

[12] M.H. Miles and M. Fleischmann, New Approaches to Isoperibolic Calorimetry, *ICCF-15 Proceedings*, ENEA Rome, Italy, 2009 (in press).

[13] M.H. Miles, M. Fleischmann, and M.A. Imam, Calorimetric analysis of a heavy water electrolysis experiment using a Pd- alloy cathode, Naval Research Laboratory Report Number NRL/MR/6320-01-8526, Washington, DC, March 26 (2001) 1–155.

[14] M.H. Miles, Electrochemistry and calorimetry of ruthenium co-deposition, *Proceedings of ICCF-16*, Chennai, India, 2011 (submitted).

[15] M. Fleischmann and M.H. Miles, The Instrument Function of Isoperibolic Calorimeters: Excess Enthalpy Generation Due to Parasitic Reduction of Oxygen, in *Condensed Matter Nuclear Science: Proceedings of the $10^{th}$ International Conference on Cold Fusion*, Cambridge MA, August 24–29, 2003, P.L. Hagelstein and S.R. Chubb, Editors, World Scientific Publishing Co., Singapore, pp. 247–268 (2006).

[16] M.H. Miles and M. Fleischmann, Accuracy of isoperibolic calorimetry used in a cold fusion control experiment, in *Low Energy Nuclear Reactions Sourcebook*, ACS Symposium Series 998, 71, J. Marwan and S. Krivit, Editors, pp. 153–171 (2008).

[17] M.H. Miles and M. Fleischmann, Twenty year review of isoperibolic calorimetric measurements of the Fleischmann–Pons effect, ICCF-14 Proceedings, Vol. 1, Washington, DC, 2008, pp. 6–10. (See also http://www.lenr-canr.org/acrobat/MilesMisoperibol.pdf).

# Experimental Results on Excess Power, Impurity Nuclides, and X-ray Production in Experiments with a High-voltage Electric Discharge System

## A.B. Karabut[*]

*Samar+ COMPANY, Belay Dacha, 13, ap. 54, city Kotelniky, Moscow Region, 140055, Russia*

## E.A. Karabut

*Moscow Power Engineering Institute (Technical University)*

**Abstract**

We review results on low energy nuclear reaction (LENR) processes in a high-voltage (1000–4000 V) electric discharge system. The experimental results are divided into three sets: excess heat measurements; yield of impurity nuclides (nuclear ash); X-ray measurements. Up to 8 W of excess power was observed, with a power gain of up to 170% was seen in glow discharge experiments. Up to 300 W of excess power, with a power gain up to 340% was observed in experiments using a high voltage electrolysis cell. The impurity nuclide yield showing a shift of up to a few per cent from natural isotopic abundances was detected by spark mass spectrometry, by secondary ionic mass spectrometry, and by secondary neutral mass spectrometry. X-ray emission in the range of 0.6–6.0 keV, and up to 0.1 W/cm$^2$ has been observed. Based on these experimental results we propose a phenomenological model for LENR based on the interaction of an electric discharge with condensed matter (of the cathode).
© 2012 ISCMNS. All rights reserved. ISSN 2227-3123

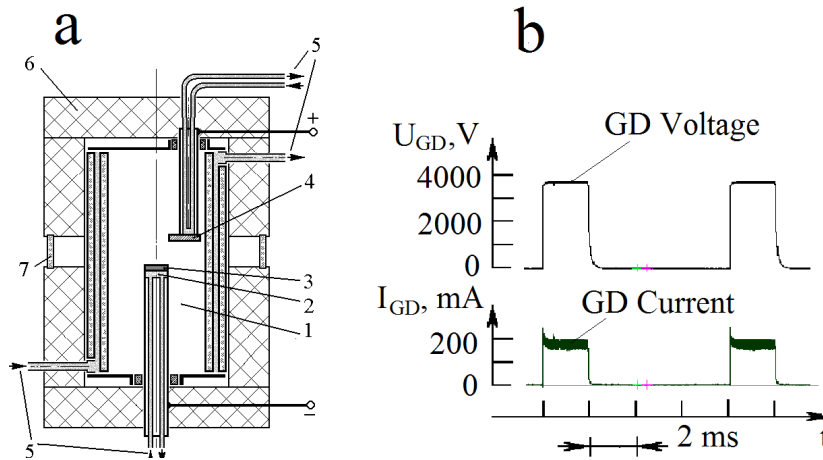*Keywords:* Electrolysis, Excess heat, Impurity nuclides

## 1. Introduction

We have identified phenomena associated with the Fleischmann–Pons effect in the solid cathode of a high-voltage electrolysis cell and a high-voltage glow discharge system; including excess heat production, transmutation, and X-ray emission. In this work we will review experimental results on excess heat production in the glow discharge system (up to 8 W, and 170% power gain), and in the electrolysis cell (up to 300 W, and 340% power gain). We also describe the results of experiments which show transmutation products. Detailed experimental results on X-ray emission are

[*]E-mail: karab.ab@mail.ru; Tel.: (495) 5508129; Fax: (495) 5508129

**Figure 1.** Schematic representation of the experiment: (a). Glow discharge device, 1 – discharge chamber, 2 – cathode holder, 3 – cathode sample, 4 – anode, 5 – cooling water; Be foil screens, 6 – heat insulation cover, 7 – windows in heat insulation cover. (b) Glow discharge voltage and current oscillograms.

discussed in another paper in this proceedings. These include the observation of collimated X-ray emission from the cathode, which is a new fundamental effect that has not been reported prior to our experiments.

Based on these observations, we have developed some theoretical ideas that may be helpful in understanding the experimental results. We propose that long-lived metastable states are generated at solid density in the cathode with excitation energies in the keV range. In the glow discharge, a flux of ions with kinetic energies on the order of 500 eV to 2 keV is incident on the cathode; the appearance of X-rays in the 600 eV to 6 keV range implies that there is a physical mechanism capable of converting the incident ion energy into long-lived (up to tens of millisecond long) excitation of the electronic-nuclear system of the cathode. We observe characteristic X-ray emission of the cathode elements, suggesting that L and M excitation occurs in the cathode. Observations of excess power and transmutation products indicates that nuclear reactions occur, and it may be that these reactions occur as a consequence of the high effective temperature that might be associated with the strongly non-equilibrium conditions implied by the long-lived highly excited states. We propose that such reactions are responsible for LENR effects in our experiments.

## 2. Excess Power Measurements in Glow Discharge Experiments

The measurements were carried out using a glow discharge [5] consisting of a water-cooled vacuum chamber, cathode and anode assemblies as shown in Fig. 1(a). The cathode holder can accept cathodes made of different metals, and the discharge occurs between the cathode and anode in the low pressure gas inside the chamber. Periodic pulses are supplied by a high-voltage power source. We used flow calorimetry, with independent water cooling channels supplied to the cathode, the anode, and to the chamber. Each cooling channel included two thermal sensors differently turned on at the input and output and a cooling water flow meter. The excess power parameters (determined from input from the temperature sensors and the flow-meter), and the electric parameters (the glow discharge current and voltage), were

recorded using a data acquisition board. The excess power $P_{xs}$ was determined as the difference between the output thermal power and input electrical power.

The discharge current and voltage was measured with a two-channel data acquisition board. The use of 8-bit analog digital oscilloscope conversion (with 50 MHz clock frequency) allowed us to achieve about 1% measurement accuracy of electric parameters. Instantaneous current and voltage values were multiplied digitally and the resulting estimate for electric power was made; with the average electric power value obtained from

$$P_{el} = \frac{1}{T} \int_T V(t) I(t) \, dt. \tag{1}$$

We used a numerical integration based on

$$P_{el} = 1 \, T \sum_i \frac{1}{2} (I_i V_i + I_{i+1} V_{i+1})(t_{i+1} - t_i). \tag{2}$$

Here $T$ (the pulse-repetition period) is set by the power supply driving generator with accuracy no less than 0.1%; $I_i V_i$ and $I_{i+1} V_{i+1}$ represent electric power values for the different times $t_i$ and $t_{i+1}$. The number of steps was determined by the condition that the electrical power must be linear over a time step.

The thermal power carried away by the anode, cathode and chamber cooling water channels, respectively, is determined by

$$\begin{aligned}
P_A &= C_w \cdot G_{WA} \cdot \Delta T_A, \\
P_C &= C_w \cdot G_{WC} \cdot \Delta T_C, \\
P_{Ch} &= C_w \cdot G_{WCh} \cdot \Delta T_{Ch}.
\end{aligned} \tag{3}$$

Here $C_w$ stands for the water specific heat; and $G_{WA}$, $G_{WC}$, and $G_{WCh}$ are the anode, cathode and chamber cooling water flow rate, respectively. The temperature differences $\Delta T_A$, $\Delta T_C$, and $\Delta T_{Ch}$ denote the difference between the anode, cathode and chamber input and output cooling water temperature readings. The water flow rate is measured by volume flow meters with $\pm 0.2\%$ relative measurement error.

The actual error of the calorimetric system was determined in tests by a resistive heater. The resistance of the calibration heater was close to the glow discharge resistance (about 5 k$\Omega$); and was characterized by its own small specific heat and adequate thermal insulation. In test experiments the heater was powered by the periodic pulse power supply (similar to the power supplied to the glow discharge). The procedure used in processing of results was the same as that used in glow discharge experimentation. In so doing the electric power of calibration heaters was defined and measured. The temperature difference for calibration was determined by

$$\Delta T_A = \frac{P_{el,A}}{C_w G_{WA}},$$

$$\Delta T_C = \frac{P_{el,C}}{C_W G_{WC}}, \tag{4}$$

$$\Delta T_{Ch} = \frac{P_{el,Ch}}{C_W G_{WCh}}.$$

**Figure 2.**   (a) Excess power a a function of input electric power for a Pd cathode sample, $d = 9$ mm, current is 50–100 mA; (b) Dependence of the ratio of thermal power to electrical input power as a function of the glow discharge voltage. 1 – deuterium pre-charged Pd cathode samples in $D_2$, Xe and Kr discharges, current is 50– 100 mA, 2 – non-deuterium pre-charged Pd cathode in Kr discharge.

Here $P_{el,A}$, $P_{el,C}$, and $P_{el,Ch}$ denote electric power (values) of calibration heaters in the anode, cathode and chamber water channels, respectively. The results of such calibration experiments show that the measurements actual error at rather high power levels did not exceed $\pm 1.0$ %.

If excess power is present, we can determine its value using

$$P_{xs} = (P_C + P_A + P_{Ch}) + P_{loss} - P_{el} \pm \Delta P_{error}. \tag{5}$$

The heat power losses into environment $P_{loss}$ in the first approximation may be presented as being proportional to the magnitude of the total thermal power $\Sigma$:

$$\Sigma = P_C + P_A + P_{Ch} \tag{6}$$

and it may be accounted for by introduction of the glow discharge efficiency coefficient $\eta$

$$\eta = \frac{P_A + P_C + P_{Ch}}{P_A + P_C + P_{Ch} + P_{loss}}. \tag{7}$$

The efficiency $\eta$ is determined in experiments under operational regimes in which excess heat is not observed.

The Pd samples used in glow discharge calibration experiments with Xe and Kr were not pre-charged with deuterium, and relatively high values for the thermal efficiency were achieved. Following calibration, deuterium is loaded into the Pd. In these experiments the current density did not exceed 100 mA/cm$^2$. At such values of the discharge current density in $D_2$, a continuous loading of $D_2$ into Pd ran up to saturation. The amount of deuterium loaded into palladium was determined by the volume of the gas absorbed from the discharge chamber. When saturation was achieved, the value of the D/Pd ratio was close to 1. Then, experiments were carried out with Pd cathode samples in $D_2$, and also with deuterium pre-charged Pd cathode samples in Xe and Kr discharges. Relatively high values of excess power were achieved for deuterium pre-charged cathode samples in Xe and Kr discharges [6] (see Fig. 2(a)). No excess power

**Figure 3.** Schematic of a high-voltage electrolysis device, set up as a heat capacity and flow calorimeter; 1 – electrolyte chamber, 2 – cathode holder, 3 – cathode sample, 4 – thermal insulation cover, 5 – mixer, 6 – anode, 7 – temperature sensors, 8 – flow meter, 9 – thermocouple, 10 – cooling water.

was observed in the cathode samples made of pure Pd (not deuterium pre-charged) in Xe and Kr discharges, as can be seen in Fig. 2(b). The biggest values of power gain were observed under conditions when the glow discharge voltage ranged between 1000 and 1300 V (Fig.2(b)).

We interpret this as showing two requirements for excess power generation: (1) deuterium should be loaded into the solid-state crystal lattice medium; (2) the crystal lattice should get an initial excitation, so that high-energy long-lived excited levels are created in the cathode sample solid. These excited conditions could be created by an additional source (for example by a flux of inert gas ions).

## 3. Excess Power Measurements in the High-Voltage Electrolysis Cell

The measurements were carried out using high-voltage electrolysis cell; which consists of two flanges made of stainless still with fastening units for the anode and the cathode assembly as shown in Fig. 3. An electrolysis chamber (1) in the form of quartz glass tube is set between the flanges, and another cylindrical tube set co-axially serves as the chamber

cooling jacket. The electrolysis chamber volume was 95 $cm^3$. The cathode units were provided with changeable cathode holders (2) that allowed us to use different cathode samples (3) with associated fasteners to hold the samples.

The discharge chambers were wrapped up into a thermal insulation cover (4), that reduced thermal losses into the environment. The three units of the device (the cathode, anode and chamber) had independent channels of water cooling. Each cooling channel included two temperature sensors (at the input and output) and a volumetric counter of the cooling water flow. The stirrer (5) and the thermocouple (9) were fixed upon the anode (6) flange inside the chamber. A pulsed power supply was used in the experiments. The electrolysis voltage in different experiments ranged from 500 to 2500 V, with the current in the range of 0.5–2.0 A. Pd, Ni and Pt cathode samples were used in the experiments; the cathode diameter was 11 mm.

The high-voltage electrolysis cell device was used in the two experimental runs:

(1) Experiments based on heat capacity calorimetry. The cooling water (10) of the cathode, anode, and discharge chamber, was absent in these experiments.
(2) Experiments based on continuous flow calorimetry.

Pre-deuterated Pd cathode samples and Ni cathode samples were used in high-voltage electrolysis cell experiments with excess power being measured.

## 3.1. Pre-deuterated Pd cathode sample preparation

Bombardment by $D_2$ ions in the glow discharge is viewed as the most effective procedure for loading deuterium into Pd [7]. The measurements were carried out using the glow discharge device consisting of a water-cooled vacuum chamber (1000 $cm^3$), and cathode and anode assemblies. The chamber design allowed the placement of cathode samples made of various materials on a water-cooled surface. The experiments were carried out using a high-current glow discharge in $D_2$, with Pd samples. The power supply feeds the glow discharge with a periodic pulse direct current, and allows the generation of desired current forms (with various pulse length and pulse period) to obtain the required current voltage and current. We observed good $D_2$ loading into Pd cathodes with this approach. The glow discharge current was from 30 up to 300 mA, the voltage was from 500 to 1400 V, and the gas pressure in the chamber was between 1 torr and 25 torr.
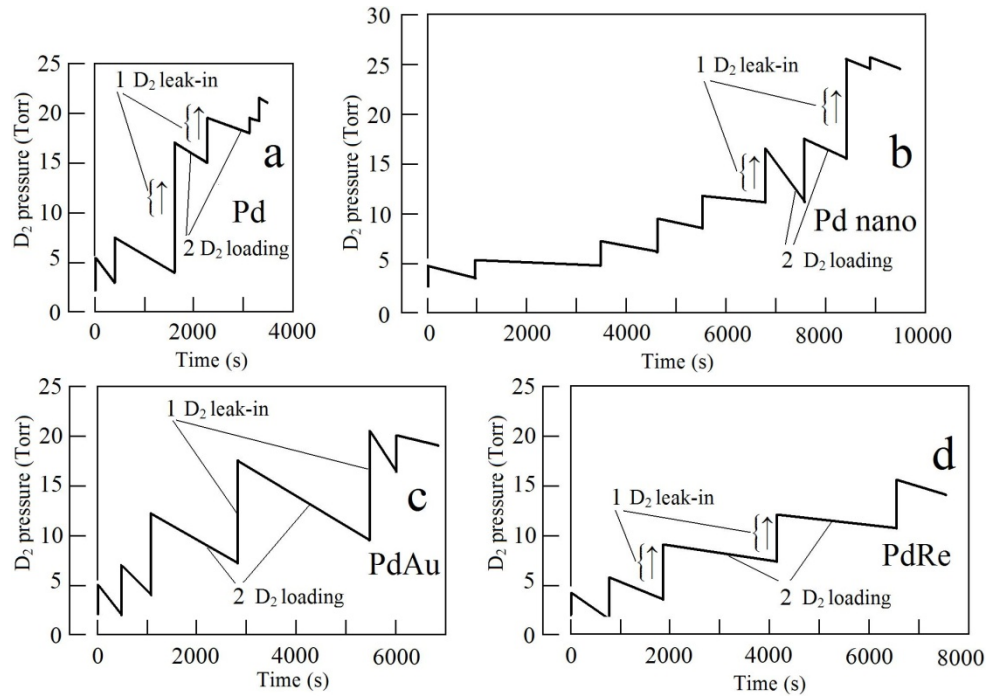
The loading procedure can be summarized as:

(1) First pump the gas out of the discharge chamber.
(2) Bleed deuterium into the chamber until the pressure builds up to several torr.
(3) Switch on the glow discharge and commence operation.

The $D_2$ pressure is observed to decrease steadily when loading into the cathode Pd. Then the glow discharge is switched off, with $D_2$ being pumped again into the chamber. The above procedure is repeated several times, the gas pressure being increased each time as shown in Fig. 4. During the experiment the D/Pd ratio was determined by summing up the pressure drops.

## 3.2. Heat capacity calorimetry in high-voltage electrolysis cell experiments
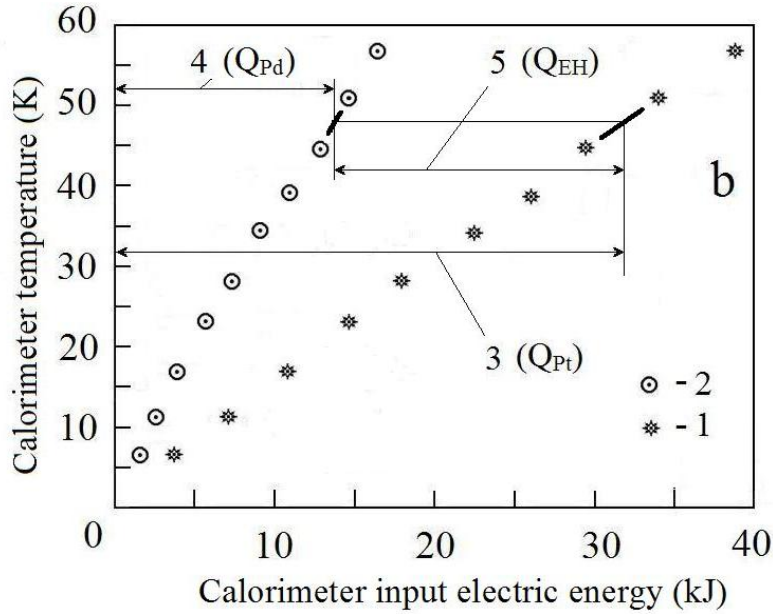
A variety of calorimetry experiments were carried out in the high-voltage electrolysis cell to study excess power generation. For control experiments, we used Pt cathodes (which do not load, and which produce no excess power). Excess power measurements were made on Pd cathodes that were pre-loaded with deuterium, and also with Ni cathodes. The electrolysis was done in light water.

**Figure 4.**   Time history of the $D_2$ pressure in the glow discharge chamber; (a) $D_2$ loading in Pd foil sample; (b) nanostructured Pd cathode sample, (c) Pd foil coated Au cathode sample, (d) Pd foil coated Re cathode sample.

In heat capacity calorimetry, estimation of the excess energy is made by comparing the temperature increase measured with deuterated Pd or Ni cathodes with the temperature rise of the Pt control. For the control experiment, a calibration of temperature versus electrical input energy is established as shown in Fig. 5. When a Pd cathode pre-loaded with deuterium is used, the temperature rise is much faster, also illustrated in Fig. 5. To estimate the excess energy, we begin with the observed temperature as a function of input electrical energy; for each observed temperature we determine how much input energy is needed to produce such a temperature in the Pt control experiment, and then determine the excess energy as the difference between the two (the estimated energy produced minus the input electrical energy). The electric discharge was switched off when the calorimeter temperature reached 57°C.

It is possible to develop estimates for the excess power produced from such measurements by determining the incremental excess energy produced during the time between successive temperature measurements. This approach was used for the estimated excess power in the different experiments of Figs. 6–10. We see from these measurements that the excess power produced reached 280 W, with a power gain (ratio of thermal output power to electrical input power) as high as 340%.
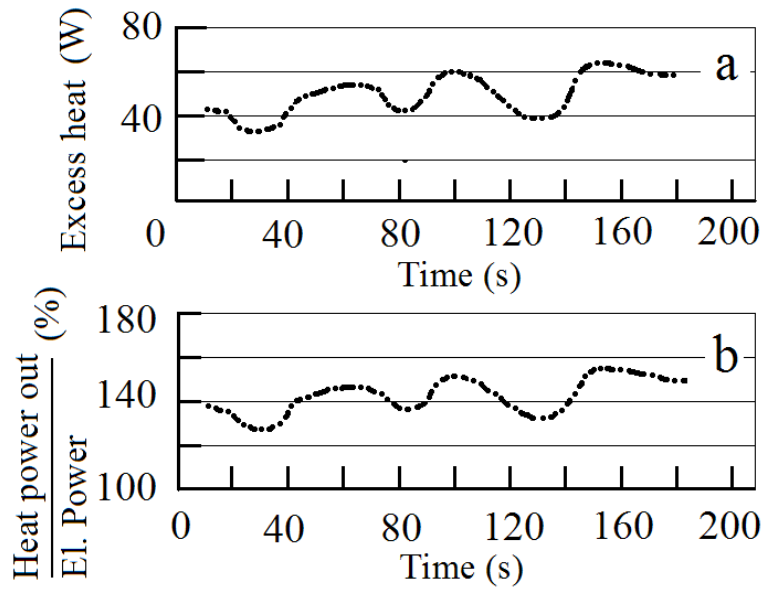
**Figure 5.** Dependence of the calorimeter temperature up input electric energy value; 1 – electrolysis in $H_2O$ with the Pd cathode, 2 – electrolysis in $H_2O$ with a Pt cathode, 3 – input electric energy in calorimeter with Pt cathode, 4 – input electric energy in calorimeter with Pd cathode, 5 – excess energy with pre-loaded Pd cathode.

### 3.3. Flow calorimetry in high-voltage electrolysis cell experiments

Our flow calorimetry in the high-voltage electrolysis cell is similar to the calorimetry described above for the glow discharge experiments. Independent cooling water flow was channeled to the cathode, anode and to the chamber. Measurements of the temperature difference between the input and output of the different channels was used to determine the thermal power associated with the cathode, anode and chamber individually, according to

$$P_A = C_w \dot{G}_{WA} \dot{\Delta} T_A,$$

$$P_C = C_w \dot{G}_{WC} \dot{\Delta} T_C, \tag{8}$$

$$P_{Ch} = C_w \dot{G}_{WCh} \dot{\Delta} T_{Ch},$$

where $P_A$, $P_C$, and $P_{Ch}$ are the thermal powers of the anode, cathode, and chamber; where $C_w$ is the heat capacity of water, where the flow rates are denoted by $G_{WA}$, $G_{WC}$ and $G_{WCh}$, and where the measured temperature differences are $\Delta T_A$, $\Delta T_C$, and $\Delta T_{Ch}$. The local average electrical power was again determined from

**Figure 6.** (a) Excess energy as a function of time. (b) Power gain as a function of time. Electrolysis in $H_2O$ with a pre-loaded Pd foil cathode; cathode – anode voltage is 700 V, and current is 0.7 A.
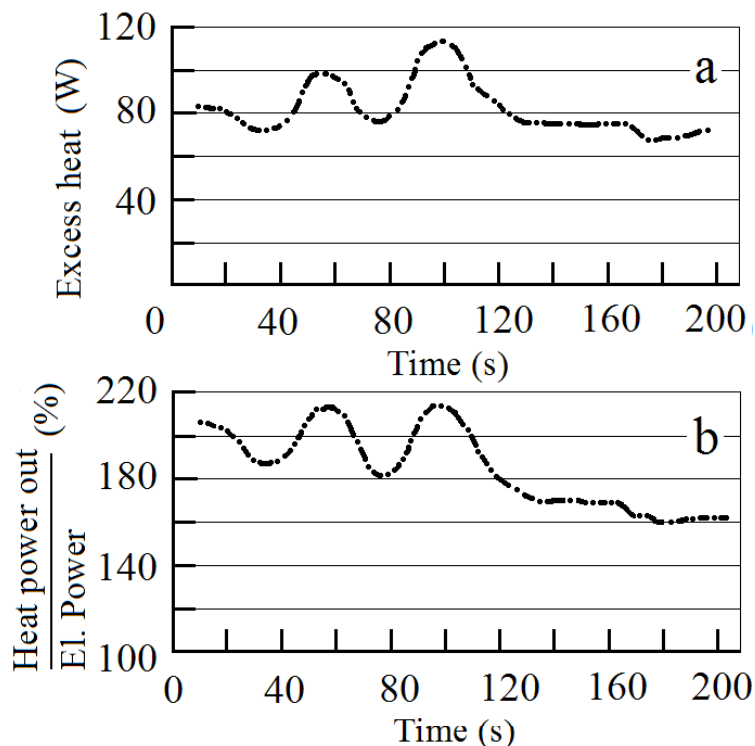
$$P_{el} = \frac{1}{T} \int_T V(t) I(t) \, dt, \tag{9}$$

where $V(t)$ and $I(t)$ are the voltage and current associated with a pulse of length $T$. The excess power $(P_{xs})$ is determined from the difference between the total thermal output power and the electrical input power $(P_{el})$

$$P_{xs} = (P_C + P_A + P_{Ch}) - P_{el}. \tag{10}$$

In this case, we determined the calorimeter efficiency $\eta$ according to

$$\eta = \frac{P_C + P_A + P_{Ch}}{P_{el}}. \tag{11}$$

Experimental results are tabulated in Tables 1–3 for Pt control experiments, and for experiments with Ni cathodes. No excess power was observed with Pt cathodes, and the measured calorimeter efficiency was between 94% and 97%. Excess power gain was seen with Ni cathodes with good reproducibility; the largest excess power observed was 230 W with a power gain of 280%. The effect of the mixer (stirrer) can be seen in the greater proportion of power showing up in the chamber flow channel with the mixer on.

**Figure 7.** (a) Excess power as a function of time. (b) Power gain as a function of time. Electrolysis in $H_2O$ with a $D_2$ pre-charged Pd foil coated Re cathode; cathode – anode voltage is 700 V, and current is 0.7 A.
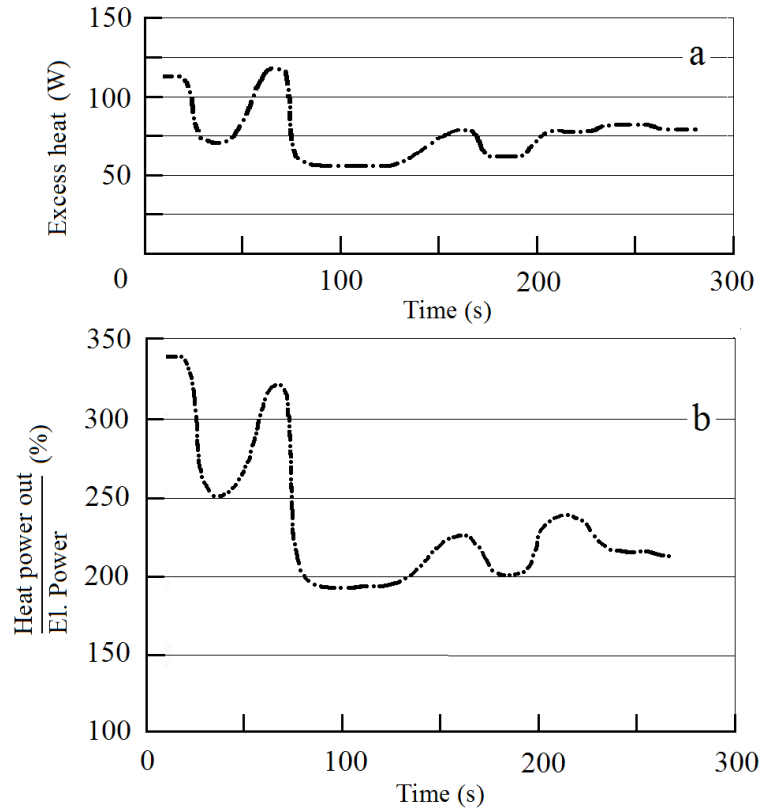
**Table 1.** Flow calorimetry results for high-voltage electrolysis cell calorimetry; Pt cathode, $H_2O$ electrolyte with working mixer.

| No. Exp. | Current, | Voltage | Elec. power | Thermal power, cathode | Thermal power, chamber | Thermal power, anode, | Total thermal power, | Excess power | Effici- ency |
|---|---|---|---|---|---|---|---|---|---|
| | $I$ (A) | $V$ (V) | $P_{el}$ (W) | $P_C$ (W) | $P_{Ch}$ (W) | $P_A$ (W) | $P_\Sigma$ (W) | $P_{el}$ (W) | $\eta$ (%) |
| 1 | 1.13 | 600 | 169 | 23.6 | 124 | 15.5 | 163 | no | 96 |
| 2 | 1.6 | 443 | 178 | 26.6 | 128.5 | 16.6 | 172 | no | 96 |
| 3 | 1.11 | 295 | 82 | 10.7 | 57 | 9.5 | 77.2 | no | 94 |
| 4 | 0.99 | 256 | 64 | 9.4 | 45 | 6 | 60.4 | no | 94 |
| 5 | 1.4 | 380 | 132 | 24 | 100 | 15.2 | 147 | no | 95 |
| 6 | 1.05 | 837 | 220 | 21 | 174 | 11 | 206 | no | 94 |
| 7 | 0.62 | 730 | 113 | 14.5 | 90.7 | 6.9 | 112 | no | 97 |
| 8 | 0.64 | 1525 | 245 | 15.1 | 145.4 | 74.3 | 234 | no | 96 |

## 4. Nuclear Product Measurements

### 4.1. $^4$He measurements

There has been interest in the field in the issue of $^4$He production in association with excess energy production. We reported measurements of $^4$He in our early experimental results reported in [1]. We sent some of our Pd cathodes along
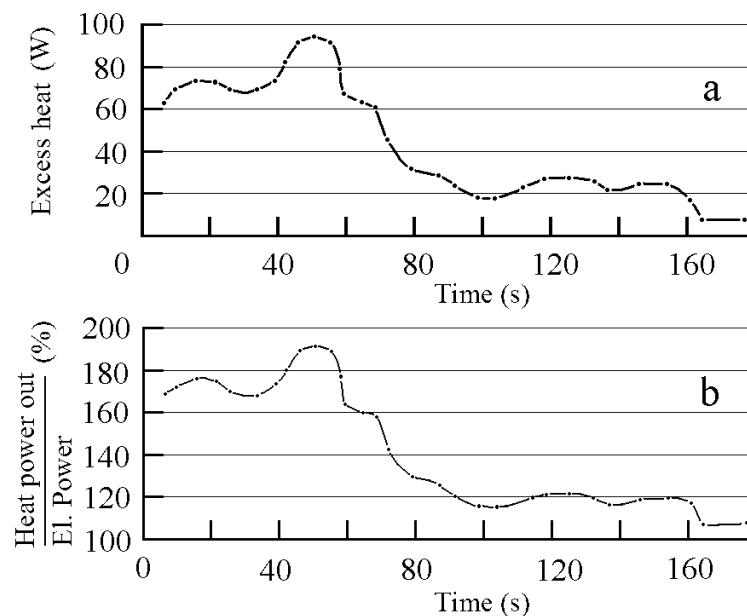
**Figure 8.** (a) – Excess power as a function of time. (b) Power gain as a function of time. Electrolysis in $H_2O$ with a $D_2$ pre-charged Pd cathode with nanostructure; cathode – anode voltage is 700 V, and current is 0.55 A.

**Table 2.** Flow calorimetry results for high-voltage electrolysis cell calorimetry; Ni cathode, $H_2O$ electrolyte without working mixer.

| No. Exp. | Current, | Voltage | Elec. power | Thermal power, cathode | Thermal power, chamber | Thermal power, anode, | Total thermal power, | Excess power | Efficiency |
|------|------|------|------|------|------|------|------|------|------|
| | $I$ (A) | $V$ (V) | $P_{el}$ (W) | $P_C$ (W) | $P_{Ch}$ (W) | $P_A$ (W) | $P_\Sigma$ (W) | $P_{el}$ (W) | $\eta$ (%) |
| 1 | 0.49 | 1506 | 183 | 93.2 | 128.3 | 57.4 | 279 | 88 | 148 |
| 2 | 0.54 | 1960 | 265 | 80.3 | 199 | 81 | 354 | 89 | 134 |
| 3 | 0.49 | 1700 | 207 | 94.2 | 198.3 | 30.6 | 323 | 116 | 156 |
| 4 | 0.84 | 840 | 178 | 27 | 163.5 | 41.7 | 232 | 54 | 131 |
| 5 | 0.63 | 1460 | 229 | 156.4 | 165.6 | 42.7 | 365 | 137 | 160 |
| 6 | 058 | 1770 | 212 | 128.8 | 127.6 | 63.5 | 320 | 108 | 151 |

**Figure 9.** (a) – Excess power as a function of time. (b) Power gain as a function of time. Electrolysis in $H_2O$ with a $D_2$ pre-charged Pd cathode with nanostructure; cathode – anode voltage is 520 V, and current is 2.1 A.

with reference samples to be analyzed at the Rockwell International Laboratory (Oliver's group). A small increase in $^3He$ concentration, and a large increase in the $^4He$ concentration, were found in Pd samples from glow discharge experiments; results are indicated in Table 4.

**Table 3.** Flow calorimetry results for high-voltage electrolysis cell calorimetry; Ni cathode, $H_2O$ electrolyte with working mixer.

| No. Exp. | Current, | Voltage | Elec. power | Thermal power, cathode | Thermal power, chamber | Thermal power, anode, | Total thermal power, | Excess power | Efficiency |
|---|---|---|---|---|---|---|---|---|---|
| | $I$ (A) | $V$ (V) | $P_{el}$ (W) | $P_C$ (W) | $P_{Ch}$ (W) | $P_A$ (W) | $P_\Sigma$ (W) | $P_{el}$ (W) | $\eta$ (%) |
| 1 | 0.42 | 1110 | 109 | 15.8 | 113.5 | 21 | 150 | 40 | 136 |
| 2 | 0.68 | 1400 | 239 | 50 | 201 | 57.3 | 308 | 69 | 129 |
| 3 | 0.58 | 1070 | 151 | 28.2 | 162.5 | 17 | 207.6 | 56 | 137 |
| 4 | 0.25 | 1840 | 115 | 26.6 | 95.2 | 11.5 | 133 | 18.3 | 116 |
| 5 | 0.48 | 1530 | 184 | 45 | 188.5 | 13.2 | 247 | 63 | 134 |
| 6 | 0.4 | 620 | 62 | 16.7 | 93.8 | 7.9 | 118 | 56.3 | 190 |
| 7 | 0.84 | 654 | 138 | 60.7 | 286.5 | 20.9 | 368 | 230 | 280 |
| 8 | 0.88 | 634 | 139 | 42.7 | 268 | 20.8 | 332 | 180 | 240 |

**Figure 10.**   (a) – Excess power as a function of time. (b) Power gain as a function of time. Electrolysis in $H_2O$ with a Ni cathode; cathode–anode voltage is 600 V, and current is 0.7 A.

### 4.2. Stable impurity nuclei measurements

We carried out elemental and isotopic assays of cathode sample before and after glow discharge experiments to search for possible nuclear reaction products. This was done using X-ray fluorescent spectrometry, spark mass spectrometry, secondary ionic mass spectrometry, and secondary neutral mass spectrometry.  In the case of secondary ion mass spectrometry, the procedure that we used was

(1) removal the upper 1.5 nm-thick defect layer by plasma etching,
(2) scanning the first and the second layers in 5 nm increments, while determining the content of the impurity nuclides,

**Table 4.**   Relative content of $^3He$ and $^4He$ in Pd cathode samples from a glow discharge experiment. The cathode was Pd, the gas was $D_2$, the current was 35 mA, and the experimental run time was 4 h.

| No. | $^3He_{after\ discharge}/\ ^3He_{initial}$ | $^4He_{after\ discharge}/\ ^4He_{initial}$ |
|-----|------------------|------------------|
| 1 | Up to 10 times | Up to 100 times |
| 2 | Up to 2 times | Up to 35 times |

**Figure 11.**　Impurity nuclei content in the surface layer of the cathode sample (with a thickness of $100\mu$m) after glow discharge; Pd cathode, $D_2$ gas, 100 mA current, and 22 h run time.

    (3)　removal of a layer with the thickness of 700 nm, and repeated scanning of the third and fourth layers in 5 nm increments while again determining the content of the impurity nuclides.

The initial impurity content was a few ten ppm. We measured impurity nuclei with masses both less than, and greater than, that of Pd as depicted in Fig. 11.

    The primary impurity nuclei observed, with an abundance of more than 1%, include $^7$Li, $^{12}$C, $^{15}$N, $^{20}$Ne, $^{29}$Si, $^{44}$Ca, $^{48}$Ca, $^{56}$Fe, $^{57}$Fe, $^{59}$Co, $^{64}$Zn, $^{66}$Zn, $^{75}$As, $^{107}$Ag, $^{109}$Ag, $^{110}$Cd, $^{111}$Cd, $^{112}$Cd, $^{114}$Cd, as shown in Fig. 11. The total content of these impurities amounts to $10^{17}$. The experiment duration in this case is up to $2 \times 10^4$ s. The deviation from the natural isotope ratio for these impurity nuclei is up to several tens of times. Interestingly, the following isotopes were absent: $^{58}$Ni, $^{70}$Ge, $^{73G}$e, $^{74}$Ge, $^{113}$Cd, $^{116}$Cd, as shown in Fig. 12. These peculiarities are also registered within 1 $\mu$m thick surface layer, the observed natural Pd isotopes ratio of the sample being changed (Fig. 13).

    The main recovered impurity nuclides (with more than 1% content) are $^7$Li, $^{12}$C, $^{15}$N, $^{20}$Ne, $^{29}$Si, $^{44}$Ca, $^{48}$Ca, $^{56}$Fe, $^{57}$Fe, $^{59}$Co, $^{64}$Zn, $^{66}$Zn, $^{75}$As, $^{107}$Ag, $^{109}$Ag, $^{110}$Cd, $^{111}$Cd, $^{112}$Cd, $^{114}$Cd (Fig. 11). The total content of these impurities amounts to $10^{17}$, the experiment duration being up to $2 \times 10^4$ s. The observed change of natural isotope ratio for these impurity nuclides is up to several tens of times, some main isotopes of impurity elements (with high natural abundance percentage) being absent. The following isotopes were registered as being absent: $^{58}$Ni, $^{70}$Ge, $^{73}$Ge, $^{74}$Ge, $^{113}$Cd, $^{116}$Cd (Fig. 12). Modifications in the isotopic abundances of the Pd isotopes were seen in the surface layer (1 $\mu$m thick), as shown in Fig. 13. We observed $^{57}$Fe production,
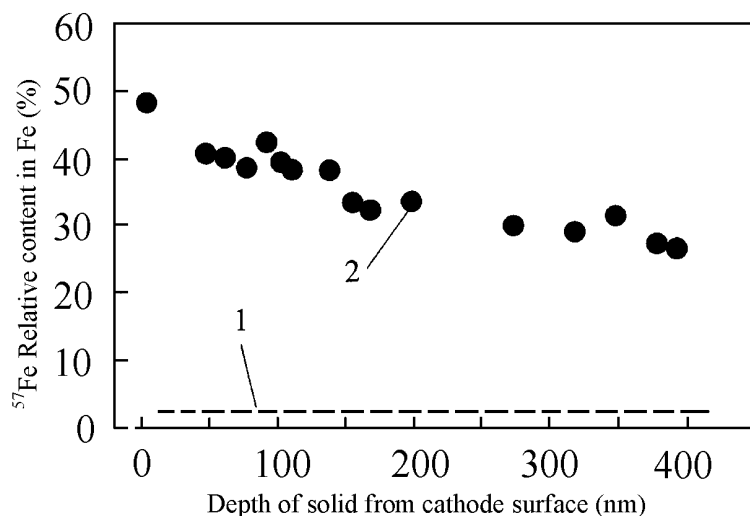
**Figure 12.** Impurity nuclei ratio change in the surface layer of the cathode sample (with thickness of $100\mu$m) after glow discharge run; Pd cathode, $D_2$ gas, 100 mA current, and 22 h run time. 1 – natural abundance, 2 – post-run ratio, 3 – absence of natural nuclei.

which is a characteristic feature of low energy reactions (Fig. 14).



**Figure 13.** Pd isotope ratio change in the surface layer of the cathode sample (with thickness of 100 $\mu$m) following a glow discharge run; Pd cathode, $D_2$ gas, 100 mA current, and 22 h run time. 1 – natural ratio, 2 – ratio after glow discharge.

**Figure 14.** The relative abundance of $^{57}$Fe nuclei in the surface layer of the Pd cathode.

## 5. X-ray Measurements

We have observed both diffuse and collimated X-ray emission in the keV region in a large number of experiments carried out over the past decade; in this section we will provide a brief overview of some of our results. Experiments were carried out using a glow discharge system, with a variety of X-ray diagnostics; including an X-ray pinhole camera, thermo-luminescent detectors with foils, scintillation detectors with a photomultiplier, and a curved mica spectrometer with X-ray film. Experiments were carried out on different metal cathode materials, including Al, Sc, Ti, Ni, Nb, Zr, Mo, Pd, Ta, and W. Different gasses were also used, including $D_2$, $H_2$, He, Kr and Xe. The power supply delivered a train of pulses, as illustrated in Fig. 1(b), with pulse durations between 0.1 and 2.0 ms, and periods between 0.3 and 100 ms. We used currents between 30 and 300 mA, and voltages between 1500 and 4300 V; the gas pressure in the chamber was 3–5 torr.

### 5.1. Pinhole camera experiments

The X-ray emission was of sufficiently high intensity that it was possible to image the cathode using a pinhole camera. We used a transverse 0.3 T magnetic field to verify that the image was not due to charged particles [6]; it was observed that the image was nearly the same with and without the magnetic field.

### 5.2. Thermo-luminescent detector experiments

We used crystalline $Al_2O_3$ thermo-luminescent detectors covered with Be foils of different thicknesses in order to estimate the average energy of the X-ray emission [4]. We found that the main component was between 1.3 and 1.8

keV, with evidence of a higher energy component as well. These measurements showed that the X-ray intensity from the cathode surface increased exponentially with an increase in the discharge voltage, reaching as upper limit of 1 W.

## 5.3. Scintillator and photomultiplier experiments

We made use of PMMA scintillators with the optical scintillation detected using a photomultiplier and scope, to study the energy-dependence, spatial-dependence, and the time-dependence of the X-ray emission [6]. Tests with a transverse 0.3 T magnetic field again showed that the radiation was not composed of charged particles. We measured the transmission through 15 and $30\mu$m thick Be foils, and the difference in transmission was consistent with an average energy in the range of 1.0–2.5 keV. It was found that the average energy for different cathode materials in these measurements were in good agreement with the thermo-luminescent detector measurements discussed above. We also did time-resolved measurements which showed that the diffuse radiation was produced while the discharge was on, and collimated emission was observed in bursts that followed the switching off of the discharge with some delay.

## 5.4. Curved mica spectrometer experiments

Many experiments were carried out with the curved mica crystal spectrometer to give energy-resolved X-ray spectra on X-ray film [7]. A variety of spectral features were observed. We saw characteristic X-ray emission from Kr and Xe which showed up as strong spectral lines on the film. We also saw weaker characteristic X-ray emission from transitions in the host metal atoms. There was a continuum apparent that originated from the cathodes surface, centered roughly near 1.5 keV, with somewhat different widths depending on the discharge voltage, and with an intensity that was weakly correlated with the cathode material. An example of this continuum emission is shown in Fig. 15. Finally, we saw extremely strong micro-beam emission that was sufficiently intense to cause a bleaching (the proper technical term is solarization) of the film, and which appeared on the film as spots (instead of as spectral lines) and curves (consistent with a spot which moved during the emission).

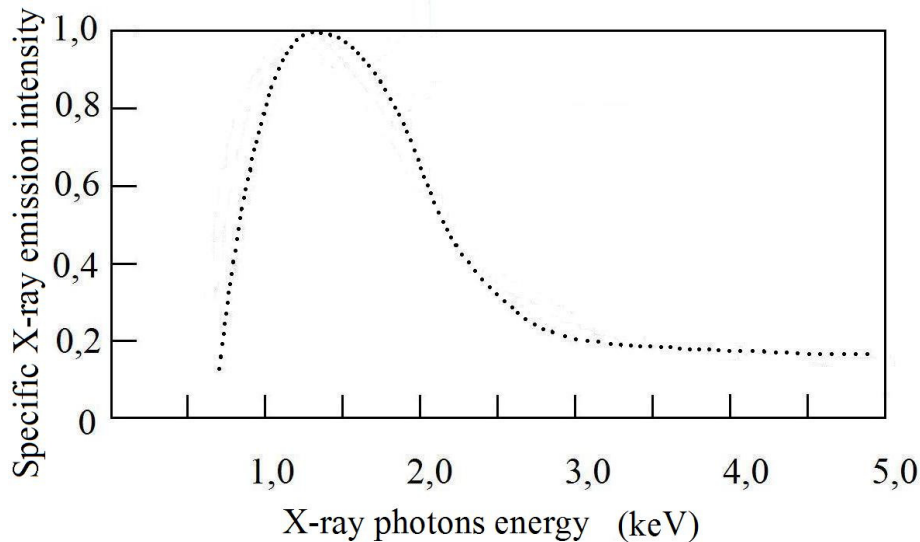## 6. Interpretation and Proposed Physical Mechanisms

Based on the experimental results reviewed in the previous sections, we can consider possible physical processes that might be involved. Presumably, some excited energetic levels are formed in the cathode solid when its surface is exposed to bombardment by the ions flux generated in plasma or electrolyte medium. It would follow that the observed X-ray emission occurs as a result of de-excitation of these energetic levels.

(1) Deuterium ion acceleration in the glow discharge near-cathode region produced ion energies from several hundred eV up to a few thousand eV.
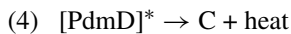(2) Deuterium ions collide with the atoms of the crystal lattice ions.

Presumably, some long-lived excited levels with energies up to several kilovolts are formed in the cathode solid. Under the resulting highly non-equilibrium conditions there exists an excited state population that can be characterized by an effective temperature on the order of 1–3 keV, which in our view are the conditions necessary for low energy nuclear reactions to occur.

Within this framework, we can think about what kinds of reactions in particular might lead to the formation of stable transmutation products. The following reactions may be possible:

(1) $Pd + mD \rightarrow [PdmD]^*$
(2) $[PdmD]^* \rightarrow Pd^* + {}^4He + heat$
(3) $[PdmD]^* \rightarrow A^* + B^* \rightarrow A + B + heat$

**Figure 15.** Continuum X-ray emission measured with the curved mica crystal spectrometer from a glow discharge experiment with a Pd cathode and $D_2$ gas.
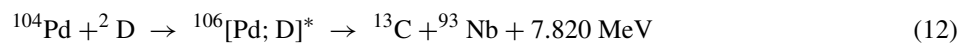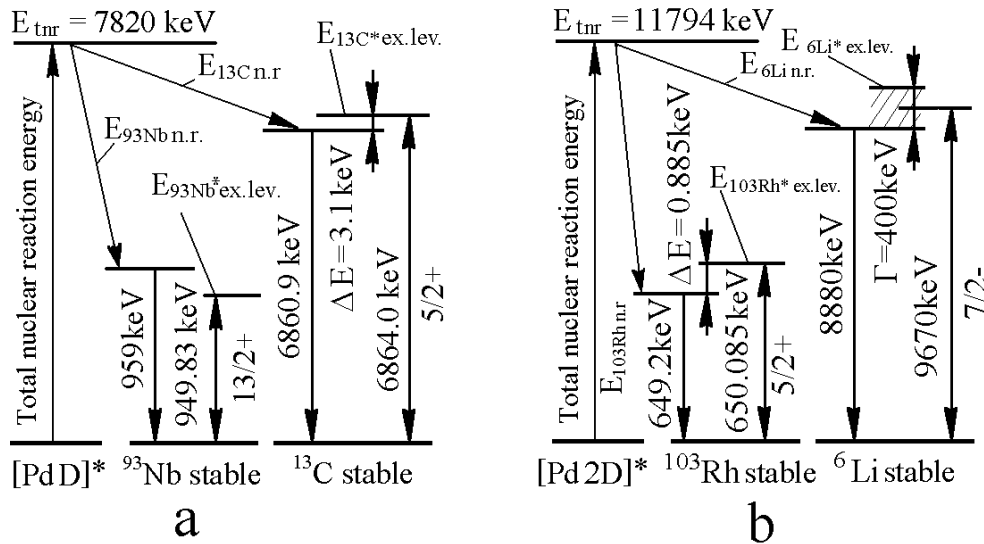
(4)  $[PdmD]^* \rightarrow C + heat$

where $[PdmD]^*$ is a short-lived intermediate compound nucleus; where $m = 1, 2, 3, \ldots$; where $A^*$, $B^*$ denote nuclear isomers of nuclei with masses less than that of Pd; where A, B are stable nuclides; and where C stands for a nuclide with a mass more than that of Pd. The first step in the proposed process is the formation of an excited state compound-nucleus. Then one of three possible modes is realized:

(1) the compound nucleus may lose its excitation and form an exited Pd nucleus and $^4$He.
(2) the compound nucleus may split into two nuclear fragments with masses less than that of Pd. In so doing the two nuclei should be in excited isomer state (experiments show that the nuclear reactions energy is not produced as kinetic energy of nuclear fragments).
(3) the compound nucleus may lose its excitation and form a stable nucleus of a heavier than Pd element.

To determine the specific physical mechanism for these reactions will require additional research.

One possible type of reaction for forming the impurity nuclides can be a long-range (resonant) nuclear reaction. The mechanism of such long-range reactions can be explained using as an example a specific transmutation reaction for Pd + D (Fig.16(a)) and Pd + 2D (Fig.16(b)) [4]. The formation of significant $^{13}$C nuclei and $^{93}$Nb nuclei was recorded in the experiments. In this case we assume that the reaction can proceed as

$$^{104}Pd +^2 D \ \rightarrow \ ^{106}[Pd; D]^* \ \rightarrow \ ^{13}C +^{93} Nb + 7.820 \, \text{MeV} \tag{12}$$

**Figure 16.** Schematic of proposed long-ranged (resonant) nuclear reactions; (a) for Pd + D transmutation reaction; (b) for Pd + 2D transmutation reaction.

Momentum and energy conservation dictates that the product nucleus $^{13}$C should receive 6.8609 MeV, and that the product nucleus $^{93}$Nb should receive 0.959 MeV (in connection with the reaction scheme of Fig. 16(a)). Note that a nuclear excited state (nuclear isomer) with an energy of 6.864 MeV (and excited level width of 6keV) exists for $^{13}$C, and that an excited level with an energy of 0.94983 MeV exists for $^{93}$Nb. The difference between the energy received by nuclide $^{13}$C and the energy of the excited level is 3.1 keV. If the crystalline lattice has available 1.5 keV, and given the 6 keV width of the excited energy level, one might expect that there should be a high probability for such a long-range (resonant) nuclear reaction to occur.

Consider the reaction (shown in Fig. 16(b))

$$^{105}\text{Pd} + 2\,^2\text{D} \;\rightarrow\; [\text{Pd2D}]^* \;\rightarrow\; ^{93}\text{Rh} +^6 \text{Li} + 11.794 \text{ MeV} \tag{13}$$
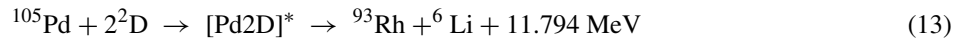
Energy and momentum conservation again dictate that the product $^6$Li nucleus should end up with an energy of 8.880 MeV. A nearby excited state is available, so a similar situation can occur as indicated in Fig. 16(b).

The totality of the experimental results allows us to assume that the energy of the excited nuclear levels of the product nuclei is converted into heat. The specific physical mechanism of such conversion will require additional research.

## 7. Conclusions

We have reviewed many results that we have obtained in glow discharge experiments and in high-voltage electrolysis experiments. We have observed excess power in glow discharge experiments up to 10 W/cm$^2$, and with a power gain of

up to 170%; in the high-voltage electrolysis experiments we have seen excess power up to 300 W, with a power gain as high as 340%. These experiments clearly demonstrate the presence of an interesting new source of thermal power and energy. We have reviewed results obtained in our search for nuclear products, where many new elements and isotopes appear to have been produced. We have observed both collimated and diffuse X-ray emission in the keV regime, which constitutes a new fundamental effect that we discovered. Finally, we have presented a discussion of our results in terms of conjectures and hypotheses concerning physical mechanisms and reactions that may be involved (but which will require further study in order to determine whether they are correct or not).

## Acknowledgment

## References

[1]  A. B. Karabut, Ya. R. Kucherov and I. B. Savvatimova, *Phys. Lett. A.* **170** (1992) 265.
[2]  A. B. Karabut, Analysis of experimental results on excess heat power production, impurity nuclides yield in the cathode material and penetrating radiation in experiments with high current glow discharge, *Proceedings of the 8th International Conf. on Cold Fusion*, Italy 21–26 May 2000, p. 329.
[3]  A.B. Karabut, Experimental registration of a high current glow discharge of the exited long living atomic levels with the energy of 1–3 keV and nuclear products emission in the solid medium, *Proceedings of the 11 International Conference on Emerging Nuclear Energy Systems (ICENES 2002)*, 29 September–4 October 2002, Albuquerque, New Mexico, USA, 1995, pp. 408–416.
[4]  A.B. Karabut, Production of excess heat, impurity elements and unnatural isotopic ratios formed at excited long-lived atomic levels with energy of more than 1 keV in a solid cathode medium during high-current glow discharge, *Proceedings of the 10th International Conference on Cold Fusion*, August 24–29, 2003, Cambridge, MA, USA.
[5]  A.B. Karabut, Excess heat productionin Pd/D during periodic pulse discharge current in various condition, *Proceedings of the 11th International Conference on Cold Fusion*, 31 October–5 November, 2004, France, pp. 178–193.
[6]  A.B. Karabut, Research into low energy nuclear reaction in cathode sample solid with production of excess heat, stable and radioactive impurity nuclides, *Proceedings of the 12th International Conference on Cold Fusion*, December 2–7, 2006, Japan, pp. 214–230.
[7]  A.B. Karabut and E.A. Karabut, Study of deuterium loading into pd cathode samples of glow discharge, *Proceedings of 9th International Workshop on Anomalies in Hydrogen/Deuterium Gas Loaded Metals*, 6–11 September 2010, Siena, Italy.
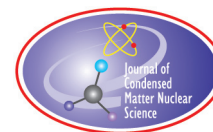
Research Article

# Research into Excited 0.6–6.0 keV Energy Levels in the Cathode Solid Medium of Glow Discharge by X-ray Spectra Emission

## A.B. Karabut*

*Samar+ COMPANY, Belay Dacha, 13, ap. 54, city Kotelniky, Moscow Region, 140055, Russia*

## E.A. Karabut

*Moscow Power Engineering Institute (Technical University)*

## Abstract

The results of X-ray spectra registration are presented. The X-ray spectra were registered in film using a curved mica crystal X-ray spectrometer. The experiments were carried out using a high-current glow discharge device, which consisted of a water-cooling chamber, water-cooling cathode and anode units. X-ray emission was detected through a diagnostic window placed above the cathode. The discharge was performed in $H_2$, $D_2$, Ar, Kr and Xe at pressure ranging from 1 to 5 Torr, using cathode samples made of Al, Sc, V, Ti, Ni, Zr, Nb, Mo, Pd, Ta, and W. Current ranged from 50 up to 300 mA and discharge voltage was 1500–4300 V. A pulse-periodical power supply was used to generate the glow discharge. The X-ray spectrum were registered both as bands of the continuum with energies ranging 0.6–10.0 keV and as spots resulting from the emission of series of high-density monoenergetic X-ray beams (with energies of 0.6–10.0 keV) characterized by small angular divergence. The X-ray spectra were repeatedly recorded during the Glow Discharge operation and after the Glow Discharge current switch off (for up to 20 h afterwards). The obtained results were direct experimental evidence of excited long living energy levels with the energy of 0.6–6.0 keV in the solid cathode sample.

© 2012 ISCMNS. All rights reserved. ISSN 2227-3123

*Keywords:* Cathode, Glow discharge, X-ray spectra

## 1. Introduction

Experimental detection of excess heat nuclear reaction products in the high-current glow discharge cathodes prove that there exist certain conditions and mechanisms that lead to the initiation of Low Energy Nuclear Reactions (LENR) in the condensed medium of the solid cathode. Theoretical estimation shows that a nuclear reaction in solid (for $10^{27}$ atom/m$^3$) requires of the production of the excited states with the excitation energy of 1–2 keV. Such excited energy levels can be produced by the mechanism of converting the initial energy of the ions plasma flux, which have the energy
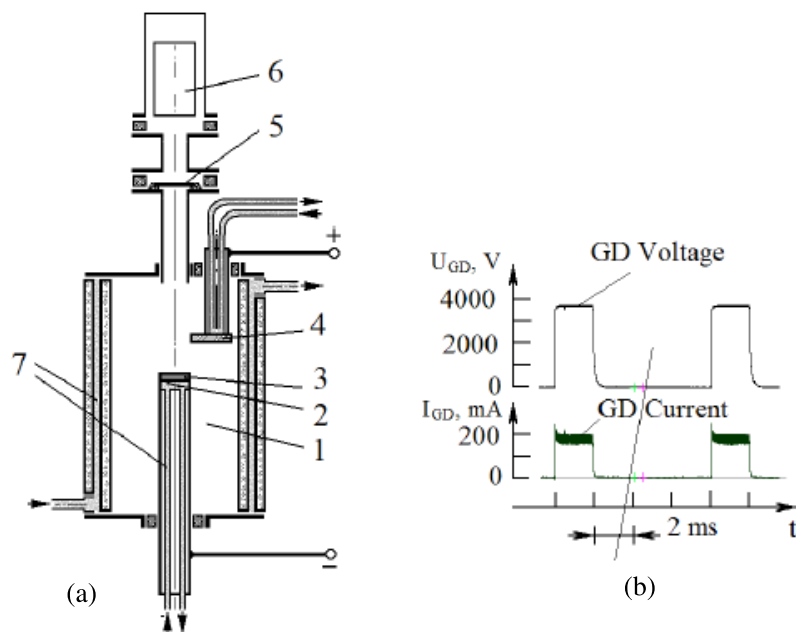
**Figure 1.** Schematic representation of the experiment. (a) Glow discharge device, 1– discharge chamber, 2– cathode holder, 3– cathode sample, 4– anode, 5– Be foil screens, 6– X-ray detectors different kind (pinhole, TLD detectors, scintillator- photomultiplier, spectrometer), objective, 7 –cooling water; (b) Glow discharge voltage and current oscillograms.

0.5–2.0 keV, into the high energetic (0.6–10.0 keV) excitation of a nuclear-electronic solid state system. This should occur in the solid such as a cathode when it is bombarded by the discharge plasma ions. The deexitation occurs by X-ray emission. An X-ray emission experiment was made to elucidate the LENR triggering process.

## 2. The X-ray Emission Spectra Detection

### 2.1. Glow discharge device

The measurements were carried out using the Glow Discharge device [1] consisting of a water-cooled vacuum chamber, the cathode and the anode assemblies (Fig. 1(a)). The cathode design allowed the placement of cathode samples made of various materials on a water-cooled surface. The experiments were carried out using a high-current glow discharge in $D_2$, $H_2$, He, Kr and Xe and the cathode samples being made of Al, Sc, V, Ti, Ni, Nb, Zr, Mo, Pd, Ta, and W.

In previous experiments [2,3] X-ray detection was carried out with X-ray pinhole, thermo-luminescent detectors, and scintillation detectors with photomultiplier. The energy spectrum of the X-ray emission was registered with the help of a curved mica crystal spectrometer. The Glow Discharge Device power supply is designed to feed the Glow Discharge with a pulse-periodic direct current and that allows us to generate the desired current forms of various pulse length and pulse period and to obtain the required current voltage and meaning (Fig. 1(b)). In the separate experiments the pulse duration varied from 0.1 up to 1.0 ms, and the period was from 0.3 up to 100 ms. The Glow Discharge conditions were as follows: current (amplitude) was from 30 up to 300 mA, voltage 1000–4300 V, and gas pressure in the discharge chamber was 3– 10 Torr.
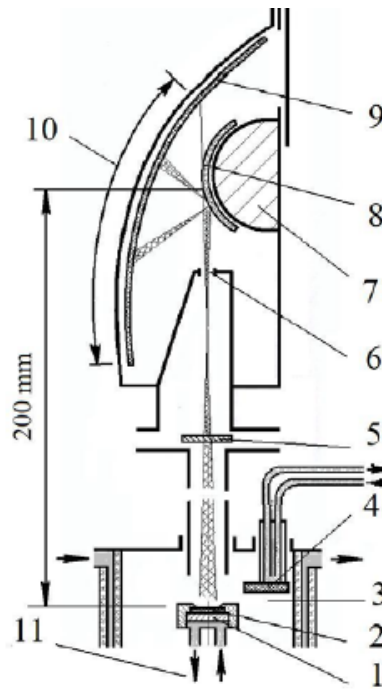
**Figure 2.** X-ray spectrometer 1–cathode holder, 2–cathode sample, 3–vacuum discharge chamber, 4–anode, 5–15 $\mu$m Be screen , 6– input slit of spectrometer, 7– crystals holder, 8–curved mica crystal, 9–X-ray film, 10–area of reflection spectra , 11–input and output cooling water.

## 2.2. X-ray spectrometer and procedure

The X-ray emission spectra were measured using the curved mica crystal X-ray spectrometer (the mica crystal holder is 50 mm diameter), with the spectrum being registered on X-ray film (Fig. 2). The film includes the refraction spectra, the direct X-ray lighting, and reflection spectra. The reflection spectra were used for data processing. The direct X-ray lighting limits the reflection spectra in the high energy area. The wavelength and the energy of the X-ray were determined according to the expression: $m\lambda = 2d \sin \theta$; $E_{X-ray} = 1.235/\lambda$.

Where $m$ is the spectrum order, $\lambda$ stands for the X-ray emission wavelength in nm, $2d$ is the constant of the mica crystal lattice ($2d = 2.0$ nm), and $\theta$ represents the reflection angle. The exposure times were 1– 5 h. The X- ray negative films were scanned with resolution 4800 points in color modes. The spectra were repeatedly recorded during the glow discharge operation with the exposure time 1– 5 h and after the glow discharge current switch off (for up to 20 h afterwards). The spectra pattern includes bands, dark and light spots (consisting of multiple tiny dark and light dots) and separate dark and light small spots. The bands and spots were located in spectral areas specific for a given cathode material used. The registered energy of the X-ray emission bands and spots (the energetic position of the bands and spots within the spectrum) was dependent upon the cathode material used. The registered X-ray spectra in experiments were similar to characteristic X-ray spectra. The X-ray monoenergetic beams with small angular divergence were recorded as dark spots and in case of the emission beam high density they turned white solarization spots of the photoemulsion. The "solarization" is produced by a photographic negative in response to high energy density irradiation.
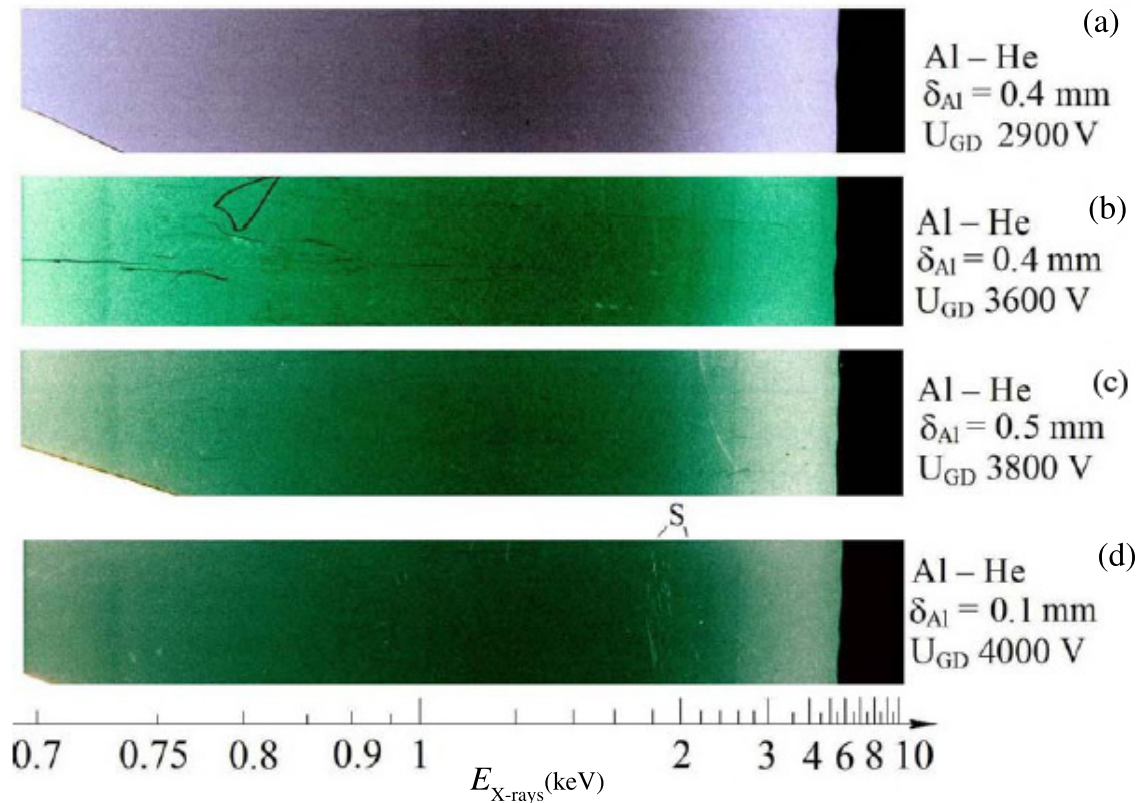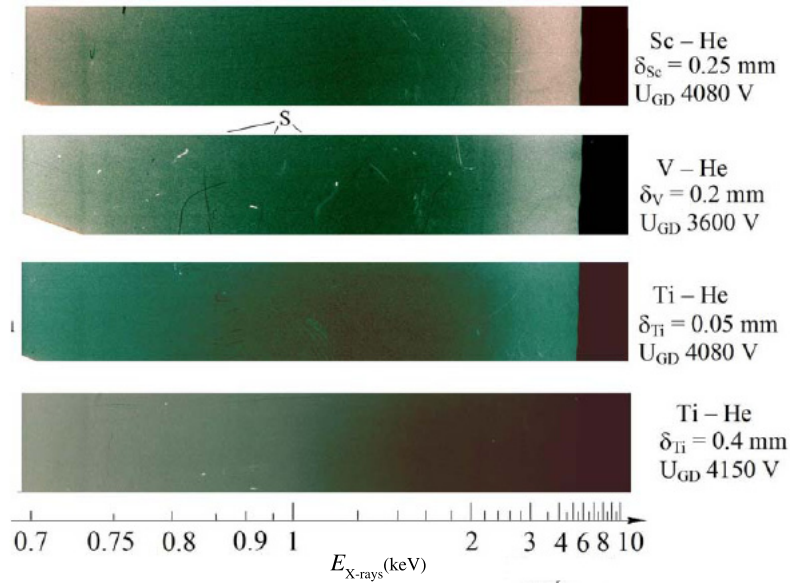
**Figure 3.** X-ray energy spectra from Al cathode different thickness ($\delta_{Al}$). He discharge. $U_{GD}$ is Glow Discharge voltage. S – white solarization spots of photoemulsion from X-ray monoenergetic beams with small angular divergence.

### 2.3. X-ray spectra registration in the continuum modes for different cathode materials and gases during the glow discharge operation

An energy area of X– ray spectra in the continuum modes is 0.6– 6.0 keV (may be up to 10 keV). The maximum of specific X-ray emission intensity reside in 1–2 keV energy area for different cathode materials and gases.

### 2.4. X-ray energy spectra in the spot modes for different cathode materials and gases during the glow discharge operation
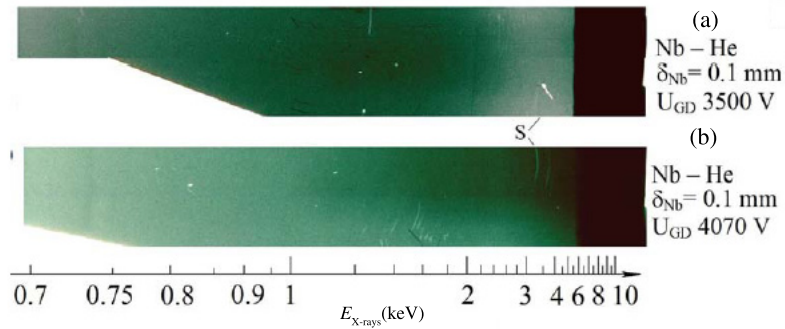
The X-ray monoenergetic beams with small angular divergence were recorded as dark spots and in case of the emission beam high density they turned white solarization of the photoemulsion. The beams were recorded as dark spots and in case of the emission beam high density they turned white (solarization of the photoemulsion). The "solarization" is produced by a photographic negative in response to high energy density irradiation.
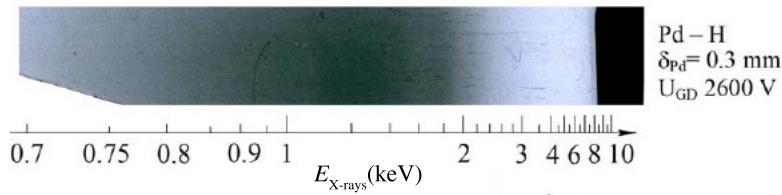
**Figure 4.**    Figure 4. X-ray energy spectra from Sc, V, and Ti cathodes different thickness.  He discharge.  $U_{GD}$ is Glow Discharge voltage.  S –
white solarization spots of photoemulsion from from X-ray monoenergetic beams with small angular divergence.
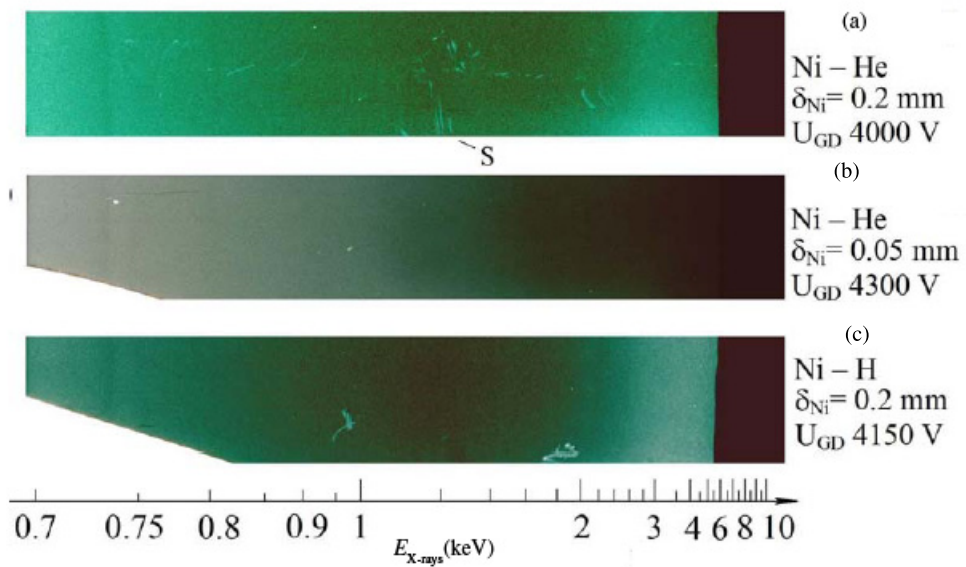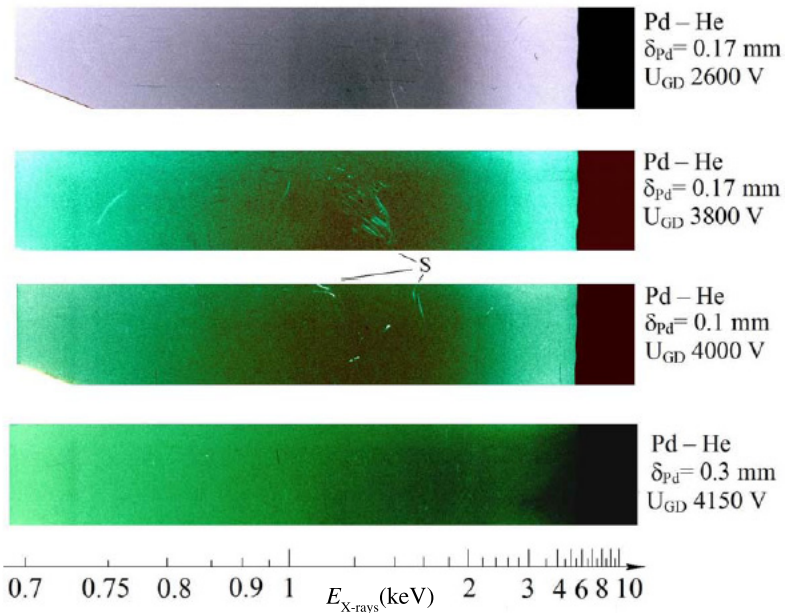


**Figure 5.**    X-ray energy spectra from Ni cathodes different thickness. He and H discharge. $U_{GD}$ is Glow Discharge voltage. S–white solarization
spots of photoemulsion from X-ray monoenergetic beams with small angular divergence.

**Figure 6.** X-ray energy spectra from Nb cathode different thickness. He discharge. $U_{GD}$ is Glow Discharge voltage. S – white solarization spots of photoemulsion from X-ray monoenergetic beams with small angular divergence.

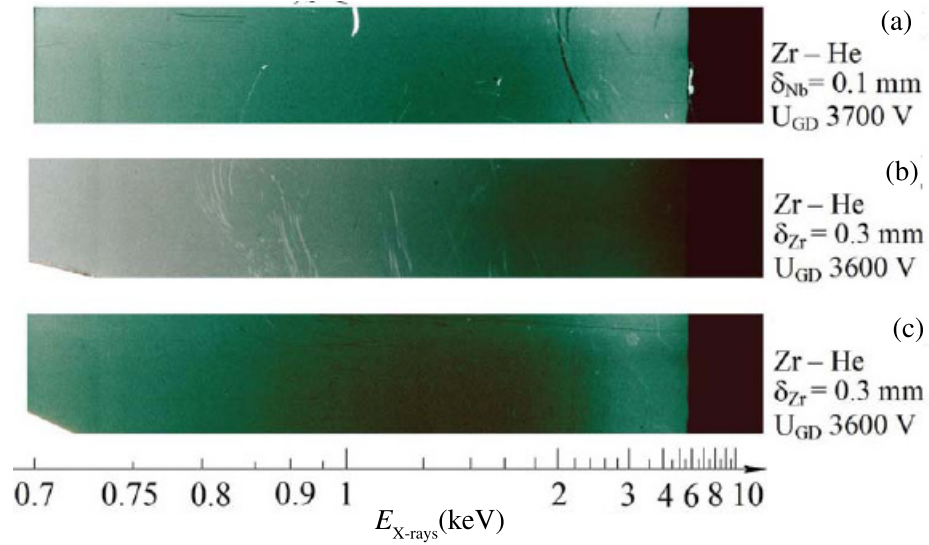

**Figure 7.** X-ray energy spectra from Pd cathode B $H_2$ discharge.



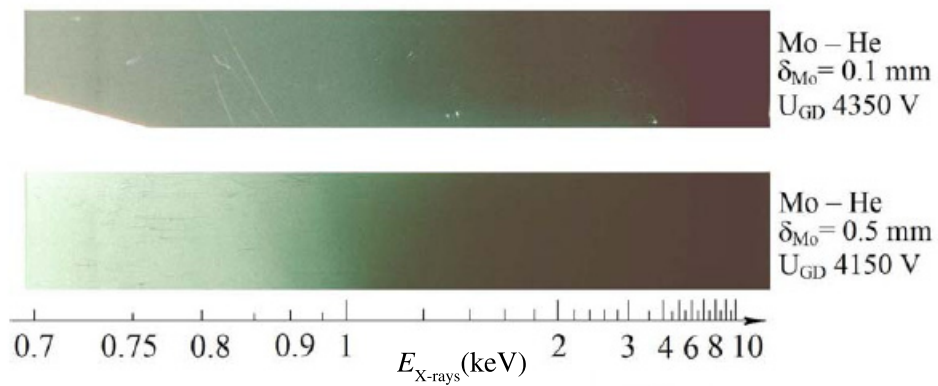**Figure 8.** X-ray energy spectra from Pd cathode different thickness $\delta_{Pd}$. He discharge. $U_{GD}$ is Glow Discharge voltage. S – white solarization spots of photoemulsion from X-ray monoenergetic beams with small angular divergence.

**Figure 9.** X-ray energy spectra from Zr cathode different thickness $\delta_{Pd}$. He discharge. $U_{GD}$ is Glow Discharge voltage. S–white solarization spots of photoemulsion from X-ray monoenergetic beams with small angular divergence.



**Figure 10.** X-ray energy spectra from Mo cathode different thickness $\delta_{Mo}$. He discharge. $U_{GD}$ is Glow Discharge voltage. S – white solarization spots of photoemulsion from X-ray monoenergetic beams with small angular divergence.
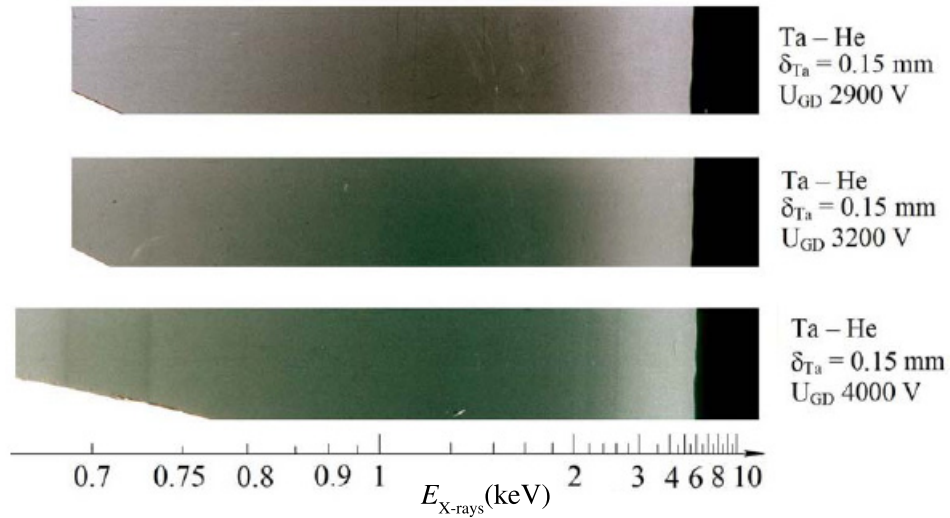
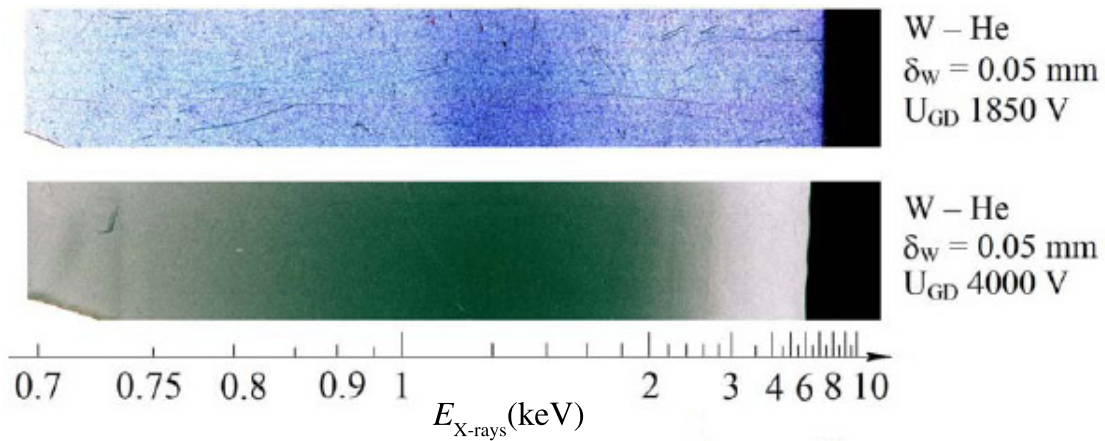**Figure 11.**   X-ray energy spectra from Ta cathode different thickness $\delta_{Ta}$. He discharge. $U_{GD}$ is Glow Discharge voltage.



**Figure 12.**   X-ray energy spectra from Mo cathode different thickness $\delta_W$. He discharge. $U_{GD}$ is Glow Discharge voltage.
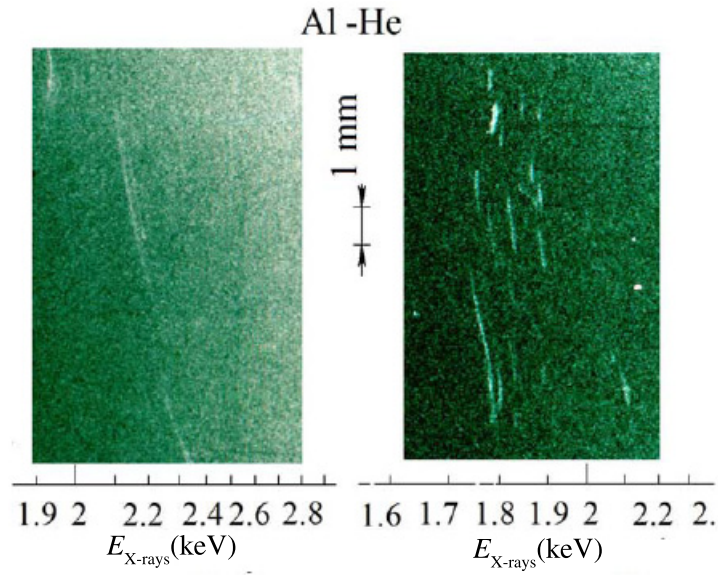
**Figure 13.** X-ray energy spectra in the spot modes for Al cathode, He discharge.
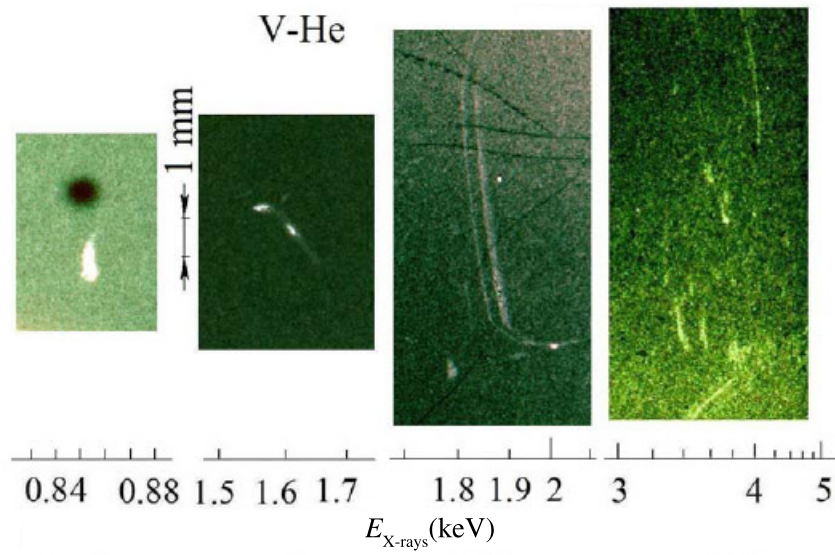


**Figure 14.** X-ray energy spectra in the spot modes for V cathode, He discharge.

**Figure 15.**   X-ray energy spectra in the spot modes for Ni cathode, H and He discharge.



**Figure 16.**   X-ray energy spectra in the spot modes for Zr cathode, He discharge.

**Figure 17.**   X-ray energy spectra in the spot modes for Nb cathode, He discharge.
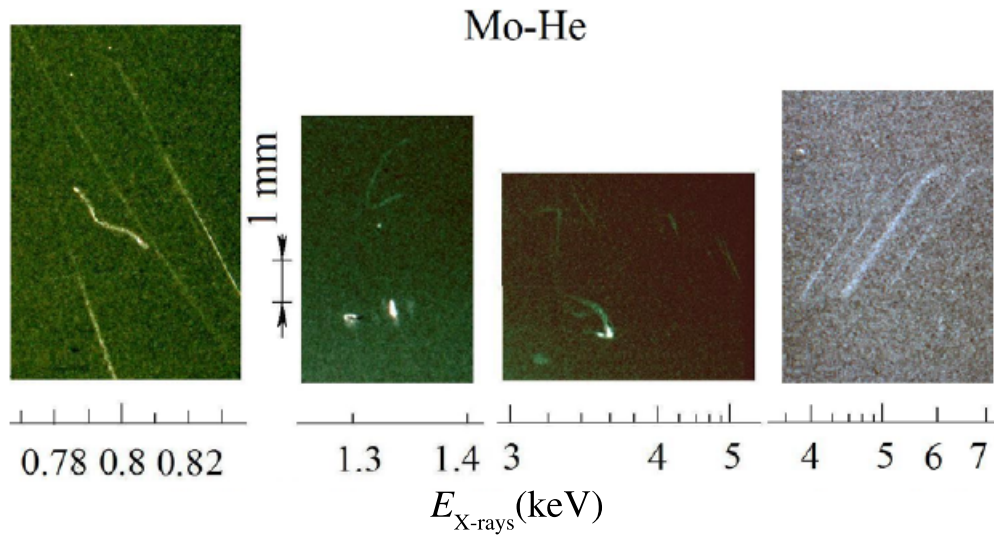


**Figure 18.**   X-ray energy spectra in the spot modes for Mo cathode, He discharge.
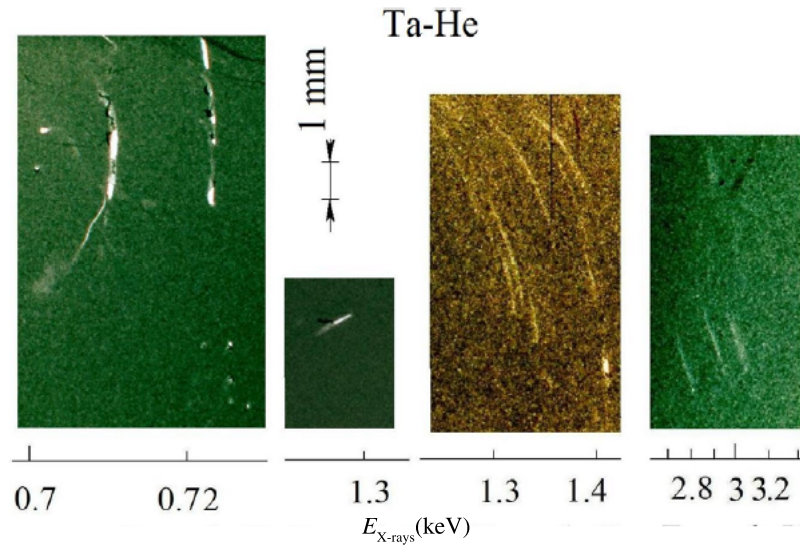
**Figure 19.** X-ray energy spectra in the spot modes for Ta cathode, He discharge.
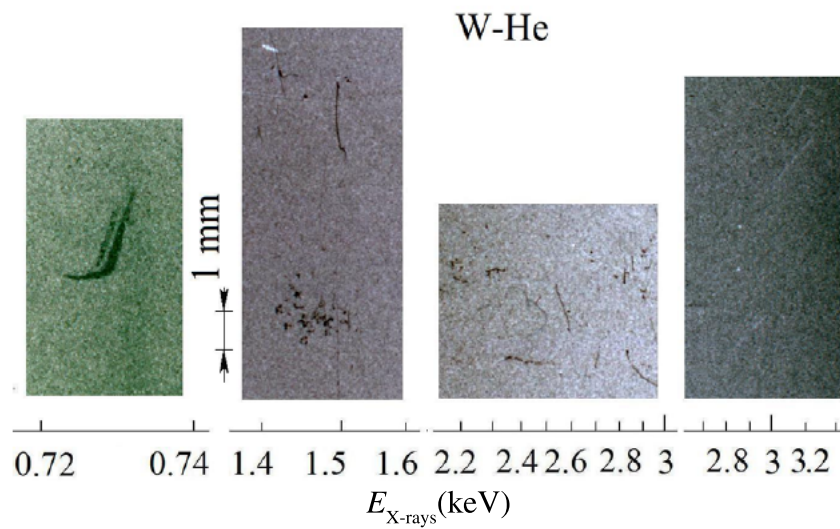


**Figure 20.** X-ray energy spectra in the spot modes for W cathode, He discharge.
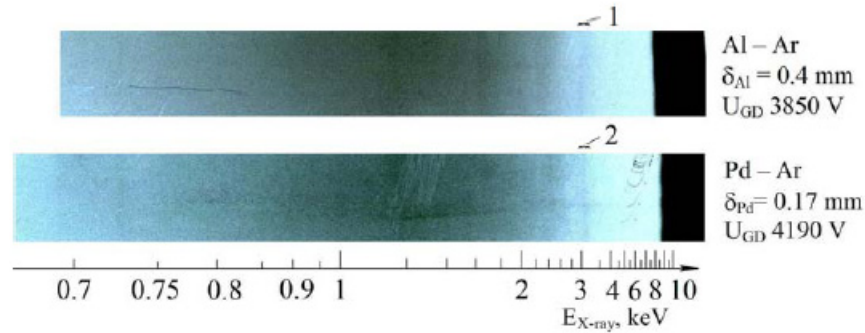
**Figure 21.** X-ray energy spectra in the band modes. 1,2 – energy is 3.19 keV, K–$M_3$ transition for Ar.
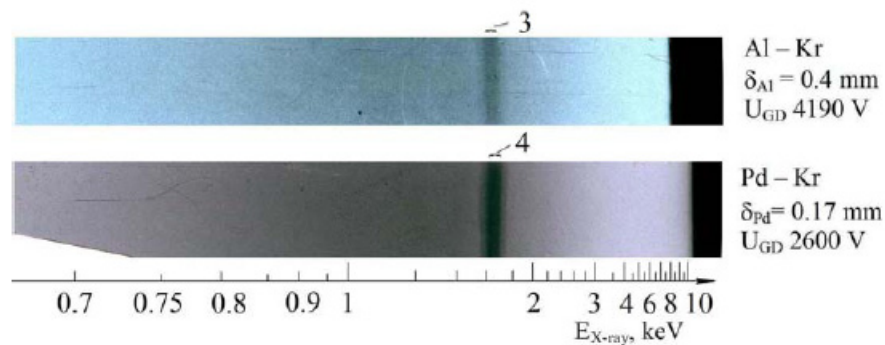


**Figure 22.** X-ray energy spectra in the band modes. 3,4 – energy is 1.65 keV, L3-M1 transition for Kr.

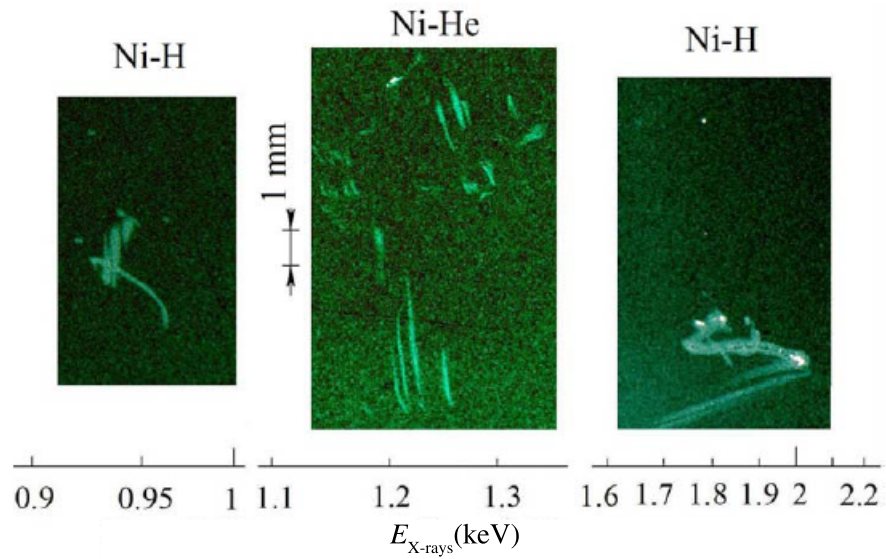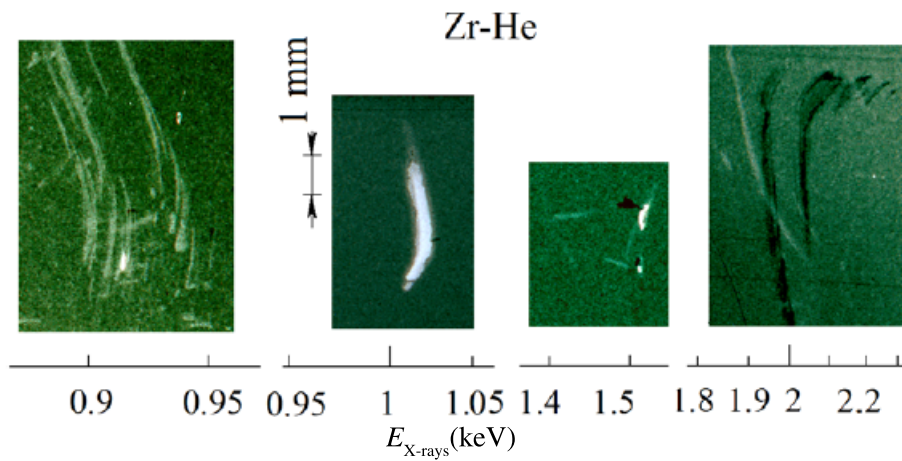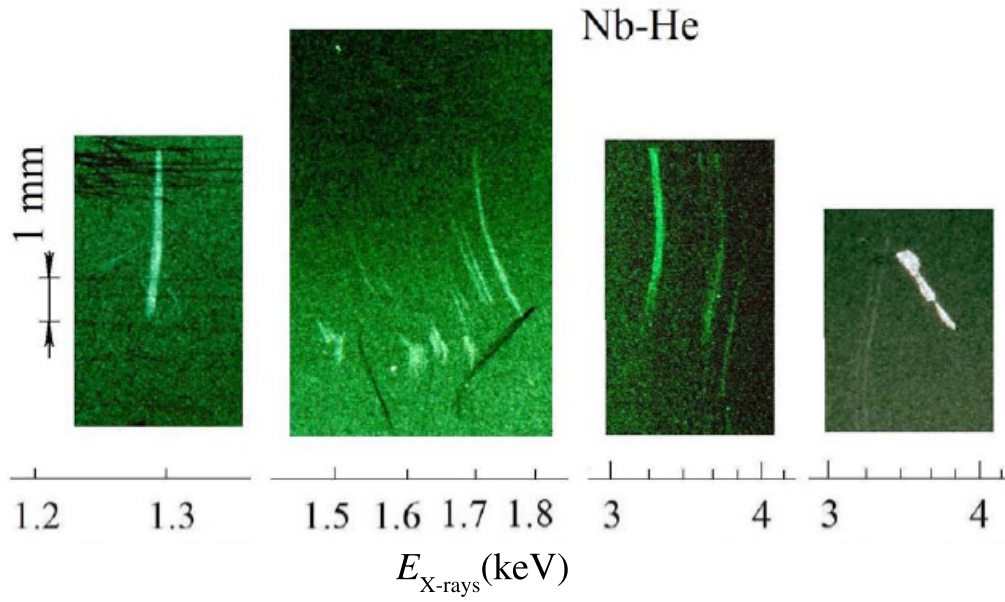### 2.5. X-ray energy spectra in the band modes for different cathode materials and gases during the glow discharge operation

It was assumed that the diffusion component of the X-ray emission was registered on the spectrum as a series of bands. The X-ray emission bands energy correlated with K–L and L–N X-ray transitions. X-ray spectra include bands: K–$M_3$ X-ray transitions with 3.19 keV energy for Ar (discharge in Ar), $L_3$–$M_1$ (1.65 keV) for Kr (discharge in Kr), $L_1$–$N_3$ (2.503 keV) for Zr (discharge in He), $L_2$–$M_4$ (2.395 keV) and $L_2$–$N_2$ (2.623 keV) for Mo (discharge in He). X-rays emit from the solid cathode medium.

### 2.6. X-ray Energy spectra in the spots and bands modes for different cathode materials after the glow discharge switch off

X-ray energy spectra were registered in the black spots and bands modes. An energy area of X-ray spectra were determined the cathode materials.
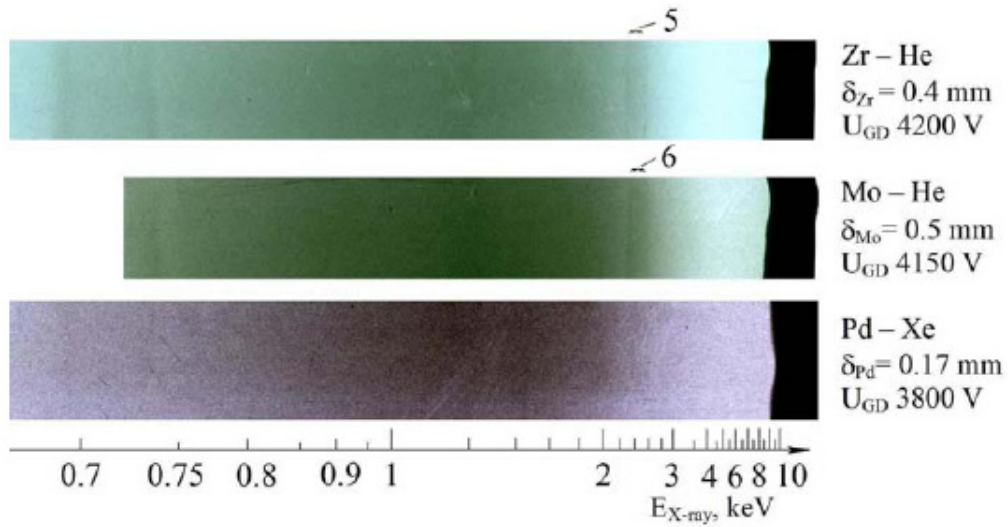
**Figure 23.**   X-ray energy spectra in the band modes.  5 – energy is 2.503 keV, L1-N3 transition for Zr, 6 – energy is 2,395 keV, L2- M4 transition for Mo.
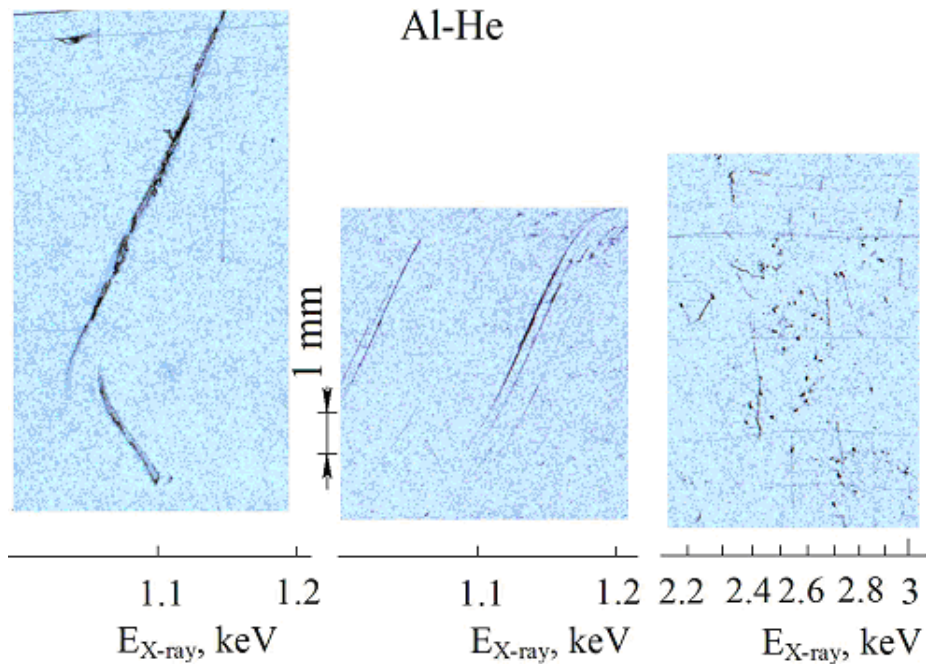


**Figure 24.**   X-ray energy spectra in the spots and bands modes for Al cathode after the He glow discharge switch off. Exposition time is 20 h.
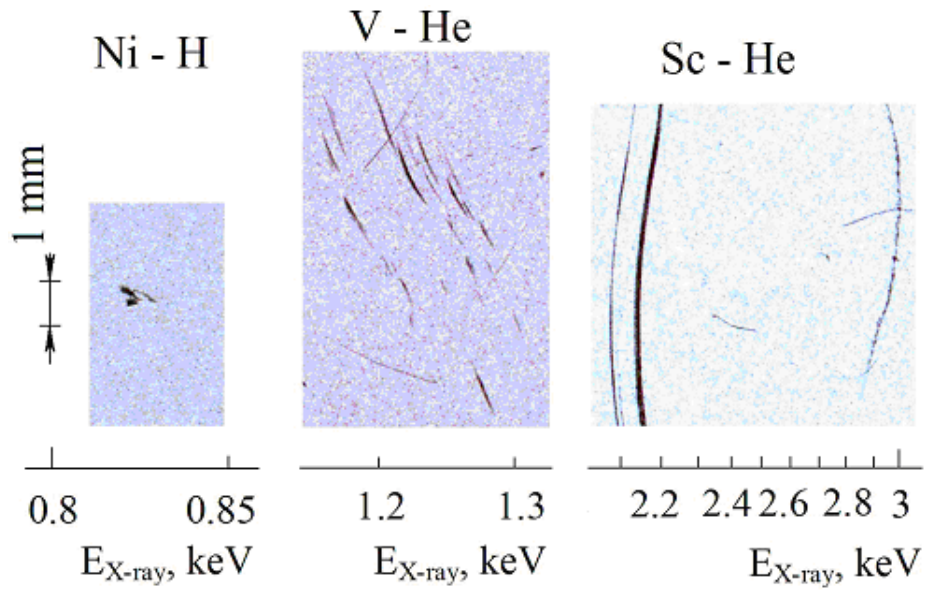
**Figure 25.**   X-ray energy spectra in the spots and bands modes for Ni, V, and Sc cathodes after the He glow discharge switch off. Exposition time is 20 h.
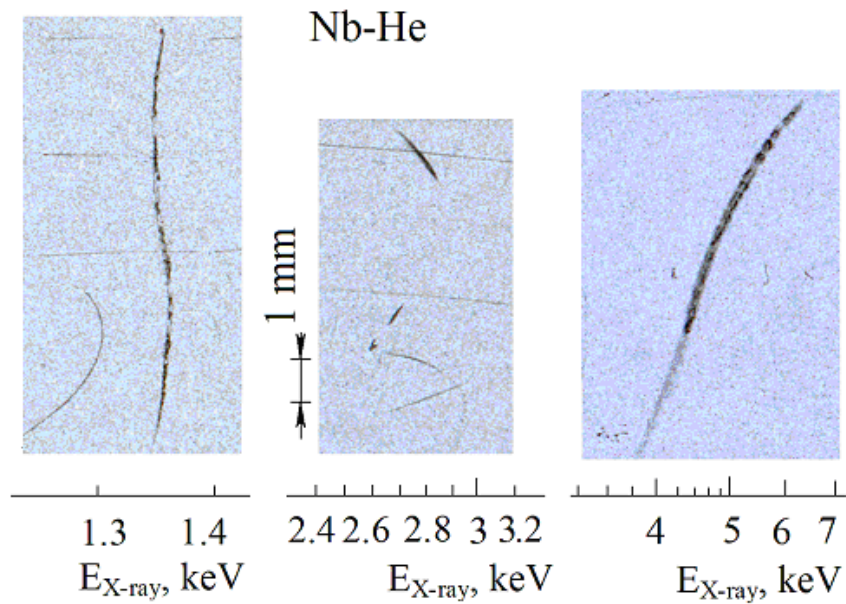


**Figure 26.**   X-ray energy spectra in the spots and bands modes for Nb cathode after the He glow discharge switch off. Exposition time is 20 h.
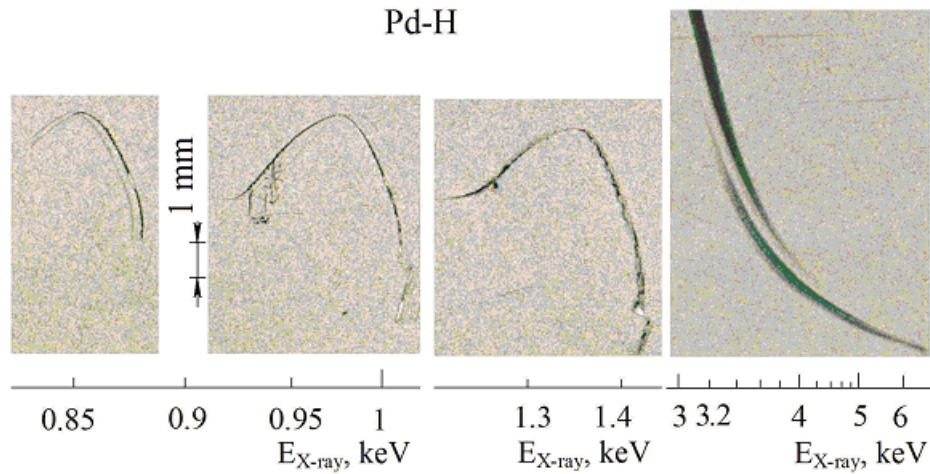
**Figure 27.** X-ray energy spectra in the spots and bands modes for Pd cathode after the H$_2$ glow discharge switch off.
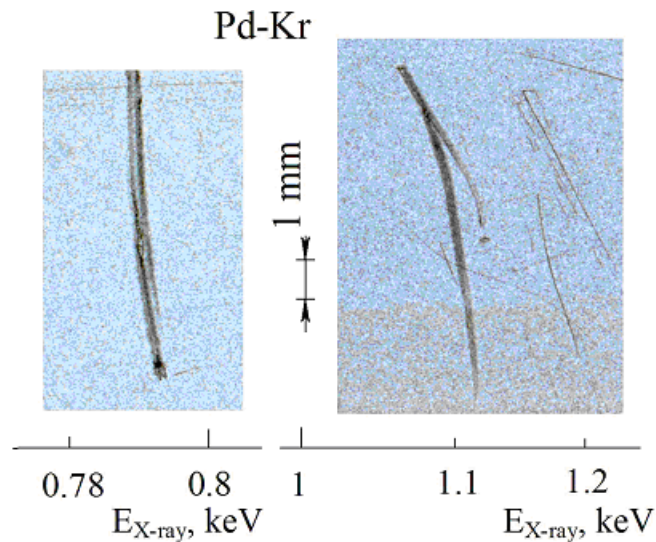


**Figure 28.** X-ray energy spectra in the spots and bands modes for Pd cathode after the Kr glow discharge switch off. Exposition time is 20 h.

## 3. Conclusion

The obtained experimental results allow us to consider the possible energy processes in the cathode solid material. The following processes may lead to initiation of LENR reactions. Presumably, some excited energetic levels are formed in the cathode solid when its surface is exposed to bombardment by the ions flux generated in plasma or electrolyte medium. The X-ray emission occurs as a result of de-excitation of these energetic levels.

The obtained results show that creating optically active medium with long-living levels with the energy of 0.6–6.0 keV and more is possible in solid matter.
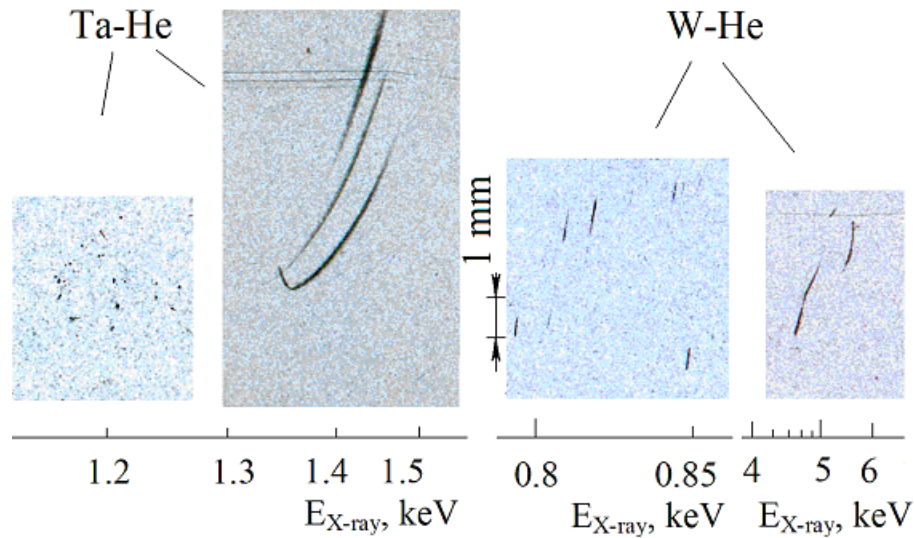
**Figure 29.** X-ray energy spectra in the spots and bands modes for Ta and W cathodes after the He glow discharge switch off. Exposition time is 20 h.

## References

[1] A.B. Karabut, Ya.R. Kucherov and I.B. Savvatimova, Nuclear product ratio for glow discharge in deuterium, *Phys. Lett.* A. **170** (1992) 265.

[2] A.B. Karabut, Research into powerful solid X-ray laser (wave length is 0.8-1.2nm) with excitation of high current glow discharge ions, *Proc. 11 Int. Conf. Emerging Nuclear Energy Systems*, 29 September–4 October 2002, Albuquerque, New Mexico, USA, pp. 374–381.

[3] A.B. Karabut, Research into characteristics of x-ray emission laser beams from solid-state cathode medium of high current glow discharge, *Proc. 11th Int. Conf. on Cold Fusion,* 31 October–5 November, 2004, France, pp. 253–257.

[4] A.B. Karabut and E. A. Karabut, Study of Deuterium Loading into Pd Cathode Samples of Glow Discharge, Proceedings of 9th International Workshop on Anomalies in Hydrogen / Deuterium Gas Loaded Metals, 6-11 September 2010, Siena, Italy.

Research Article

# Stimulation of Metal Deuteride Wires at Cryogenic Temperatures

## Francis Tanzella, Jianer Bao and Michael McKubre[*]

*SRI International, 333 Ravenswood Ave., Menlo Park, CA 94025, USA*

## Peter Hagelstein

*MIT, Cambridge, MA 02139, USA*

**Abstract**

Several groups have reported anomalous effects (heat and nuclear products) in thin $PdD_x$ materials stimulated by different forms of electro-diffusion. Using our cryogenic calorimeter we have measured the energy released from destructive electro-diffusion of a highly loaded $PdH(D)_x$ wires, co-deposited $PdH(D)_x$ on highly loaded $PdH(D)_x$ wires, and $NiH(D)_x$ wires. Generally, the D loaded metals yielded greater and more reliable excess energy than seen with the H loaded metals. The co-deposited $PdD_x$ on highly loaded $PdD_x$ wires yielded greater excess energy than the bulk wire hydrides or $PdD_x$ co-deposited on Ag wires as predicted by the calculations of Hagelstein and DeChiaro. The addition of a partial monolayer of a recombination poison yields a highly loaded $PdD_x$ cathode. Electro-stimulation of $NiH(D)_x$ wires have also shown excess energy, suggesting that renewed interest in this system may be justified.

© 2012 ISCMNS. All rights reserved. ISSN 2227-3123

*Keywords:* Calorimetry, Cold fusion, Deuterium, Electrochemistry, Excess heat, Helium, Palladium

## 1. Introduction

Several groups [1,2] have reported anomalous effects (heat and nuclear products) in thin $PdD_x$ materials stimulated by different forms of electro-diffusion. The ultimate extrapolation of this technology is the electrical heating of thin $PdD_x$ wires resulting in destructive high-speed melting-"exploding wires". Exploding wire technology has been used for over 150 years to make fine metal particles [3]. Additionally, the nickel–hydrogen system has recently received renewed interest in its ability to yield anomalous effects.

Celani et al. [4–6] have reported loading thin Pd wires electrochemically up to high loading and sealing their surface electrochemically. Tripodi [6] reported that such sealed wires can be immersed in liquid nitrogen (LN) and analyzed for anomalous effects at those temperatures or soon after warming up. As such, electrically exploding such loaded wires while immersed in LN should release the deuterium and cause the evolution of gaseous $N_2$ equal to the electrical energy passed through the wire due to the heat capacity and enthalpy of vaporization of LN.

---

[*]E-mail: michael.mckubre@sri.com

One of the authors has proposed that if a vacancy-containing Pd lattice were formed and then deuterided by either exposure to $D_2$ gas or $D_2O$ electrolysis, $D_2$ molecules would diffuse to re-form in these vacancy locations. Hagelstein has hypothesized that these sigma-bonded $D_2$ molecules would allow interstitial $D_2$ to be converted to $^4$He in the solid state. The creation of large numbers of vacancies using electron or ion beams is possible, but quenching of many of the vacancies occurs over hours, limiting the concentration to the 0.1% level. The vacancies are stabilized by H or D at high loading, but they do not diffuse near room temperature. Co-deposition of Pd (as in the Szpak protocol) when the D/Pd loading is above 0.95 will produce a large vacancy fraction. We have tested this hypothesis by examining the co-deposition of $PdH(D)_x$ on $PdH(D)_x$ and Ag, which does not forma hydride, wires. We also chose to examine the co-deposition of $NiH(D)_x$ on Ni wires.

## 2. Experimental

The formation of highly loaded $PdH(D)_x$ wires has been described elsewhere [7]. We have also carried out a series of co-deposition (codep) experiments by co-depositing metal + H/D on various substrates. The codep process generates a significant amount of Pd point vacancies in the co-deposited layer and these vacancies are immediately filled by co-deposited D(H) or $D_2(H_2)$. According to our hypothesis, these vacancies are able to host molecular $D_2$, and are necessary for excess heat generation in Fleischmann–Pons type experiments [8]. We first co-deposited $PdD_x$ on 50 $\mu$m $PdD_x$ wire substrate. The wire was first loaded to a high D:Pd ratio ($>0.9$) in 50 $\mu$M $SrSO_4$ solution using the previously referenced experimental protocol, then a few milliliters of 250 $\mu$M $Hg_2SO_4$ was added to increase and stabilize the loading. After that, saturated (70–100 $\mu$M) $PdSO_4$ was added to the cell 1 ml at a time, each time allowing all of the $Pd^{2+}$ to be fully reduced and deposited on the substrate surface. It is important is to co-deposit at high current density, so the Pd concentration in the electrolyte has to be relatively low in order for the Pd to co-deposit without flaking off. Figure 1 plots the variation of applied current density and resistance ratio of a typical wire during loading and co-deposition versus time. The current density is generally around 20–60 mA/cm$^2$. High current density would probably raise the temperature of the thin wire and cause de-loading.

The resistance of the wire usually does not change significantly, indicating that the deuterium loading at the bulk wire is not changing significantly. Also, because the amount of $Pd^{2+}$ added is limited due to the low solubility of $PdSO_4$, the codep layer does not grow by more than 1 $\mu$m in most of the experiments. At the end of the codep process, Hg was added again to seal the loading, and the wire is transferred to the cryogenic calorimeter for testing. Note, $PdCl_2$ has much higher solubility by forming $[PdCl_4]^{2-}$ complex. However, $PdCl_2$ was not used because in the presence of $Hg_2SO_4$, insoluble $Hg_2Cl_2$ would quickly precipitate.

Similarly, Pd and D were also co-deposited on Ag wire substrates. No $PdSO_4$ was added until a steady state Ag wire resistance was seen after the initial application of current. The axial resistance of the wire was measured and recorded over the time. No appreciable resistance change was observed during the codep process, since the $PdSO_4$ concentration is very low, and the resulting the codep layer is usually less than 1 $\mu$m thick. At the end of the co-deposition, Hg was also added to stabilize the loading of the codep layer. EDX analysis was used after the cryogenic calorimeter test to see if any measurable Pd was deposited on the Ag surface.

Since the Ni/H system has been in the spotlight recently, we also performed a series of codep experiments using Ni wire substrates. To remove the oxide at the surface, anodic stripping was used at the beginning of each codep. An anodic current of 1 mA was typically applied for about 5 min. Both concentrated $NiSO_4$ (0.1–0.2 M) solutions and a mixture of $SrSO_4$ and $NiSO_4$ were used in forming the co-deposited layer. The morphology of the surface was examined. Pre-loading of the Ni wire is possible, but the process is painfully slow compared with that of Pd. Furthermore, hydride formation embrittles the Ni wire significantly and makes the process of transferring the loaded wire into the calorimeter very difficult. Therefore, in most of the experiments, the bulk Ni wire was not loaded. To complete the Ni system, we also tested the codep of Ni and D on Ni wires using the same experimental protocol.
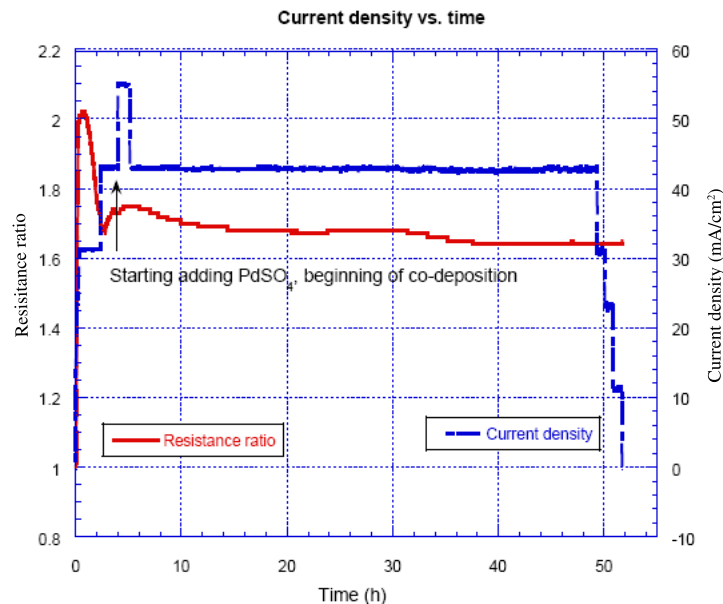
**Figure 1.**   Variation of current density and resistance ratio versus time during the loading/codep process.

After all the loading and codep processes were done, the wires were quickly transferred to the cryogenic calorimeter for excess energy testing as described above. SEM characterization and EDX analysis, and optical microscope observation were generally carried out after the calorimeter testing, to determine the quality of the deposited film, and any possible relationship between the surface morphology and the excess energy.

The wires are then immersed in liquid nitrogen in a cryogenic nitrogen boil-off calorimeter, shown in Fig. 2, which also shows the cathode connection blocks to be immersed in the LN. The copper probes hold the sample via a set-screw in each probe. This probe is then immersed in the LN, sealed with a low temperature O-ring, and held tight with two clamps.

The measured input energy from the pulse boils off a known amount of nitrogen, which is measured by a calibrated thermal mass flow meter (MFM). By using different length pulses into a 50 W 1 $\Omega$ current shunt immersed in the LN calorimeter, we calibrated the volume of $N_2$ evolved at different input energies. In the case of $PdD_x$, the energy from the input pulse will boil off a known volume of nitrogen. The voltage, current, and time were measured using a high-speed data acquisition system and transferred digitally to the computer. The analog output of the MFM is also measured by the high-speed data acquisition systems.

We also used nine 50 $\mu$m pure Pd wires to calibrate the calorimeter. The results are shown in Fig. 3 and indicate an error range for this calorimeter to be $\pm0.25$ ml. This error was obtained by analyzing a large amount of base flow rate fluctuation data over the time. This error id due to is a systematic variation caused by environmental temperature fluctuations. From the heat of vaporization of LN at 77 K we calculate that a temperature change of 1 K should result in a flow rate change of 8 ml/min for a typical test setting.

In Fig. 3 the resistor calibrations all fell directly on the calculated line. It is seen that all the calculated evolved gas volumes match well with the input energy and no excess energy has been seen. The input energy for pulses that break the wires is usually between 0.4 and 0.8 J, and the wire usually breaks in 3–6 ms. Using the heat capacity and heat of

fusion (melting) data provided by the computer program HSC$^{®}$ (Outokumpu), 0.75–0.9 J is needed to melt a 5–6 cm long Pd wire of 50 $\mu$m diameter in LN, neglecting the thermal conduction between the wire and the LN. However, the wire usually breaks at a weak point in around 1 ms, and the input energy is generally less than 0.1 J. The average response time for blank wires with diameter of 50 $\mu$m was 1.22 s, with a standard deviation of 0.035 s. Therefore, for the ease of calculation and minimal error, a response time of 1.2 s was used in calculating the volume of gas evolved after pulse input. All of the wires discussed here were stimulated using either a 50 V, 8 A, four-quadrant power supply (Kepco BOP 50-8, Flushing, New York) or a 20 V, 20 A, four-quadrant power supply (Kepco BOP 20-20, Flushing, New York).
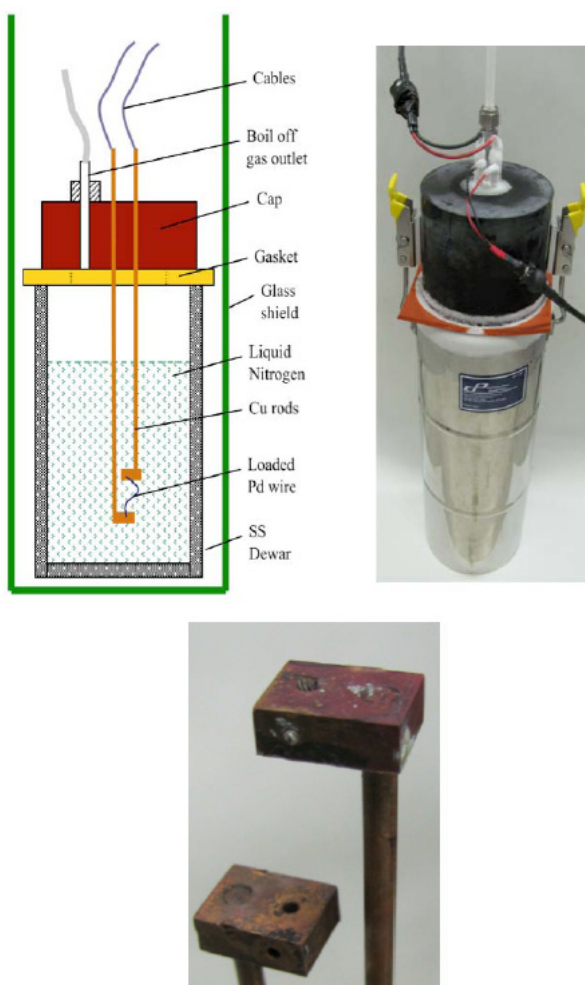


**Figure 2.** Photographs of the cryogenic calorimeter and its cathode connection blocks.
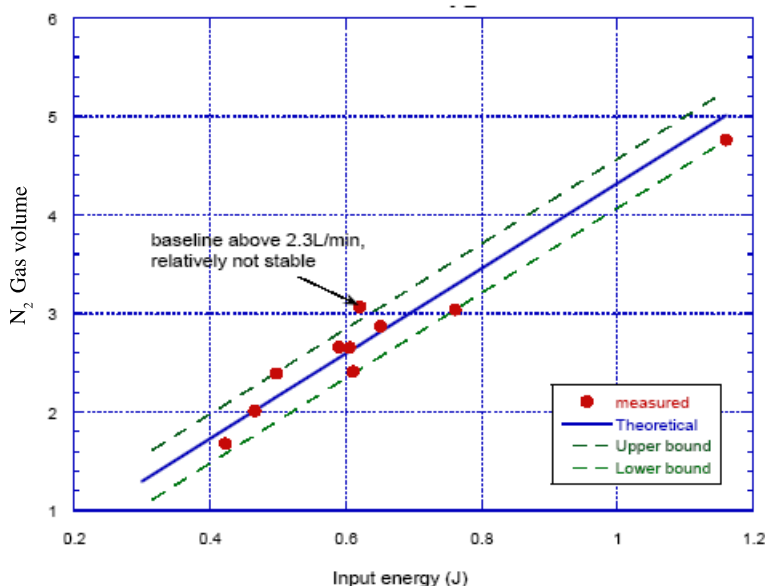
**Figure 3.**    Calibration of the cryogenic calorimeter with thin Pd wires. Error range is ±0.25 ml.

## 3. Results

Loading of H into 50 $\mu$m Pd wire is relatively easy. The ratio of resistance for the wire being loaded to that of the original wire usually passes through the maximum (indicating the formation of $PdH_{0.75}$) within an hour and then starts dropping. The final ratio H:Pd is generally near or greater than 1. High loading of D into 50 $\mu$m Pd wire (D:Pd) > 0.9) is difficult to achieve. Adding Hg could partially suppress the deuterium recombination process and increase the loading into the bulk, up to 0.97–0.98. After water ($D_2O$) splits into H(D) and oxygen at the surface of the cathode and anode, respectively, loading of H(D) is a result of competition between the surface recombination of H-H or D–D and the diffusion into the bulk as Pd is both a good catalyst and allows for fast diffusion of H(D). Initial surface condition and impurities in the system could significantly affect the loading. Table 1 lists the wire number, its final resistance ratio and the loading level for H or D, in the case of 50 $\mu$m Pd wires.

The development of a large number of Pd vacancies is the key issue [9] here for excess heat production, since molecular $D_2$ can form in one of the octahedral sites around a vacancy in PdD. The electron density is too high in bulk PdD, so that occupation of anti-bonding orbitals occurs, and the deuterium atoms are pushed apart. Co-deposition at high loading (D/Pd > 0.95) can produce the vacancies, and high loading (D/Pd > 0.85) causes the other octahedral-sites near the vacancy to be occupied which is required to stabilize the $D_2$.

We first tested the vacancy hypothesis by co-depositing various amount of Pd and D on highly loaded 50 $\mu$m $PdD_x$ wires. The substrate wire was usually loaded to $x$ > 0.92 in pure 0.05 M $SrSO_4$solution, then partially sealed by a few monolayers of Hg. $PdSO_4$ solution was then added 1ml at a time. After adding Pd, the resistance could either go up or go down, with the former indicating that the de-loading of the substrate wire may be the dominating process and the later indicating that the codep process is the most dominating. Table 2 lists the Pd wires that were first loaded and then subjected to the co-deposition of various amount of Pd and D. Scanning electron micrographs shows that these co-deposited Pd films are composed of nano-particles and dendrites. The size of nano-particles is usually less than

200 nm.

Since our hypothesis is that the codep layer is key in contributing to the generation of excess heat, we need to differentiate its contribution from the bulk-loaded wire, and demonstrate its role in the generation of excess heat. We carried out the co-deposition of Pd and D on Ag wire substrate, since Ag does not load H(D), and therefore does not participate in the process of excess energy generation. If excess heat is still seen without a highly loaded Pd bulk, it could indicate the importance of the codep layer, and meanwhile, indicate to which degree, the codep layer contributes to the overall process in a highly loaded Pd wire.

Electrolysis was first carried out on an Ag wire in pure $SrSO_4$ electrolyte where no resistance change was seen and the wire remained intact. After that, $PdSO_4$ solution was added usually 1 ml at a time. Only small variations of resistance were seen, since the amount of Pd deposited (within 1 $\mu$m) was negligible compared to the diameter of the Ag wire (50 $\mu$m). Therefore, the loading level in the codep layer was also not clear. Table 3 summarizes the experimental conditions for all the codep experiments on Ag wire substrate. Generally, a nice film could be seen using an optical microscope.

**Table 1.** Final resistance ratio and corresponding loading levels for 50 $\mu$m Pd wires.

| Wire No. | Diameter ($\mu$m) | Composition | Final ratio | Loading ($x$) |
|---|---|---|---|---|
| 9 | 50 | $PdH_x$ | 1.27 | $\sim 1$ |
| 10 | 50 | $PdH_x$ | 1.16 | $> 1$ |
| 11 | 50 | $PdH_x$ | 1.18 | $> 1$ |
| 19 | 50 | $PdH_x$ | 1.28 | $\sim 1$ |
| 20 | 50 | $PdH_x$ | 1.31 | $\sim 1$ |
| 8 | 50 | $PdD_x$ | 1.77 | 0.88 |
| 12 | 50 | $PdD_x$ | 1.58 | 0.98 |
| 13 | 50 | $PdD_x$ | 1.7 | 0.93 |
| 14 | 50 | $PdD_x$ | 1.65 | 0.95 |
| 15 | 50 | $PdD_x$ | 1.62 | 0.96 |
| 16 | 50 | $PdD_x$ | 1.6 | 0.97 |
| 17 | 50 | $PdD_x$ | 1.61 | 0.97 |
| 18 | 50 | $PdD_x$ | 1.79 | 0.90 |

**Table 2.** Summary of $PdD(H)_x$ co-deposited on $PdD(H)_x$ wires.

| Wire No. | Diameter ($\mu$m) | Composition | $PdSO_4$ (ml) | Final ratio | Loading $x$** |
|---|---|---|---|---|---|
| 23 | 50 | $PdD_x/PdD_x$ | 1* | 1.94 | 0.85 |
| 24 | 50 | $PdD_x/PdD_x$ | 3.5 | 1.74 | 0.92 |
| 25 | 50 | $PdH_x/PdH_x$ | 10 | 1.44 | 0.92 |
| 26 | 50 | $PdD_x/PdD_x$ | 5.5 | 1.66 | 0.95 |
| 29 | 50 | $PdD_x/PdD_x$ | 3 | 1.75 | 0.91 |
| 30 | 50 | $PdD_x/PdD_x$ | 6 | 1.65 | 0.94 |
| 31 | 50 | $PdD_x/PdD_x$ | 9 | 1.65 | 0.94 |
| 32 | 50 | $PdD_x/PdD_x$ | 8 | 1.62 | 0.96 |
| 37 | 50 | $PdD_x/PdD_x$ | 12 | 1.72 | 0.93 |
| 38 | 250 | $PdD_x/PdD_x$ | 3 | 1.85 | 0.88 |
| 39 | 250 | $PdD_x/PdD_x$ | 13 | 1.84 | 0.89 |
| 40 | 250 | $PdD_x/PdD_x$ | 10 | 1.74 | 0.92 |
| 42 | 250 | $PdD_x/PdD_x$ | 5 | 2.00 | 0.76 |
| 43 | 250 | $PdD_x/PdD_x$ | 10 | 1.95 | 0.84 |

*1 ml of 0.05 M $PdCl_2$ was added, which caused the precipitation of $Hg_2Cl_2$ when $HgSO_4$ was added.
**Loading of the bulk wire.

The nickel–hydrogen system has been of great interest in this field for a long time. Various results have been reported including transmutation products and radiation emission, besides excess heat [10]. In this work, we have also carried out Ni/natural water electrolysis experiments. Since codep generally gave us more excess heat in the PdD$x$ system, codep of Ni and H/D was subjected to a similar experimental protocol. The morphology of electrodeposited Ni film can vary significantly from a nice crystalline film to poorly adhered dendrites, depending on the solution used and current density applied. Our experimental results confirmed those variations, as will be discussed below.

Several solution combinations were used to test our hypothesis and determine the morphological changes of the codep layer and its effect on the excess heat generation: pure 0.1 and 0.2 M $NiSO_4$, mixtures of $NiSO_4$ and $SrSO_4$ solutions. Currents from 2 to 5 mA were applied, corresponding to $\sim$250–600 mA/cm$^2$ for 50 $\mu$m diameter, 5 cm long wires. Pre-loading of Ni with H was tried at the beginning. It was found that loading was very slow with resistance increase similar to that of Pd wires. However, as noted above, the hydrided Ni wires became extremely brittle making the transfer process very difficult. Therefore, it was later preferred not to load the Ni wire before codep (it is likely that loading and codep could occur at the same time when a high over-potential is seen at the surface). The local loading at the surface only needs to be H/Ni > 0.7 for vacancies to form, which seems probable at high codep current density.

When the codep started after adding $NiSO_4$ to $SrSO_4$, the wire was observed to be surrounded by a layer of green solution. After a while, the green layer dispersed, and the wire resistance started to decrease continuously. When the green $NiSO_4$ was depleted, the resistance stopped decreasing and more $NiSO_4$ was added. If pure $NiSO_4$ was used to begin with, the wire resistance kept dropping quickly (though the resistance drop gradually leveled off as the current density continued to decrease with increasing surface area). The experiment was stopped at a certain resistance ratio and a few milliliters of $Hg_2SO_4$ were added before turning down the current in order to stabilize the loading in the codep layer. The amount of Ni deposited could be calculated from the final resistance of the wire, assuming a homogeneous film growth and that the resistance of the codep layer is similar to that of the bulk. Table 4 summarizes the codep experimental conditions of the Ni wires that have been tested. The calculated final wire diameter and film thickness are also shown. Generally, a nice, smooth metallic finish was obtained, with 10 $\mu$m grain size, when the applied current density was low and the cell thoroughly cleaned. Dendrites are usually formed in the presence of additives.

Table 5 summarizes the calorimetric results for loaded wires: $PdH_x$ and $PdD_x$. It is interesting to note that after a large amount of testing with thin Pd wires, it seems that whether the wire disintegrates into fine powders or simply breaks is determined by the nature and pre-history of the wire itself, and possibly has nothing to do with loading and generation of excess energy. If the wire has defects, it would break at the weakest point(s). Otherwise, the wire will completely disintegrate, whether it is loaded or blank. If the defect is very weak, then the input pulse energy is also very low, as the input energy is an indication of the energy to break the wire. It is also interesting to note that the wire with the highest deuterium loading was very brittle. When transferring it to the calorimeter, it broke several times near the point fixed to the calorimeter, and finally became too short to measure. Whether it is due to the high loading or an intrinsic defect within the wire is unknown since it happened only on one occasion.

**Table 3.** Summary of the experimental conditions for codep on Ag wires.

| Wire No. | Diameter ($\mu$m) | Material | $PdSO_4$ (ml) |
|---|---|---|---|
| 33 | 50 | Ag/PdD$_x$ | 8 |
| 34 | 50 | Ag/PdD$_x$ | 14 |
| 36 | 50 | Ag/PdD$_x$ | 16 |
| 41 | 50 | Ag/PdD$_x$ | 15 |
| 44 | 250 | Ag/PdD$_x$ | 15 |
| 45 | 250 | Ag/PdD$_x$ | 15 |
| 46 | 50 | Ag/PdD$_x$ | 12 |

**Table 4.**   Summary of codep experimental conditions for Ni wires and the thickness of deposited film.

| Wire No. | Composition | Electrolyte | Final ratio | Final diameter ($\mu$m) | Film thickness ($\mu$m) |
|---|---|---|---|---|---|
| 47 | Ni/NiH$_x$ | 0.2 M NiSO$_4$ | 0.062 | 201 | 75.5 |
| 48 | Ni/NiH$_x$ | 0.1 M NiSO$_4$ | 0.074 | 184 | 67 |
| 49 | Ni/NiH$_x$ | 0.2 M NiSO$_4$ | 0.083 | 174 | 62 |
| 50 | Ni/NiH$_x$ | 1.5 ml | 0.300 | 91 | 20.5 |
| 51 | Ni/NiH$_x$ | 1.5 ml with Ag, D$_2$O* | 0.961 | – | – |
| 52 | Ni/NiH$_x$ | 1 ml with Ag, D$_2$O* | 0.992 | – | – |
| 53 | Ni/NiH$_x$ | 0.5 ml with Ag, D$_2$O* | 0.986 | – | – |
| 54 | Ni/NiH$_x$ | 4 ml NiSO$_4$ + 2 ml Ag + 1 ml D$_2$O | 0.183 | 117 | 33 |
| 55 | Ni/NiH$_x$ | 2 ml NiSO$_4$ + 1 ml Ag + 0.3 ml D$_2$O | 0.143 | 132 | 41 |
| 56 | Ni/NiH$_x$ | 2.5 ml NiSO$_4$ + 0.8 ml Ag + 0.8 ml D$_2$O | 0.322 | 88 | 19 |
| 59 | Ni/NiD$_x$ | 0.1 M NiSO$_4$ | 0.165 | 123 | 36.5 |
| 60 | Ni/NiD$_x$ | 0.1 M NiSO$_4$ | 0.186 | 116 | 33 |
| 61 | Ni/NiD$_x$ | 0.1 M NiSO$_4$ | 0.216 | 108 | 29 |

* The amount of Ag and D$_2$O is about 1–2% of the mass (or volume?) of Ni.

**Table 5.**   Summary of the cryogenic calorimeter test results for loaded PdD$_x$ and PdH$_x$ wires.

| WireNo. | Composition | Final ratio | $x$ | Input energy (J) | Output energy (J) | Excess energy (J) | Excess% |
|---|---|---|---|---|---|---|---|
| 8 | PdD$_x$ | 1.77 | 0.88 | 0.12 ± 0.01 | 0.7 ± 0.12 | 0.6 ± 0.13 | 500 ± 100 |
| 9 | PdH$_x$ | 1.27 | $\sim 1$ | 0.68 ± 0.01 | 0.7 ± 0.12 | 0.1 ± 0.13 | 8 ± 18 |
| 10 | PdH$_x$ | 1.16 | $> 1$ | 0.64 ± 0.01 | 1.0 ± 0.12 | 0.3 ± 0.13 | 50 ± 19 |
| 11 | PdH$_x$ | 1.18 | $> 1$ | 0.37 ± 0.01 | 0.49 ± 0.06 | 0.12 ± 0.07 | 32 ± 16 |
| 12 | PdD$_x$ | 1.58 | 0.98 | 0.71 ± 0.01 | 0.84 ± 0.06 | 0.13 ± 0.07 | 18 ± 8 |
| 13 | PdD$_x$ | 1.7 | 0.93 | 0.94 ± 0.01 | 1.22 ± 0.06 | 0.28 ± 0.07 | 30 ± 6 |
| 14 | PdD$_x$ | 1.65 | 0.95 | 0.63 ± 0.01 | 0.70 ± 0.06 | 0.07 ± 0.07 | 10 ± 10 |
| 15 | PdD$_x$ | 1.62 | 0.96 | 0.53 ± 0.01 | 0.51 ± 0.06 | – 0.02 ± 0.07 | –4 ± 11 |
| 17 | PdD$_x$ | 1.61 | 0.97 | 0.50 ± 0.01 | 0.70 ± 0.06 | 0.20 ± 0.07 | 40 ± 12 |
| 18 | PdD$_x$ | 1.79 | 0.9 | 0.82 ± 0.01 | 1.25 ± 0.06 | 0.43 ± 0.07 | 52 ± 7 |
| 19 | PdH$_x$ | 1.28 | $\sim 1$ | 0.10 ± 0.01 | 0.37 ± 0.06 | 0.27 ± 0.07 | 270 ± 60 |
| 20 | PdH$_x$ | 1.31 | $\sim 1$ | 0.61 ± 0.01 | 0.66 ± 0.06 | 0.05 ± 0.07 | 8 ± 10 |

*Note*: The error percentage is calculated by dividing the inherit system error range 0.06J by the input energy of that specific wire.

Among the listed wires, eight wires were loaded with deuterium and five showed the generation of excess energy significantly higher than the error range. The amount of excess energy varies from 18 ±8% to 52 ± 7% (excluding wire No. 8, which has an excess percent of 500 ± 100%, but the N$_2$ flow rate baseline was unstable). One wire showed no significant amount of excess energy, one wire showed slight deficient energy, and one wire was not measured. No obvious correlation can be made between excess energy production and bulk loading level. Of the five wires loaded with hydrogen, three showed the generation of excess energy significantly higher than the error (note, wires Nos.9 and 10 were measured when the base flow rate was above 2 l/min or 1.9 l/min, and thus had relatively higher error). In one case, wire No.19, 270 ± 60% of excess energy was generated while the wire probably broke at a very weak point with the input pulse energy only at 0.1 J.

Wire No.18 is particular interesting. This wire generated the most excess energy, at 0.43 J. The wire broke at only one spot, and the remainder of the wire seems intact. However, two metal beads were seen at both of the broken ends.

**Table 6.**　Summary of the calorimetric test results for co-deposited Pd wires.

| WireNo. | Diameter ($\mu$m) | Composition | PdSO$_4$ added (ml) | $x$ | Input energy (J) ±0.0 1 | Measured energy (J) ±0.06 | Excess energy (J) ±0.07 | Excess % |
|---|---|---|---|---|---|---|---|---|
| 25 | 50 | PdH$_x$/PdH$_x$ | 10 | 0.92 | 0.74 | 0.99 | 0.25 | 34 ± 9 |
| 23 | 50 | PdD$_x$/PdD$_x$ | 1 | 0.85 | 0.44 | 0.73 | 0.29 | 66 ± 16 |
| 24 | 50 | PdD$_x$/PdD$_x$ | 3.5 | 0.92 | 0.29 | 0.61 | 0.32 | 110 ± 24 |
| 26 | 50 | PdD$_x$/PdD$_x$ | 5.5 | 0.95 | 0.47 | 1.26 | 0.79 | 168 ± 16 |
| 29 | 50 | PdD$_x$/PdD$_x$ | 3 | 0.91 | 0.59 | 0.88 | 0.29 | 49 ± 12 |
| 30 | 50 | PdD$_x$/PdD$_x$ | 6 | 0.94 | 0.73 | 1.99 | 1.26 | 173 ± 10 |
| 31 | 50 | PdD$_x$/PdD$_x$ | 9 | 0.94 | 0.89 | 1.92 | 1.03 | 116 ± 8 |
| 32 | 50 | PdD$_x$/PdD$_x$ | 8 | 0.96 | 0.93 | 2.23 | 1.30 | 140 ± 8 |
| 38 | 250 | PdD$_x$/PdD$_x$ | 3 | 0.88 | 0.98 | 2.20 | 1.22 | 124 ± 7 |
| 39 | 250 | PdD$_x$/PdD$_x$ | 13 | 0.89 | 0.89 | 1.39 | 0.50 | 56 ± 8 |
| 40 | 250 | PdD$_x$/PdD$_x$ | 10 | 0.92 | 3.13 | 3.51 | 0.38 | 12 ± 2 |
| 42 | 250 | PdD$_x$/PdD$_x$ | 5 | 0.76 | 5.08 | 8.98 | 3.90 | 77 ± 1 |
| 43 | 250 | PdD$_x$/PdD$_x$ | 10 | 0.84 | 1.82 | 2.56 | 0.74 | 41 ± 9 |

One of the beads is about 250 $\mu$m in diameter, and the other is smaller. Two other melted but unbroken spots are also seen in other regions of the wire. These two melts are relatively smaller in size. Since the wire was immersed in liquid nitrogen at 77 K, and the melting point for Pd is 1827 K, the melting of the wire indicates that at least some of the regions were heated up to at least 1827 K and melted to liquid. Melting a 250- $\mu$m-diameter ball of Pd from 77 K would require approximately only 0.02 J, which can be ignored in this analysis, given that the excess energy is estimated to be 0.43 J. The calculation is based on the density of Pd (12g/cm$^3$), the enthalpy of melt (157 J/g), and the temperature-dependent heat capacity provided by HSC$^{©}$ by Outokumpu.

Table 6 summarizes the calorimetric test result for codep experiments on highly loaded Pd wires. It is important to note that the H(D) loading at the surface is expected to be higher than the bulk loading reported in this table, such that many of the substrate wires will have surface loadings of 0.95 or greater.

Table 7 summarizes the calorimetric test result for all the codep experiments on Ag wires. It is seen that when a similar amount of PdSO$_4$ is deposited on a Ag wire, the amount of excess heat generated is much less than that generated from the PdD$_x$ codep on highly loaded PdD$_x$ wires. In fact, the level of excess energy generated for all of these Ag wires is around 0.5 J or below, similar to the loaded Pd wires.

**Table 7.**　Summary of the calorimetric test results for Pd/D$_x$ co-deposited Ag wires.

| Wire No. | Diameter ($\mu$m) | Material | PdSO$_4$ added (ml) | Input energy (J) ±0.01 | Measured energy (J) ±0.06 | Excess energy (J) ±0.07 | Excess % |
|---|---|---|---|---|---|---|---|
| 33 | 50 | Ag/PdD$_x$ | 8 | 0.31 | 0.84 | 0.53 | 170 ± 23 |
| 34 | 50 | Ag/PdD$_x$ | 14 | 0.98 | 1.21 | 0.23 | 23 ± 7 |
| 36 | 50 | Ag/PdD$_x$ | 16 | 0.48 | 0.96 | 0.48 | 100 ± 15 |
| 41 | 50 | Ag/PdD$_x$ | 15 | 0.55 | 0.52 | –0.03 | –5 ± 13 |
| 46 | 50 | Ag/PdD$_x$ | 12 | 0.52 | 0.77 | 0.25 | 48 ± 13 |

Both the Ni/H$_2$O (natural) and Ni/D$_2$O systems were studied, using 0.1 M or 0.2 M NiSO$_4$ solution, or by adding 0.1 M NiSO$_4$ to the dilute SrSO$_4$ solution. A summary of the calorimetric test results for all the Ni codep wires is

**Table 8.** Calorimetry results summary for co-deposited NiH(D)$_x$ wires.

| Wire No. | Composition | Codep film thickness ($\mu$m) | Input energy (J) | Measured energy (J) | Excess energy (J) | Excess % |
|---|---|---|---|---|---|---|
| 47 | Ni/NiH$_x$ | 75.5 | $0.91 \pm 0.01$ | $1.7 \pm 0.06$ | $0.79 \pm 0.07$ | $87 \pm 8$ |
| 48 | Ni/NiH$_x$ | 67 | $1.57 \pm 0.01$ | $1.55 \pm 0.06$ | $-0.02 \pm 0.07$ | $-1 \pm 4$ |
| 49 | Ni/NiH$_x$ | 62 | $4.53 \pm 0.01$ | $5.56 \pm 0.06$ | $1.03 \pm 0.07$ | $23 \pm 2$ |
| 50 | Ni/NiH$_x$ | 20.5 | $0.87 \pm 0.01$ | $1.28 \pm 0.06$ | $0.41 \pm 0.07$ | $47 \pm 8$ |
| 59 | Ni/NiD$_x$ | 36.5 | $0.25 \pm 0.01$ | $0.76 \pm 0.06$ | $0.51 \pm 0.07$ | $204 \pm 28$ |
| 60 | Ni/NiD$_x$ | 33 | $0.32 \pm 0.01$ | $0.81 \pm 0.06$ | $0.49 \pm 0.07$ | $153 \pm 22$ |
| 61 | Ni/NiD$_x$ | 29 | $1.59 \pm 0.01$ | $2.45 \pm 0.06$ | $0.86 \pm 0.07$ | $54 \pm 4$ |

shown in Table 8. All the experiments were performed using 50 $\mu$m Ni wires. Again the H(D) loading at the surface is expected to be higher than the bulk loading reported in this table, such that many of these wires can have surface loadings of at least 0.7.

## 4. Conclusions and Future Work

We have shown that we can load and seal 50 $\mu$m diameter PdH$_x$ and PdD$_x$ wires electrolytically and transfer those wires to a cryogenic calorimeter without loss of loading. Our cryogenic calorimeter can resolve as little as 0.4 J of input energy with a reproducibility of ∼0.06 J.

As reported earlier, we performed our cryogenic stimulation on seven deuterided Pd wires and five hydrided (natural) Pd wires. Excess energy had been measured from five of the seven PdD$_x$ wires and from three of the five PdH$_x$ wires. Generally, the amount of excess energy was greater for the deuterided system than for those electrolyzed in natural H$_2$O.

In this paper, we extended this technology to hydrides and deuterides co-deposited on highly loaded wires of similar composition. The relevant hypothesis here is that vacancies can be produced in abundance if (Pd or Ni) co-deposition occurs near 300 K at above a high threshold surface loading (0.95 or 0.70), and that at high loading sigma-bonded D$_2$ or HD can form at an octahedral site near the vacancy (as long as the other octahedral sites are occupied). This hypothesis also claims that these diatoms are important to the excess energy production process.

As can be seen in Table 6, all 12 of the co-deposited PdD$_x$ on PdD$_x$ wires showed excess energy. The largest amount of excess (3.9 J) occurred when the greatest input energy (5.08 J) was required due to the thickness (250 $\mu$m) of the wire. This showed that both the reproducibility and the absolute energy produced was greater with the co-deposited PdD$_x$ than with the bulk PdD$_x$ wire. In addition the one PdH$_x$ on PdH$_x$ wire also showed excess energy. However, due to the poor statistics we cannot draw any important conclusions from this latter result.

To test the importance of the substrate wire acting as a reservoir for the H(D) to maintain the high loading of the co-deposited PdH(D)$_x$, we co-deposited the palladium hydride on to pure Ag wire. Since Ag does not from a hydride or allow for H diffusion, this permitted comparison of a substrate that can act as a hydrogen reservoir to one that cannot, and therefore cannot sustain a de-loading flux from the bulk metal. As can be seen from Table 7, the co-deposited material on Ag showed less absolute and percentage excess energy (and on one occasion none at all) than did the material co-deposited on PdD$_x$. This suggests that a well-loaded H(D) reservoir helps achieve high surface loading. Hence, we feel that at least in this system, the presence of H$_2$ or D$_2$ in an octahedral site around a vacancy in the Pd lattice and a substrate that acts as an H or D reservoir acts to enhance the amount of excess energy yielded during stimulation.

Because of recently publicized reports of excess energy in the Ni/hydrogen system we re-examined the nickel/natural water system. Because of the apparent success of producing excess heat with our co-deposition experimental protocol,

we adopted this protocol for Ni system, instead of electrolyzing in aqueous carbonate or sulfate as have been reported elsewhere [11]. We performed four electrolysis experiments using natural $H_2O$ and three using $D_2O$. As seen in Table 8, the results suggest that the nickel/natural hydrogen system can be a viable system to produce excess energy. Wire No.61 (Ni/NiD$_x$) showed the largest excess energy density since it was performed using the thinnest co-deposition layer. This suggested that the nickel/deuteride or mixed nickel deuteride/hydride system may be an appropriate material to produce excess energy without using the expensive precious metals.

These results distinctly demonstrate the importance of this co-deposited layer, and that the reservoir of D/H could enhance the generation of excess heat, which substantiates our hypothesis. Also, The destructive stimulation method leads to excess energy in most of the systems studied and never when applied to pure Pd wires.
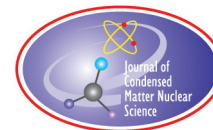
We intend to perform gas phase measurement of He isotopes from the headspace of future stimulated calorimeter experiments and on some of the electrolysis cells' headspace gas. We also anticipate using our metal vaporization inlet to the He isotope mass spectrometer to analyze any Pd fragments for anomalous He isotopic ratio.

## Acknowledgements

## References

[1] E. Del Giudice et al., The Fleischmann–Pons effect in a novel electrolytic configuration, in *Proc. 8th Int. Conf. on Cold Fusion,* The Italian Physical Society, 2000, pp. 47–54.

[2] C. Manduchi et al., Electric-field effects on the neutron emission from Pd deuteride samples, *Nuovo Cimento della Societa Italiana di Fisica, A Nuclei, Particles and Fields* **108A** (10) (1995) 1187–205.

[3] M. Faraday, Experimental relations of gold (and other materials) to light, *Philos. Trans. Roy. Soc.* London **147** (1857) 145–181.

[4] F. Celani et al., High hydrogen loading into thin palladium wires through precipitate of alkaline-earth carbonate on the surface of cathode: evidence of new phases in the Pd–H system and unexpected problems due to bacteria contamination in the heavy water, in *Proc. 8th Int. Conf. on Cold Fusion,* Italian Physical Society, 2000, pp. 181–190.

[5] F. Celani et al., Reproducible D/Pd ratio >1 and excess heat correlation by 1-micro s-pulse, high-current electrolysis, *Fusion Technol.* **29**(3) (1996) 398–404.

[6] P.Tripodi et al., Temperature coefficient of resistivity at compositions approaching PdH, *Phys. Lett.* A **276**(1–4) (2000) 122–126.

[7] F. Tanzella, J. Bao and M. McKubre, Calorimetry of Pulse Electro–Melting of PdDx Wires, *Proc. 15th Int. Conf. on Condensed Matter Nuclear Science*, ENEA (2009), pp. 42–46.

[8] D. Letts and P. Hagelstein, *J. Cond. Matter Nucl. Sci.* **6** (2011) 44.

[9] P. Hagelstein and I.U. Chaudhary, *J. Cond. Matter Nucl. Sci.* **6**( 2011) 169.

[10] G.H. Miley and P.J. Shrestha, Transmutation reactions and associated low-energy nuclear reactions effects in solids, *ACS Symposium Series*, **998** (Low-Energy Nuclear Reactions Sourcebook), 2008, pp. 173–218.

[11] R.L. Mills and S.P. Kneizys, Excess heat production by the electrolysis of an aqueous potassium carbonate electrolyte and the implications for cold fusion, *Fusion Technol.* **20**(1) (1991) 65–81.

Research Article

# What is needed in LENR/FPE studies?

Michael C.H. McKubre * and Francis L. Tanzella

*SRI International, Menlo Park, California, CA, USA*

Francis L. Tanzella

*Vittorio Violante, ENEA, Frascati, Rome, Italy*

## Abstract

ICCF16 marks nearly 22 years of research into the phenomenon first called "cold fusion". This new field has expanded in breadth to the point that numerous acronyms compete to describe overlapping effects. Two of these are: LENR (Low Energy Nuclear Reactions) and its subset FPE (the Fleischmann Pons Effect). Research to elucidate the basic processes and shed light on mechanisms has proceeded effectively continuously since March 1989 at SRI and elsewhere, and diligently and as "time and funds" have allowed at numerous other accomplished institutions worldwide. It is now clear to a well-informed but relatively small group of scientifically interested individuals that the deuterium-palladium systems conceals a heat source with energy exceeding by several orders of magnitude mechanical, lattice storage or chemical energy effects. Evidences of possible dd fusion products have been widely and numerously observed, at least partially ratifying the original speculative designation of "cold fusion". The effect, however, is apparently not limited to deuterium as a fuel, to helium as a product or to palladium as a matrix, hence the classification of the field as Condensed Matter Nuclear Science (CMNS) to differentiate these "new" effects from those observed in the rarified environments of particle and plasma physics. The materials-related issues associated with the so-called irreproducibility of CMNS effects presents the greatest barrier to the advancement and acceptance of the field. Precisely because we are dealing with condensed matter, micro-structural and micro-impurity control is difficult and expensive, requiring specialized equipment, control and skill. Problems of similar scale (and origin) have been faced and overcome in the past in the development of technologies having similar significance for mankind. Two (of many) examples are: the development of solid-state semiconductors; implementation of conventional nuclear power (and weapons). Absent another Bell Labs or Manhattan Project how should the CMNS field best proceed? Several overlapping options will be discussed. It is well within the capability of "mainstream" scientists and engineers in academia, and in national and private laboratories to resolve the materials issues and the questions of whether or not specific products are or are not present. Without funding they will not be encouraged to do so; without (a higher degree of) acceptance, adequate funding will not be made available. This paper will address various options and strategies to surmount this logical dilemma.
© 2012 ISCMNS. All rights reserved. ISSN 2227-3123

*Keywords:* Calorimetry, Cold fusion, Deuterium, Electrochemistry, Excess heat, Helium, Palladium

## 1. Introduction

The broadening of definition from "cold fusion" to "condensed matter nuclear science" reflects a marked expansion of avenues of research, interest and opportunity. This ICCF conference series has heavily focused on deuterium/palladium studies with a large emphasis on electrochemical studies as originally taught by Fleischmann and Pons [1]. This paper reflects that emphasis as it relies on experimental evidence generated at SRI in the years 1989–2011, almost exclusively in Pd/D studies of both electrochemical and gas loading systems. At the outset, however, it is worth noting that the work of Piantelli, Focardi and Rossi [2,3] in nickel/natural hydrogen, gas-loading systems has recently risen to interesting prominence. If demonstrated either by commercial application or by scientific acclaim as the result of publication, this "light" branch offers substantial advantage over more expensive routes employing palladium and deuterium, particularly if these alternate paths avoid electrochemical processes that are more challenging and potentially hazardous.

The process of selecting effective pathways forward remains the same whichever the route (or whatever, since others are imaginable). We are concerned with answers to the following questions:

1. What is the present state of knowledge?

   - What do we think we know?
   - Why do we think we know it?

2. How did we arrive at this position?
3. Why do doubts remain in the broader scientific community?
4. How do we propose to make progress?
5. What are the effective ways to proceed?

Salient questions on experimental procedure and observation emerged in 1989 and 1990 that were addressed in the experiments that followed. Here we pose some of the more relevant assertion and briefly address answers to them.

### 1.1. The experiments cannot be reproduced.

With the advantage of hindsight, Questions 1 and 2 above can be addressed effectively by answering Question 3. After 15 International Conferences in the ICCF series alone, thousands of published papers detailing nuclear products and heat effects consistent with nuclear but not chemical energies, why does doubt persist regarding the existence of condensed matter nuclear effects? What is the basis for this confusion?

We have previously addressed the issue and importance of replication in CMNS studies [4] and what Martin Fleischmann has referred to as "pathological criticism" [5]. However, the importance of "replication" and "reproducibility" (or its lack) in the criticisms of "cold fusion" cannot be overstated. First, it is worth noting that the key test in science is consistency, not identicality, but where do claims that CMNS experiments and results are not reproducible come from? Were these claims ever sensibly and scientifically correct? Are they correct now?

A large part of the apocrypha of irreproducibility was established by two highly influential early papers, authored by major institutions, Caltech [6] and MIT [7]. At the time in late 1989 and early 1990 when these papers were published, the importance and relative difficulty of loading deuterium (D, rather than protium, H) cathodically into palladium was recognized as an issue but had not been addressed fully. In the first Annual Conference on Cold Fusion [1] in early 1990 the SRI group made the comment that *"none of the "cold fusion" electrolysis experiments described to date contain any means of determining the D/Pd content in situ. Yet this ratio may be a crucial difference between those experiments that have produced a Fleischmann–Pons effect and those that have not"*. By making systematic study of D/Pd loading in situ, and its effect on Fleischmann–Pons excess heat product, it subsequently became clear that this was a threshold phenomenon [2], with a failure to load being a sufficient reason for the "negative" (more correctly null) results reported from Caltech [6] and MIT [7].

The experimental program at SRI was designed to pursue the hypothesis that *"an unexpected source of heat can be observed in the D/Pd System when Deuterium is loaded electrochemically into the Palladium Lattice, to a sufficient degree"*. This was the fundamental (and potentially transformational) claim of Fleischmann and Pons [1]. It was also clear from many decades of work with the electrochemical D/Pd system that no anomalous heat was observed in the well-studied region of low loading. Looking a little further ahead to a possible nuclear hypothesis one might also have predicted that the concentration of the most likely reactant (D) could play a role in the magnitude of the effect. It took several years of work at SRI [8–11] and elsewhere [12,13] to develop strong evidence corroborating the claim of Fleischmann and Pons [1] and supporting the hypothesis that deuterium plays a crucial and threshold effect in producing nuclear-level excess heat in the electrochemical deuterium-palladium system.

Figure 1 presents as a histogram an accumulation of positive excess heat results obtained at SRI (Menlo Park, US) and ENEA (Frascati, Italy) versus the maximum D/Pd loading obtained by the cathode. Also plotted are the null results (no measured thermal anomaly) obtained at Caltech [6] and MIT [7], versus the "expected" loading of their calorimetric cathodes. Neither Caltech nor MIT measured loading in situ, and instead compared the loading of calorimetric cathodes to values measured by weighing "similar cathodes" in a similar electrochemical environment [6,7].

With the advantage of hindsight we can make three observations:

1. The D/Pd loading of the population of successful excess heat producing cathodes at SRI and ENEA is clearly different from that of the cathodes unsuccessfully operated at Caltech and MIT.
2. Variability in loading is such that unless loading is poor (i.e. close to the equilibrium value with the 1 atmosphere of D2 bathing the cathode under conditions of vigorous electrolysis where D/Pd ∼ 0.7) then measurements of
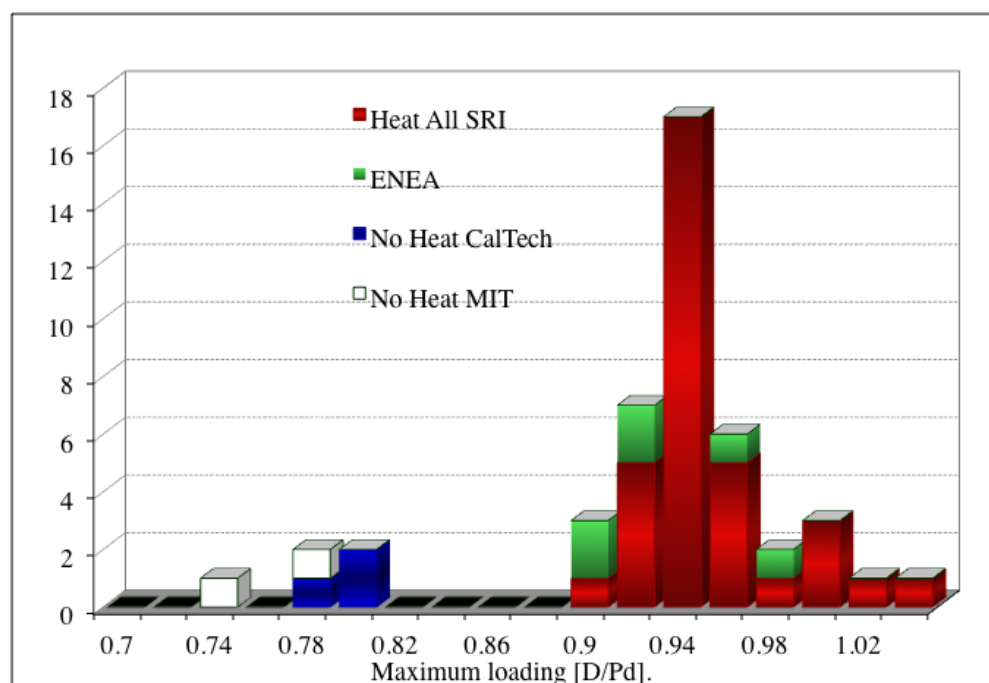


**Figure 1.**    Histogram of excess heat results obtained at SRI, ENEA Frascati, Caltech [6] and MIT [7].

loading made on "fraternal" cathodes are unlikely to be representative.

3. Only with great difficulty, with attention to cathode metallurgical and surface condition, scrupulous avoidance of deleterious impurities and slow and patient electrochemical skill driven primarily by feedback from the measured loading [3] can cathodes be loaded reliably to the minimum value of successful excess heat production shown in Fig. 1.

Obviously these details were unknown in 1989. Although the critical effect of loading might have been anticipated, the only error was over-simplification leading to a rapid rush to negative judgment that was inappropriate and unfortunate in a matter of such import. With a collective sigh of relief (and sometimes sharper tones) a majority in the establishment of physicist and physical chemists returned to what they were doing before 23 March 1989, effectively convinced by the lack of evidential support of the claims of Fleischmann and Pons in the work of Caltech [6] and MIT [7] (and also Harwell in England [14]).

In his definitive study of the Fleischmann Pons heat effect Beaudette [5] draws an excellent distinction between validation and corroboration. Corroboration shows that the initial report was not figmentary, but it does not exclude the possibility of some systematic error in the experiment. That one gets similar results from similar experiments is altogether expected. The argument surrounding the important null results cited above is the implicit claim that these researchers had done similar experiments (electrochemically) but had not obtained similar calorimetric results to Fleischmann and Pons. Leaving aside the (stated) assertion that Fleischmann and Pons were delusional, only two scientific conclusions are possible: either the experiments of Fleischmann and Pons were subject to systematic error, or the two sets of experiments were not similar in one or more detail that was important to the effect.

The Fleischmann–Pons Effect (FPE) has now been validated in numerous laboratories around the world [15,16], in independent experiments with no possibility of systematic overlap with the original experiments. It is also now evident that more than one detail must be attended to before the effect can be observed. One such detail relates to the precise metallurgy of the cathode. Figure 2 plots excess thermal power as a percentage of input electrochemical power for a set of cathodes manufactured at ENEA Frascati from different stock palladium and with subtly varied metallurgical processing [17]. Two sets of experiments were run, all with $\sim 50\,\grave{\i}$m thick foil cathodes in similar cells with similar electrochemistry. Calorimetric measurements were made of all of the material lots, either at ENEA, SRI or both; excess power was not observed for those material lots without data points. Two conclusions are clear: materials that did not yield excess power in one laboratory also did not in the other; when excess power was observed in one laboratory it was seen at similar percentage in the other.

The apparent discrepancy for L17 material is worth noting and elaborating, as this touches on another detail of difference between the original Fleischmann and Pons results and those of Caltech and MIT. The FPE has two active Modes referred to by us as "A" and "B". Mode A has been best studied using bulk wire cathodes and requires high loading ($x^{\mathrm{o}} = $ D/Pd $> \sim 0.9$), long initiation times (100's of hours at loading), and produces excess power:

$$P_{xs} = M\,(x - x^{\circ})^2\,(i - i^{o})|i_{\mathrm{D}}|, \tag{1}$$

where $i$ is the electrochemical current density and $i^{\circ}$ the current threshold and $|i_{\mathrm{D}}|$ is the magnitude of the deuterium flux permeating the interface. Although not extensively studied, Mode B excess heat production may have a lower loading threshold, at least when loading is measured as the bulk average value, and appears to be a feature of small dimension electrodes or regions. This mode can appear very early in an experiment and is not strongly or positively influenced by current density. Accordingly Mode B can appear with a large percentage excess power since the denominator (IV) can have small values and still achieve an excess heat effect. The L17 cathodes experienced at SRI showed reproducible excess power in Mode A of 12% and 13%, but 500% excess power at ENEA in Mode B.

Four factors are important in explaining the inability of earlier workers to produce and measure excess heat in electrochemical deuterium–palladium studies:
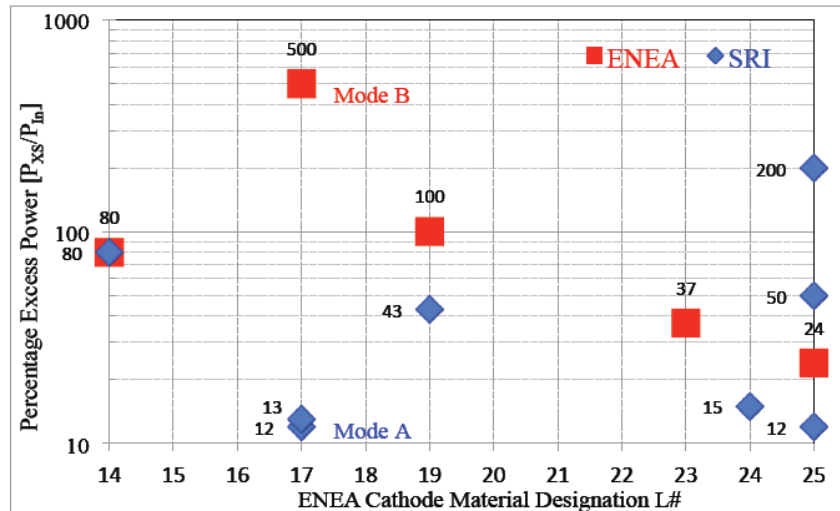
**Figure 2.** Excess power as a percentage of input power in experiments run at SRI and ENEA, Frascati, for different lots of 50 ìm foil cathodes manufactured at ENEA.

1. As indicated in equation[1] electrodes must be loaded above the loading threshold ($x^° \sim 0.875$ for Pd wire cathodes). This was very likely not achieved at Caltech and MIT.
2. The current density must be above a significant threshold value also probably not attained in the experiments performed at Caltech and MIT.
3. The condition of the cathode/electrolyte interface must be such that it is facile to deuterium exchange to promote or permit a significant iD flux. The value of this flux is undetermined in the Caltech and MIT experiments because loading was not measured in situ. Nevertheless, because the loading measured in parallel experiments was low it is unlikely that the calorimetric experiments performed at Caltech and MIT achieved a facile surface condition sufficiently free of impurity to promote a high value of $i_D$.
4. An initiation period orders of magnitude longer than the deuterium diffusional time constant must occur before any excess power is observed in Mode A [4].

This last point is exemplified in Fig. 3 that shows the time of first appearance of excess power for 1–3 mm dia. Pd wire and 50–100 ìm thick Pd foil cathodes for sets of experiments run at SRI and ENEA. For thin foils the earliest appearance of Mode A excess heat was 50 h with one electrode requiring 500 h despite our ability to fully load these cathodes with deuterium in less than 5 h. For the much thicker wires (with cylindrical geometry) Mode A excess heat was first seen at 200 h with one electrode requiring 950 h, although full loading can be achieved in less than 1 day. Clearly some other process is occurring which, if mass transport is involved, has a diffusion coefficient at least 1–2 orders of magnitude less than that of deuterium in the $PdD_x$ lattice.

### 1.2. The results are inaccurate.

The first place to look when seeking to explain an unpredicted result is error in measurement. For the unexpected results reported by Fleischmann and Pons [1] and for those seeking to verify or refute the FPE, there are two places where such errors might occur. Having first ensured that your experiment faithfully replicates the experimental conditions of the original work (see above) then one must set about measuring accurately the total power that enters the calorimeter, and
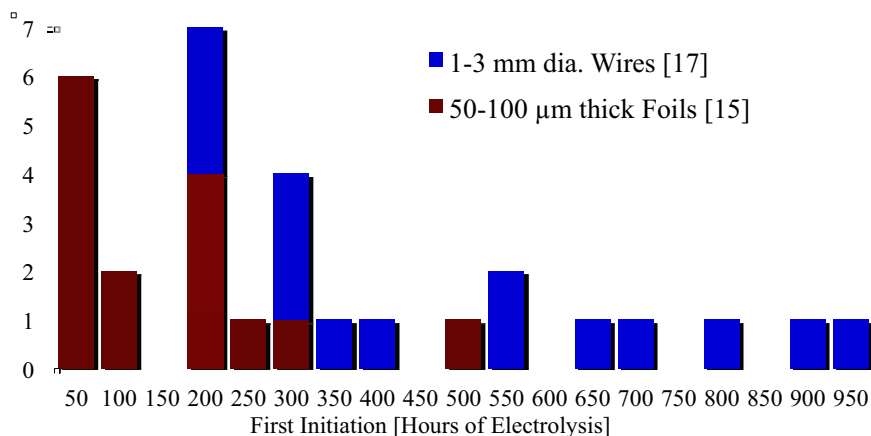
**Figure 3.** Time of first initiation of excess power for 1–3 mm dia. Pd wire and for 50 ìm Pd foil cathodes in experiments performed at SRI and ENEA, Frascati.

the sum of all heat that results. If more heat is yielded than input then one is measuring excess power, the integral of which is excess energy or heat. If the amount of excess is larger than can be accounted by energy storage or chemical effects then one must look at alternate explanations, potentially nuclear, and seek products (see discussion below).

This sequence and process of scientific discovery occupied perhaps the first 3 or 4 years of the modern "cold fusion" saga. Many hundreds of papers have been published and presented detailing different modes of calorimetry. These have been well reviewed by Storms [15] and constitute an impressive consensus. Using different approaches, different methods to measure input power, different instrumentation, and different calorimetric methadologies, in different laboratories worldwide, a concurrence of agreement has emerged. With attention paid to the (now) known initiating conditions excess power, energy and heat can be measured in the D/Pd system at levels statistically far in excess of the uncertainties associated with the measurement of electrical (and other) input and system thermal output.

## 1.3. The source of heat is mundane.

The power of the argument and evidence alluded to in the preceding section is essentially overwhelming. This has caused those, more experienced with measurement (and having read the literature), to look for an alternate explanation for the excess heat. It has been proposed that the excess heat is real but is due to unknown or unaccounted chemical effects or lattice energy storage. This argument can be refuted quantitatively. The heat observed as integrated excess power in many (but not all) FPE experiments exceeds the sum of all possible chemical or mechanical energy storage effects by factors of hundreds or thousands, or more.

The partial molar enthalpy of absorption of hydrogen (deuterium) in palladium varies with the state of loading but is always less than 1 eV per H or D atom added to the lattice [18]. Chemical reaction energies can range up to ∼3 eV. The largest continuous excess energy production observed at SRI was slightly greater than 2000 eV/Pd atom (or lattice D atom at ∼1:1 loading). Even more impressive numbers were reported by Energetics [19] who measured in a single burst lasting ∼17 h a net excess energy of 4.8 keV/Pd atom (with input electrical energy <200 eV/Pd). The system exhibited a second burst of 15.1 keV/Pd atom after a period of thermal neutrality (zero excess and no endothermic process), for a total of nearly 20 keV/Pd atom [5].

Energy densities at this level are inconsistent with known chemistry and one must look to the nuclear realm for possible explanations. Although "weak" nuclear reactions are known on the scale of keV, more typically these occur

with scale $\sim$1, 10 or even 100 MeV/nucleus. Thus the energies measured in FPE experiments are consistent with known nuclear effects if only a small fraction of he lattice participates simultaneously in the process, but are not consistent with known lattice storage or chemical effects even if all of the lattice participates. Clearly the source of FPE heat is not mundane, and may be sufficiently exotic to be of potential practical interest.

## 1.4. The nuclear products are missing

At this point we can begin to interrogate the nuclear question directly. The effect reported by Fleischmann and Pons was initially called "cold fusion", a name already in use for muon catalysis of two-body d–d fusion. Whatever Fleischmann and Pons saw it was clearly not that since the anticipated products of the fusion of two deuterons isolated from all other matter [6] are energetic neutrons and radioactive tritium. That these were not seen in quantitative or temporal correlation with the FPE heat production caused some to question the nuclear hypothesis. This was discussed, apparently with complete absence of chemical intuition, as the "problem of" the missing "nuclear ash" [20].

In a series of papers [21–24] Miles and Bush first communicated information regarding the nuclear process at the core of the FPE, in correlated observation of FPE excess heat and $^4$He. These authors reported results of excess heat and helium gas analyses performed on evolved gas samples taken from thermodynamically open FPE cells, some of which exhibited excess heat and others did not. Miles and Bush were able to show by statistical analysis of 17 samples that when excess heat was present, so was $^4$He, and when excess heat was not present neither was $^4$He. The probability of their results occurring by random chance were computed as 1 in 750,000.

Miles and Bush demonstrated not only a statistical correlation between the appearance of FPE excess heat and $^4$He, but also a near-quantitative correlation with the putative net reaction of two deuterons to form one $^4$He with the release of $\sim$24 MeV of energy inside the calorimeter [7]. Their result was "near-quantitative" in that the average value of measured helium was only $1.4 \pm 7 \times 10^{11}$ $^4$He s$^{-1}$ W$^{-1}$, 54% of "expected" value of $2.5 \times 10^{11}$ $^4$He s$^{-1}$ W$^{-1}$. Working at SRI using a more robust and accurate metal-sealed calorimeter Bush later confirmed this result [25], measuring $1.5 \pm 2 \times 10^{11}$ $^4$He s$^{-1}$ W$^{-1}$ - 58% of "expected" value.

In attempting to define the reaction "$Q$" value to gain insight into the overall reaction process, it is appropriate to ask "where is the missing $^4$He" or "is $^4$He missing"? In 1996 Gozzi reported some very striking results [26] in which bursts of excess energy were time-correlated with bursts of $^4$He observed in the gas stream [8]. When compared one at a time, the number of helium atoms detected per burst was on the order of what might be expected from 23.8 MeV per $^4$He measured, but varying between 25 and 100% of this amount. If the energy production in these experiments is in fact due to a net reaction consistent with D + D $\rightarrow$ $^4$He + 23.8 MeV, then it seems that some of the helium may enter the gas stream and some remain within the metal. More recent work at ENEA Frascati also supports these conclusions.

In two experiments, one performed at SRI [28] and the other at ENEA [17] efforts were made to scavenge near-surface $^4$He and make it available in the gas phase for analysis. At SRI the experiment was performed in a helium leak-tight, all-metal and metal gasketed calorimeter. Samples were transferred in metal gas sample flasks to be analyzed for $^4$He by the U.S. Bureau of Mines at Amarillo, Texas. The initial value of $^4$He was $0.34 \pm 0.007$ ppmV/V in the D$_2$ gas used to charge the cell.

Figure 4 traces the history of the cell, M4, from four helium samples taken after excess power was observed as shown in Fig. 5. The upper solid line in Fig. 4 is the expectation for helium concentration presuming: (i) an initial value of 0.34 ppmV/V, and (ii) that $^4$He is produced in a reaction that delivers 23.8 MeV of thermal energy to the calorimeter. The first gas sample taken shortly following the second heat burst of Figure 5 yielded a value of $1.556 \pm 0.007$ ppmV/V $^4$He, which is about 62% of its expected value, and consistent with the earlier observations by Miles et al. [21–24] and also Gozzi and collaborators [26,27]. A second sample taken about six days after the first showed a measurable
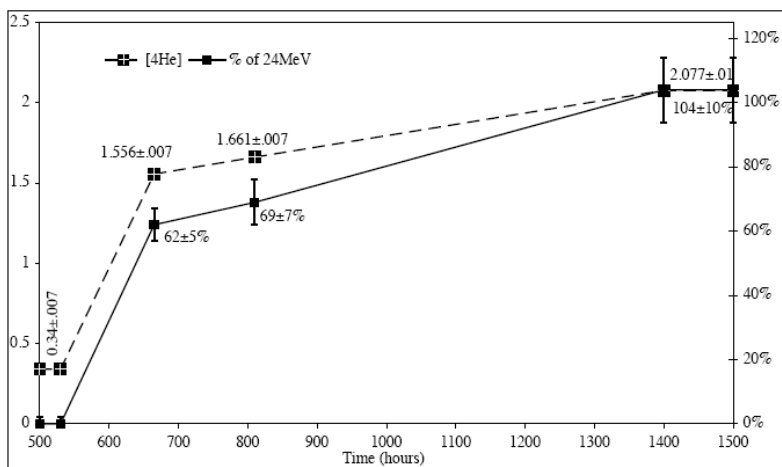
**Figure 4.**   Measured $^4$He concentration in a metal sealed electrochemical cell and mass flow calorimeter (data from Fig. 5, *left scale*) expressed as a percentage of the $^4$He expected from D+D $\rightarrow$ $^4$He $+ 23.8$ MeV heat (*right scale*).

increase in $^4$He content instead of the decrease that would be expected since, to maintain positive cell pressure, the gas taken for the first sample had been replaced with cylinder $D_2$ containing a lower level of $^4$He (0.34 ppmV/V). These findings support earlier observations that helium is released slowly from the palladium after an initial delay.

After making these measurements, an attempt was made to dislodge near surface $^4$He by D atom motion, by subjecting the cathode to a period of compositional cycling, while still sealed in the calorimeter. Square and sine wave modulations of varying period and amplitude were imposed on the dc (negative) potential at the Pd electrode in an attempt to flux deuterium atoms through the interface and thus act to dislodge near-surface ad- or absorbed $^4$He atoms.

At the end of this period, the potential was reversed to withdraw all deuterium atoms from the Pd bulk. No excess heat was observed during the periods of oscillation although calorimetric uncertainties were large due to the strong departures from the steady state that accompanied the pulsing. Gas samples were taken before this procedure, again after purging the cell and refilling with $D_2$ from the gas bottle with 0.34 ppmV $^4$He, and once more after cycling. The latter sample exhibited the highest concentration of $^4$He measured in this cell, specifically $2.077 \pm 0.01$ ppmV/V. By making a proper mass balance of the helium lost through sampling and purging, and that gained through make-up from the gas bottle, it is possible to assess with defined uncertainty the results of deuterium fluxing in freeing lightly trapped $^4$He. The final integral mass balance yielded a value of $104 \pm 10\%$ of the expected value if the excess power in Fig. 5 is due to a net reaction of the sort $D + D \rightarrow$ $^4$He $+ \sim 23.8$ MeV (heat).

## 2.  Conclusions

In this brief review we have attempted to demonstrate that the Fleischmann–Pons Effect (FPE) is a conditioned response of suitably prepared palladium cathodes to prolonged electrolysis in heavy water. The effect occurs when relatively high atomic deuterium loadings are achieved and maintained within a palladium cathode in the presence of suitable lattice
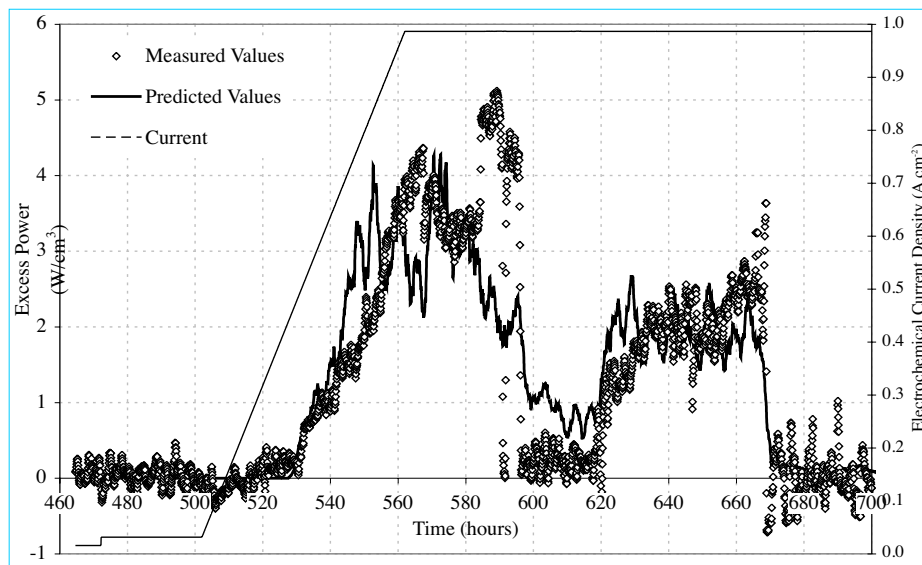
**Figure 5.** Excess power from a 1 mm × 10 cm Pd wire cathode electrolyzed in 1 M LiOD, in a metal sealed mass flow calorimeter measured and predicted from equation[1] (*left axis*), and electrochemical current density (*right axis*).

stimulation. The reasons for and nature of this stimulation has not been elaborated in this review, although suitable stimuli have been shown to include highly modulated electrochemical driving currents, high axial and interfacial current densities and induced deuterium atom fluxes.

The conditions necessary for the effect were not known or anticipated by early experimenters attempting to replicate the thermal anomalies reported initially by Fleischmann and Pons. Accordingly, these experiments mostly failed to produce the effect, which is now seen in amounts that are large both statistically, thus ruling out measurement error, and in absolute terms. Excess heat is measured in quantities greatly exceeding all known chemical processes and the results are many times in excess of determined errors using several kinds of apparatus. Nuclear products have been sought and found to be associated with the excess heat consistent with an overall reaction $D + D \rightarrow {}^4He + \sim 23.8$ MeV (heat), although a great deal more work is needed to elucidate a detailed reaction mechanism. Although not discussed here, the effect also appears in gas phase experiments employing Pd and $D_2$, with similar correlation between measured heat and helium production.

### References

[1] M. Fleischmann, S. Pons, and M. Hawkins, *J. Electroanal Chem.* **201** (1989) 301; Errata, **263**, 187 (1990). See also M. Fleischmann, S. Pons, M.W. Anderson, L.J. Li, and M. Hawkins, J. *Electroanal. Chem.* **287** (1990) 93.
[2] S. Focardi, R. Habel, and F. Piantelli, Anomalous heat production in Ni–H systems, *Il Nuovo Cimento* **107** (1994) 163.
[3] A. Rossi, *Method And Apparatus For Carrying Out Nickel And Hydrogen Exothermal Reactions,* US 2011/0005506 (2011).
[4] M.C.H. McKubre, The importance of replication, *in ICCF-14*, *Int. Conf. Condensed Matter Nuclear Science,* Washington, DC (2008).

[5]   C.G. Beaudette, *Excess Heat: Why Cold Fusion Research Prevailed*, Concord, NH: Oak Grove Press (2002).

[6]   N.S. Lewis et al., Searches for low-temperature nuclear fusion of deuterium in palladium, *Nature (London)* **340** (1989) 6234 and 525.

[7]   D. Albagli et al., Measurement and analysis of neutron and gamma-ray emission rates, other fusion products, and power in electrochemical cells having Pd cathodes, *J. Fusion Energy* **9** (1990) 133.

[8]   M.C.H. McKubre et al., Calorimetry and electrochemistry in the D/Pd system, in *The First Annual Conference on Cold Fusion,* University of Utah Research Park, Salt Lake City, Utah: National Cold Fusion Institute (1990).

[9]   M.C.H. McKubre et al., Isothermal flow calorimetric investigations of the D/Pd system, in *The Science of Cold Fusion,* T. Bressani, E. Del Giudice, and G. Preparata (Eds.), Conference Proceedings, Vol. 33, Italian Physical Society, Bologna, p. 419 (1992).

[10]  M.C.H. McKubre et al., Excess power observations in electrochemical studies of the D/Pd system; the influence of loading, in *Third International Conference on Cold Fusion, "Frontiers of Cold Fusion",* Nagoya Japan, Univ. Acad. Press Inc., Tokyo, Japan (1992).

[11]  M.C.H. McKubre et al., Isothermal flow calorimetric investigations of the D/Pd and H/Pd systems, *J. Electroanal. Chem.* **368** (1994) 55.

[12]  E.K. Storms, Some characteristics of heat pProduction using the 'Cold Fusion' effect, *Trans. Fusion Technol.* **26**(4T) (1994) 96.

[13]  F. De Marco, A. De Ninno, A. Frattolillo, A. La Barbera, F. Scaramuzzi, and V. Violante, Progress report on the research activities on Cold Fusion at ENEA Frascati, *Proc. ICCF6*, p. 145 (1996).

[14]  D.E. Williams et al., Upper bounds on 'Cold Fusion' in electrolytic cells, *Nature* **342** (1989) 375.

[15]  E. Storms, *The Science of Low Energy Nuclear Reactions,* World Scientific, Singapore, 2007.

[16]  P.L. Hagelstein, M.C.H. McKubre, D.J. Nagel, T.A. Chubb, and R.J. Hekman, New physical effects in metal deuterides, in *11th Int. Conf. on Cold Fusion,* J.-P. Biberian (Ed.), Marseilles, France, p. 23 (2004).

[17]  M. Apicella, E. Castagna, L.Capobianco, L.D'Aulerio, G. Mazzitelli, F. Sarto, A. Rosada, E. Santoro, Violante, M. McKubre, F. Tanzella, and C. Sibilia, Some Recent Results at ENEA, *Proc. ICCF12*, p. 117 (paper presented at ICCF11).

[18]  Y. Sakamoto, M. Imoto, K. Takai, T. Yanaru, and K. Ohshima, Calorimetric enthalpies for palladium–hydrogen (deuterium) systems at H(D) contents up to about [H]([D])/[Pd] = 0.86, *J. Phys.: Condensed Matter* **8**(16), 1088 (1996).

[19]  I. Dardik, T. Zilov, H. Branover, A. El-Boher, E. Greenspan, B. Kachatorov, V. Krakov, S. Lesin, and M. Tsirlin, Excess heat in electrolysis experiments at Energetics Technogies, in *11th Int. Conf. Cold Fusion,* J.-P. Biberian (Ed.), Marseilles, France, p. 84 (2004).

[20]  F. Close, *To Hot to Handle: the Race for Cold Fusion*, Princeton Univ. Press (1991).

[21]  M. Miles et al., Heat and helium production in cold fusion experiments, in *Second Annual Conference on Cold Fusion, "The Science of Cold Fusion",* Como, Italy: Societa Italiana di Fisica, Bologna, Italy (1991).

[22]  B.F. Bush, J.J. Lagowski, M.H. Miles, and G.S. Ostrom, Helium production during the electrolysis of $D_2O$ in cold fusion, *J. Electroanal. Chem.* **304** (1991) 271.

[23]  M.H. Miles, R.A. Hollins, B.F. Bush, J.J. Lagowski, and R.E. Miles, Correlation of excess power and helium production during $D_2O$ and $H_2O$ electrolysis using palladium cathodes, *J. Electroanal. Chem.* **346**, 99 (1993).

[24]  M.H. Miles and B. Bush, Search for Anomalous effects involving excess power and helium during $D_2O$ Electrolysis Using Palladium Cathodes, in *3rd International Conference on Cold Fusion,* Ikegami, H., Nagoya, Japan, p. 189 (1992).

[25]  M.C.H. McKubre et al., Energy Production Processes in Deuterated Metals, EPRI Report TR-107843-V1 (1998).

[26] D. Gozzi, R. Caputo, P.L. Cignini, M. Tomellini, G. Gigli, G. Balducci, E. Cisban, S. Frullani, F. Garibaldi, M. Jodice, and G.M. Urciuoli, Excess heat and nuclear product measurements in cold fusion electrochemical cells, in *4th Int. Conf. on Cold Fusion,* T.O. Passell, Lahaina, USA, Vol. 1, p. 2–1 (1993).

[27] F. Cellucci, P.L. Cignini, G. Gigli, D. Gozzi, M. Tomellini, E. Cisbani, F. Frullani, M. Garibaldi, M. Jodice, and G. M. Urciuoli, *Proc. ICCF6*, p. 3 (1996).

[28] M.C.H. McKubre, F.L. Tanzella, T. Tripodi, and P.L. Hagelstein, The emergence of a coherent explanation for Anomalies observed in D/Pd and H/Pd systems; evidence for $^4$He and $^3$H production, in *8th Int. Conf. Cold Fusion,* F. Scaramuzzi, Lerici, Italy, p. 3 (2000).
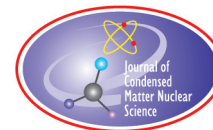
Research Article

# Piezonuclear Neutrons from Iron

Fabio Cardone* and Andrea Petrucci [†]

*Istituto per lo Studio dei Materiali Nanostrutturati (ISMN–CNR) Via dei Taurini–00185, Roma, Italy*

Roberto Mignani [‡]

*GNFM, Istituto Nazionale di Alta Matematica "F.Severi" Città Universitaria, P.le A.Moro 2–00185, Roma, Italy*

## Abstract

We report the results of neutron measurements carried out during the application of ultrasounds to bars of iron and Steel. Like in our previous similar works with cavitated solutions of iron, neutrons were emitted in bursts and the spectrum of this peculiar emission was measured for the first time. A further and very interesting outcome of these experiments was the unexpected appearance of circular, macroscopical and regular damages on the lateral surface of the bars which was not directly in contact with the sonotrode. The superficial elemental micro-analysis on these spots showed some interesting and macroscopic departures of the concentration of chemical elements from that of the undamaged surface, which may suggest that, along with the emission of neutrons, some transmutations occurred as well.

## 1. Introduction

In the last six years, we carried out experiments about piezonuclear reactions [1,2] in which we applied ultrasounds to solutions of water containing atoms of iron and from which, thanks to cavitation, that brings about a violent bubble collapse, we obtained neutron emission. In the wake of these experiments we decided to move our experimental campaign a bit further and apply ultrasounds to bars of iron or steel instead of to solutions of iron. We hypothesized that a similar process to bubble collapse in liquids might take place in solid bars too, due to the gas that they absorb during the casting process and that forms gas porosity. This conjecture was supported by some interesting experimental evidences obtained by a research team at the Polytechnical University of Turin [3–5]. They applied pressure by a press onto granite samples up to their brittle fracture. The fracturing sample was surrounded by neutron detectors both passive

*Also at GNFM, Istituto Nazionale di Alta Matematica "F.Severi" Città Universitaria, P.le A.Moro 2–00185, Roma, Italy

[†]Corresponding author. E-mail: petruccia@fis.uniroma3.it

[‡]Also at Dipartimento di Fisica "E. Amaldi", Universitµa degli Studi "Roma Tre" Via della Vasca Navale, 84–00146, Roma, Italy and I.N.F.N., Sezione di Roma III, Italy

(bubble detectors) and active ($^3$He). At fracture both types of detectors always recorded a burst of neutrons many times higher than the measured neutron background. According to our phenomenological model, thanks to the phenomenon of cavitation, which makes the bubble of gas, contained in the liquid, collapse abruptly, the atoms of iron entrapped in the interface gas-liquid of the bubble get accelerated towards eachother as the bubble collapses. The theory proposed by two of us (F. C. and R. M.) [9–11], predicts that if the bubble collapse succeeds in concentrating the iron atoms in a certain region of space, within a certain time interval and with an amount of energy greater than 367.5 GeV , these atoms undergo a new type of nuclear reactions which we baptized piezonuclear reactions. As to the cavitation process in solids, we imagined that the gas porosity within the metallic lattice be made of tiny bubbles of gas whose interface gas-metal is entirely made of iron atoms. Ultrasounds exert a pressure on these micro-cavities and bring about a process that can generate the energy–space–time conditions needed to start piezonuclear reactions. On the basis of this heuristic conjecture, we designed our experimental set-up by taking advantage of the experience gained in the experiments with ultrasounds and solutions [1,2,12–14], but aware of the big differences between iron in a solution and solid iron.
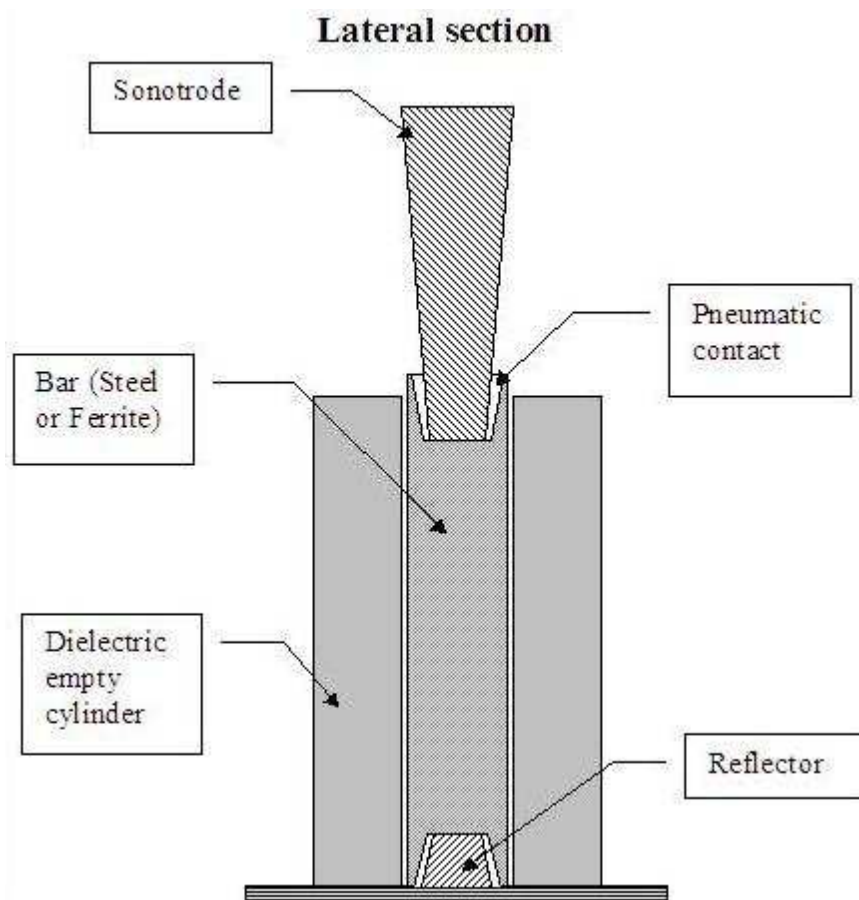
## 2. Experimental Set-up

The experimental set-up was made of an ultrasonic machine, called reactor R-1-S, pretty much similar to that one used in our previous experiments [1,2,12–14]. This reactor was suitably designed and assembled by Startec Ltd. It had a converter unit with piezoelectric ceramics and a truncated conical sonotrode mechanically connected to it. A suitably designed metallic frame held the converter-sonotrode unit aligned with the iron bar to be treated by ultrasounds Fig. 1.

Moreover this frame could be shifted vertically and a pneumatic system allowed one to vary the contact strength between the sonotrode and the bar and hence vary the transmitted power. The bar was held in the upright position by a dielectric cylinder through which the bar was inserted. The shaping of the top and bottom tip of the bar was studied and made in order to have within it both a direct and a reflected wave. Since these two waves are longitudinal waves moving along the same direction but in opposite verses, the transverse planes of the bar with respect to its length find themselves squeezed between these two waves (patent pending on the experimental equipment) [15].

## 3. Neutron Measurements

The experiments we carried out had three main targets: check whether neutrons would be actually emitted by such a different device with respect to solutions of water and iron; obtain for the first time the neutron spectrum of these emissions; check the time of the beginning of neutron emission. This last information had to be correlated with that of the previous experiments [1,2], where neutrons began to be emitted after 40–50 min. We will come back to this point later on. We used two types of neutron detectors: a neutron counter HDS-100GN by Mirion $^{\text{TM}}$ (Ref. [6]) and a neutron spectrometer MICROSPEC2 $^{\text{TM}}$ Neutron Probe by BTI [7,8]. The former is a gamma detector and spectrometer with CsI(Tl) scintillator for low energy gamma rays and silicon diode for the high-energy ones. Besides, it contained also a neutron detector with a LiI(Eu) scintillator. The latter is made up of two parts: the multichannel MICROSPEC2 $^{\text{TM}}$ and the neutron detector Neutron Probe with an He$^3$ counter for thermal neutrons up to 800 keV and a liquid scintillator for neutrons from 500 keV to 5 MeV .

We put in contact the sonotrode and the tip of the bar like in Fig. 1 and applied a pressing force on it, so that the transferred ultrasonic power into the bar was 19 W. The frequency of ultrasounds was 20 kHz like in the previous experiments with solutions, and the amplitude of the vibration of the sonotrode tip was 15 $\mu$m. We treated two different types of bars: bars made of sintered Ferrite ($\alpha$-iron) and bars made of steel with hardened surface by carbon steel and Dysprosium carbide. All of them were treated with the same ultrasonic parameters just mentioned. The two instruments, HSD-100GN and MICROSPEC Neutron Probe were brand new and had their own calibration certificates. By a standard source of AmBe at the Euratom Laboratory Ispra it was verified the compatibility of the readings of the two instruments

**Figure 1.**    Experimental set-up. Lateral section.

with the certification. First of all, we carried out prolonged measurements by the HDS-100GN with ultrasounds turned off, in order to get a fairly long history of the neutron background variations. Besides, by turning on ultrasounds, with the sonotrode not in contact with the bar, we checked that both of the measuring instruments were not affected by the operation of the ultrasound machine. In all of the measurements of neutrons with ultrasounds turned on, a couple for each bar, several neutron bursts were detected. The height of these bursts were 25% higher than the maximum value of the neutron background. This was the first evidence that we meant to obtain by the HDS-100GN. The second information, that could be obtained by this instrument, had to do with the instant of time when the first neutron burst would appear. In the previous experiments [1,2], as we stated above, neutron emission began about 40–50 min after ultrasounds had been turned on. In this case, conversely, the first burst appeared always within about 5 min after the turning on of ultrasounds. Let us make the meaning of this evidence more explicit. In the experiments with solutions of iron the density of the liquid was about 1 g/cm$^3$,the first burst appeared after about 40–50 min of ultrasounds and the transferred ultrasonic power was about 130 W. Conversely, always working at the same frequency, in the solid case

the mass density is that of the iron, 7.8 g/cm$^3$, the first bursts appeared after about 5 min and the transferred ultrasonic power was about 19 W. We report these numbers in Table 1. Very interestingly, we see that when the density of the material increases to eight times, the interval of time and the power to obtain neutrons decreases with the same factor.

**Table 1.** Comparison between liquids and solids – Density of the material, Minutes for the first bursts of neutron to appear, Power of ultrasounds.

| – | Density | Minutes | Power |
|---|---|---|---|
| Liquids | 1 | 40 | 130 |
| Solids | 7.8 | 5 | 19 |
| Liquids/Solids | $\approx 1/8$ | $\approx 8$ | $\approx 7$ |

This evidence is interestingly in agreement with the prediction of the theory as to the relation existing between the occurrence of piezonuclear reactions and the amount of energy present in the system, the system being nuclei per unit volume i.e. mass density. Necessary but not sufficient condition for piezonuclear reactions to take place is to overcome a threshold of energy in a suitable volume or, in other words, a threshold of energy density, which is more promptly overcome in denser materials.

As we reported above, the HDS-100GN was also equipped with a gamma detector by which we could check the absence of any peak of gamma rays consequent to the detected neutron bursts. After the completion of these measurements by the neutron detector, we began the measurement of neutron spectrum, within the same experimental set-up. In Fig. 2 we present two neutron spectra obtained during 1 h of application of ultrasounds to one bar of ferrite (a) and one bar of steel (b) and in (c) the neutron spectrum of the background, i.e. with ultrasounds turned off.

The difference between the two spectra (a) and (b) with the spectrum (c) can be easily spotted. Moreover, the spectra (a) and (b) have a fairly clear lognormal shape which, from an intuitive and qualitative point of view, gives a fairly sound evidence of the existence of the phenomenon.

## 4. Bar Damages

We present here a further interesting evidence that appeared on the lateral surface of the bars and that was completely unexpected. As is visible in Fig. 1, in the experimental set- up, the bar treated by ultrasounds, was held vertically with its axis aligned with that of the sonotrode by an empty cylinder made of dielectric material. Once the bar was pulled out of the empty cylinder, we noticed, with great surprise, that on its lateral surface peculiar circular spots had appeared as in Fig. 3.

As is possible to see from Fig. 3, the ruler next to the bar clearly shows that these amazingly circular spots have a diameter that ranges from 2 to 3 mm. The surface of the bar on them is rougher and the roughness increases moving from the border of the circle to its centre. All of the spots have a fairly good circular simmetry at the unaided eye. While the colour of the bar is metallic grey as it normally is for steel, the predominant colour of these spots is brownish in a ring bound by two concentric circles and whitish in a circular central area. At a first sight, neither the distribution of these circles on the lateral surface of the bar had any particular symmetry, nor the distances between the centres of two spots apparently had any proportionality among them and/or with the dimensions of the bar. We would like to stress that these spots showed up on all of the bars, but they were more clearly visible on the bars of carbon steel. If one considers this last fact, i.e. a carbon steel bar, together with the ultrasonic energy conveyed into the bar, that was 19 *W*, one cannot be but puzzled. From a metallurgic point of view such a power, applied to the bar in the experimental conditions mentioned above, is just too low to produce these damages on a bar whose surface had been hardened by carbon steel and Dysprosium carbide. However, the first thing that we checked was the presence of any possible ferric
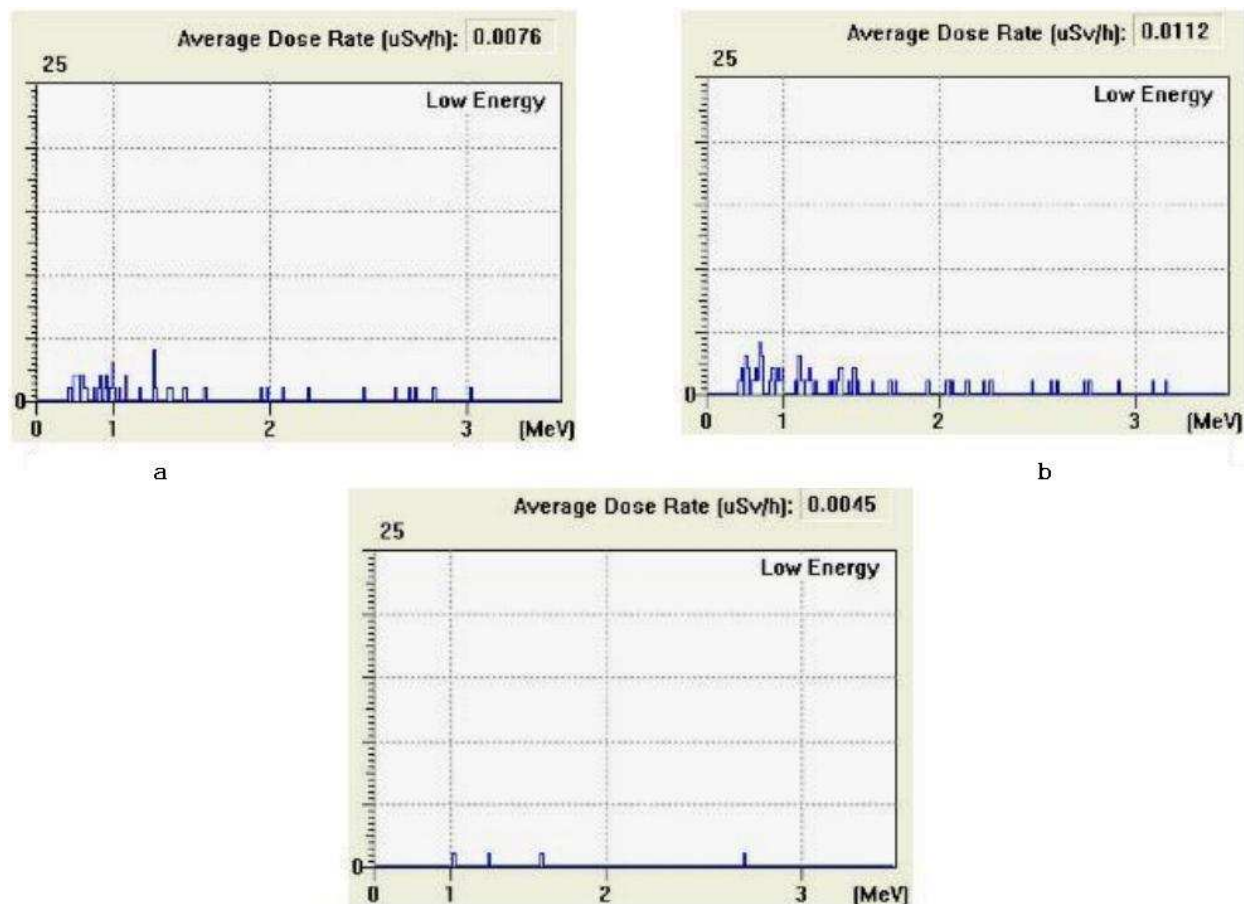
**Figure 2.**   (a) Neutron spectrum from the bar of Ferrite, (b) Neutron spectrum from the bar of steel and (c) Neutron spectrum of the background.

oxide or hydroxide on the damaged surface. We decided to treat some of the bars with these circular spots by a solution of hydrochloric acid at 33%. We immersed the bars into the solution and kept them submerged for 1 h. Once we took them out of the solution of HCl and rinsed them, we noticed straight away that this treatment had had no effects on the damaged parts, whose morphology and colour had not changed. In order to obtain further information about the features of these damaged parts, we performed on them a semi-quatitative micro-analysis by a Zeiss Supra 40 FESEM with the electron beam at 20 keV and equipped with an Oxford INCA energy dispersive X-ray detector Si(Li) whose resolution at MnK$\alpha$ is 133 eV. Of course, we analysed by the same technique some areas of the undamaged surface as well and found out a sound homogeneity of the concentrations of elements.

In Fig. 4 we show the magnification of one of the damaged parts with the three spots where the EDX microanalysis was performed.
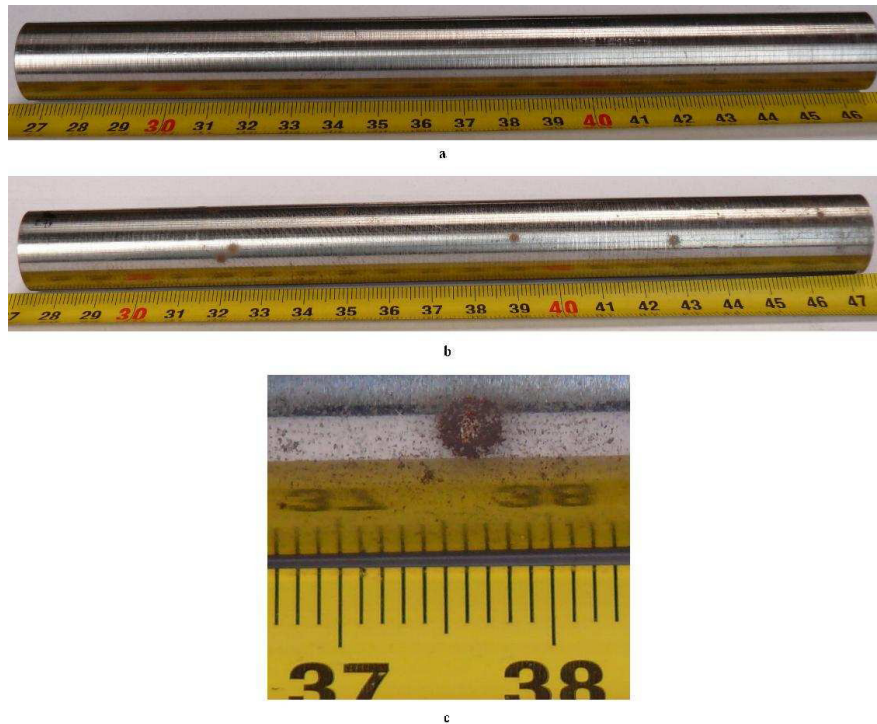
**Figure 3.** (a)–(b)–(c).

In Table 2, the concentrations in weight of the elements are reported. Particular attention has to be paid to the variations of carbon, oxygen, iron and dysprosium. In Table 2, we reported the values of concentration that were obtained at the centre of the circular damage. In Fig. 5, we show two EDX spectra obtained on the undamaged surface of the bar and on one of the damaged spots. Beyond the amazingly macroscopic variation of concentration of the four elements mentioned above, some other elements appeared that were not part of the superficial composition of the bars. We highlight the remarkable fact that the decrease in weight of iron seems to be counterbalanced by the sum of the increase in weight of carbon and oxygen.

## 5. Discussion of the Results

Let us first remark the lack of gamma emission higher than the background, that conforms to the outcomes of our previous experiments [1,2]. Some discussion is duly needed both for the neutron spectra and for the peculiar marks that appeared on the surface of the bars. Let us refer to Fig. 2. Despite the fairly clear difference between the spectra a and b and the spectrum c, one might be dissatisfied with the poor height of the bars of the histograms a and b. Two main reasons can be presented as the possible explanations of this fact. First of all, from our experience of measurements of this kind of peculiar neutron emission which happens in bursts [1,2], that stick out over a neutron background, we can state that the detection efficiency of active detectors is very poor. This is due to their dead times that make them miss some consecutive bursts or miss the entire height of a burst and to the software that controls them which tends to average

**Table 2.** Concentration in weight of elements before and after ultrasound treatment. Particular attention has to be paid to the amazing variations of Carbon, Oxygen, Iron and Dysprosium.

| Before ultrasound | | After ultrasound | |
|---|---|---|---|
| Element | Weight% | Element | Weight% |
| C, Carbon | 2.37 | C, Carbon | 19.80 !!! |
| – | – | O, Oxygen | 29.27 !!! |
| – | – | Na, Sodium | 1.20 |
| – | – | Mg, Magnesium | 0.19 |
| – | – | Al, Aluminium | 0.53 |
| Si, Silicon | 0.21 | Si, Silicon | 0.49 |
| – | – | S, Sulfur | 0.27 |
| – | – | Cl, Chlorine | 1.61 |
| – | – | K, Potassium | 0.54 |
| – | – | Ca, Calcium | 0.68 |
| Mn, Manganese | 0.66 | Mn, Manganese | 0.47 |
| Fe, Iron | 91.92 | Fe, Iron | 44.45 !!! |
| W, Tungsten | 0.53 | W, Tungsten | 0.50 |
| Dy, Dysprosium | 4.12 !!! | – | – |
| Cr, Chromium | 0.18 | – | - |

the bursts to the neutron background. The second reason has to do again with the emission in bursts. These bursts are not isotropically emitted over $4\pi$ steradians, but they are rather concentrated along a direction in space that apparently changes for every burst, as it is well evident in Fig. 3 where the damage spots on the bar are randomly scattered on its surface. With this in mind one understands that a neutron monitor will be able to detect only those bursts emitted aligned with it and will miss all the others. Let us now move to the second evidence of these experiments, that is the presence of macroscopical damages on the surface of the bars. The comparison of the X-ray microanalyses performed both on undamaged parts of the surface and on damaged ones showed macroscopical variations of the concentration of iron, oxygen, carbon and dysprosium and the appearance of elements that were not initially present. Let us refer to Table 2: the percentages of disappeared iron and dysprosium are 47.47% and 4.12%, respectively, while the percentages of appeared carbon and oxygen are 17.43% and 29.27%, respectively. Very interesting is the balance between the concentration of the disappeared iron and appeared carbon and oxygen, in particular:
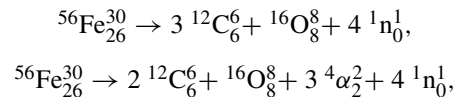
$$\text{disappeared iron } 47.47\% \simeq 46.70\% \text{ appeared (carbon + oxygen).}$$

If one counts in the decreasing of dysprosium and the appearance of other elements as in Table 2, one finds out the following balance of concentrations:
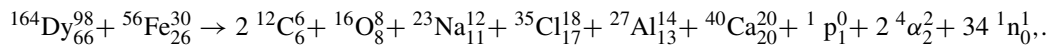
$$\text{disappeared (iron + dysprosium) } 51.59 \% \simeq 51.72 \% \text{ appeared (carbon + oxygen + the rest).}$$

The emission of neutrons, that was detected during the application of ultrasounds to the bars, certainly raises many questions of theoretical but also of phenomenological and experimental nature; for instance, as to where these bursts were emitted from. The macroscopical damages on the surface of the bars along with the variations and balances of the concentration of elements might be the possible answer to these questions. More explicitly one may think that the first balance means that iron turned into carbon and oxygen and the second balance means that iron plus dysprosium turned into carbon, oxygen and the other elements. The use of the verb "turn into" was done in purpose, since we did not want to use either the word fission nor the word lysis, nor the fusion nor the word synthesis. Both of them remind too much of the well-known nuclear processes which, according to our theory [9,11], have nothing to do with the nuclear processes in a piezonuclear reaction. Piezonuclear processes take place in the microscopically deformed spacetime that surrounds

the nuclei, hence the various calculations to establish whether a nuclear reaction is endothermic or exothermic, based on the binding energy per nucleon, are not valid in this context, since the variation of the space time deformation, that occurs during the process, contributes to the energy balance. From this perspective we can give some examples of the piezonuclear reactions that might take place. We want to stress that, by presenting the following reactions, we are in no way stating that these are the actual reactions that took place. The purpose is just to put forward a new type of nuclear reactions trying to follow the hints that nature gives us through experiments. If we consider the first balance between iron, carbon and oxygen, we can hypothesize the following reactions:

$$^{56}Fe^{30}_{26} \rightarrow 3\ ^{12}C^6_6 + \ ^{16}O^8_8 + 4\ ^1n^1_0,$$

$$^{56}Fe^{30}_{26} \rightarrow 2\ ^{12}C^6_6 + \ ^{16}O^8_8 + 3\ ^4\alpha^2_2 + 4\ ^1n^1_0,$$

Otherwise, if we consider dysprosium together with iron, the possible reactions might be:

$$^{164}Dy^{98}_{66} + \ ^{56}Fe^{30}_{26} \rightarrow 2\ ^{12}C^6_6 + \ ^{16}O^8_8 + \ ^{23}Na^{12}_{11} + \ ^{35}Cl^{18}_{17} + \ ^{27}Al^{14}_{13} + \ ^{40}Ca^{20}_{20} + \ ^1\ p^0_1 + 2\ ^4\alpha^2_2 + 34\ ^1n^1_0,.$$

These reactions, that do not have to be read as fission or fusion as stated before, produce neutrons as experimentally ascertained and alpha particles as well. If the latter were produced by piezonuclear reactions that take place on the surface of the bars, it should be easy to detect them. If these kind of reactions, starting from medium weight or heavy
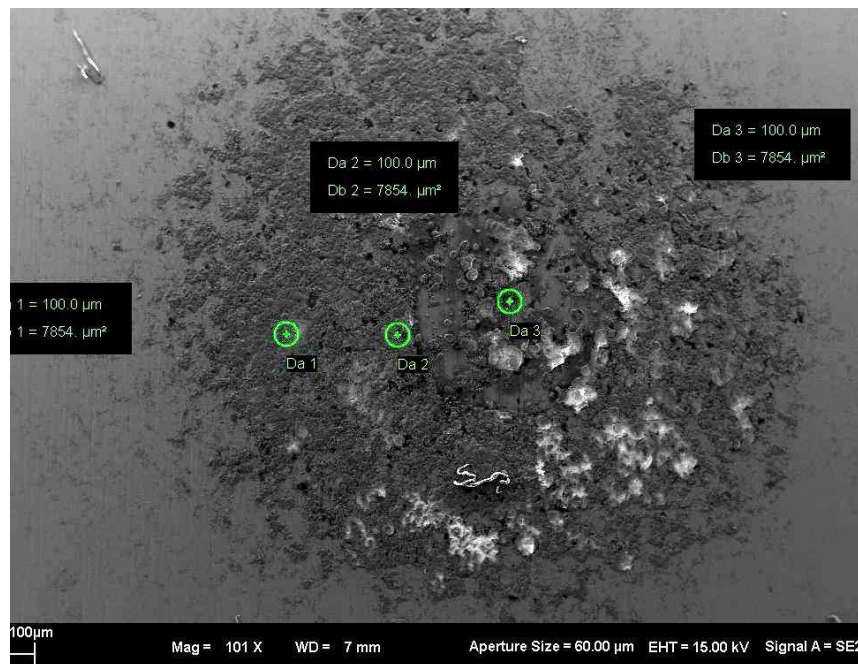


**Figure 4.** Magnification 101x of one of the damaged parts with the three spots where micro analysis was performed.
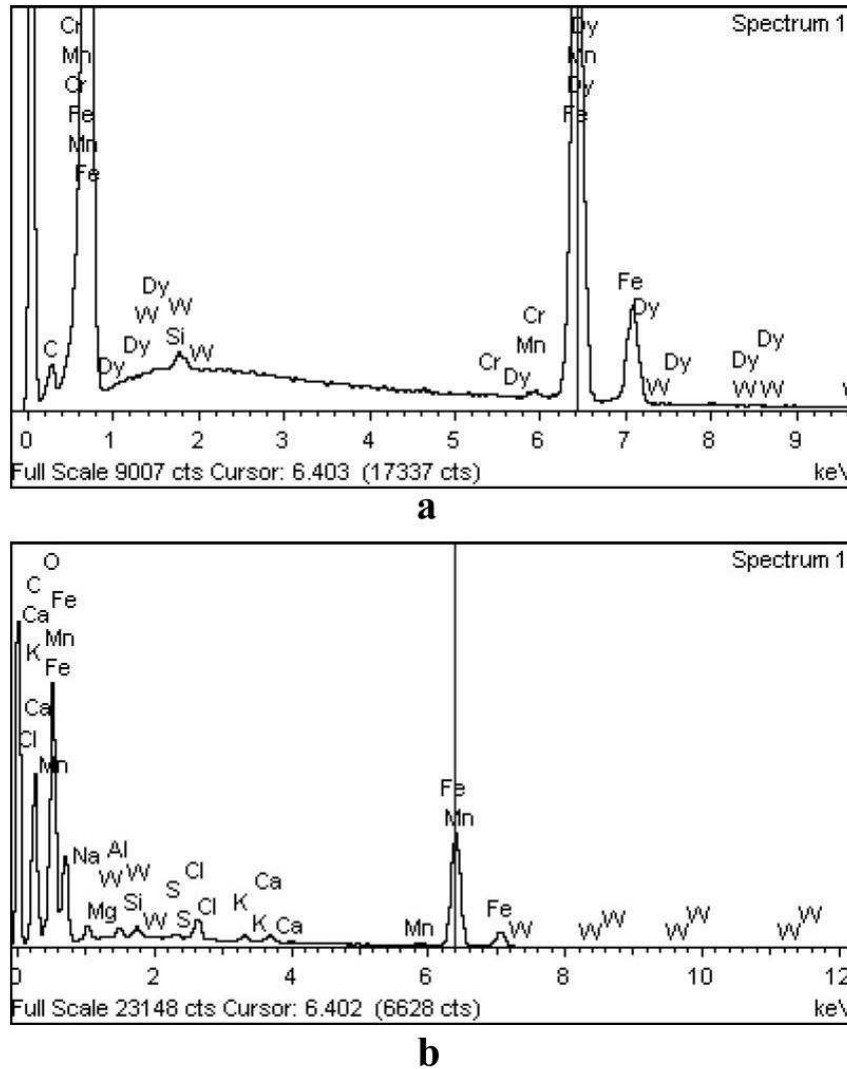
**Figure 5.** Two examples of EDX spectra. In (a) is shown the spectrum of elements on the undamaged part of the surface. In (b) is shown the spectrum of elements on the central spot of one of the circular damaged zones.

nuclides and yielding lighter ones, take place also in CMNS/LENR experiments, one might argue that these alpha particles might account for the extra Helium [16], whose measured quantity is usually higher than that expected to be produced by d–d fusion. Besides, the presence of these alpha particles might also account for some of the extra heat [16] due to their high linear energy transfer (LET) in the condensed matter where these reactions take place.
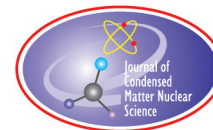
Let us make one last consideration about the processes that may occur during the application of ultrasounds to the bars. We are strongly convinced that the volumes where most of the mechanical energy gets released and converted are both the grain boundaries and the microcavities that contain gas. The metallic lattice can elastically absorb and release energy but not these two kinds of discontinuities. From this point of view, we cannot disregard the chance that the released energy can locally (microscopically) increase the temperature and generate the suitable conditions for a microplasma to ignite. In this sense, it will be necessary to discern whether the piezonuclear neutrons, that were measured, were produced by a microplasma, generated by a quantistic cavitation at nuclear dimensions, or by the local deformation of space-time generated by a suitable local density of energy. From this point of view, further experiments will have to be performed on degassed and non-degassed solids.

## 6. Perspectives

The evidence of transmutations of macroscopical quantities of elements are certainly encouraging to carry on these kinds of experiments with solid bars that could be made of different compositions but always containing iron, in order to study the way of making these transmutations predictable. In this respect, we would like to report a private communication [17] in which the researchers showed us their results of neutron measurements during the application of ultrasounds to basalt, a rock containing iron. With all of this in mind, it is just one step forward to imagine similar experiments on bars of radioactive metals in order to check whether these 'piezo-transmutations' make them loose their radioactivity by the catalysis of ultrasonic piezonuclear reactions in close analogy with what was found out in radioactive liquids treated by ultrasonic cavitation [17].

## References

[1]  F. Cardone, G. Cherubini, and A. Petrucci, A.: *Phys. Letts.* A **373** (2009) 862.
[2]  F. Cardone, G. Cherubini, R. Mignani, W. Perconti, A. Petrucci, F. Rosetto, and G. Spera, *Ann. Fond. L. de Broglie* **34** (2009) 183.
[3]  A. Carpinteri, F. Cardone, and G. Lacidogna, *Proc. Turin Academy Sci.* **23**(V) (2010) 33, **27** (2009); *Exp. Mech.* **50** (2010) 1235.
[4]  F. Cardone, A. Carpinteri and G. Lacidogna, *Phys. Lett.* A **373** (2009) 4158.
[5]  A. Carpinteri, A. Chiodoni, A. Manuello, R. Sandrone, *Strain* (2010) (doi:10.1111/j.1475-1305.2010.00767.x).
[6]  http://www.istimaging.com/en/products/datasheets/hp/144211EN-B_HDS100GGN.pdf
[7]  http://www.bubbletech.ca/radiation_spectrometers_files/m2.html
[8]  http://www.bubbletech.ca/radiation_spectrometers_files/neutron_probe.html
[9]  F. Cardone and R. Mignani, *Energy and Geometry* (World Scientific, Singapore, 2004).
[10] F. Cardone and R. Mignani, *Int. J. Modern Phys.* E **15** (2006) 911.
[11] F. Cardone and R. Mignani, *Deformed Spacetime* (Springer, Heidelberg, 2007).
[12] CNR (National Research Council of Italy) Patent Office number: WO/2008/041253.
[13] CNR (National Research Council of Italy) Patent Office number: WO/2008/041254.
[14] CNR (National Research Council of Italy) Patent Office number: WO/2008/041255
[15] "Dispositivo e metodo per rilasciare neutroni", application number MI2010A001263, (http://files.splinder.com/b71bec46d5c814ba46ff4c474a090e03.pdf)
[16] E. Storms, *The Science of Low Energy Nuclear Reactions* (World Scientific, Singapore, 2007).
[17] A. Manuello Bertetto, Presentation at the ICCF16, Neutron emission measurements during loading tests on solid specimens and confirmations by EDS analysis, A. Carpinteri, G. Lacidogna, A. Manuello, O. Borla.
[18] F. Cardone, R. Mignani and A. Petrucci, *Phys. Lett.* A **373** (2009) 1956.

Research Article

# Fabrication, Characterization, and Evaluation of Excess Heat in Zirconium–Nickel–Palladium Alloys

D.A. Kidwell [*], M.A. Imam and D.D. Dominguez

*Naval Research Laboratory, Washington, DC 20375, USA*

**Abstract**

Prior gas loading experiments of Zirconium–Nickel–Palladium alloys have been reported to generate a greater amount of heat with deuterium than with hydrogen. What is intriguing about these experiments was the long-term heat observed. Others, using commercial materials of similar composition, have been unable to observe long-term heat. We also have been unable to observe long-term heat in the commercial materials and materials prepared at NRL. Furthermore, when tested using our gas-loading protocol of measuring both the heat during pressurization and evacuation, these alloys do not show much, if any, excess heat and the majority of the heat observed can be attributed to chemistry.
© 2012 ISCMNS. All rights reserved. ISSN 2227-3123

*Keywords:* Excess heat, Gas loading, LENR, Melt-spinning, Nanoparticles

## 1. Introduction

Zirconium–Palladium and Zirconium–Nickel–Palladium alloys were originally studied as hydrogen storage media [1–4]. In a number of publications, Arata and Zhang have reported that pressurizing these alloys with deuterium produces considerably more heat and for a longer period of time than does pressurization with hydrogen (Fig. 1) [1–3]. The excess heat was attributed to a Low-energy Nuclear Reaction (LENR) when the palladium nano-particles become loaded with deuterium. Kitamura and co-workers also performed similar experiments with commercially available catalysts and reported excess heat with deuterium compared to hydrogen but not long-term heat [1–3].

We have been using nano-particles of palladium and other metals in zeolites and on alumina supports that can be in the size range hypothesized to be necessary for good loading under moderate gas pressures. When these materials are pressurized with hydrogen almost all the heat is recovered upon depressurization (Fig. 2). In contrast, when the materials are pressurized with deuterium, only one-fourth of the heat is recovered. The ratio of $Heat_{GasIn}:Heat_{GasOut}$ can be up to eight for deuterium whereas hydrogen is invariably equal with any difference being attributed to oxygen impurities in the hydrogen [1].

---

[*]E-mail: David.Kidwell@nrl.navy.mil

**Table 1.** Heat of absorption (and spillover), Pd:H ratios, and estimated particle sizes for palladium prepared by various techniques. Data from Chen et al. [1] with particle size estimates calculated from dispersion measurements. The initial heat of adsorption appears higher than the approximate 100 kJ/mol value reported by Chou and co-workers with Pd on Alumina [1]. The different support may account for the higher heat measurements or Chou may have had larger particles.

| Preparation | Estimated particle size (nm) | Initial heat of hydrogen adsorption (kJ/mol) | Ratio H:Pd at 0.2 bar |
|---|---|---|---|
| Pd powder | 9 | 94 | 0.55 |
| 1.86% Pd/SiO$_2$ | ∼ 4 | 92 | 0.68 |
| 10% Pd/SiO$_2$ | 1.1 | 131 | 0.9 |
| 5% Pd/SiO$_2$ | 1 | 183 | 1.05 |

The Zirconium–Palladium alloys of Arata and Zhang are claimed to have nano-sized palladium particles trapped in a zirconia matrix with the palladium particles estimated to be 5–10 nm in diameter [1]. Bulk palladium loads with hydrogen or deuterium to a Pd:D ratio of less than 0.7 at pressures of 500 bar [1]. The loading decreases with temperature and very slowly increases with pressure. Also, deuterium loads more slowly than hydrogen. In a previous paper, we discussed that results from electrochemical loading experiments of palladium indicate that the loading should be above a Pd:D ratio of 0.9 [1,2]. If this criterion is necessary to observe LENR for gas loading experiments in bulk palladium, the required pressure would be above $10^5$ bar. As the palladium particles get smaller, the loading can increase rapidly (Table 1) but the size must be in the region of 1 nm or else the palladium acts like bulk material.

In gas pressurization experiments both the Heat$_{GasIn}$ and Heat$_{GasOut}$ must be measured. This eliminates reversible reactions and only irreversible reactions remain. Irreversible reactions may be chemistry (e.g., reduction of oxides or reaction of trace oxygen with hydrogen) or new physics (LENR). Frequently, relative rather than absolute temperature measurements are not made so that establishment of a stable baseline is important. Measuring both parts of the
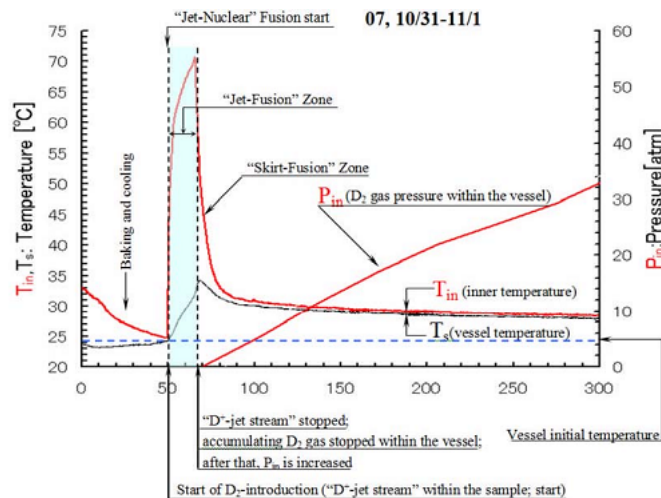


**Figure 1.** Results of Arata and Zhang on pressurization of Zr–Ni–Pd alloys. Note that much of the heat is generated during the first part of the pressurization. During the later long-term heat, the pressure is constantly increasing. The *X*-axis was not labeled in the original but is in minutes. Figure reproduced from Yoshiaki Arata and Y.-C. Zhang Establishment of the 'Solid Fusion' Reactor, *Proc. the 14th Int. Conf. on Condensed Matter Nucl. Sci. and the 14th Int. Conf. on Cold Fusion (ICCF-14)*, 10–15 August 2008, Washington DC, p. 756.

pressurization/depressurization cycle allows the temperature to return to baseline if long-term heat is suspected. Return of the temperature to the baseline upon removal of the gas is an important control as the system may have instrumental problems such as:

- Drift in the temperature of the room.
- Drift in the temperature measurement system.
- Inadequate initial baseline stabilization. The baseline should be taken while the system has air present (or better an inert gas such as helium) to reduce artifacts as:
  - The initial evacuation can remove materials, such as water, and be endothermic and change baseline.
  - Heat losses of the evacuated vs. pressurized cell must be considered due to conduction because hydrogen and deuterium have different thermal conductivities.

Several pressurization-depressurization cycles must be done to:

- Deplete chemistry (as chemistry could be confused as LENR)
- Indicate catalyst degradation by particle growth or poisoning, which is important for any practical use of technology
- Regenerate catalysts chemically (oxidation) or physically (heating) risks introducing new chemistry that may be interpreted as anomalous heat
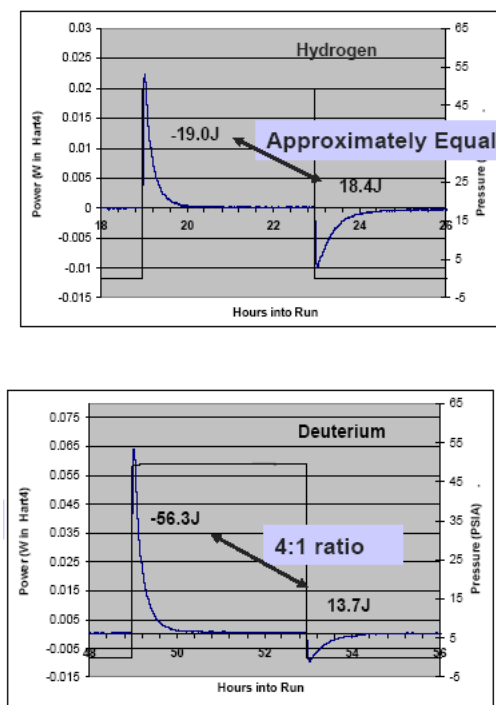


**Figure 2.** Typical pressurization cycles for nano-palladium in zeolite $13\times$. Pressurization with hydrogen the $Heat_{GasIn} \approx Heat_{GasOut}$ whereas with deuterium the $Heat_{GasIn} \neq Heat_{GasOut}$.

Gas pressurization experiments readily lend themselves to using hydrogen controls on the same materials. Hypothetically, LENR should not occur with all isotopes of hydrogen at the same rate. For good controls, they should be run under the same conditions as deuterium with the pressure, timing, temperature the same as possible and hydrogen being run first on fresh material to avoid D–H exchange reactions (D–H exchange on the Zr–Ni–Pd systems should be minimal as not much water or OH groups are present)[1]. Finally, gas pressurization techniques allow testing at several temperatures, which may be useful to distinguish chemistry from physics as generally reaction rates change with temperature.

After several pressurization-depressurization cycles, chemical reactions should be reduced in magnitude as the reactive chemicals are depleted. For the Zr–Ni–Pd systems, these chemical reactions include reduction of the palladium ions (as oxide) to palladium metal nano-particles and the formation of water from oxides (such as NiO). Ignoring small isotopic effects, both hydrogen and deuterium should produce similar chemical heats in the initial cycles. After this chemistry is depleted, the pressurization heat pulse can arise from three areas.

- Work of pressurization (PV work, the adiabatic temperature rise due to compression of the gas), which is reversible (recoverable) upon depressurization of the cell. However, to make accurate measurements, the rate of pressurization and depressurization should be similar. If the pressurization is slow, then the heat of pressurization can be at such a low value as to be misidentified as baseline drift. The magnitude of the heat of pressurization can be calculated [13].Other sources of heat due to chemistry such as the Joule–Thompson effect or ortho–para conversion are typically small. One form of chemistry that is not small and would be different with hydrogen vs. deuterium is D–H exchange, which was discussed in previous papers [13].
- Absorption of deuterium/hydrogen into the palladium particles and spillover onto the support. For nano-particles the absorption reactions can be quite rapid but the spillover can be slow. The possibility of spillover makes measurement of the Pd:D(H) ratio difficult, as not all the deuterium is associated only with the palladium [1–3]. Generally, particle size of palladium is best measured by probe molecules that interact poorly with the support [1]. The reverse reaction (desorption) from decomposition of the hydride and removal of spillover can be slow. In the case of palladium in zeolites, we have observed deuterium desorption hours after the start of the depressurization at 40°C, which makes accounting for all the reverse heat more difficult. However, the kinetics of desorption of hydrogen and deuterium are similar so that one can control for the other. Additionally, the number of moles of gas present after a few hours is small so that the total missing heat would also be small. Presumably, the deuterium/hydrogen is desorbed from the support first (spillover hydrogen) than only slowly from the particles. This makes resetting the particles difficult for subsequent pressurization/depressurization cycles, as discussed below in Fig. 6.
- New physics such as LENR.

Similar systems to the Zr–Ni–Pd alloys of Arata et al. such as Zr–Ni alloys, have also been studied as hydrogen storage materials [1]. The Zr–Ni alloys take-up considerable hydrogen in a very exothermic manner at higher temperatures when zirconium metal (as opposed to the oxide) is present. The long-term heat shown in Fig. 1 could have been produced by chemical processes. The continually and slowly increasing pressure allows new chemistry to occur (e.g. formation of hydrides in larger and larger particles). As the endothermic heat during depressurization is not measured, partially reversible reactions such as hydride formation may be overlooked. Additionally, if the palladium nano-particles needed to be in a size regime of 1 nm (much smaller than reported by Arata et al. for their palladium alloys) to load sufficiently, then these systems should not load to high levels of deuterium and consequently not work. Even with these experimental deficiencies, the results were intriguing. We made a series of Zr–Ni–Pd alloys by a similar process as described by Yamaura and characterized them by X-ray diffraction (XRD), Thermogravimetric Analysis (TGA), and gas pressurization experiments at various temperatures. By recording both the $Heat_{GasIn}$ and $Heat_{GasOut}$ and running hydrogen controls, we found that the large amount of heat generated with these types of materials is likely chemical in

**Table 2.** Alloys prepared. The italicized values for the alloys produced the most heat during pressurization.

| Zr (%) | Ni (%) | Pd (%) |
|--------|--------|--------|
| 69.5   | 30     | 0.5    |
| 69     | 30     | 1      |
| *68*   | *30*   | *2*    |
| 64     | 30     | 6      |
| 70     | 30     | 0      |

origin.

## 2. Experimental

The alloys Zr–Ni–Pd with different compositions were prepared by arc melting of high-purity elements (3 N) in an argon atmosphere using a water-cooled copper hearth. Alloy ribbons were then fabricated from these ingots by a single-wheel melt-spinning technique as shown in Fig. 3. A quartz crucible with an orifice of about 0.75 mm and a Cu wheel with a surface velocity of 45 m/s were used to produce ribbons with a width of ∼2 mm and thickness of ∼20–40 $\mu$m.

Various alloys were prepared as listed in Table 2. After preliminary tests, the Zr68–Ni30–Pd2 alloy produced the most heat so it was prepared in a large batch and used for all the tests presented here. The heat treatment conditions are listed in Table 3. The percent oxidation was determined from weight gain by assuming that all the weight difference was due to oxygen uptake and that only Pd and Zr was oxidized. Percentages above 100 indicate partial oxidation of the nickel. The amount of oxide formation varied even under similar conditions (compare samples 3 and 6).

Thermogravimetric analysis (TGA) was performed using a TA Instruments Q600 TGA/Differential Scanning Calorimeter (DSC). Measurements were determined by heating approximately 50 mg samples from room temperature to 1000°C at a rate of 10°C min$^{-1}$ in air flowing at 50 cm$^3$ min$^{-1}$. Figure 4 shows a TGA–DSC analysis of one alloy. Note that the oxidation only occurs readily after about 500°C.

Pressurization cycles were either done in a precision oven system or a Hart calorimeter, both with an automated manifold and custom collection electronics and software, as described elsewhere [13].

XRD samples were taken on a Bruker D8 Advanced and are shown in Fig. 5 for a before and after sample. Not much change in the diffraction pattern is evident. However, note that even though $ZrO_2$ dominates the XRD spectra, this batch of material was only 37% oxidized.

An attempt to measure radiation was conducted on a sample of Zr68–Ni30–Pd2 alloy heated to 510°C for 17 h (21% oxidized, not shown in Table 3). Thermal measurements taken concurrently to the X-ray measurements showed heat evolution. An AmpTek XR-100CR thin beryllium window Si–PIN X-ray detector was mounted though a Cajon seal directly over the powder contained in plastic cap along with a NTC thermistor. The system was sealed with O-rings, evacuated and then pressurized. The deuterium pressure was limited to 2 bar to avoid damaging the Be window. No increase in radiation during pressurization was observed.

## 3. Results and Discussion

Initially, we prepared our alloys as outlined by Yamaura et al. [1], but found that these materials did not absorb hydrogen or deuterium. However, after a series of tests, air oxidation at approximately 500°C, rather than 280–400°C in the Yamaura ptrotocol, allowed some materials to absorb hydrogen in an exothermic reaction [2]. Extended periods of oxidation reduced the hydrogen reaction and short oxidation times made materials that were hard to crush. After

**Table 3.** Heat treatment conditions and oxidation percentage for Zr68–Ni30–Pd2. The italicized values for the sample conditions produced materials that showed the most heat during pressurization.

| Sample number | Temp/time | % Oxidation to $ZrO_2$ and PdO |
|---|---|---|
| 2 | 513°C/2 h | 11 |
| 1 | 513°C/20 h | 37 |
| *5* | *675°C/2 h* | *19* |
| 3 | 675°C/20 h | 85 |
| 6 | 675°C/20 h | 101 |
| 8 | 780°C/2 h | 40 |
| 7 | 780°C/20 h | 148 |

exposure to deuterium/hydrogen the alloys became finely divided when heat was produced and retained the original texture when only minor heat was produced.

A pressurization cycle for four selected samples from Table 3 is shown in Fig. 6. Only sample 5 showed substantial heat and was finely divided when removed. The integrated heat for pressurization/depressurization cycles at various temperatures is shown in Fig. 7. Note that in the first cycle, a very large heat pulse was observed during pressurization. Additionally, $Heat_{GasIn} \gg Heat_{GasOut}$. What appears to be happening is that a chemical reaction occurs during the first exposure to deuterium/hydrogen, likely due to reduction of oxides and absorption of deuterium/hydrogen into the matrix. At 40°C, the desorption of deuterium/hydrogen is very slow so that in subsequent cycles, that heat is missing. Monitoring the pressure and gases during evacuation also indicates that deuterium/hydrogen is constantly evolving. At higher temperatures, the removal of deuterium/hydrogen occurs more readily but is still somewhat slow. Even at 200°C, the heat evolution does not display a single exponential (Fig. 6, inset). Desorption of spillover deuterium/hydrogen followed by slow removal from hydrides in the matrix may account for the shape of this desorption curve.

Of the seven samples examined, only sample 5 exhibited substantial amounts of heat. The heat observed for sample No. 5 was 20–100× larger than observed for the Pd on alumina or Pd in zeolites [13]. To quantify the heat, an aliquot of Zr68–Ni30–Pd2 (heated to 650°C for 3 h 15 m, 66% oxidized) was run in the Hart calorimeter at 40 $^o$C and found
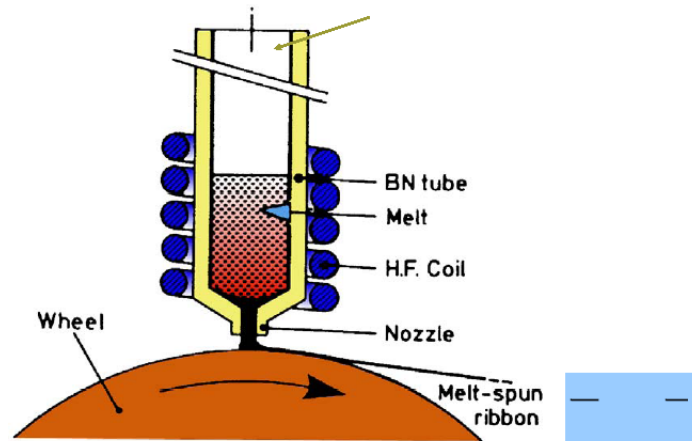


**Figure 3.** Melt-spinning set-up.

to be about 339 J/g. Water formation was minimal as measured by the RGA. Arata found larger amounts of heat (550–1000 J/g) with his Zr64–Ni30–Pd6 depending on his experimental protocol [22]. All these numbers are LESS than has been calculated for the reaction $Zr_2Ni + 2.25H_2 \rightarrow ZrH_2 + ZrNiH_2$; (–274.4 kJ/mol [21] or 1138 J/g), ignoring the approximately 10 J/g contribution from the formation of PdD with Pd at 6% [21]. *Therefore, chemistry canaccount for ALL the abnormal amounts of heat during pressurization and no new processes need be invoked.* Kitamura and co-workers also saw large amounts of heat during pressurization of Zr65.4–Pd34.6 (the depressurization, endothermic reaction was not measured) [8]. They observed slightly more heat with deuterium than hydrogen but the pressurization rates were not the same. They calculated an energy of 2.4 eV/Pd atom, which would be beyond chemistry, but they attributed all the heat to reaction only with palladium rather than the whole matrix [2].

Both Kitamura and our work used materials prepared as described by Arata et al. In catalysts preparations, it is possible that impurities or slight procedural changes will affect the catalytic activity. It is possible that Kitamura and our results would be different if the same catalyst was tested. However, there are several procedural issues with the experiment by Arata and Zhang depicted in Fig. 1. (1) The endothermic heat during depressurization was not measured. (2) The pressure was continually and slowly increasing, which performs PV work on the system producing heat (should be small). However, the higher deuterium pressures allow new chemistry to happen and because the endothermic heat during depressurization was not measured it is difficult to separate the chemistry of deuterium absorption and adsorption and PV work from LENR. The long-term heat was also not measured for a sufficiently long time to unambiguously determine that chemical energy is not being observed. Having the heat decrease in an exponential manner looks suspiciously like the depletion of a chemical reaction. (3) Few hydrogen controls were reported to help elucidate chemistry. (4) It was not clear from their papers or presentations if the samples were cycled so that the presented data may be due to reduction of oxides, which in the case of nickel and palladium is exothermic. Kitamura and coworkers did cycle a palladium black sample three times. The first cycle was higher but after this cycle, the deuterium and hydrogen numbers were the same [8]. They did not cycle their Zr65.4–Pd34.6 system.

In the Zr–Pd or Zr–Ni–Pd systems, if the sample was partially oxidized, there would be enough chemical energy present to account for the observed heat. Air oxidation using Yamaura's protocol [2] leaves considerable metallic zirconium present. Determining the oxidation state of the zirconium from only the XRD spectra is difficult as it can
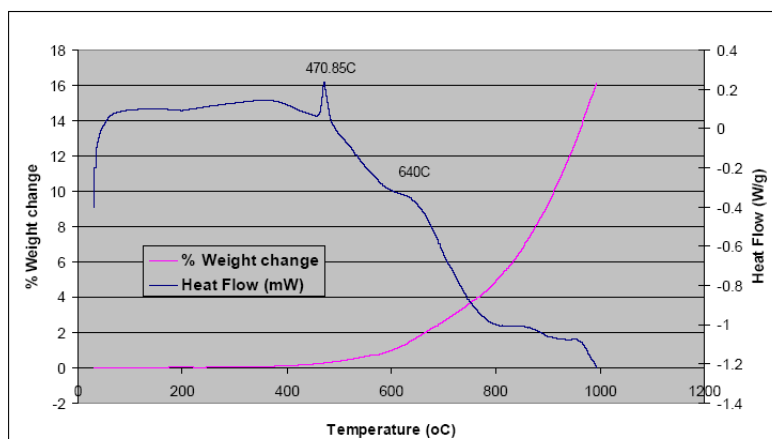


**Figure 4.** Thermal Gravimetric analysis of Zr68–Ni–30–Pd2. Most of the weight gain occurs above 600°C, showing that lower temperatures do not oxidize the Zr. Similar results were observed for the 6% Pd alloy, but the exotherms at 470°C and 640°C were much larger.
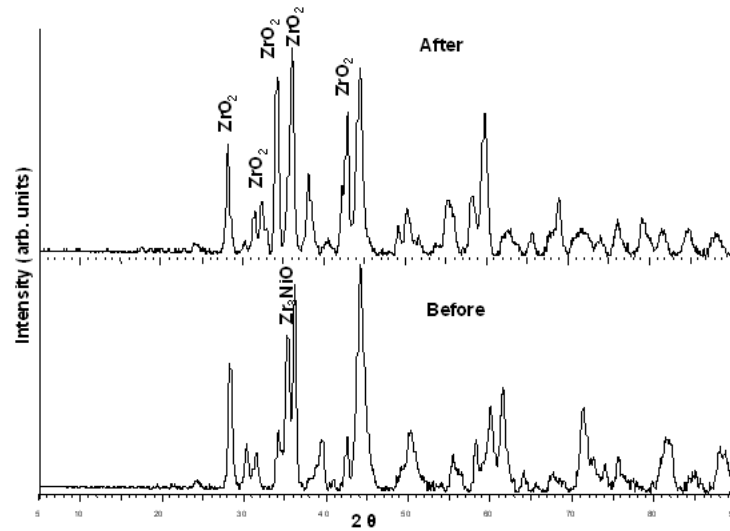
**Figure 5.** The XRD patterns of Sample 1 (Table 3) before and after cycling. The spectra are dominated by phases of $ZrO_2$ even though it was incompletely oxidized. After cycling certain oxides are reduced, which makes the $ZrO_2$ appear larger.

miss amorphous regions such as present in melt-spun alloys. The data in Fig. 6 illustrate why cycling and measurement of both $Heat_{GasIn}$ and $Heat_{GasOut}$ is important. Stopping with the initial pressurization may miss important chemistry and lead to the incorrect conclusion that the heat is due to a non-chemical process. Also, attributing all the heat to only a single chemical species, such as palladium, is clearly in error. Not measuring the heat absorbed during depressurization can miss reversible chemical reactions such as hydride formation. Likewise, having similar amounts of heat generated for deuterium vs. hydrogen (at 300°C in Fig. 7) implies a chemical process rather than new physics, such as LENR, as similar rates of some kind of unknown nuclear event are unlikely with both deuterium and hydrogen.
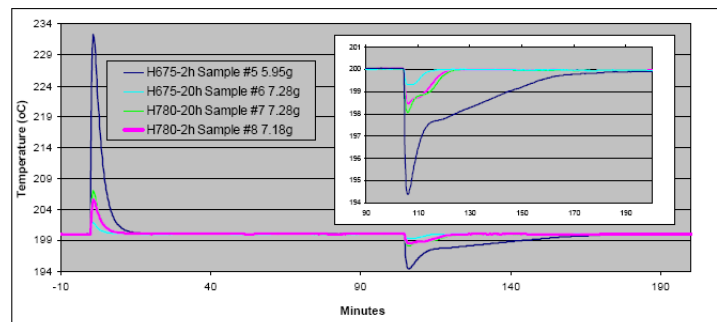


**Figure 6.** Typical deuterium pressurization/depressurization cycle for four samples (Nos. 5–8) from Table 3 carried out at 200°C in a precision oven. This cycle was taken after several other cycles at lower temperatures depleted the irreversible chemistry. Note the absence of long-term heat as the heat pulses return to the baseline.
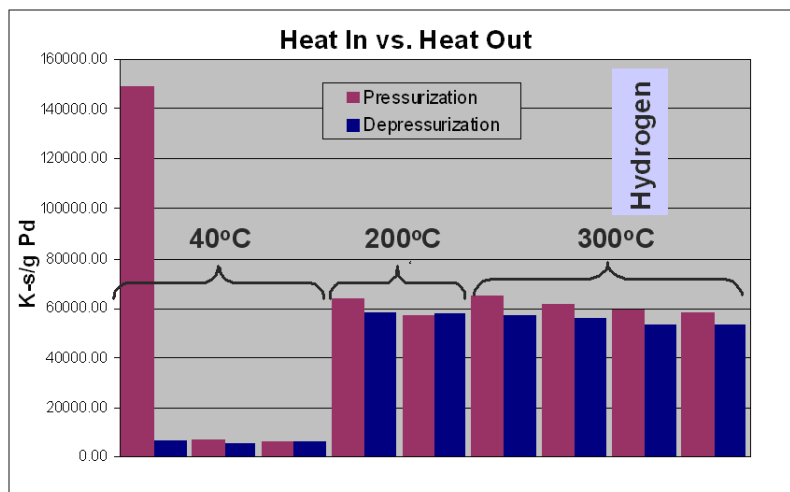
**Figure 7.** Integrated temperature curves for Sample No. 5 at various temperatures. The heat evolved in the precision oven system is difficult to accurately calibrate because the cells are air-cooled by forced convention whose patterns vary slightly between each set-up. However, relative measurements within a set are reproducible. There appears to be excess heat when comparing $Heat_{GasIn}$ vs. $Heat_{GasOut}$. The excess is about 10% of the total and may be a measurement error as the integrated temperature for the depressurization part of the cycle is less accurate because the heat evolves over a much longer period of time than the heat during pressurization and some baseline drift may occur. Note at 40°C the initial heat is not recovered in subsequent pressurization cycles because not all the deuterium is removed by just evacuating the sample. Therefore, subsequent pressurizations do not have the benefit from the heat of forming $ZrD_x$. The unit K-s/g is a derived unit related to energy.

## 4. Conclusions

Preparation of Pd–Zr-Pd via the route outlined by Arata et al. produced materials that were not very exothermic when exposed to hydrogen/deuterium. Modifying the procedure by heating at higher temperatures partially oxidized the alloys and allowed hydrogen/deuterium to absorb in an exothermic reaction but highly oxidized materials do not take-up hydrogen or deuterium. Measuring the weight gain during oxidation helps determine the oxidation state. By recording both the $Heat_{GasIn}$ and $Heat_{GasOut}$, cycling the materials, and using both hydrogen and deuterium, we found that the large amount of heat generated with these alloys is more consistent with known chemistry rather than invoking LENR. The small amount of heat unaccounted for ($<10\%$ of the total) is most likely unidentified chemistry or measurement error. Whether or not it is a new phenomenon that may be worth exploring cannot be definitively ruled-out from our results. It may be that the size of the Pd nano-particles in the matrix varies with preparation conditions and that a certain size of particles is required to allow LENR to occur. The size requirements and production processes to produce these particles (if that is important) still need to be delineated.
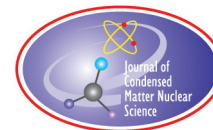
# References

[1]  Shin-ichi Yamaura, Ken-ichiro Sasamori, Hisamichi Kimura, Akihisa Inoue, Yue Chang Zhang and Yoshiaki Arata, Hydrogen absorption of nanoscale Pd particles embedded in ZrO2 matrix prepared from Zr–Pd amorphous alloys, *J. Mater. Res.*, **17** (2002) 1329–1334.

[2]  S. Yamaura, H. Kimura and A. Inoue, Hydrogen absorption of oxide composite materials prepared from melt-spun Zr–Pd–Ni alloys, Annual Fall Meeting of the Japan-Institute-of-Metals Location: Osaka, Japan, *Materials Trans.* **44** (2002) 696–699.

[3]  Yoshinori Arachi, Shuichi Emura, Akira Omura, Masanobu Nunogaki, Takeshi Asai, Shunichi Yamaura, Akihisa Inoue and Yoshiaki Arata, Structural analysis of nano-sized-Pd/ZrO2 composite after H(D) absorption, *Solid State Ionics* **177** (2006) 1861–1864.

[4]  Yamazaki Toshimitsu, Sato Masaharu and Itoh Satoshi, Discovery of spontaneous deformation of Pd metal during hydrogen absorption/desorption cycles, *Proc. the Japan Academy Series B-Physical and Biological Sci.* **85** (2009) 183–186.

[5]  Y. Arata and Y.-C. Zhang, Development of 'DS-Reactor' as the practical reactor of 'cold fusion' based on the 'DS-cell' with 'DS-cathode', *Proc. ICCF12*, World Scientific, Singapore, 2006, pp. 44–54.

[6]  Yoshiaki Arata and Y.-C. Zhang, Establishment of the solid fusion reactor, *Proc. the 14th Int. Conf. on Condensed Matter Nucl. Sci. and the 14$^{th}$ Int. Conf. on Cold Fusion (ICCF-14)*, 10–15 August 2008, Washington DC, p. 756.

[7]  Y. Arata and Y. Zhang, The establishment of solid nuclear fusion reactor, *J. High Temperature Soc.* **34** (2008) 85–93 (in Japanese).

[8]  Akira Kitamura, Takayoshi Nohmi, Yu Sasaki, Akira Taniike, Akito Takahashi, Reiko Seto and Yushi Fujita, Anomalous effects in charging of Pd powders with high density hydrogen isotopes, *Phys. Lett.* **A373** (2009) 3109–3112.

[9]  Y. Sasaki, A. Kitamura, T. Nohmi, Y.Miyoshi and A. Taniike, Anomalous heat generation in charging of pd powders with high density hydrogen isotopes (i) results of absorption experiments using Pd powders, presented in the*15th Int. Conf. on Condensed Matter Nucl. Sci.*, 2009, Rome, Italy.

[10]  A. Takahashi, A. Kitamura, Y. Sasaki, Y. Miyoshi, T. Nohmi, A. Taniike, R. Seto and Y. Fujita, Anomalous heat generation in charging of pd powders with high density hydrogen isotopes (ii) discussions on experimental results and underlying physics, presented in the 15$^{th}$ *Int. Conf. on Condensed Matter Nucl. Sci.*, 2009, Rome, Italy.

[11]  For Heat$_{GasIn}$ (pressurization) and Heat$_{GasOut}$ (depressurization or evacuation) the In/Out refers to the movement of the gas not the flow of heat, which is generally in the opposite direction.

[12]  P.L. Levine and K.E. Weale, The palladium + hydrogen equilibrium at high pressures and temperatures, *Trans. Faraday Soc.* **56** (1960) 357–362.

[13]  David A. Kidwell, Allison E. Rogers, Kenneth Grabowski and David Knies, Does gas loading produce anomalous heat? *15th Int. Conf. on Condensed Matter Nucl. Sci.*, Rome, Italy, October 5–9, 2009 (in Press).

[14]  D.A. Kidwell, D.L. Knies, A.E. Moser and D.D. Dominguez, Yes, virginia there is heat, but it is likely of chemical origin, 9$^{th}$ *Int. Workshop on Anomalies in Hydrogen/Deuterium Loaded Metals*, Certosa di Pontignano in Siena, Italy, 17–19 September 2010.

[15]  Sheng-Yang Huang, Chin-Da Huang, Boh-Tze Chang and Chuin-Tih Yeh, Chemical activity of palladium clusters: sorption of hydrogen, *J. Phys. Chem.* B **110** (2006) 21783–21787.

[16]  Shu-Chin Chou, Shu-Hui Lin and Chuin-Tih Yeh, lsosteric heat of sorption of dihydrogen on alumina-supported palladium, *J. Chem. Soc. Faraday Trans.* **91** (1995) 949–951.

[17]  L.F. Chen, J.A. Wang, M.A. Valenzuela, X. Bokhimi, D.R. Acosta, and O. Novaroc, Hydrogen spillover and structural defects in a PdO/zirconia nanophase synthesized through a surfactant-templated route, *J. Alloys Compounds* **417** (2006) 220–223.

[18]  Often a control for spillover is testing the support without a catalyst present and generally the support does not absorb hydrogen. This is problematic because a catalyst is required to activate the hydrogen for spillover to occur. Other measurements such as the uptake vs. pressure are also problematic because both spillover and absorption into the particles can occur at similar rates. Thus, there are no good techniques for measuring Pd:H ratios on supported nanoparticles.

[19]  Pen Chou and M.A. Vannice, Calorimetric Heat of Adsorption Measurements on Palladium I. Influence of Crystallite Size and Support on Hydrogen Adsorption, *J. Catalysis* **104** (1987) 1–16.

[20]  Pen Chou and M.A. Vannice, Calorimetric Heat of adsorption measurements on palladium I. Influence of crystallite size and support on hydrogen adsorption II. Influence of crystallite size and support on CO adsorption, *J. Catalysis* **104** (1987) 17–30.

[21] P. Dantzer, W. Luo, T.B. Flanagan and J.D. Clewley, Calorimetrically measured enthalpies for the reaction of h(g) with Zr and Zr alloys, *Metallurgical and Materials Trans.* A **24** (1993)1471–1479.

[22] Y. Arata, Y.C. Zhang and X.F. Wang, Production of helium and energy in the solid fusion, presented at the*15th Int. Conf. on Condensed Matter Nucl. Sci.* 2009, Rome, Italy, S4–01.

[23] Kitamura *et al.*, Measure about 2.3 kJ/g of Zr65.4–Pd34.6. Formation of ZrH1.5 would produce about 0.9 kJ/g, formation of PdH0.7 would produce about 0.12 kJ/g and reduction of PdO would yield 0.65 kJ/g. These reactions total to 1.67 kJ/g, much lower than that measured. Some other reaction must be occurring to produce the measured heat, which may bear investigating.

Research Article

# Are Oxide Interfaces Necessary in Fleischmann–Pons-type Experiments?

D.D. Dominguez,* D.A. Kidwell, D.L. Knies, K.S. Grabowski and G.K. Hubler

*U.S. Naval Research Laboratory, Washington, DC 20375, USA*

J.H. He

*Nova Research Inc., Alexandria, VA, USA*

V. Violante

*ENEA, Frascati, Italy*

## Abstract

The generation of excess power in a palladium deuteride electrochemical system is often difficult and time consuming. Long incubation times, on the order of weeks or months, are necessary presumably for the basic electrolyte to dissolve and redeposit essential impurities onto the cathode surface. To accelerate this process, we added chemical additives to the electrolyte once the palladium was loaded with deuterium. Chemicals that produce oxide interfaces on the palladium surface seemed to occasionally produce apparent excess power. A single $Pd_{90}Rh_{10}$ cathode generated a total apparent excess energy on the order of 10 kJ after a series of additions in an experiment that only took one week. The results are encouraging and may lead to an understanding of what triggers excess power production in Fleischmann–Pons-type experiments. A hypothetical model describing the possible role of oxide interfaces is described..

© 2012 ISCMNS. All rights reserved. ISSN 2227-3123

*Keywords:* Chemical additives, Deuterated palladium cathodes, Electrochemical, Excess power

## 1. Introduction

Since the initial publication by Fleischmann and Pons [1], numerous accounts of excess power production in palladium cathodes electrochemically loaded with deuterium have been reported [2]. Research at SRI International (SRI) initially identified three criteria necessary for the excess power generation: (1) high cathode loading with a D/Pd ratio near one, (2) maintenance of high loading for considerable periods of time and (3) an interfacial current density above a critical threshold [3]. Later, other conditions were also thought to be important for the successful initiation of excess power

---

*E-mail: dawn.dominguez@nrl.navy.mil

production such as the presence or absence of certain impurities and the application of external stimulation to produce non-equilibrium conditions [4,5]. Although these factors were recognized by the community, it remained difficult to achieve high loading in Pd cathodes and irreproducibility of excess power production in Fleischmann–Pons-type electrochemical experiments continued to plague the field.

A number of technical advances occurred during the last decade. In 2003, Dardik (Energetics Technologies (ET), Israel) reported on the use of SuperWaves[TM] excitation to accelerate the rate and extent of electrochemical loading of deuterium into Pd cathodes [6]. When SuperWaves[TM] were used in lieu of D.C. current to drive electrolysis experiments, a significant amount of excess heat was generated in three ENEA-produced palladium cathodes [7]. These results, presented at the 11th International Conference on Cold Fusion (ICCF11) in 2004, remain among the largest reported to date.

Violante's group (ENEA, Italy) focused on the metallurgical aspects of Pd that led to high deuterium loading. For a particular batch of commercial material, they initially defined a process consisting of cold rolling and annealing that produced an optimized Pd metallurgical structure that reduced the internal stresses and concentration gradients generated in the material during deuterium loading. With the appropriate metallurgy, it was shown that the extent of deuterium loading increased, loading to high D/Pd ratios at relatively low current densities was easier, the reproducibility of excess heat production and the magnitude of excess heat generated were enhanced [8]. At ICCF 14 in 2008, further results on the systematic characterization of the metallurgical properties of Pd cathodes in experiments at ENEA, SRI and ET were presented [9–11]. From the more recent studies, the ENEA group identified additional features necessary for successful excess heat production. These included (a) a spectrum of Pd contaminants that give rise to grains with a nominal size on the order of 100 $\mu$m with predominately $\langle 100 \rangle$ crystal orientation after annealing and well defined grain boundaries following a chemical etch in aqua regia, and (b) a textured Pd electrode surface morphology showing pseudo-periodic patterns with a period in the range of tenths of microns.

Because of these developments, NRL embarked on an experimental program in collaboration with ENEA, ET, and SRI. The objective of the effort was to further explore excess power generation in deuterated palladium electrochemical systems with the goal of trying to understand the nature of the palladium interface and its role in the production of excess power. In this paper, the results from over 100 calorimetric experiments are presented on Pd foil cathodes electrochemically loaded with deuterium in thermodynamically closed electrochemical cells under either constant input power or constant current conditions. The experiments were driven by both D.C. current and superwave excitation.

Generally, long incubation times, on the order of weeks or months, are thought to be necessary to observe excess power, although loading of thin electrodes to high levels of deuterium takes hours. During this extended time, the electrochemistry presumably is concentrating some essential impurities onto the cathode surface. We chose to speed-up this process by making intentional chemical additions while the cells were running and after deuterium loading had occurred. Excess power was not observed in the majority of experiments described until elements known to form oxides (and possibly magnetic interfaces) in highly basic solutions were added to the electrolytes. The effect of the additions on excess power production in Pd cathodes is reported.

## 2. Experimental

Two types of calorimeters were used: flow calorimeters designed by ET and SRI and a four-position heat-conduction calorimeter (Hart Scientific) described previously [12]. In both, closed electrochemical cells were employed with 50 $\mu$m thick palladium foil cathodes obtained from different commercial sources and two 99.9% platinum foil anodes in a symmetric "sandwich" configuration. Most Pd cathodes were processed (rolled, annealed and chemically etched) using procedures optimized at ENEA for high loading and excess power production [8,11]. Additional Pd cathodes were custom-fabricated to produce morphologically interesting surfaces. The heavy water electrolyte was either 0.1 M or 1 M LiOD freshly prepared in a glove bag prior to each new electrochemical experiment by dissolving lithium
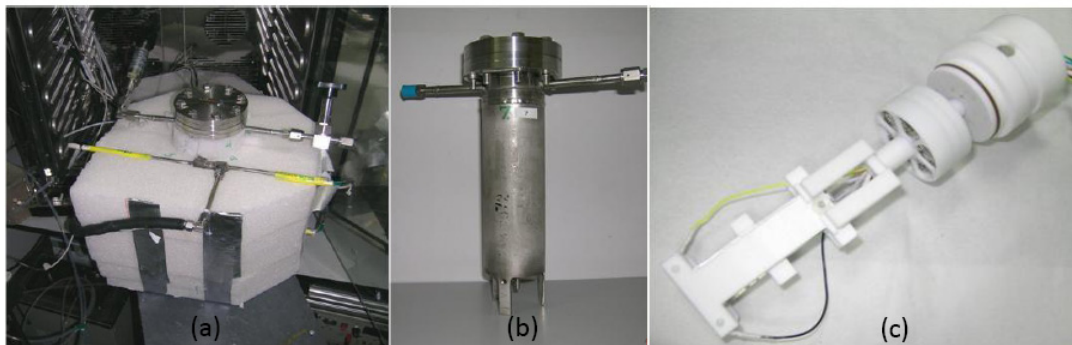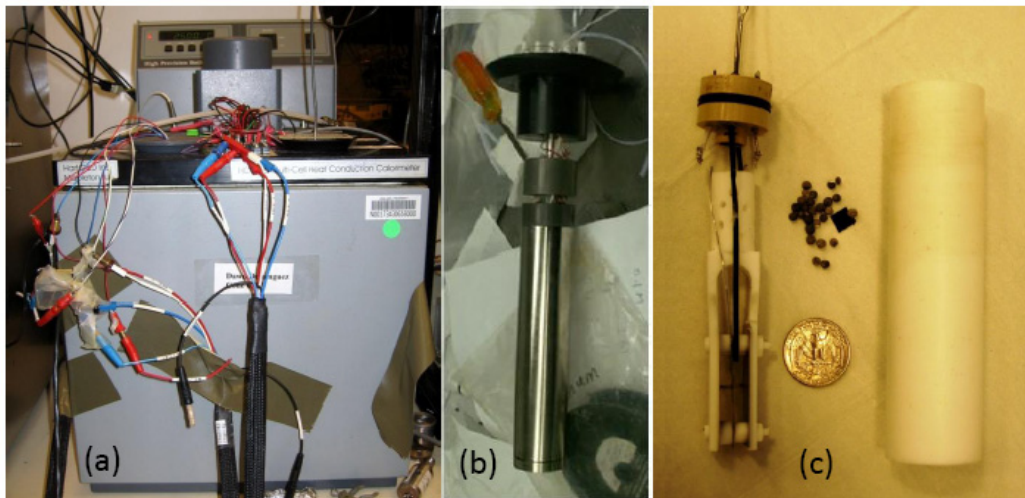
**Figure 1.** Photographs showing (a) ET flow calorimeter, (b) Teflon-lined stainless steel cell, and (c) all-Teflon interior cell parts.

foil (Johnson Matthey, 99.9%) or lithium deuteride (Aldrich, 98 atom % D) in deuterium oxide (CIL, Aldrich, Alfa Aesar). Light water electrolyte (0.1 M LiOH) was made from lithium deuteride and distilled water. High surface area catalysts, 0.5% Pd on alumina (Sud-Chemie) and Pt electrode on carbon fiber paper (Johnson Matthey), were used to recombine the evolved deuterium/hydrogen and oxygen gases. Chemical additives were reagent grade and used without purification. The chemicals were added to the electrolyte (24 mL volume) in the Hart cells in 5–10 mg quantities. Electrochemical experiments were usually operated in the galvanostatic mode, but some experiments were conducted with SuperWaves$^{TM}$ excitation and some with constant input power. Experiments in the ET calorimeters were run for 1–3 months while those in the Hart calorimeters were carried out over approximately a 1 week period. No measurement of D(H)/Pd loading was made in any of the experiments because a four point probe measurement is a possible source of extra power.

Teflon-lined stainless steel cells (5 cm internal diameter, 23 cm length), with spiral cooling water pipes embedded in the walls, were used in the ET flow calorimeters. A flow calorimeter, cell and all-Teflon interior cell parts are shown in Fig. 1. Two opposite outlets with VCR connectors are located at the top of the cell. A pressure transducer and a pressure relief valve are attached to the cell via one of the connectors. The second connector, for coupling to a mass spectrometer for He detection, was plugged in our work. The sealed stainless steel cell was covered with Rohacell foam for thermal insulation and two tubes that connected to the cooling water pipes passing around the exterior of the cell were inserted through the foam. The inlet and outlet temperatures of the water were each measured with two PT-100 platinum resistance temperature devices (RTDs) inserted into the tubes attached to the cooling water pipes. The cooling water temperature was maintained at 5.00 or 20.00 ± 0.01°C using an external chiller and the entire calorimeter assembly was held at a constant temperature (8 or 22°C) in an incubator with a thermal stability of ±0.1°C. The mass flow rate of the cooling water was determined using a Bronkhorst mass flow controller. Experiments carried out in three ET cells/calorimeters used a Pd cathode (80 mm × 10 mm × 50 $\mu$m) between two Pt foils (80 mm × 20 mm × 110 $\mu$m) and a cathode–anode spacing of 5 mm. Teflon-coated Pt wires were spot-welded to the electrodes and electrical connections inside the cell and to external instrumentation were made via multi-pin connectors located on the sealing flange.

Teflon cells (25 mm internal diameter, 13.5 cm length) based on the ENEA/Violante design were used in three of the four available positions in the Hart calorimeter. Photos of the Hart calorimeter, the anodized aluminum cell holder, internal cell parts and Teflon cell are presented in Fig. 2. The electrode dimensions for the Hart cells were: cathode (40 mm × 10 mm × 50 $\mu$m), anode (45 mm × 20 mm × 180 $\mu$m) and cathode–anode spacing of 5 mm. Teflon-coated Pt wires were attached by spot-welding to the electrodes and to Pt wires extending through the PEEK cell top. Two SS

**Figure 2.**   Photographs showing (a) Hart calorimeter, (b) anodized aluminum cell holder, and (c) internal cell parts and Teflon cell.

syringe needles were inserted through the PEEK top to allow chemical additions to the electrolyte. Black polyethylene tubing was attached to one of the syringe needles so that electrolyte could be drawn into the syringe from the bottom of the cell. The Hart calorimeter was typically maintained at temperatures of 20.00, 21.10, 25.00 or 40.00°C in a water bath with a thermal stability of $\pm 0.001$°C.

Scanning electron microscopic images were acquired on a Carl Zeiss SMT (formerly LEO) Supra 55 instrument. It is a Schottky thermal field emitting microscope capable of high-resolution imaging at primary beam voltages from 200 V–30 kV. X-ray diffraction measurements were made on a high-resolution 250 mm Rigaku diffractometer using Cu-K$\alpha$ radiation from a 12-kW rotating anode generator. X-ray photoelectron spectroscopy (XPS) analysis was run on a Thermo-Scientific K-Alpha XPS instrument.

## 3.  Results and Discussion

Table 1 shows a listing of the different cathode materials investigated in both the ET and Hart calorimeters and the number of electrochemical experiments performed in each. As seen from the Table, 63 cathodes produced from eight commercial sources of Pd were examined in heavy water electrochemical experiments through the end of 2010 and 15 cathodes from five commercial sources of Pd were used in light water experiments. In addition, 34 heavy water experiments included some custom Pd foils produced in our laboratory as well as some other metal foil cathodes. Finally, one Ni/LiOH experiment and two experiments with Pd foil cathodes in KOD and $H_2SO_4$ electrolytes were carried out.

Pd from three, Engelhardt, Platexis and Holland Moran, of the eight commercial sources of Pd used in the heavy water experiments, were acquired prior to 2005. The impurities present in these materials differed significantly from those obtained more recently. Inductively Coupled Plasma Mass Spectrometry (ICP-MS) analysis showed that the older materials contained substantial quantities of rhodium (12–31 ppm) and platinum (30–190–ppm) whereas the

**Table 1.** A listing of cathode materials used in electrochemical experiments performed in the ET and Hart calorimeters from January 2009 to December 2010. The foils highlighted in bold faces were used in the initial experiments where no chemical additive was added to the electrolyte

| | ET | HART | Total |
|---|---|---|---|
| Pd/LiOD | | | |
| Engelhardt | **2** | **8** | |
| Platexis | **9** | **7** + 2 | |
| Holland Moran | **1** | | |
| ESPI | **7** | **1** + 5 | |
| Johnson Matthey | **1** | | |
| Goodfellow | 2 | **2** + 14 | |
| Alfa Aesar | | **1** | |
| G&S | | 1 | |
| Total | 22 | 41 | 63 |
| | | | |
| Pd/LiOH | | | |
| ESPI | **2** | **3** + 1 | |
| Johnson Matthey | **2** | | |
| Goodfellow | | 3 | |
| Alfa Aesar | | **2** | |
| G&S | | 2 | |
| Total | 4 | 11 | 15 |
| | | | |
| x/LiOD | | | |
| Pd/0.25% B | | **1** + 1 | |
| Pd/0.75% B | | 2 | |
| Pd–C nanofoam | | **1** | |
| | | | |
| Pd nanoparticles innanoporous Au | | **1** | |
| Nanoporous Pd–Co | | **1** | |
| Pd/5% Ru | | 2 | |
| Pd 98%/Pt 1%/Rh 1% | | 2 | |
| Pd 90%/Rh10% | | 1 | |
| Ni/Pd | | 2 | |
| Ni/Pd/Ni | | 1 | |
| Ni | | 3 | |
| Nb | | 3 | |
| Ta | | 2 | |
| Pt | **6** | 5 | |
| Total | 6 | 28 | 34 |
| | | | |
| Misc | | | |
| Ni/LiOH | | 1 | |
| Goodfellow Pd/KOD | | 1 | |
| Platexis Pd/H2SO4 | | **1** | |
| Total | | 3 | 3 |
| Grand Total | | | 115 |
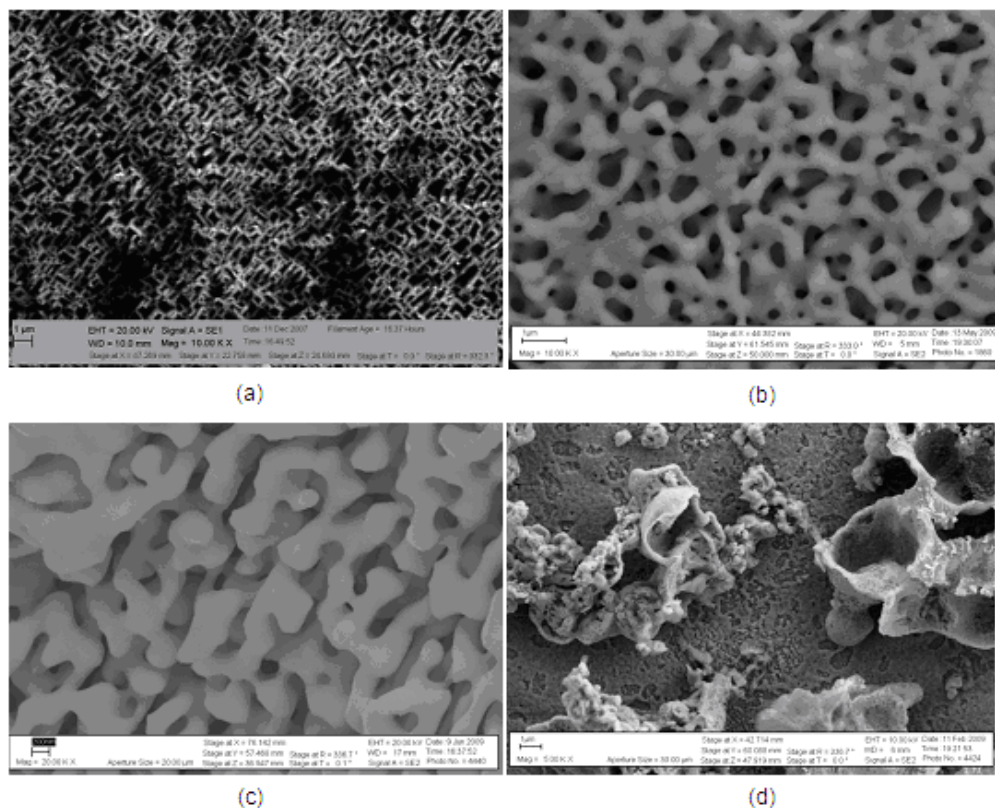
**Figure 3.** SEM images showing surface morphology of selected cathode foils as follows: (a) ET experiment 64a Pd at 10 k× (1 $\mu$m scale bar), (b) electrochemically de-alloyed $Pd_{20}Co_{80}$ at 10 k× (1 $\mu$m scale bar), (c) chemically de-alloyed $Au_{30}Ag_{70}$ at 20 k× (200 nm scale bar) and (d) surface oxidized/reduced Pd at 5 k× (1 $\mu$m scale bar).

newer materials had less of these elements, but included higher amounts of zirconium, yttrium and hafnium [13]. The different impurity profiles of the materials likely reflect alterations in Pd processing outcomes that occurred after 2005.

The Pd foil cathode used in ET experiment 64a is the "gold standard" for the production of excess power (25 ×) in Pd foil cathodes [7]. The crystallographic orientation of the foil was mostly $\langle 100 \rangle$. The morphology of the foil was characterized by grains 100s of $\mu$m in size and a well-defined "2D grating" surface structure after etching. Attempts to make cathodes with similar surface morphology were undertaken during the course of our work. Examples of some of the cathode surfaces produced are shown in Fig. 3. Presented in the figure (and included in Table 1) are an electrochemically de-alloyed Pd-Co material, a chemically de-alloyed Au–Ag material and a surface oxidized/reduced Platexis Pd foil. Other techniques used for cathode development include surface templating and ion implantation (not shown).

Highlighted in Table 1 are 59 cathodes that failed to produce excess power in our earliest calorimetric experiments. These experiments were carried out without the addition of chemical additives to the electrolyte. Of these, 15 cathodes (nine Pd cathodes run in light water electrolyte and six Pt cathodes run in heavy water) were run as controls and were not expected to generate excess power. Experiments with 43 of the other 44 early Pd cathodes were carried out in LiOD
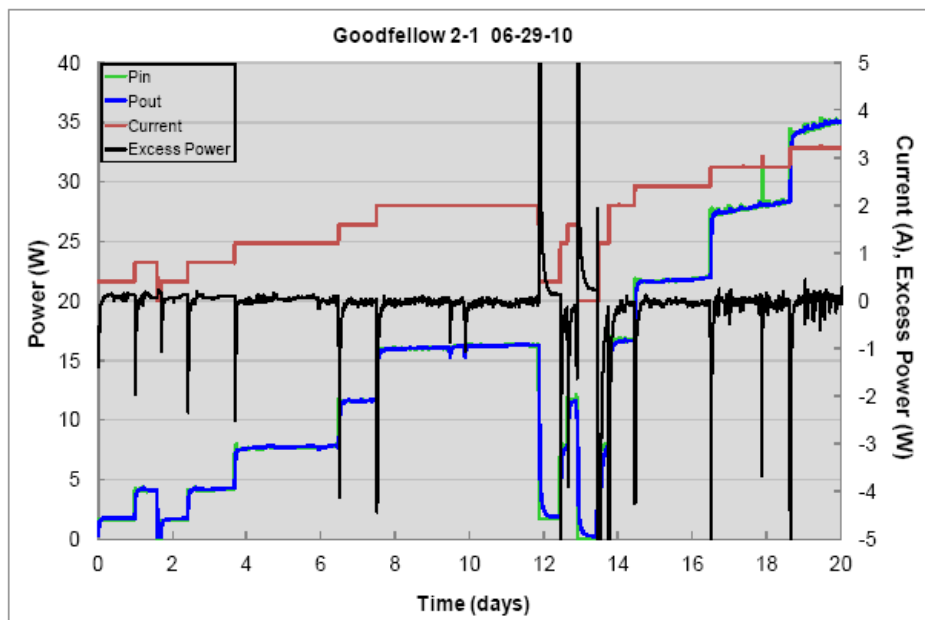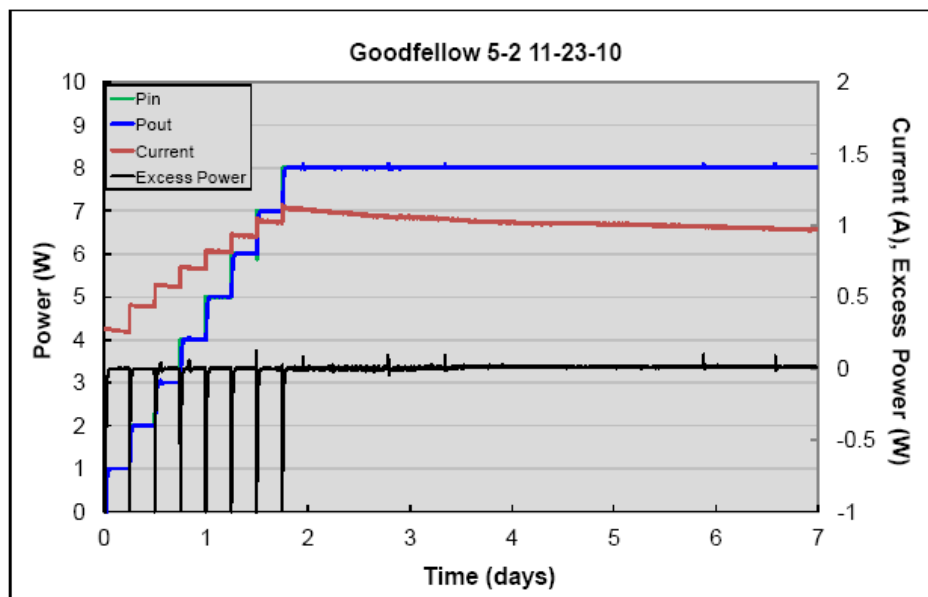
**Figure 4.** Plots of input power, output power, current and excess power as a function of time for the first 20 days of a Goodfellow Pd cathode run in 0.1 M LiOD at 40°C in the ET flow calorimeter without any chemical additions. During this time, the current and input powers were increased to 3.2 A (400 mA cm$^{-2}$) and 35 W, respectively.

and 1 Pd cathode was run with sulfuric acid electrolyte. The custom Pd cathodes shown in Fig. 3 were included among the unproductive materials examined.

The early experiments demonstrated the behavior of the ET and Hart calorimeters. In most experiments, the electrochemical cell was operated in the constant current mode with the current increased stepwise from 0.01 to 2000 mA as the experiment progressed. The input and output powers to the calorimeters were calculated at each step and the data were fitted using the initial steps as calibration assuming that no excess power was being produced. The Hart fitting coefficients each varied by less than 1% over a several month period. The consistency of the fitting coefficients confirmed the stable performance of the Hart calorimeter.

Examples of data obtained during electrolysis experiments in the ET and Hart calorimeters when no chemical additions were made to the 0.1 M LiOD electrolyte solution are displayed in Figs. 4 and 5, respectively. The figures show plots of the electrochemical input and output powers to the cell that were fit during the initial current steps, the current and the excess power ($P_{out} - P_{in}$). The data clearly show that no excess power was produced in either of the cells during the times shown.

After running nearly 60 calorimetric experiments over a year and a half with no excess power observed, we began to make chemical additions to the electrolyte in the Hart cells. The purpose of the additions was to accelerate the initiation of the excess power by forming oxides or other reactive species on the cathode surface. Chemicals were added to the electrolyte at high current (power) levels so as not to hinder the loading of the cathode. The additions were made by placing a small amount (few mg) of solid additive in a syringe, drawing up some electrolyte solution into the syringe and re-injecting the solution + additive into the cell. In this way, the additions were made without exposing the electrolyte to the ambient atmosphere. Some of the additions occasionally produced a small, nearly constant apparent excess power
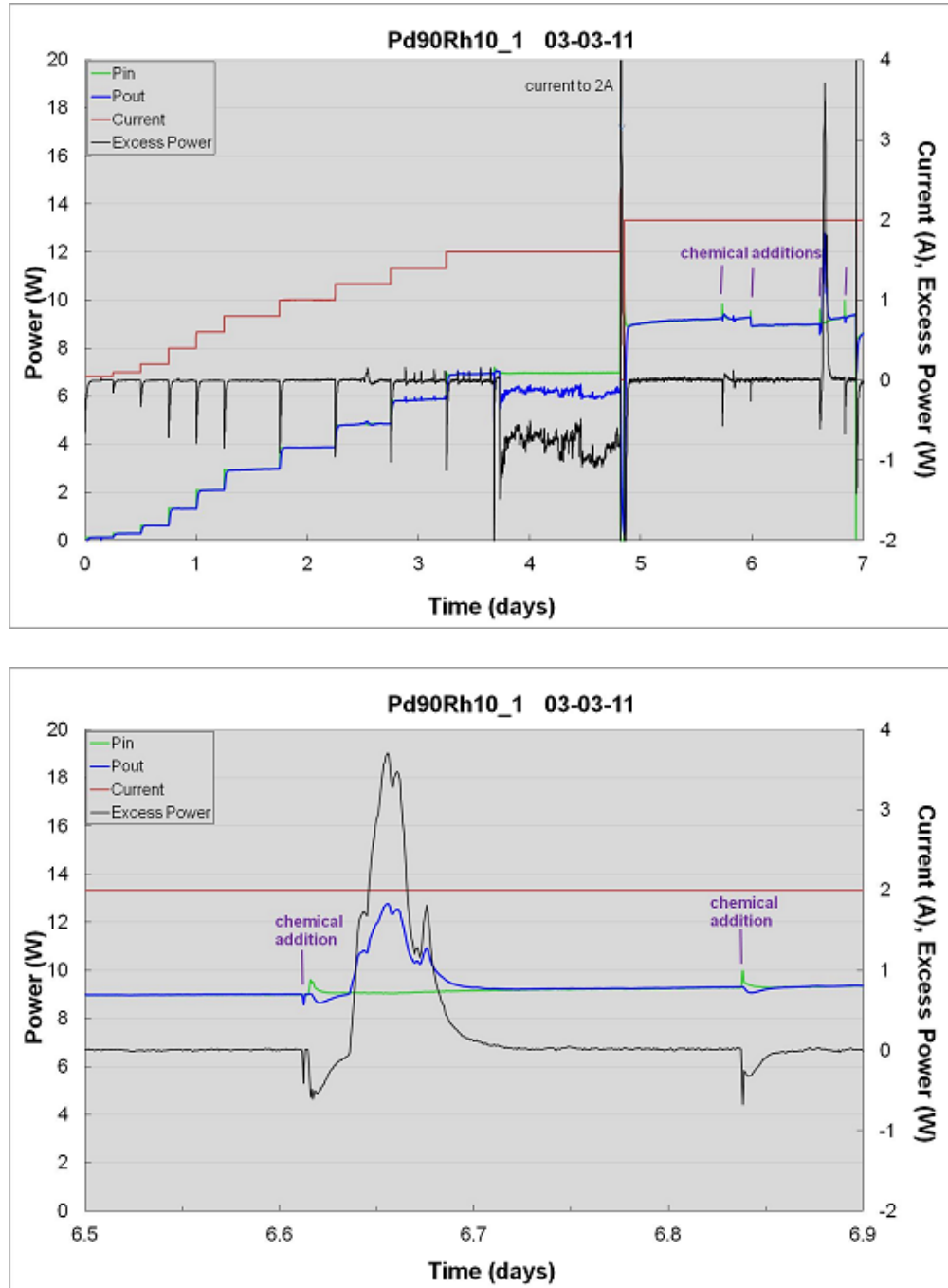
**Figure 5.** Plots of input power, output power, current and excess power as a function of time since the start of the experiment for a Goodfellow Pd cathode run in 0.1 M LiOD at 40°C in the Hart calorimeter without any chemical additions. During this time, the current and input powers were increased to 1 A (250 mA cm$^{-2}$) and 8 W, respectively.

(20–100 mW) event following the addition. The generation of an effect by the chemical addition was intriguing, but its small magnitude and constant offset from the baseline caused us to question the source of the heat. One possibility was that the chemical addition changed the resistance of the electrolyte so that the power distribution in the cell was shifted between the electrode and the catalyst regions. Experiments with resistors in the cell indicated that the point of power generation did not greatly affect the heat measurement by the Hart, so the observations of long-term, small amounts of excess power still are unexplained.

In many calorimetric experiments, more than one chemical addition was made when no response from an individual additive was apparent. One such experiment with a Pd$_{90}$Rh$_{10}$ cathode in 1 M LiOD is shown in Fig. 6. At about 3.7 days, an instability occurred due to a loose connection on the Hart calorimeter that persisted until the system was temporarily stopped, repaired and restarted at a current of 2 A. Once the system regained stability several chemicals were added sequentially to a Hart cell. No apparent excess power was produced after the first two additions. However, a large spike of apparent excess power was generated following the third addition. The apparent excess power spike peaked at a maximum of almost 4 W and persisted for approximately 2 h. Thus, the total apparent excess energy produced was on the order of 10 kJ. This was the largest apparent excess power event seen in our laboratory to date. The chemical energy produced by the additions of a few mg of metal salts cannot account for the 10 kJ excess observed in this experiment. A second identical addition to the electrolyte solution following the appearance of the spike and recovery of the baseline had no effect on the excess power production. At this point, it is not known whether the third chemical addition alone was responsible for the power spike or whether some synergism among the different additives occurred. This is under investigation.

Shown in Fig. 7 are some SEM images taken of the Pd$_{90}$Rh$_{10}$ cathode surface after removal from the Hart cell and

**Figure 6.**   (a) Plots of input power, output power, current and excess power as a function of time for a $Pd_{90}Rh_{10}$ cathode run at 25°C in the Hart calorimeter with chemical additions as indicated and (b) an enlargement of the plots shown above from 6.5 to 6.9 days. Prior to the apparent excess power event, the input current and power were 2 A and 9 W, respectively.
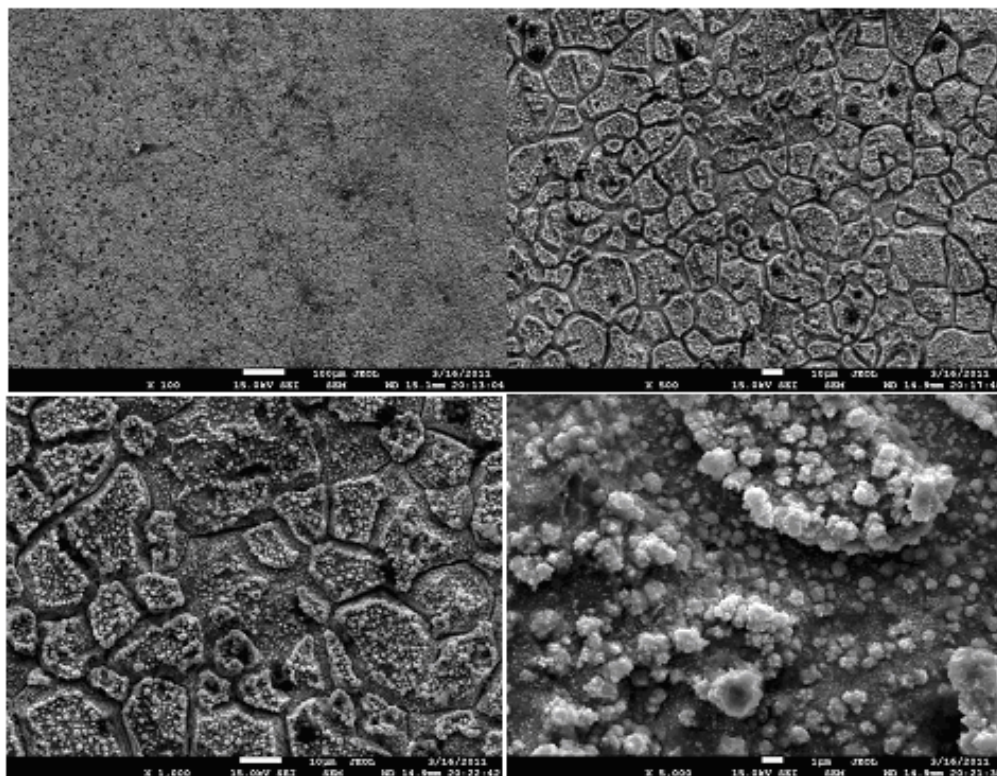
**Figure 7.** SEM images at 100 (100 $\mu$m scale bar), 500 (10 $\mu$m scale bar), 1000 (10 $\mu$m scale bar) and 5000 × (1 $\mu$m scale bar) magnification of the $Pd_{90}Rh_{10}$ cathode surface after 7 days in the Hart calorimeter. Chemical additions were made to the cell at 2 A/ 9 W input power and an apparent excess power event occurred after the third addition. The images show a white, crystalline material deposited around the grains and in the grain boundaries of the cathode. The white material appears to be a lithium aluminate.
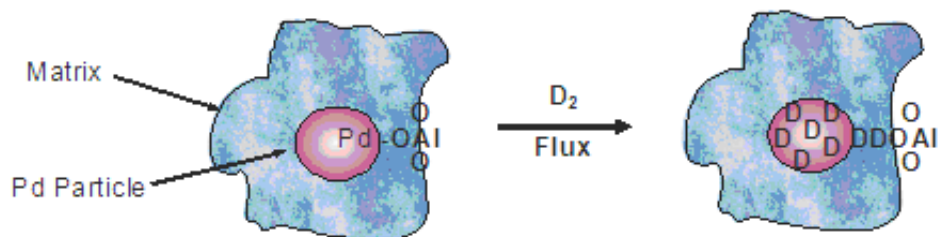


**Figure 8.** A hypothetical model illustrating the possible role of oxides on the palladium surface in the generation of excess power. The oxides are known to produce strong electric fields up to 9.5 V/nm which might enable the deuterium atoms to approach closely enough to undergo an unknown reaction.

rinsing with distilled water. The images show a white, crystalline material deposited around the grain edges and in the grain boundaries of the cathode. The deposited material contained aluminum and oxygen by XPS and energy dispersive X-ray (EDX) analysis. X-ray diffraction analysis of another cathode foil identified the white material found on that foil as lithium aluminate. The white material usually forms in the cell as a large deposit at the base of the catalyst cage and is presumed to originate as the electrolyte leaches alumina from the catalyst. It is not often observed on the surface of cathodes taken out of the Hart cells.

The surface of the $Pd_{90}Rh_{10}$ cathode was examined by XPS after removal from the Hart cell. Besides carbon and oxygen, a number of elements were identified in the analysis. These included aluminum (supposedly from the catalyst), uranium, copper, nickel, cobalt, sulfur and platinum as well as possibly zinc, lead and tin. The stainless steel syringe needles were thought to be a likely source of most of the metallic impurities. Uranium may have been introduced inadvertently as cross contamination from an earlier experiment. It is not known whether any of these impurities played a role in the excess power generation.

Figure 8 shows a hypothetical model illustrating the possible role of oxides on the palladium surface in the generation of excess power. According to the literature, oxides produce strong electric fields up to 9.5 V/nm [14]. The high electric fields might enable two deuterium atoms to approach each other close enough to form $D_2$ molecules in the oxide interface that formed on the surface of the electrode during electrolysis. Thus, the presence of a strong electric field might be a requirement for excess power generation in Fleischmann–Pons-type electrochemical experiments.

## 4. Conclusions

The results of over 100 calorimetric experiments on palladium, palladium alloys and other materials electrochemically loaded with both deuterium and hydrogen were presented. Nearly 60 experiments run without the addition of chemical additives produced no excess power. These experiments were considered as controls showing that the calorimetry is being performed properly. Some chemical additions that could form an oxide interface on the palladium resulted in yet unexplained small, long-term apparent excess power. One palladium–rhodium cathode produced a strong, positive response that could be excess power after a series of additions. Attempts to reproduce and understand this result are continuing in our laboratory. Finally, a model describing the possible role of oxides interfaces in generating high electric fields that might be a requirement for excess power production is proposed.

## References

[1] M. Fleischmann and S. Pons, *J. Electroanal.l Chem.* **261** (1989) 301–308.
[2] *Proceedings of the International Conference on Cold Fusion from ICCF1* (1990) – ICCF14 (2008)
[3] M.C.H. McKubre, R.C. Rocha-Filho, S.I. Smedley, F.L. Tanzella, S. Crouch-Baker, T.O. Passell and J. Santucci, in *The Science of Cold Fusion*, T. Bressani, E. Del Giudice and G. Preparata (Eds.), Conference Proceedings Vol. 33, Italian Physical Society, Bologna, Italy (1991), pp. 419–443

[4]   M.C.H. McKubre, S. Crouch-Baker, A.M. Riley, S.I. Smedley and F.L. Tanzella, Proceedings of the 3rd International Conference on Cold Fusion, *"Frontiers of Cold Fusion"*, H. Ikegami (Ed.), Universal Academy Press Inc., Tokyo, Japan, (1992), pp. 139–150

[5]   E. Storms, *J. Fusion Technol.* textbf29 (1996) 261–268.

[6]   I. Dardik, H. Branover, A. El-Boher, D. Gazit, E. Golbreich, E. Greenspan, A. Kapusta, B. Khachatorov, V. Krakov, S. Lesin, B. Michailovitch, G. Shani and T. Zilov, *Proceedings of the 10th International Conference on Cold Fusion*, ICCF-10, Cambridge, MA (2003).

[7]   I. Dardik, T. Zilov, H. Branover, A. El-Boher, E. Greenspan, B. Khachatorov, V. Krakov, S. Lesin, and M. Tsirlin, Presented at the *11th International Conference on Cold Fusion*, ICCF-11, Marseilles, France (2004).

[8]   V. Violante, F. Sarto, E. Castagna, M. McKubre, F. Tanzella, G. Hubler, D. Knies, K. Grabowski, T. Zilov, I. Dardik and C. Sibilia, in *8th International Workshop on Anomalies in Hydrogen / Deuterium Loaded Metals*, Sicily, Italy (2007).

[9]   V. Violante, F. Sarto, E. Castagna, M. Sansovini, S. Lecci, D.L. Knies, K.S. Grabowski and G. Hubler, *Proceedings of the 14th International Conference on Cold Fusion*, ICCF-14, Washington, DC (2008).

[10]  F. Sarto, E. Castagna, M. Sansovini, S. Lecci, V. Violante, D.L. Knies, K.S. Grabowski and G. Hubler, *Proceedings of the 14th International Conference on Cold Fusion*, ICCF-14, Washington, DC (2008).

[11]  E. Castagna, M. Sansovini, S. Lecci, A. Rufoloni, F. Sarto, V. Violante, D.L. Knies, K.S. Grabowski, G. Hubler, M. McKubre and F. Tanzella, *Proceedings of the 14th International Conference on Cold Fusion*, ICCF-14, Washington, DC (2008).

[12]  S. Barrowes and H. Bergeson, *Fusion Technol.* **26** (1994) 365–368.

[13]  V. Violante, F. Sarto, E. Castagna and S. Lecci, Presented at the *15th International Conference on Cold Fusion*, ICCF-15, Rome, Italy (2009).

[14]  C. Otero Arean, *Chem. Phys. Lett.* **370** (2003) 631–635.